Miniature bioanalytical assays utilizing mechanical actuation of microspheres

by

Emily B. Hanhauser

B.S., University of Wisconsin - Madison (2012)
S.M., Massachusetts Institute of Technology (2017)

Submitted to the Department of Mechanical Engineering
in partial fulfillment of the requirements for the degree of

Doctor of Philosophy in Mechanical Engineering

at the

MASSACHUSETTS INSTITUTE OF TECHNOLOGY

September 2023

Authored by: Emily B. Hanhauser
Department of Mechanical Engineering
August 25, 2023

Certified by: Rohit N. Karnik
Tata Professor of Mechanical Engineering
Thesis Supervisor

Accepted by: Nicolas Hadjiconstantinou
Department of Mechanical Engineering Graduate Officer

Miniature bioanalytical assays utilizing mechanical actuation of microspheres

by

Emily B. Hanhauser

Submitted to the Department of Mechanical Engineering
on August 25, 2023, in partial fulfillment of the
requirements for the degree of
Doctor of Philosophy in Mechanical Engineering

Abstract

An estimated 70% of medical decisions rely on diagnostic results, yet half of the global population lacks access to diagnostic testing. Geography contributes to this gap, with decreased access found in decentralized settings, which can lack the physical and labor infrastructure necessary for gold standard bioanalytical assays. In such settings, lateral flow affinity assays remain the technique of choice, due to their fast time-to-result, ease-of-use and deliverable geometry. However, these assays suffer in sensitivity, with limits of detection 10 - 1000x higher than their gold standard counterparts. Capitalizing on transport advantages at small scales, many microfluidic devices enable high sensitivity assays in a compact form, but their translation to the field is often challenging due to their complexity and the required supporting instrumentation. As a result, gaps in diagnostics, suitable for the realities of operating in decentralized settings, remain.

Inspired by challenges demonstrated during the height of the COVID-19 pandemic, this thesis introduces an affinity assay platform that utilizes simple mechanical, non-fluidic actuation of microspheres on a sensing surface to quantify bioanalytes in liquid samples. The assay integrates two processes, capture of analytes during bead sedimentation, and analysis based on bead interactions with a sensing surface using optical microscopy and image processing. The assay can be performed in a standalone device using minimal manual steps and in less than 30 minutes. Combined with single molecule sensitivity demonstrated by previous bead-based assays, this platform has the potential to enable high sensitivity bioanalysis with the ease-of-use profile required for decentralized settings.

In the first part of this thesis, we describe a framework for predicting bead-analyte capture over a range of bioanalytes to aid in design across applications. We apply this method to design and analyze our proposed capture method, and to examine and predict transport advantages that arise from settling microspheres. In the second part, we investigate multiple simple actuation mechanisms that lead to bioanalyte quantification based on bead-surface interactions. While nearly all mechanisms show initial efficacy, thermal diffusion was selected for further development, with

demonstrated picomolar limits of detection using a model assay, and bead sliding is also explored for its potential versatility and simplicity of imaging. As nonspecific binding of beads to the surface limits sensitivity, we also theoretically model and experimentally investigate surface coating techniques to minimize this effect and demonstrate preliminary enhanced assay sensitivity using a zwitterionic coating.

Finally, using a simple device prototype, we demonstrate the ability of our assay to quantify cardiac troponin I (cTnI), an established biomarker for cardiac injury. Because elevated levels can indicate heart attack or other critical conditions, measuring cTnI accurately and rapidly is essential. cTnI is quantified via immunoaffinity techniques, with current generation high sensitivity lab assays reaching 0.001 ng/mL limit of detection (LOD) in 30 minutes to one hour and bedside point-of-care (POC) devices having 20x higher LOD but in 15 minutes. The instrumentation requirements of these assays make them expensive and challenging to perform in decentralized settings. As the global leading causes of death continue to transition from infectious to chronic diseases, increasing access to cTnI diagnostics will be crucial to improving health outcomes.

Our results show that our integrated assay can detect cTnI at 0.01 ng/mL in buffer and at 0.1 - 1 ng/mL in 10x diluted serum in a 1% BSA buffer in under 30 minutes. This is a clinically-useful result, with our assay showing LODs 5-25x higher than current bedside POC assays and on par with previous generation high sensitivity lab assays (0.1 – 1 ng/mL), but in a format that requires a single manual transfer step and no specialized or dedicated instrumentation. The performance of the current assay is limited by sensing surface variability, which could be improved by optimization of surface chemistry and blocking reagents. Overall, the platform presented in this thesis could enable quantification of bioanalytes at sensitivities approaching current standard methods but in a user-friendly, high-throughput, distributable and rapid format, an important step forward towards filling the gap in technology for decentralized diagnostics and for other monitoring applications, such as those in water and food safety.

Thesis Supervisor: Rohit N. Karnik
Title: Tata Professor of Mechanical Engineering

Acknowledgments

This PhD journey, from biologist to mechanical engineer, was not without its challenges, but overall, has brought immense personal and professional growth and much joy. It has been my good fortune to be surrounded by people who have supported me throughout and continue to offer their encouragement as I transition to whatever comes next. Thank you to everyone with whom I have interacted with over the past years. My success on this path would not have been possible without you. I particularly wish to thank the following people:

- My advisor, Professor Rohit Karnik, who never saw my background as a barrier to achieving to my goals. He is one of the smartest, kindest and humblest people I've ever known, and exemplifies what it means to be a rigorous and ethical engineer and a conscientious human. Thank you for taking a chance on me and making this journey possible.

- My committee members, Professors Scott Manalis and John Hart, whose feedback challenged me to think of things from a different perspective and made this work stronger. I have learned much from our interactions and appreciate your consistent enthusiasm for my ideas and skills.

- Other mentors at MIT, who are relentlessly committed to education and embody mind, hand and heart, including Professor Giovanni Traverso, Professor Ellen Roche, Professor David Wallace, Professor Amos Winter, Professor Evelyn Wang, Pratik Shah, Nevan Hanumara, Bavand Keshavarz and Benita Comeau.

- Mentors from outside of MIT, whose willingness to teach and encouragement of curiosity has given me confidence to pursue my interests. I especially would like to thank my internship mentors at Amgen and Illumina, as well as my pre-MIT lab at BWH including Tim Henrich, Athe Tsibris, Jon Li and Nina Lin.

- The members of the Micro- and Nanofluidics Research Lab and the Mechanosynthesis Lab, who have provided technical support and general grad school com-

radery. Special thanks to Mary Strawser, Michael Bono, Krithika Ramchander and Chun Man Chow, with whom I worked closely.

- The administrative staff of MIT MechE, who answer all of our questions and keep us on track with a smile, including Alexandra Cabral, Leslie Reagan, Saana McDaniel and Una Sheehan.

- The Tata Center at MIT and all of the wonderful collaborators I met through the center, including Chintan Vaishnav, Robert Stoner, Professor Indra Sen, Harsha Karumanchi, Professor Suman Chakraborty and Dr. Satadal Saha. It is a rare opportunity to conduct on-the-ground, immersive fieldwork, and our work together convinced me of its importance on top of being deeply enriching.

- The members of Deutsches Haus, who have provided mutual support and comedic relief, as well as given me a home on MIT's campus. It's been beyond wonderful to be your GRA – danke schön!

- Friends old and new, near and far, who have kept me balanced and laughing, taught me the power of vulnerability and lifted me up during challenging times, especially Emeline, João, Marghe, Uzo, Marti, Manu, Isa, Rafa, Daniela, Mali, Victor, Marie, Eesh, Esther, Katerina, Adrienne, Catherine, Gabi, Pablo and Sahil. Your support means the world to me.

- My family, whose enthusiasm, support and encouragement of fun has remained steadfast since the beginning. Your constant reminders that I am stronger than I know, and that I am but one being in the web of the world, has guided my path, and I am lucky to have your love as a foundation on which I continue to build.

Finally, these years would have not been possible without financial support from the following organizations and fellowships: the Abdul Latif Jameel Water & Food Systems Lab (J-WAFS), the MIT Tata Center for Technology and Design, the National Science Foundation Graduate Research Fellowship Program, the MathWorks Graduate Student Fellowship and Hugh Hampton Young Memorial Fellowship.

Contents

List of Figures

THIS PAGE INTENTIONALLY LEFT BLANK

List of Tables

Chapter 1

Introduction

1.1 Gaps in diagnostic access

Protecting human, animal, and environmental health relies on accurate quantification of biological analytes from diverse sample matrices to inform decisions on an individual and societal level. In healthcare, it is estimated that more than 70% of medical decisions are based on diagnostic results [1]. The consequential nature of diagnostics is recognized by the World Health Organization (WHO), which in 2018, started an Essential Diagnostics Lists to complement their Essential Medicine List [2].

Over the past few decades, technological advancements have made medical diagnosis more sensitive, faster, higher throughput and cheaper, which has increased access across the globe. An example of this is genomic sequencing, the cost of which, thanks to developments in chemistry, automation and bioinformatics, has fallen from $2.7 billion during the Human Genome Project in 2000 to less than $1000 today [3]. This precipitous decrease in price has the potential to revolutionize medicine and bring society closer to realizing highly personalized medical treatments.

Despite these advances, major gaps in medical diagnostics remain. According to a 2021 study in the Lancet, in the treatment of several chronic and infectious diseases, the largest drop in patient retention occurs at the diagnostic stage (Figure 1-1 [4]). It is estimated that nearly half of the global population lacks access to medical diagnostics [4]. Not only does this gap affect individual patient health, but the lack of

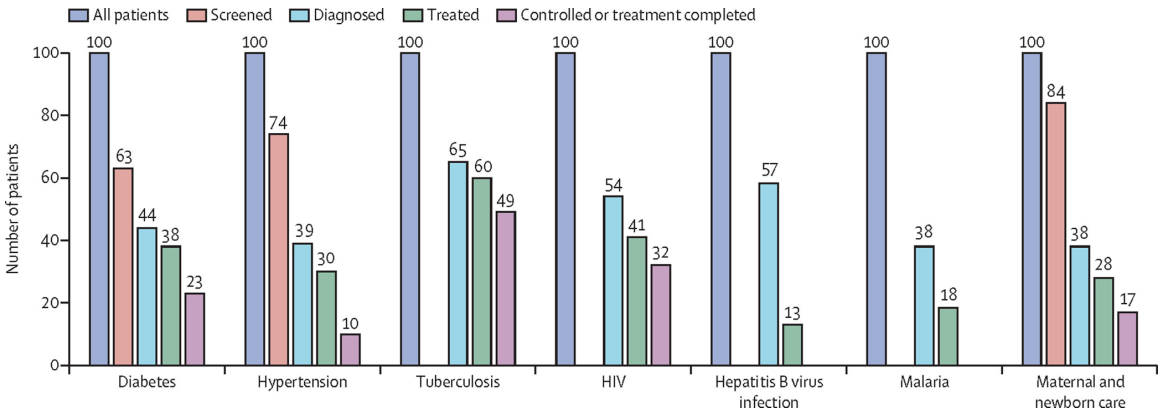

Figure 1-1: **Patient retention at each treatment stage in seven health conditions.** The largest gap is found at the diagnostic stage. Reproduced from [4] with permission through license signed with MIT.

data also restricts public health monitoring campaigns, pandemic surveillance, and global health security [5].

Maps of medical test availability suggest that geography contributes to this gap. Figure 1-2 illustrates the proportion of the population that has access to tests for human immunodeficiency virus (HIV) or glucose in Malawi and Senegal [4]. Access to HIV tests is better than access to glucose tests, reflective of the large international investment in HIV testing and treatment. In contrast, access to glucose tests is much poorer, with less than 20% of the population having access over the majority area of each country. The areas that do have high access tend to be in urban or peri-urban centralized settings, which have relatively greater infrastructure and resources than decentralized settings. Though diagnostic literature has often focused on lower- and middle-income countries (LMIC), disparities in access also are present in high income countries. For example, Figure 1-3 shows a similar picture of decreased decentralized access but in the state of Illinois in the United States, where travel time to testing sites at the beginning of the COVID-19 pandemic could be greater than two hours [6]. Together, these data suggest that improving diagnostic access will require appropriate technology and policy for decentralized settings.

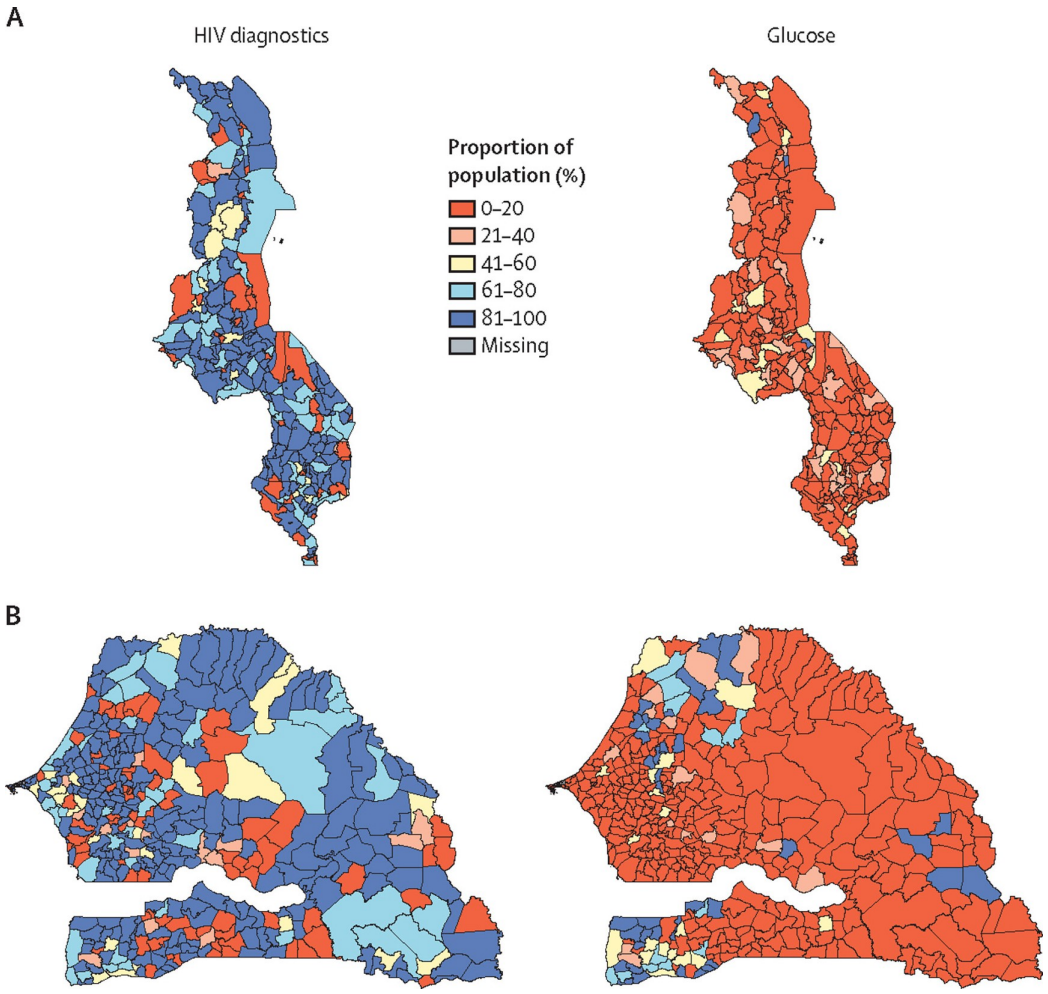

Figure 1-2: **Geographic access to HIV diagnostics or glucose tests in Malawi (top row) and Senegal (bottom row).** Access to HIV diagnostics is greater than for glucose diagnostics, reflective of the historical funding for infectious disease diagnostics. Reproduced from [4] with permission through license signed with MIT.

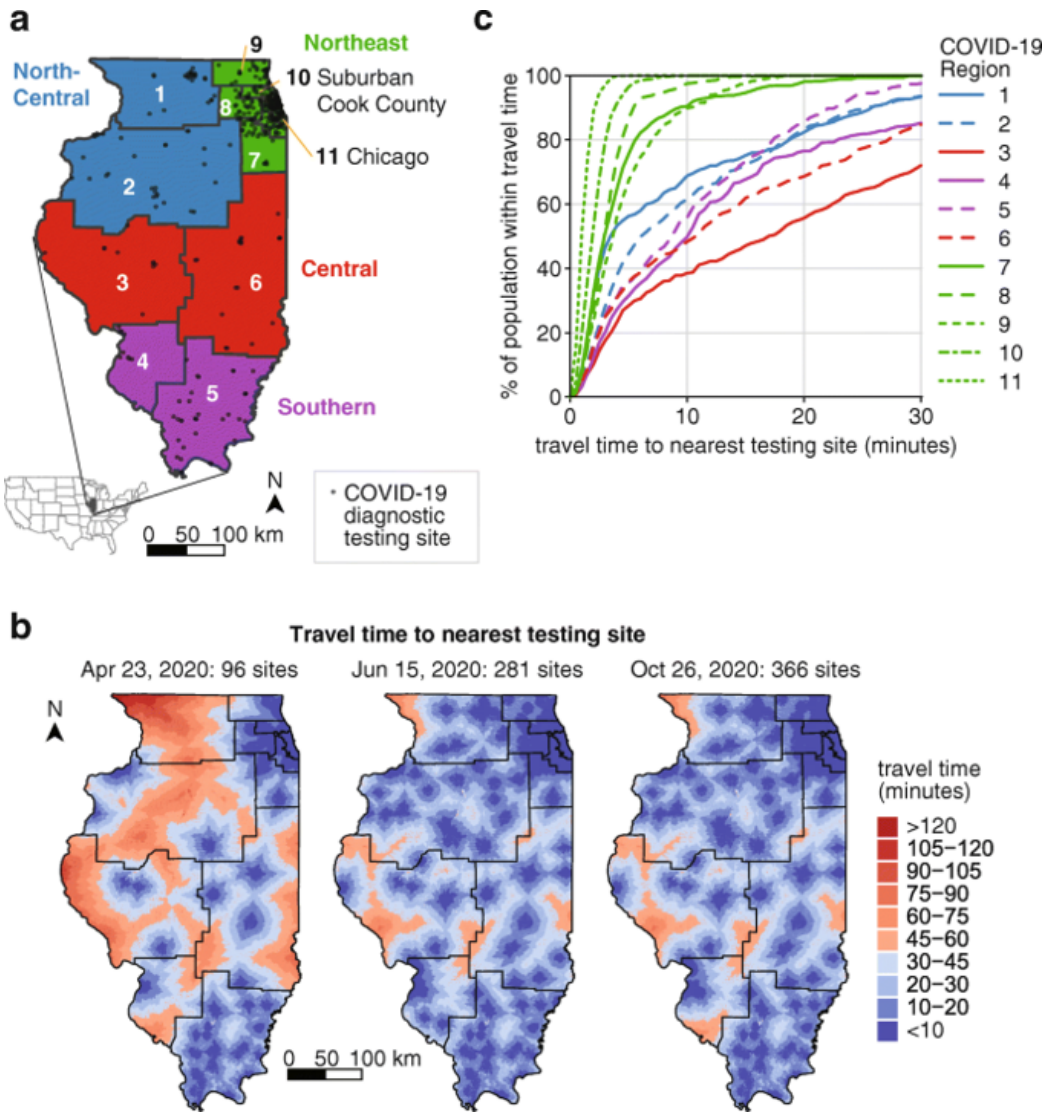

Figure 1-3: **Access to COVID-19 diagnostics in Illinois, USA at the beginning of the pandemic**. Reproduced from [6] with permission through license signed with MIT.

1.2 Current diagnostics in decentralized settings

What is the difference between diagnostic assays typically used in centralized versus in decentralized settings? Diagnostics ideal to each of these settings reflect the healthcare infrastructure and the realities of operating there. To compare assays, we use the axes in Figure 1-4. On the y-axis is operational complexity, a qualitative measure that takes aspects other than analytical performance into account. This includes attributes such as cost, user-friendliness, time-to-result, required infrastructure and deliverability. The x-axis is the limit of detection (LOD), the lowest analyte concentration that can be sensed reliably by a given assay. In general, it is desirable for the LOD to be as low as possible, but the required concentration for a specific application depends on the target analyte.

Centralized settings often have large, tertiary hospitals and commercial diagnostic laboratories. This level of infrastructure supports high-throughput, parallelized analysis using instrumentation which is operated and supported by trained technicians and scientists [4]. Because of these resources, diagnostics in centralized settings fill the entire range from routine to specialized, possess sensitivities required for specific applications (which can approach 10^{-18} molar [M]) and can tolerate higher costs and longer times to return results (Figure 1-4a) [7, 8].

In contrast, healthcare facilities in decentralized settings are generally limited to primary health clinics which have, at most, basic laboratory infrastructure to support routine analyses [4, 5]. Another example of a decentralized setting is sites which are set up on demand for outbreak or public health responses. These sites can consist of little more than a tent in a parking lot, as was seen during the COVID-19 pandemic [9]. Assays appropriate for these settings are low-cost, rapid enough to return a result within the length of a patient visit (<30 minutes) and operable without extensive training or supporting instrumentation. Ideally, these assays are also quantitative with LODs relevant for clinical decisions (10^{-15} - 10^{-12} M) [7, 8].

With poor access to diagnostics in decentralized settings, where do current technologies fail with respect to the ideal characteristics outlined above? Diagnostic assays

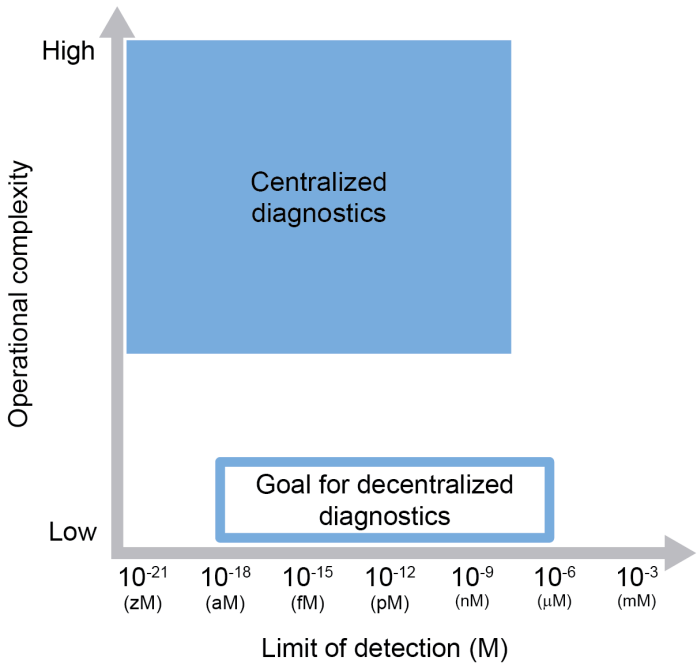

(a)

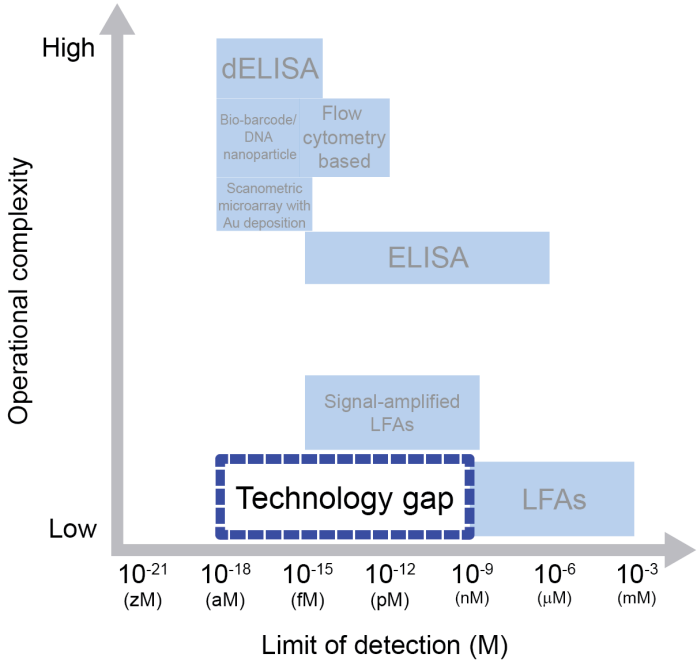

(b)

Figure 1-4: **Current affinity assay landscape has gaps for decentralized assays.** (a) Assays suitable for decentralized settings have detection limits similar to those in centralized settings, but with much lower operational complexity. (b) Current affinity assays generally either have high sensitivity but lack user-friendliness, or are very user-friendly but lack sensitivity, leading to a technology gap for decentralized diagnostics.

generally fall into two broad categories: affinity and molecular. The current gold standard decentralized diagnostics, affinity assays, rely on agents that specifically bind a target analyte in a liquid sample and generate a quantifiable physical or chemical signal [7, 10]. A wide variety of affinity agents, specific to proteins, nucleic acids, chemical species and whole cells, are available and give this assay category broad applicability. The other type of assay, molecular assays, measure specific nucleic acid sequences via amplification or enzymatic reactions. Examples of these types of assays include polymerase chain reaction (PCR) and variations thereof, as well as CRISPR-based assays [11], which are a relatively recent addition. Molecular assays have superior sensitivity to affinity assays, but their application to decentralized analysis has been historically hampered by the need for instruments with precise thermal control, reagent supply chains, and sample preparation, as well as by their sensitivity to contamination. New advances in chemistry and assay digitization, which makes them more quantitative and less susceptible to contamination, have removed many of these barriers and it is plausible that molecular assays may replace affinity assays for many analytes in the future. However, not all medical conditions can be diagnosed or monitored via nucleic acid analysis. Because of this, there will always be a need for affinity assays and their optimization remains essential to improving diagnostic access.

Two versions of affinity assays are common in clinical use. The enzyme-linked immunosorbent assay (ELISA) utilizes enzyme-conjugated affinity agents to generate a quantifiable colorimetric or fluorescent signal indicative of the analyte concentration in the sample (Figure 1-5). These well-established, quantitative assays can have sensitives approaching 10^{-15} M and are performed in a high-throughput manner in 96 well plates [10, 12]. However, what ELISAs have in sensitivity they lack in usability. Relying on diffusion for analyte-affinity agent binding, ELISAs can take 4-8 hours to return a result. They also require several reagent additions and washing steps, and necessitate use of a plate reader to generate quantitative results. These usability challenges make ELISA hard to perform reliably in decentralized settings.

The other version of the affinity assay, the lateral flow assay (LFA), uses a porous

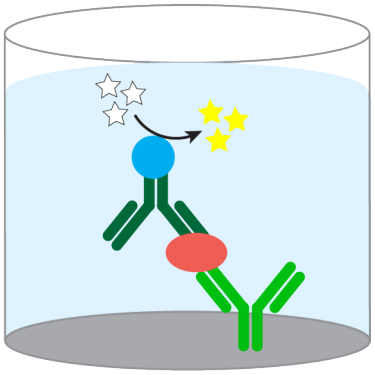

Figure 1-5: **The enzyme-linked immunosorbent assay (ELISA)** A capture affinity agent is affixed to the bottom surface of a well (bright green) and binds to analyte (pink oval) upon sample introduction. The detection affinity agent subsequently binds to the analyte (dark green), creating the sandwich structure. The detection agent creates a signal, either via enzymatic digestion of a colorimetric or fluorescent substrate (white stars), which is quantified to determine the analyte concentration.

substrate to wick a fluid sample along the length of a test strip via capillary action. Analytes bind affinity agents as the liquid sample flows across the strip and finally end up at a designated detection zone, which changes color if analyte is present. Examples of LFAs include pregnancy tests and COVID-19 rapid tests [13]. Conventional LFAs are easy-to-use, low-cost (<$1 per test [12]) and return results in <30 minutes, making them widely used in decentralized settings. What they have in usability, LFAs lack in sensitivity, with LODs in the micromolar (10^{-6} M) range, and this test format is qualitative or semi-quantitative. Modifications to increase LFA sensitivity, through methods such as incorporating electrochemical or fluorescent signals, have been widely investigated and have resulted in improved assays with 10^{-12} M LODs [12]. However, this comes at the cost of increased assay complexity, as these read-out methods often require a separate dedicated instrument with associated cost and usability concerns, which complicates deployment of these improved LFAs to decentralized settings.

1.3 Microfluidic diagnostics: their advantages and challenges

Emerging several decades ago [14], microfluidics manipulates small quantities of fluids in devices with micrometer-sized features. At this scale, fluid flow is laminar and predictable, which allows for the controlled deposition and movement of reagents, and mass and heat transfer occur rapidly [14–16]. Capitalizing on these advantages, scientists and engineers have used microfluidic tools to miniaturize biological and chemical assays, chemical synthesis, and single-cell studies, among other applications [14–18]. Apart from the microscale physical phenomena that allow assays to be performed faster and with higher sensitivity, microfluidic devices can have compact, centimeter-scale footprints and utilize smaller reagent and sample volumes, both of which contribute to assay parallelization capabilities and overall lower cost. These advantages are appealing in particular for decentralized diagnostics [15, 17].

Scientific literature is ripe with microfluidic demonstrations of conventional assays, including ELISA [19] and PCR [20], as well as assay types that utilize novel sensing methods including temperature [21] and gas generation [22]. The current most sensitive commercially-available microfluidic affinity assay is the single molecule array (SiMOA), a digital ELISA (dELISA) method which captures analytes using antibody-functionalized beads, compartmentalizes single beads into microwells and senses analytes using enzyme-catalyzed fluorescence (Figure 1-6) [23–25]. Due to signal enhancement that comes from compartmentalization, this method can detect single analytes, improving on conventional ELISA with LODs in the attomolar (10^{-18} M) range, time-to-result on the order of several hours and a compact device footprint. This assay has also been demonstrated in a droplet-based format [24], and is the core technology of Quanterix, Inc. Other affinity assays that utilize microfluidics and/or bead-based sensing include biobarcode assays [26], scanometric assays based on nanoparticle growth [27] or bead-based flow cytometry or laser-assisted assays, such as those commercialized by Luminex, Inc.

Despite the advantages of microfluidics and years of academic development, trans-

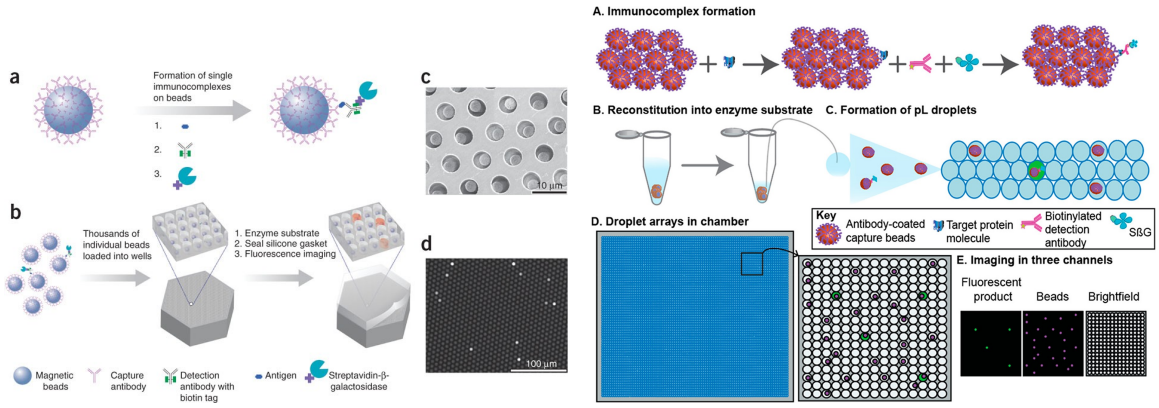

(a) (b)

Figure 1-6: **Current most sensitive digital ELISA assays enabled by microfluidics.** Digitization is accomplished by compartmentalization in microwells (a) or in droplets (b). Reproduced from [23] and [24], respectively, with permission through license signed with MIT.

lating these tools to the field remains a challenge and relatively few microfluidic devices have made it to the commercial market [15, 16, 28]. A major barrier arises due to the instrumentation required for robust and reliable device operation. Precisely tuned and timed pumping, which is nontrivial to start and maintain, is necessary for accurate control of incubation times and volume or reagent metering. Furthermore, full sample-to-result processing requires sample preparation and/or extraction, assay steps and signal readout, which decrease usability if performed manually or requiring multiple devices. Because of this, custom instrumentation and software is often designed to carry out microfluidic assays. Maintaining instrumentation and reagents requires supply chains, technical support and transportation, each of which can be unreliable in decentralized settings. The result of these challenges, among others, is that microfluidic technologies remain largely confined to academic labs and have not made the impact projected by their advantages. Shields IV summarized this in a 2017 publication [18]:

"Device-related barriers typically arise from the focus of research labs to produce new technologies, often at the expense of practicality for the end-user."

Because of the unoptimal performance of current affinity assays and translation

barriers encountered by microfluidics, there remains a technology gap for decentralized diagnostics (Figure 1-4b). Filling this gap requires assays that have sensitivities similar to those of ELISAs but with the low operational complexity of LFAs.

1.4 Opportunity: diagnostic devices without fluidic manipulation

Much of the above-described instrumentation needed to operate microfluidic devices is the fluidic circuitry and pumping. Devices that avoid fluidic manipulation and instead rely on moving beads or other surfaces relative to the fluid sample could enable easier device operation and widely distributable assays. This thesis introduces one such platform, for which an embodiment and workflow is shown in Figure 1-7. A liquid sample (in this illustrative case, saliva), is deposited into a small cuvette-like device, which contains affinity-agent functionalized particles. The device is capped, inverted several times to mix the particles with the fluid sample and promote analyte-affinity agent binding, and then set upright such that the beads settle under their own mass. The beads settle onto a functionalized surface and interact with the surface via a natural driving force (such as gravity-induced rolling or natural thermal motion), or a force applied via simple instrumentation that might be found in a lab, such as a centrifuge or a cell phone vibration motor. The interaction between the beads and the surface under this actuation indicates the presence or absence of analyte on the bead surface. Observation via optical microscopy and quantification of this interaction yields a measurement of the amount of analyte in the original sample.

Aside from the minimal instrumentation required by mechanical (as opposed to fluidic) manipulation, this method has several characteristics appealing for decentralized bioanalysis over other methods (Table 1.1). The assay is self-contained in a single device, requiring no reagent addition or washing steps due to the convective motion of the settling beads. Transport modeling, described in this thesis, suggests that these assays could return a result in under 30 minutes. The assay is highly amenable to

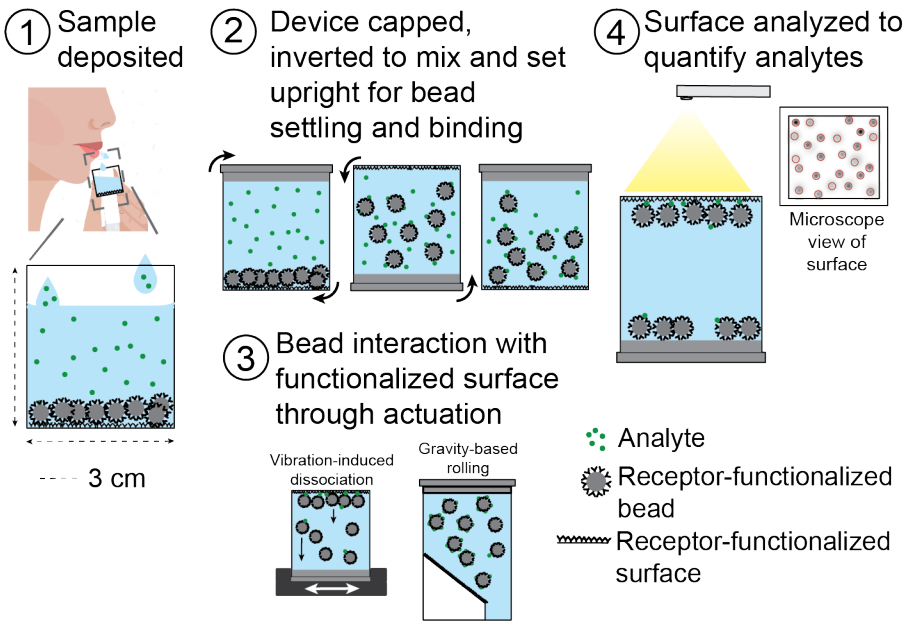

Figure 1-7: **General bead settling + mechanical actuation assay.** After sample deposition and manual mixing, beads capture analyte as they sediment naturally to a sensing surface. A mechanical actuation is applied to the beads, such that they move relative to the fluid and general a quantifiable signal reflective of the analyte concentration.

multiplexed analyses through different sized, shaped or colored particles, which would allow for parallelized tests on a single, low-volume sample. Finally, this platform is massively adaptable to different analytes (including particulate analytes) and different matrices (including nonclinical samples), as long as a suitable affinity agent specific for the analyte of interest can be found. Overall, such an assay platform could fill the gap between current affinity assays, approaching the sensitivity of ELISAs while retaining the usability of LFAs, towards improving decentralized diagnostics and access around the globe.

Table 1.1: **Affinity assays rated on ideal characteristics for decentralized settings.** Ratings go from one star (*), indicating poor performance, to five stars (*****), indicating exceptional performance.

	Quantitative	Single step	Minimally instrumented	Multiplexable	Deliverable	Data richness
LFAs [12]	**	*****	*****	*	*****	*
dELISA [23, 25]	*****	*	*	***	*	**
Bio-barcode [26]	*****	*	**	*****	*	**
Flow cytometry-based	*****	*	**	*****	*	***
This work	****	****	*****	****	*****	****

1.5 Literature review of concepts and results relevant for this thesis

1.5.1 Bead-based, surface interaction sandwich assays utilizing fluidic and non-fluiding actuation methods

Our proposed platform builds on previous studies of actuated bead-surface interactions as signals for bioanalyte concentration in sandwich assays (Table 1.2). Some of the first reported assays in this class used microfluidics to generate the shear forces required to manipulate beads and wash away nonspecifically-bound beads. For example, Mulvaney et al. created a fluidic force discrimination assay, in which functionalized beads, previously incubated with a sample, are introduced into a microfluidic channel with a functionalized surface [29–33]. The beads are allowed to briefly interact with the surface and then fluid flow washes away nonspecifically-bound beads. Beads remaining on the surface are quantified via microscopy and, using a standard curve, converted into analyte concentration. This assay platform reached femto- to attomolar LODs for DNA, staphylococcal enterotoxin B and ricin A chain in complex matrices, and in some cases showed 10 orders of magnitude in dynamic range. However, multiple

hands-on transfer and washing decrease its user-friendliness.

A modification of this FFD method was developed by Tekin et al., who used magnetic beads to enhance bead localization to the surface [34–37]. Functionalized 1.0 micron (μm) magnetic beads are patterned onto the sensing surface. Analyte is captured from a sample using functionalized 2.8 μm beads, which are then flowed across the surface in the presence of a magnetic field. The flow helps to disrupt nonspecific binding (NSB) and the larger beads are particularly attracted to the small beads through magnetic dipole-dipole forces, creating a pattern of large conglomerate bead "spots" when analyte is present. Aided by a microfluidic chip which performs all steps, the assay takes 20 minutes to run and reached 0.060 fM LOD for tumor necrosis factor alpha in serum.

Morozov and Morozova used fluid flow and other actuations to drive beads across a microarray surface, in what they term "active" bead-linked immunoassays [38–41]. These methods include electrophoresis, magnetophoresis, magnetic pulling or dragging and centrifugation. The most sensitive of these assays involves electrophoretically-assisted deposition of analyte on a functionalized surface, followed by magnetically-assisted deposition of beads in shear flow, which helps to disrupt nonspecifically-bound beads [40]. Analyte quantification occurs through counting of residual beads. Though this assay can be extremely fast ($<$5 minutes), was demonstrated complex food and water matrices and reached zeptomolar LODs, it has onerous instrumentation requirements, including a voltage source, magnets, fluidic pump and microscope.

Gravity-induced sedimentation has been investigated as a method to remove nonspecifically-bound particles from a sensing surface. In one such platform, the sensing surface is the inside cap surface of a 1.5 milliliter microcentrifuge tube [42]. The detection particles are in-house-synthesized, antibody-functionalized, 5 μm retroreflecting cubes, which reflect incident light in a narrow beam making them brighter and easier to detect than light-scattering surfaces. Cubes are incubated with sample separately to bind analytes and then injected via syringe pump into the microcentrifuge tube. After sedimentation to the surface, the tube is inverted to promote dissociation of nonspecific cube-surface interactions. Residual cubes on the surface are counted

via a CMOS camera. Despite a longer assay time of 1.5 hours, this simple assay could detect whole *Escherichia coli* or MS2 bacteriophage virions at 10^4/mL (equivalent to 0.02 fM) in a diluted serum.

Another group used in-house synthesized retroreflecting Janus spheres (0.75 μm diameter) and a microfluidic chip for a sedimentation-based assay [43]. Antibody-functionalized spheres are incubated with sample off-chip to capture analytes, injected into the microfluidic chip, and allowed to settle onto the antibody-functionalized surface. The chip is subsequently inverted to promote gravity-induced sedimentation of weakly bound beads and the residual beads on the surface are quantified using light-emitting diode illumination and a CMOS camera. The entire assays takes 35 minutes and it was demonstrated to detect creatine kinase fraction MB in serum samples at 7586 fM. Both of these sedimentation assays require little instrumentation, but utilized custom-made particles that could hinder their translation initially.

Though single particle tracking has been used in biological research for several decades [51], it is has only recently been applied to biosensors. With both extensive theoretical and experimental work, Visser et al. has explored the use of functionalized, tethered particles to detect and temporally resolve changes in biomarker concentration [44–46]. This platform involves functionalized beads that are linked to a functionalized surface via a DNA tether such that they are spatially ordered. Upon sample introduction, the analyte sandwich created between the bead and the surface confines the bead, which causes it to stick in place for a period reflective of the analyte-affinity agent bond kinetics. Such sensors are able to respond to changes in concentration, which enables continuous monitoring. Though not optimized, experiments with DNA or thrombin were able to quantify 1000 fM concentrations after 5 minutes of incubation.

Diffusion of free particles as a signal for bioanalyte concentration has been previously explored in two formats. In one format, Buskermolen et al. deposited functionalized, micron-sized beads in a chamber on a functionalized slide, introduced a sample containing analyte, monitored the diffusivity of particles over time and related the ensemble average diffusivity to the analyte concentration [47]. In addition to single

Table 1.2: **Previous bioassays using bead-surface interactions as signal.** Assays summarized include those that use fluid flow and other mechanisms.

Actuation mechanism(s)	Analytes demonstrated	Time to result (min)	Best LOD (fM)	Ref.
Shear force generated by fluid flow	Toxins, nucleic acids	25	3.5	[29–33]
Magnetic "pulling" or "scanning", centrifugation, electrophoresis	Toxins, proteins, virions	<5	$1x10^{-6}$	[38–41]
Magnetic localization aided by different sized beads and fluidic force	Proteins	20	0.060	[34–37]
Sedimentation under gravity in microcentrifuge tube using retroreflecting microcubes	Whoe bacteria, virions	90	0.02	[42]
Sedimentation under gravity in microfluidic chip using retroreflecting spheres	Protein	35	7586	[43]
Thermal gradients using tethered particles	DNA, protein	5	1000*	[44–46]
Thermal gradients using free particles	DNA, hormone	5	1000*	[47]
Thermal gradients using free particles confined in microwells	Protein	60	16	[48–50]

* Unoptimized

concentrations, the sensor can respond to step changes in analyte concentration when sample is introduced continuously. Though unoptimized, this platform pico- to nanomolar concentrations of DNA or cortisol in clinically relevant matrices.

In another format, Akama et al. used changes in free nanoparticle motion to determine analyte concentration [48–50]. These functionalized nanoparticles are incubated with sample off-chip for one hour and then introduced into a microwell-patterned microfluidic chamber. Compartmentalization of particles is achieved via magnetic deposition and wells are subsequently sealed using fluorocarbon oil to isolate each bead in a digital assay format. This platform was able to sense prostate-specific

antigen (PSA) at 16 fM in serum samples. However, detection of nanoparticle motion requires high powered darkfield microscopy that increases the instrumentation burden of this technique.

1.5.2 Nonspecific binding between beads and surfaces

The work presented in this thesis also expands understanding of NSB between beads and surfaces, adding to the foundational knowledge generated by previous studies. The majority of investigations into NSB involve the fouling of particles and surfaces by matrix proteins [52]. A common strategy to mitigate NSB is coating surfaces with polymers, such as polyethylene glycol (PEG), to make them hydrophilic and physically block proteins. Studies have established that PEG molecules in the brush conformation, extending from the surface in a layer of height L_0, are more resistant to fouling than molecules in the mushroom formation, which arises on sparsely coated surfaces [53]. L_0 is a function of the polymer grafting density σ on the surface (greater σ, more steric repulsion between chains, longer L_0) and the polymerization degree N of the chain, which is a function of the polymer molecular weight (greater N, longer L_0). Results of studies varying the molecular weight (MW) of the polymer chain have shown that fouling resistance generally increases with increasing polymer MW [54, 55]. Overall, increased fouling resistance is found with higher grafting densities and polymer degrees, though exceptions have been noted.

Brush resistance to protein adsorption depends upon the protein size [56, 57]. Proteins with characteristic length greater than L_0 cannot penetrate the brush and can only reach the underlying surface via brush compression, which is energetically unfavorable. As such, large proteins are physically kept away from the surface, minimizing bead-surface interactions. On the other hand, small proteins can penetrate the brush. When the brush grafting density is high enough, this mechanism is minimized. Many theoretical models have been proposed to predict and explain the behavior of these antifouling coatings, with the major difference between models being the assumed concentration profile of the monomers in the brush layer [53, 58, 59].

Another surface coating that has shown promise in decreasing protein adsorption

to surfaces is zwitterionic (ZI) polymers. ZI polymers are overall neutral, but contain both positively and negatively charged groups [60,61]. These coatings have been found to have higher nonfouling resistance that PEG layers, hypothesized to arise from the more tightly held solvation layer due to the charged chains. Enhanced sensitivity immunoassays in undiluted clinically relevant matrices has been reported utilizing ZI coatings [62,63].

Bead-surface NSB is inherently different from protein-surface NSB due to the difference in scale and the resulting larger contact area between the bead and the surface. Understanding NSB in these systems is important given the ubiquity of bead-surface bioassays. Few experimental studies have examined NSB in this context; here, we briefly review findings from these studies.

Upadhyayula et al. investigated NSB between bare or PEG-coated, 3 μm diameter microspheres and bare or PEG-coated glass slides [64]. The effect of PEG MW and the presence of detergent in buffer (Tween 20) on NSB was examined through experiments which utilized a magnetic field to "pull" beads off of the surface with a 1.2 piconewton (pN) force. Measurements of PEG layer thickness suggested that all coatings were in the brush conformation. Results from these experiments indicated that coating both surfaces with PEG resulted in the lowest NSB, with more beads remaining on the planar surface when either surface did not have PEG. NSB decreased with increasing PEG MW up to 5 kilodaltons (kDa), after which NSB increased slightly. The authors hypothesized that this was due to the conformation of PEG chains in the brush layer and the influence of conformation on the solvation layer, which gives PEG brushes their hydrophilicity and contributes to fouling resistance [65,66]. The effect of detergent on NSB was inconclusive in their experiments. Overall, the authors concluded that PEG grafts decrease bead-surface NSB and that the grafts must have sufficient density, in order to be effective for antifouling applications.

In another magnetic pulling study, Jacob et al. examined the dissociation kinetics of a range of bond types formed by differently functionalized beads and surfaces and revealed that the timescale of bond dissociation could differentiate types of interactions [67]. Using a pulling force of 50 pN, their results suggest the presence of

three different populations of beads: (1) nonspecifically weak binding (fast dissociation kinetics), specific binding (intermediate kinetics) and (3) nonspecific strong/multiple specific bonds (slow kinetics). In experiments approximating sandwich assays, the fraction of beads in each population changed with the concentration of the analyte and that the fraction was also dependent upon the type of sandwich formed.

Beyond PEG brushes, surfaces or surface coatings of other materials have been explored for their ability to resist NSB of particles. Sato et al. theoretically and experimentally examined NSB of uncoated silica nanospheres (25 – 550 nanometers in diameter) to 1 millimeter-thick poly(acrylamide) and poly(dimethylacrylamide) hydrogels in solutions with different refractive indices [68]. The extent of particle-surface binding was examined via quantification of the residual beads on the gel after beads were allowed to settle and subsequently washed. Several findings led to the authors hypothesizing that van der Waals (vdW) interactions caused the adhesion of particles to surfaces. First, when the particle size was decreased, the fraction of spheres remaining decreased. vdW interactions scale with particle size, so this result agrees with the expected behavior. Second, when the index of refraction of the submerging media was incrementally increased to approach that of the silica spheres, the fraction of spheres remaining on the surface decreased. The Hamaker constant, which characterizes the interactions between two materials, controls the strength of vdW interactions and is proportional to the difference between refractive indices of the interacting materials. When materials are similar, the Hamaker constant is decreased, leading to decreased vdW interactions. Based on these results, the authors concluded that vdW interactions are the primary driving force for particle-surface adhesion.

Hong et al. also examined the influence of polymeric surface coatings on the vdW forces between gold (Au) surfaces and spherical Au atomic force microscopy (AFM) probes in aqueous salt solutions [69]. The coating employed was an ethanol plasma polymer film ranging in thickness from 0-87 nanometers. The authors found that the vdW force decreased with increasing polymer film thickness. Thicker polymer coatings increase the distance between the Au surface and Au probes, which decreases the overall vdW interaction between these two elements. Inclusion of the polymer

coating adds another surface with which the Au probe interacts, but the strength of this interaction is decreased due to the similarities of the polymer coating with the surrounding aqueous medium. The authors concluded that polymer coatings can effectively reduce vdW interactions through introduction of a physical separation barrier.

1.6 Thesis organization

This thesis focuses on the theoretical and experimental development of miniaturized bioassays utilizing the mechanical actuation of microspheres. We hypothesize that mechanical manipulation methods, combined with capture-while-settling, can enable sensitive, bead-based affinity assays that are appropriate for minimally instrumented, decentralized bioanalysis. This thesis is organized around four guiding questions:

- *What bead characteristics enable analyte collection by natural bead convection?* Chapter 2 examines transport and reaction models for capture of bioanalytes by beads under the influence of fluid flow and uses results from other fields to develop a framework to aid in design across applications. We utilize our framework to analyze our proposed capture-while-settling mechanism, with fluid flow induced by bead sedimentation.

- *Which actuation mechanisms can apply sufficient force to differentiate between analyte-bound and unbound beads during interaction with a functionalized surface?* Chapters 3, 4 and 5 detail theoretical and experimental explorations of this question in a search for methods that can apply a force less than that of a specific analyte-affinity agent reaction, but more than that of a nonspecific interaction. Using a model analyte-affinity agent system, methods that showed efficacy (Chapter 5) as well as methods that proved more difficult to implement without extensive optimization (Chapters 3 and 4) are presented.

- *How can NSB between beads and surfaces be mitigated?* NSB is the major cause of decreased assay sensitivity and Chapter 6 presents physical theories of NSB to

guide surface optimization through bead size and surface passivation. Extensive experiments based on these predictions are described, ultimately leading to the identification of a promising surface chemistry based on zwitterionic hydrogels.

- *How can bead binding and surface interaction be integrated into a standalone device that enables sensitive analyte quantification?* Detection of a clinically-relevant biomarker, cardiac troponin I (cTnI), is demonstrated in Chapter 7 using an integrated, stand-alone device, achieving LODs of 0.01 and 0.1 ng/mL in buffer and diluted serum, respectively. Chapter 8 summarizes the development of the platform up to this demonstration and discusses the future outlook for its use as a decentralized diagnostic.

THIS PAGE INTENTIONALLY LEFT BLANK

Chapter 2

An analysis framework for bead-based analyte capture to aid in design across applications

2.1 Introduction

Bead-based capture is ubiquitous in bioassay literature and commercial systems, as it offers a simple method to sequester and manipulate analytes in complex matrices. Examples abound for the capture of proteins [70], whole cells including mammalian [71,72], bacterial [73–75], fungal [76] and protozoan [77], whole virions [78–80] and nucleic acids [81]. Commercialized processes include ThermoFisher Scientific's Dynabeads and StemCell Technologies' EasySep beads, both systems for cell isolation; the Luminex assay [82–84], which uses color-coded antibody-functionalized beads for high-throughput multiplexed immunoassays based on flow cytometry or laser-based analysis; and Illumina's DNA preparation kits [85], which fragment and tag nucleic acid strands on beads before sequencing.

First described in the 1980s [86, 87], a major advantage of bead-based capture is the speed. Previous to beads, separations were performed using coated surfaces, such as those in plates and test tubes, with dimensions on the order of millimeters.

These platforms relied on diffusion for analyte transport to the capture agent-coated surfaces, a process which is inefficient at large length scales. For example, a protein with a typical diffusivity of $5\text{x}10^{-12}$ square centimeters per second, traveling from the center of a typical well to the wall ($\sim$ 3 millimeter distance) takes 8 hours. Dispersing a mobile capture surface in the form of beads decreases this time by several orders of magnitude, depending upon the concentration of beads and fluid motion. Colloidal beads, which remain suspended for the time scales of the isolation process, decrease the diffusion distance in a manner inversely proportional to their concentration. For example, for one million colloidal beads in a one milliliter sample, each bead occupies a spherical volume with a 62 micron radius, which reduces the protein to capture surface travel time by nearly 50x. If there is additional fluid motion, analyte transport can be enhanced and collection time can be further reduced.

Beads are also available in a wide variety of sizes and materials, some of which impart other functionality, such as magnetism or fluorescence, and allow for analyte manipulation or analysis on-bead. The breadth of available materials also leads to a variety of functional groups on bead surfaces, including epoxy, carboxyl, amine and hydroxyl, which can be covalently coupled to an array of capture agents. In general, beads are cheap, widely available and easily modifiable, making them one of the main methods for bioanalyte separation.

With the large amount of options available, it is useful to consider which beads are most efficient for a particular application. However, a unified predictive framework for bead-analyte capture is lacking. Bioanalytes range in size from sub-nanometer to tens of microns and have diffusivities over four orders of magnitude [88], such that beads efficient for one analyte may not be optimal for a different analyte. Furthermore, most studies on bead-based capture consider only analyte diffusion as mass transport and do not examine the effects of fluid flow, which is especially relevant for larger beads and analytes [89, 90]. For engineers and scientists developing bioassays, an analysis framework, which can predict the efficiency of capture given a specific analyte and bead properties, would aid in designing bead-based capture systems for a specific application and serve as a starting point for experimental studies.

Towards this goal, this chapter outlines a framework for analyzing and predicting the efficiency of bead-bioanalyte capture. Combining results from previous studies, we first propose a scaling analysis that determines the dominant physical processes in a specific capture application based on bead, sample fluid and analyte properties. We also review models that can be used to predict analyte capture efficiency and delineate when these models are appropriate. Finally, we demonstrate the use of our framework in the design and analysis of our proposed capture process for use in integrated, mechanically actuated assays, ending with a discussion of limitations and how our framework could be made more accurate. It is our hope that the proposed framework is useful for scientists and engineers in the bioassay space.

2.2 Theory: Scaling analysis of bead-based analyte capture

Figure 2-1 depicts a prototypical isolation process and Table 2.1 defines the parameters and their units. Beads of radius r_b and material with density ρ_b are dispersed in a liquid sample of volume V_s with a target analyte. Beads are functionalized with an analyte-specific affinity receptor at a density per unit surface area of n_{ab}. Fluid properties of the sample are the density ρ_f and the dynamic viscosity μ_f. The target analyte has a radius or equivalent radius r_a and diffusivity D_a. The concentration of the beads in the sample is C_b and the concentration of free analytes in the sample is $C_a(t)$. The number of beads in the sample is n_b ($n_b = V_s C_b$). The fluid sample moves around the beads with free stream velocity U_0, which can be imposed by the bead's own settling motion or by externally imposed flow.

In the current framework, we additionally make the following assumptions and discuss the implications of some of these assumptions at the end of the chapter:

- The Reynolds number, $\mathrm{Re} = \frac{\rho_f U_0 d_b}{\mu_f}$, is much less than one, such that flow is creeping and laminar.

- Each bead is isolated and effects from neighboring beads are neglected.

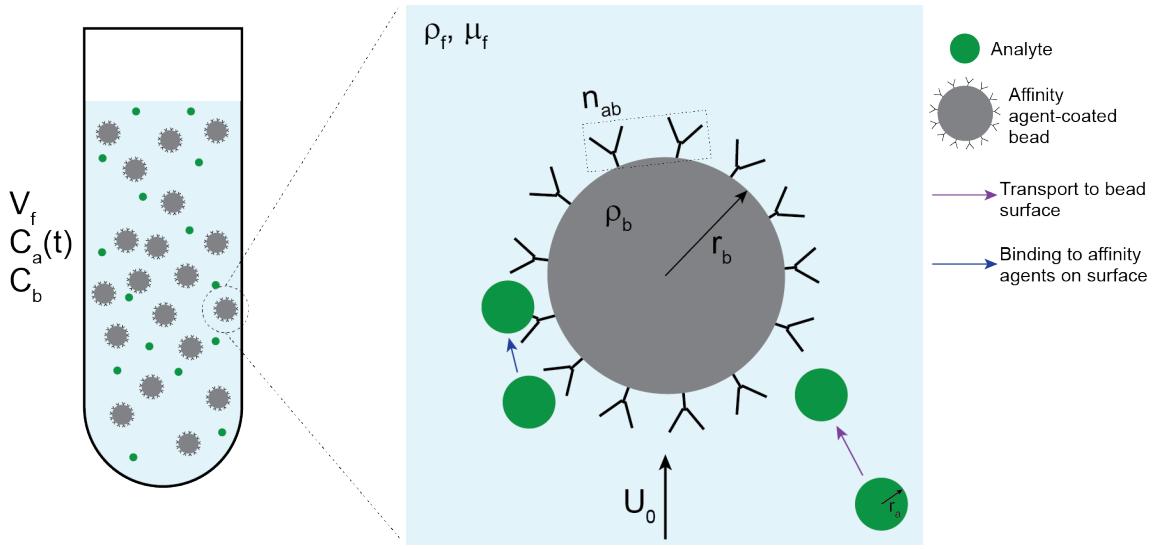

Figure 2-1: **Prototypical bead-bioanalyte binding in a fluid sample.** Beads are homogeneously dispersed in a fluid sample that flows around the bead and contains target analyte. Analyte capture requires two process to occur: the analyte must travel to the surface of the bead (purple arrow) and subsequently bind to the affinity agents on the surface of the bead (blue arrow). Parameter definition and units are given in Table 2.1.

- Analytes are considered to be rigid and we neglect any deformation that might occur due to fluid flow or other processes.

- The bead concentration is such that saturation of the beads surface with analyte can be neglected.

Additional assumptions about specific processes are stated in the corresponding sections in the following model description.

For capture, an analyte must undergo two processes in series. First, it must be transported to the surface of the bead via its own motion, fluid motion or a combination of the two. Second, it must bind to an affinity receptor on the surface of the bead. The overall capture rate is determined by these two processes, which limit the maximum rate at which capture can occur. We first consider each process in isolation (assuming that the other process is so fast as to be irrelevant) and then we consider the processes together.

Table 2.1: **Parameters, symbols and units involved in bead-based analyte capture.** These parameters correspond to those shown in Figure 2-1

Parameter	Symbol	Units	Notes
Bead radius	r_b	m	Bead diameter $d_b = 2r_b$
Bead density	ρ_b	kg/m^3	Property of the material from which the bead is made
Sample volume	V_s	m^3	
Bead concentration	C_b	#/m^3	
Number of beads	n_b		$n_b = V_s C_b$
Affinity-agent coating density on bead	n_{ab}	#/m^2	
Analyte radius	r_a	m	Analyte diameter $d_a = 2r_a$
Analyte diffusivity	D_a	m^2/s	
Analyte concentration	C_a	#/m^3	Decreases with time from initial concentration, $C_{a,0}$
Free stream velocity	U_0	m/s	

2.2.1 Mass transfer to the bead surface

As shown in Figure 2-2, the competing effects of fluid flow and diffusion set up a capture layer l_c around the bead, the thickness of which is the maximum distance away from the bead surface an analyte can be and reach the bead surface. In these laminar, creeping flow conditions, analytes travel on ordered streamlines around the bead. Three extremes arise depending on the size of the analyte, its diffusivity and fluid flow.

Capture by interception

At one end of the spectrum, when the analyte is large but its diffusivity is low (i.e., a mammalian cell), the analyte's path follows its carrying streamline. Capture occurs when this streamline is close enough to the bead for the analyte to make contact with the bead (Figure 2-2, left side). This "limiting" streamline, which separates those that lead to analyte capture by interception from those that do not, is maximally at a distance of r_a from the bead surface [91–94]. This means, on this end of the mass transport spectrum where interception dominates, $l_c = \frac{d_a}{2}$.

We definite a capture coefficient k_+ as the maximum rate of analyte mass transfer

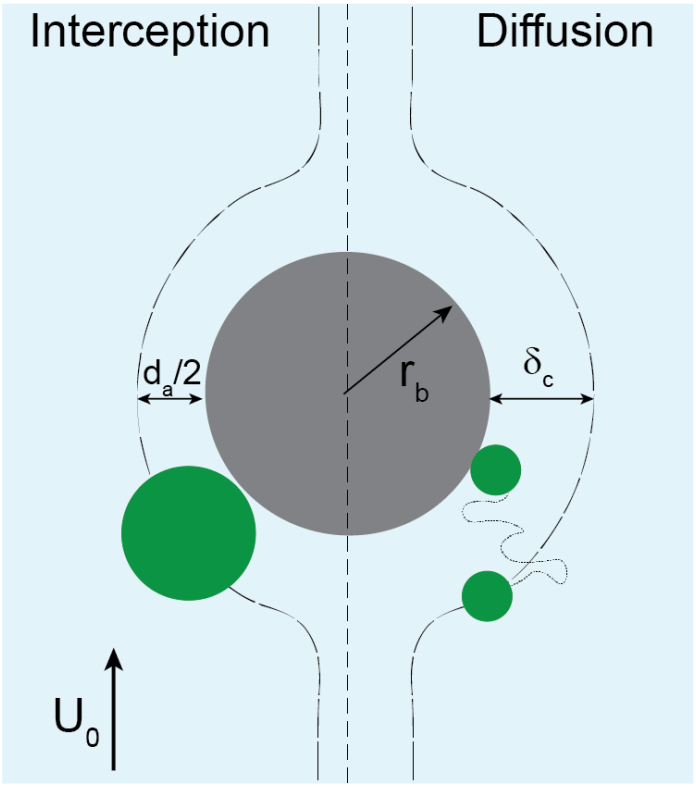

Figure 2-2: **Mechanisms involved in mass transport of the analyte to the surface of the bead.** Analytes approach the bead on fluid streamlines. When the diffusivity of the analyte is low, the analyte remains on this streamline (left side of figure). The streamline, which separates those that lead to analyte capture and those that do not, is $\frac{d_a}{2}$ away from the sphere surface. In this interception case, $l_c = \frac{d_a}{2}$. When analyte diffusivity is higher, the analyte path can deviate from the carrying streamline, creating a layer which has an analyte concentration gradient and is larger than the analyte dimensions (right side of the figure). This layer is the classic concentration boundary layer δ_c in convective diffusion, and is equal to l_c in our forumlation in the case when diffusion dominates the transport process.

to the bead surface; this is analogous to a traditional mass transfer coefficient k_m, but we name it otherwise to emphasize that our analysis extends beyond diffusive mechanisms. Assuming that analyte capture is limited by mass transport, we estimate k_+ by equating the volume of fluid swept due to convection to the traditional definition of mass transfer flux to the surface of a bead:

$$\pi d_b l_c U_{l_c} \Delta C = k_+ A_b \Delta C \rightarrow k_+ = \frac{\pi d_b l_c U_{l_c}}{A_b} \tag{2.1}$$

where A_b is the surface area of the bead ($A_b = \pi d_b^2$), ΔC is the difference between the bulk analyte concentration and the analyte concentration at the bead surface ($\Delta C = C_a(t) - C_{a,s}$). Under the current assumption that any analyte that makes it to the surface is captured, $C_{a,s} \sim 0$ and $\Delta C = C_a$.

U_{l_c} is the velocity the edge of the capture layer, which may or may not be equal to U_0 due to the velocity boundary layer δ_v that grows from the bead's surface and arises from friction [95]. We estimate U_{l_c} based on the Schmidt number (Sc), a comparison of momentum diffusivity to mass diffusivity in the fluid:

$$Sc = \frac{\nu_f}{D_a} \tag{2.2}$$

where ν_f is the kinematic viscosity of the fluid ($\nu_f = \frac{\mu_f}{\rho_f}$). If Sc$>$ 1, momentum transfer is more efficient, $U_{l_c} \neq U_0$, and velocity gradients must be taken into account to estimate U_{l_c}. On the other hand, if Sc$<$ 1, mass transfer is more efficient. In this case, velocity gradients occupy a fraction of l_c and $U_{l_c} = U_0$. In the case of fluid samples with bioanalytes, ν_f is near that of water (10^{-6} m^2/s) and D_a ranges over three orders of magnitude ($10^{-11} - 10^{-14}$ m^2/s) [88]. Thus, Sc $\sim 10^4 - 10^7$ and $U_{l_c} \neq U_0$. Assuming laminar creeping flow, the velocity profile in l_c scales linearly with distance from the bead surface by the shear rate $\dot{\gamma} \sim \frac{U_0}{d_b}$:

$$U_{l_c} \sim \dot{\gamma} l_c \sim \frac{U_0}{d_b} l_c \tag{2.3}$$

Using Equation 2.3, we can now estimate k_+ as:

$$k_+ = \left(\frac{l_c}{d_b}\right)^2 U_0 \sim \frac{\left(\frac{d_a}{d_b}\right)^2 U_0}{4} \sim \frac{R^2 U_0}{4} \tag{2.4}$$

where we define $R = \frac{d_a}{d_b}$, known as the interception parameter [93,96]. Traditional mass transfer coefficients are often nondimensionalized in a Sherwood number (Sh= $\frac{k_m d_b}{D_a}$) to compare enhancement in mass transfer over a purely diffusive (no convection) process. We also define a nondimensional capture coefficient $K_+^* = \frac{k_+ d_b}{D_a}$, which for interception becomes:

$$K_+^* = \frac{R^2 Pe}{4} \tag{2.5}$$

where Pe is the Peclet number, a nondimensional parameter that compares the rate of transport by convection to the rate of transport by diffusion. It is clear that interception becomes more significant as $R \to 1$. In filtration literature, a criterion of $R \ll 1$ is enforced [91,93] and we limit $R < 0.5$ in our current analysis.

Capture by convective diffusion and pure diffusion

At the another end of the spectrum are those analytes which are small relative to the beads and have high diffusivity, such as proteins and virions. In this case, the analyte can deviate from its carrying streamline (Figure 2-2, right side). This extra diffusive motion allows for capture of analytes at distances greater than their critical dimensions [93,97]. There is a thin layer next to the surface of the bead over which a gradient in analyte concentration forms, known as the concentration boundary layer δ_c and equal to l_c in this scenario. We can estimate l_c by equating the time required for the analyte to diffuse a distance l_c ($t_{diff} \sim \frac{l_c^2}{D_a}$) with the time required for the fluid to convect past the sphere ($t_{conv} \sim \frac{d_b}{U_{l_c}}$):

$$\frac{l_c^2}{D_a} \sim \frac{d_b}{U_{l_c}} \tag{2.6}$$

where U_{l_c} is given by Equation 2.3. Solving for l_c, k_+ and K_+^*, one obtains

$$l_c \sim \left(\frac{d_b^2 D_a}{U_0}\right)^{\frac{1}{3}} \tag{2.7}$$

$$k_+ \sim \left(\frac{D_a^2 U_0}{d_b^2}\right)^{\frac{1}{3}} \tag{2.8}$$

$$K_+^* \sim Pe^{\frac{1}{3}} \tag{2.9}$$

In cases in which convection is insignificant either due to low flow velocities and/or highly diffusive analytes (i.e., low Pe), the bead can be considered stationary compared to the analyte and mass transfer occurs by analyte diffusion alone. For this stagnant diffusion case, the capture coefficient, and subsequently the nondimensional capture coefficient, can be found by setting the diffusive flux to the bead surface equal to the definition of the mass transfer coefficient:

$$k_+ A_b \Delta C = \pi d_b D_a \Delta C \rightarrow k_+ = \frac{D_a}{r_b} \tag{2.10}$$

$$K_+^* = \frac{k_+ d_b}{D_a} = 2 \tag{2.11}$$

Nondimensional expression accounting for range of mass transport mechanisms

To account for processes that fall between these three extremes, we add the dimensionless capture coefficients in Equations 2.5, 2.9 and 2.11 to estimate an overall coefficient that considers contributions from all three mass transfer process over the range of Pe:

$$K_+^* = \frac{R^2 Pe}{4} + Pe^{\frac{1}{3}} + 2 \tag{2.12}$$

This assumption of process additivity is analogous to what has been performed in filtration literature [98]. We can check the validity of Equation 2.12 by considering its predictions at extreme values of R and Pe. When R is large and $Pe \gg 1$, $K_+^* \rightarrow \frac{R^2 Pe}{4}$, indicating that interception dominates. This occurs when analyte size increases in

significance compared to the bead size (up to $R < 0.5$ for our analysis), and convection is significant. Further validity is indicated by comparing this term to the interception capture efficiencies η_I from creeping flow mass transfer to single spheres published in the literature:

$$\eta_I = \frac{k_+ A_b}{\pi r_b^2 U_0} = CR^2 \tag{2.13}$$

where the numerator is the volume cleaned, the denominator is the volume swept and the constant C comes from curve fitting and ranges from $1.4 - 1.5$ [93, 94, 98, 99]. Our scaling expression predicts η_I to within a constant:

$$\eta_I = \frac{\left(\frac{R^2 U_0}{4}\pi d_b^2\right)}{\frac{\pi d_b^2 U_0}{4}} = R^2 \tag{2.14}$$

As R decreases but $Pe \gg 1$, convective diffusion becomes significant, the second term dominates Equation 2.12 and $K_+^* \rightarrow Pe^{1/3}$. This agrees with Sherwood numbers reported for diffusion in low Re flow for thin boundary layers and high Pe, $Sh = CPe^{1/3}$, where coefficients range from $C = 0.89 - 0.997$, depending upon the form of the profile used in the integral approximation of the concentration boundary layer [97].

We can use this combined correlation in Equation 2.12 to predict mass transfer for different combinations of bead and analyte as well as predict dimensional capture coefficients for comparison and modeling purposes:

$$k_+ = \frac{K_+^* D_a}{d_b} \tag{2.15}$$

It is useful to examine when interception or convective diffusion is more relevant in conditions were $Pe \gg 1$. Comparing the first two terms in Equation 2.12, we find a parameter C_{int} which predicts when interception dominates [100]:

$$\frac{R^2 Pe}{4} > Pe^{\frac{1}{3}} \rightarrow \underbrace{RPe^{\frac{1}{3}}}_{C_{int}} > 2 \tag{2.16}$$

2.2.2 Analyte-affinity agent reaction at the bead surface

The second process in bead-analyte capture is the reaction of the analyte with affinity receptors at the bead surface. As show in Figure 2-1, beads are covered with an affinity agent at density n_{ab}. Commonly, these affinity agents are antibodies, but other affinity agents can also be efficacious, such as polysaccharides and aptamers, depending on the analyte.

The bound analyte surface density on the beads, B, is controlled by on-rates and off-rates:

$$\frac{dB}{dt} = k_{rxn}^{on} C_{a,s}(t) - k_{rxn}^{off} B \tag{2.17}$$

where k_{rxn}^{on} is the on-rate, $C_{a,s}(t)$ is the concentration of the analytes next to the surface, and k_{rxn}^{off} is the off-rate.

The form of the on-rate varies by analyte type. For a soluble analyte, the entire analyte is the binding target and is free to move in three dimensions [101]. The analyte-receptor reaction is assumed to be monovalent with a one-to-one correspondence between analyte and receptor. In this case, $k_{rxn}^{on} = k_{on}^{3D} n_{ab}(t)$, where $n_{ab}(t)$ is the free receptor density on the bead ($n_{ab}(t) = n_{ab}(0) - B(t)$) and $k_{rxn}^{off} = k_{off}^{3D}$. A critical parameter is the equilibrium dissociation constant, $K_D = \frac{k_{off}^{3D}}{k_{on}^{3D}}$, which governs the amount of analyte that can be bound at equilibrium; lower K_D indicates stronger analyte-affinity agent binding.

Unlike soluble analytes, which are free to move in three dimensions, binding of particular analytes occurs differently. The binding target for the receptor is a surface-bound molecule on the analyte and, while the overall observed reaction is characterized by a single on-rate, the molecular interactions between analyte and bead are more complicated due to the presence of multiple binding receptors and targets in the contact area between bead and analyte [101, 102]. Studies have shown the particle capture process to be additionally dependent on the density of the binding target on the particle surface, the dimensions of the binding target and the receptor, the shear rate and the intrinsic on- and off-rates for the binding target and receptor [103–105].

To date, there is no unifying theory for prediction of overall particle on- and

off-rates given known parameters of the system. Because of this, we use overall "association" and "dissociation" rates after the methodology introduced by Haun and based on empirical experimental evidence [103]. In this case, $k_{rxn}^{on} = k_A$, the observed on-rate, and $k_{rxn}^{off} = k_D$, the observed off-rate.

When mass transfer is not limiting, $C_{a,s}(t) = C_a(t)$ and the maximum rate at which analytes can bind the bead, before analytes start to dissociate toward equilibrium, is determined by the on-rate. As was similar for mass transfer considerations, we define a maximum reaction rate k_{rxn}:

$$k_{rxn} = \begin{cases} k_{on}^{3D} n_{ab} & \text{soluble analyte} \\ k_A & \text{particulate analyte} \end{cases} \tag{2.18}$$

Due to the extrapolation involved in estimating k_A, we note that this is a major source of uncertainty in our framework.

2.2.3 Comparing mass transfer and reaction to determine the rate limiting process in bead-analyte capture

The maximum rates derived previously set limits on the overall capture rate, which can either be equal to one of these maximum rates or fall in between. It is helpful to compare the two maximum rates to predict if either process is rate limiting. This allows for insights into potential system-level optimization, as well as simplifications to models that predict capture efficiency.

This comparison is formalized in the Damkohler number (Da), which follows from nondimensionalization of governing equations (see next section on models) [89]. In our framework, it takes the following form:

$$Da = \frac{k_{rxn}}{k_+} \tag{2.19}$$

If $Da \gg 1$, reaction is faster than mass transfer and the overall capture rate can be estimated by k_+. On the other hand, if $Da \ll 1$, mass transfer is faster than reaction

and capture rate can be evaluated by considering k_{rxn} alone. For intermediate Da, neither process dominates and both need to be considered when making predictions.

2.2.4 Models for predicting the time evolution of the bead-analyte capture process

It is often desired to estimate the time required for a specific capture efficiency. Scaling analysis can point to suitable models for this purpose and using these models, scientists and engineers can iteratively optimize parameters to achieve performance goals. Literature exists on modeling bioanalyte capture by planar sensor surfaces. Excellent reviews on the physical mechanisms that dominate these geometries exist [106]. In this section, we present bead-based capture models found in the literature, ranging from the most complex with no assumptions and requiring numerical simulation to simplified analytical models that can be used when one process can be neglected.

Full three-dimensional coupled convection-diffusion-reaction equations

The most basic conservation and reactions equations in 3D apply to beads moving relative to a fluid [89]:

$$\begin{cases} \frac{dC_a}{dt} = D_a \nabla^2 C_a - u \cdot \nabla C_a & r_b < r < R_{sphere} \\ D_a \frac{dC_a}{dr} = k_{rxn}^{on}(t) C_a(t) - k_{rxn}^{off} B & r = r_b \\ \frac{dB}{dt} = k_{rxn}^{on} C_{a,s}(t) - k_{rxn}^{off} B & r = r_b \end{cases} \tag{2.20}$$

where k_{rxn}^{on} and k_{rxn}^{off} are given by the previous expressions for soluble or particulate analytes. The first equation describes the change of analyte concentration over time in the spatial domain (left-hand side) due to diffusion (first term, right-hand side) and advection (second term, right-hand side). For numerical modeling, there are multiple ways to determine the spatial domain over which each individual bead has influence. One previously used method is to assume that beads are uniformly spaced each occupying a sphere of fluid with radius $R_{sphere} = \sqrt[3]{\frac{3V_s}{4\pi n_b}}$ [89].

The second equation describes the analyte diffusive flux at the surface of the bead (left-hand side), which is balanced by the reaction of the analyte with the receptors on the bead surface. The third equation represents the change of bound analyte density with time. The equations are solved subject to the following conditions:

$$\begin{cases} \frac{dC_a}{dr} = 0 & r = R_{sphere} \\ C_a = C_{a,0}, B = 0 & t = 0 \end{cases} \tag{2.21}$$

The first condition is no flux boundary condition at the edge of the fluid sphere. The second conditions are the initial conditions. As the equations describe the process on a per-bead basis, the total number of captured analytes N_c at any time t is $N_c(t) = A_b n_b B(t)$.

Nondimensionalizing these equations gives insight into the governing physics and suggests when simplifications are justified. The following dimensionless variables are defined for this purpose:

$$\tilde{r} = \frac{r}{r_b} \tag{2.22}$$

$$\tilde{t} = \frac{D_a t}{r_b^2} \tag{2.23}$$

$$\tilde{C} = \frac{C_a(t)}{C_{a,0}} \tag{2.24}$$

$$\tilde{u} = \frac{u}{U_0} \tag{2.25}$$

$$\tilde{B} = \frac{B(t)}{C_{a,0} r_b} \tag{2.26}$$

With these variables, Equation 2.20 becomes

$$\begin{cases} \frac{d\tilde{C}}{d\tilde{t}} = \nabla^2 \tilde{C} - \left(\frac{U_0 r_b}{D_a}\right) \tilde{u} \cdot \nabla \tilde{C} & 1 < \tilde{r} < \frac{R_{sphere}}{r_b} \\ \frac{d\tilde{C}}{d\tilde{r}} = \left(\frac{k_{rxn}^{on} r_b}{D_a}\right) \tilde{C} - \left(\frac{k_{rxn}^{off} r_b^2}{D_a}\right) \tilde{B} & \tilde{r} = 1 \\ \frac{d\tilde{B}}{d\tilde{t}} = \left(\frac{k_{rxn}^{on} r_b}{D_a}\right) \tilde{C} - \left(\frac{k_{rxn}^{off} r_b^2}{D_a}\right) \tilde{B} & \tilde{r} = 1 \end{cases} \tag{2.27}$$

and is subject to the nondimensional conditions:

$$\begin{cases} \frac{d\tilde{C}}{d\tilde{r}} = 0 & \tilde{r} = \frac{R_{sphere}}{r_b} \\ \tilde{C} = 1, \tilde{B} = 0 & \tilde{t} = 0 \end{cases} \tag{2.28}$$

Two previously discussed nondimensional parameters become obvious through this process, though in slightly different form. The first is Pe ($\frac{U_0 r_b}{D_a}$ in the first equation), the value of which determines the dominant form of mass transfer. The second is Da ($\frac{k_{rxn}^{on} r_b}{D_a}$), which compares the rate of reaction to the rate of mass transport.

We include this model here to illustrate the complete picture. These coupled equations must be solved numerically and can become quite complex depending upon the nature of the flow field. For design purposes, assumptions can often be made that allow simplification of these equations that can, in some cases, be solved analytically.

Two compartment model

One simplification assumes that the analyte variation only varies in the radial direction. Often called the two compartment model, this formulation separates the spatial domain into two discrete regions, with each region having the same homogeneous analyte concentration. The outer compartment is the bulk sample solution with analyte concentration C_1. The inner compartment is immediately next to the surface of the bead and has analyte concentration C_2. Analytes move from the outer compartment to the inner compartment via mass transport and are removed from the inner compartment when they bind to an affinity agent on the bead surface. This model has been widely applied to the analysis of surface plasmon resonance (SPR) data to determine binding rates for antibodies and other affinity molecules [107]. It has also been used for estimating analyte capture in spherical systems [108].

Considering a single bead, the change in inner compartment concentration with time is a balance between transport from the outer compartment to the inner compartment and the reactive flux as analytes bind to affinity agents on the bead surface from the

inner compartment:

$$V_2 \frac{dC_2}{dt} = k_+ A_b \left(C_1 - C_2\right) - k_{rxn}^{on} A_b C_2 + k_{rxn}^{off} A_b B \tag{2.29}$$

where V_2 is the volume of the inner compartment, which is, in general, unknown.

To solve these equations, the quasisteady approximation (QSA) is often employed, which assumes that the concentration of the inner compartment does not change appreciably with time (i.e, $\frac{dC_2}{dt} \sim 0$) and the diffusive flux can be modeled by the steady state flux. Under QSA, one can solve Equation 2.29 for C_2 and substitute it into Equation 2.17 to yield a single equation that describes B:

$$C_2 = \frac{k_+ C_1 + k_{rxn}^{off} B}{k_+ + k_{rxn}^{on}} \tag{2.30}$$

$$\frac{dB}{dt} = k_{on}^{eff} C_2 - k_{off}^{eff} B \tag{2.31}$$

Two "effective" rate coefficients form in this process:

$$k_{on}^{eff} = \frac{k_{rxn}^{on}}{1 + \frac{k_{rxn}^{on}}{k_+}} \tag{2.32}$$

$$k_{off}^{eff} = \frac{k_{rxn}^{off}}{1 + \frac{k_{rxn}^{on}}{k_+}} \tag{2.33}$$

Da shows up in these rate coefficients ($\frac{k_{rxn}^{on}}{k_+}$). Together with mass conservation considerations and the initial condition $B(t = 0) = 0$, the above set of ordinary differential equations can be solved for B and, subsequently, a capture efficiency.

An advantage of the two-compartment model is that it considers both physical phenomena in a formulation that can be easily solved. It is particularly useful for systems in which neither physical process dominates (i.e. $Da \sim 1$).

Simplified models at extreme Damkohler numbers and/or early times

When $Da \gg 1$ or $Da \ll 1$, further simplifications can be made. If $Da \gg 1$, we can neglect the reaction rate and assume that the analyte concentration at the bead surface

is insignificant compared to the bulk, an assumption that is valid until enough analyte builds up on the surface. By mass balance considerations, the total mass transfer flux to the surface of n_b beads must be equal to the number of analytes removed from the sample:

$$V_s \frac{dC_a}{dt} = -k_+ n_b A_b C_a \tag{2.34}$$

which, with the initial condition of $C_a(t = 0) = C_{a,0}$, yields the following equation describing the exponential decay of analyte concentration in the sample:

$$\frac{C_a(t)}{C_{a,0}} = \exp\left(-\frac{k_+ n_b A_b}{V_s} t\right) \tag{2.35}$$

On the other hand, if $Da \ll 1$, reaction is slower of the two processes and mass transport can be neglected. At this extreme, the bound analyte density is given by Equation 2.17, with the appropriate on- and off-rates for the analyte of interest. These equations can be further simplified if the process is in the initial stages ($t < \frac{1}{k_{rxn}^{off}}$) and, assuming the affinity agents do not saturate during this time, one can neglect the off-rate and consider only the reactive flux to the bead surface:

$$\frac{dB}{dt} = k_{rxn}^{on} C_a \tag{2.36}$$

Combined with mass conservation considerations ($V_s \frac{dC_a}{dt} = -n_b A_b \frac{dB}{dt}$), analytical expressions are obtained:

$$\frac{C_a(t)}{C_{a,0}} = \exp\left(-\frac{k_{rxn}^{on} n_b A_b}{V_s} t\right) \tag{2.37}$$

In situations in which $Da \sim 1$ and at early times, the two compartment model can also be simplified to neglect the effective off rate:

$$\frac{C_a(t)}{C_{a,0}} = \exp\left(-\frac{k_{on}^{eff} n_b A_b}{V_s} t\right) \tag{2.38}$$

As a side note, we wish to highlight that k_{on}^{eff} can also be viewed from a resistance framework point of view, similar to one-dimensional models that are used in heat

transfer. By considering mass transport and reaction as two resistances in series and adding these resistances together to get the total resistance R_{total}, the equations become:

$$\frac{C_a(t)}{C_{a,0}} \approx \exp\left(-\frac{n_b A_b}{V_s}\frac{1}{R_{total}}t\right) \tag{2.39}$$

$$R_{total} = R_{MT} + R_{rxn} = \frac{1}{k_+} + \frac{1}{k_{rxn}^{on}} = \frac{1+\frac{k_{rxn}^{on}}{k_+}}{k_{rxn}^{on}} \tag{2.40}$$

2.2.5 Example application of framework to analyte of capture-while-settling mechanism

To illustrate how the proposed framework can reveal dominant phenomena in bead-based capture process and aid in design, we apply the outlined analysis to our proposed mechanism of analyte capture during bead settling ("capture-while-settling"). We are interested in exploring this mechanism because it is passive from the user point of view, which makes it appealing to integrate with a low-instrumentation detection method for decentralized bioassays.

In the absence of active mixing, the fluid flow in capture-while-settling arises from the sedimentation of beads under their own mass at their terminal velocity U_s, which is determined through a balance of the force of gravity on the bead and the drag force due to fluid friction at the bead surface:

$$U_s = \frac{\Delta\rho g d_b^2}{18\mu_f} \tag{2.41}$$

where $\Delta\rho = \rho_b - \rho_f$. We consider beads with diameters from 100 nanometers (nm) to 10 microns (μm) and made of materials ranging in density from 1.05 to 2.5 grams per cubic centimeter (g/cm^3). This range of densities reflects commercially available bead materials, from polystyrene to borosilicate glass, respectively. We assume that the fluid sample properties can be well approximated by those of water, but note that they can vary widely based on the sample type. A property that has much influence on U_s is μ_f, which can be greater than that of water in some biofluids and can slow

Table 2.2: **Bead and fluid properties used in analysis of capture-while-settling process.**

Bead diameter d_b	100 nm - 10 μm
Bead density ρ_b	1.05 - 2.5 g/cm^3
Fluid density ρ_f	1.00 g/cm^3
Fluid viscosity μ_f	0.001 Pa*s

U_s significantly. Bead and fluid properties considered in our analysis are shown in Table 2.2.

Analyte and antibody affinity agent properties used in the analysis are shown in Table 2.3. Beads are coated with the maximum antibody density described in the literature ($\frac{10^{16}}{m^2}$ [106]). Our example soluble antigen is cardiac troponin I (cTnI), which is found in a complex of three proteins in a 1:1:1 molar ratio and is indicative of cardiac injury [109]; we outline the development of an assay for this analyte in Chapter 7. Commercially available capture antibodies for cTnI have high affinity, with $K_D < 1$ nanomolar (nM; see Table 7.1).

For particulate analytes, we analyze three different examples that cover the range of analyte sizes: virions (SARS-CoV-2), bacteria (*Escherichia coli* [*E.coli*]), and mammalian cells (CD4+ T cells). To estimate on-rates for these analytes, we use the aforementioned framework from Haun et al. In a series of papers, the authors examined attachment of different-sized antibody-functionalized particles to antigen-functionalized substrates under different three shear flow conditions [103–105]. Several findings and observations from these studies are relevant for our analysis. First, it was observed that the particle on-rate k_A is a linear function of product of the bead antibody coating density n_{ab} and the surface antigen density n_{ant} over a range of particle sizes and shear rates. Additionally, the authors found that k_A is weakly dependent on the shear rate $\dot{\gamma}$, with a decrease in k_A with increasing shear rates noted for larger particles. This was hypothesized to arise from the shear force on the particle ($F_{shear} \sim A_b \mu_f \dot{\gamma}$), which increases with r_b^2.

To estimate k_A for virions, bacteria and mammalian cells, we used Haun et al.'s empirically derived linear relationship between k_A and $n_{ant} n_{ab}$ for ICAM-1 antibody-

Table 2.3: **Analyte characteristics used in analysis of capture-while-settling process.**

	Value for specific analytes			
Parameter	Antigen: cTnI	Virion: SARS-CoV-2	Bacteria: *E.coli*	Mammalian cell: CD4+ T cell
d_a (m)	7.3e-09	1.0e-07	3.7e-06[&]	7.0e-06
D_a (m^2/s) [88]	4.5e-11	5.0e-12	5.0e-13	5.0e-14
Critical shear rate (s^{-1})	N/A	3.0e05	3.0e03	6.2e01
Target surface density n_{ant} ($\#/m^2$)	N/A	7.6e14 (spike protein [110])	7.6e14[*]	6.5e14 (CD4 receptor [111])
k_{rxn} $(m/s)^+$	1.2e-05[@]	6.1e-06	1.3e-05	2.1e-05
Pe using specified beads	10^{-7} - 10^{2}	10^{-6} - 10^{3}	10^{-4} - 10^{4}	10^{-2} - 10^{4}

[&] Equivalent diameter that yields that same volume as cylinder with diameter 1 μm and height 2 μm

[*] Density of LPS or other potential antibody targets was not found in literature review, so target density on the order of the two other particulate analytes was used

[+] For particle analytes, estimated using empirical data in [103, 104], as described in the text

[@] See Table 7.1

functionalized spheres interacting with an ICAM-1 antigen-functionalized surface [103, 104]. These relationships depend upon the shear rate on the surface of the bead due to fluid flow. To determine which relationship to use, we first estimate the critical shear rate, $\dot{\gamma}_c$, at which the shear force on a bead-bound analyte would disrupt the ligand-affinity agent binding interaction. Assuming the receptors are antibodies, a lower estimate for the strength of this interaction is $F_{ant-ab} \sim 10$ piconewtons [pN] [112, 113]. An estimate for $\dot{\gamma}_c$ is found by equating the shear force on the analyte due to bead sedimentation velocity U_s to F_{ant-ab}:

$$A_a \mu_f \dot{\gamma}_c \sim F_{ant-ab} \rightarrow \dot{\gamma}_c \sim \frac{F_{ant-ab}}{A_a \mu_f} \tag{2.42}$$

where A_a is the surface area of the analyte. The shear rate at the bead surface ($\dot{\gamma} \sim \frac{U_s}{d_b}$) is <30 s^{-1} for all beads (Figure 2-3). Comparing this result to Table 2.3, we find that $\dot{\gamma}_c$ for all particulate analytes considered are at least 2x greater than the shear rate on the surface of the beads, indicating that the shear forces during bead settling are not strong enough to remove bound analytes from the surface of the bead and do not need to be accounted for during this analysis.

Haun et al. performed experiments using 100, 400 and 1000 s^{-1} shear rates [103]. As shear rates during bead settling are less than those tested, we chose to use data for the minimum shear rate, $\dot{\gamma} = 100 s^{-1}$, to estimate k_A for our target analytes (slope of k_A versus $n_{ab} n_{ant}$ =8x10^{-7} μm/s). As studies included particle sizes up to 1.1 μm, we estimated a value for CD4+ T cells via linear extrapolation and note that this a source of uncertainty in our analysis.

Mass transfer capture coefficients were estimated according to Equation 2.12 and 2.15. We restrict the analysis for each analyte to only beads with dimensions that satisfy $R < 0.5$, such that the bead is always larger than the analyte.

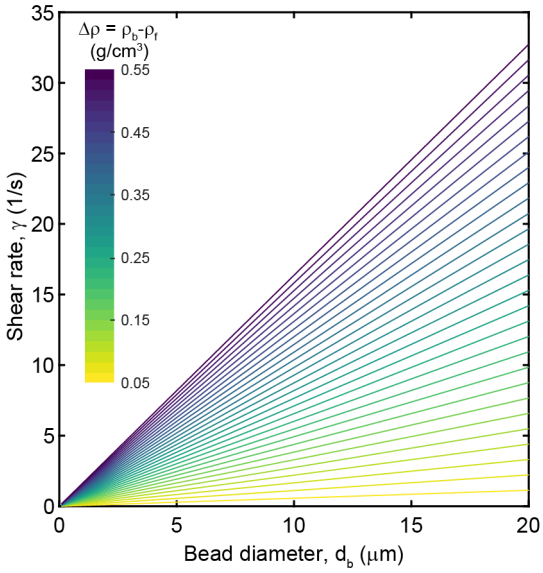

Figure 2-3: **Shear rate on bead surface due to sedimentation.** All beads considered in the analysis have shear rates < 100 s^{-1} during settling and we use empirically derived curves for particle attachment rates at 100 s^{-1} due to this. Critical shear rates for the particulate analytes considered (Table 2.3) are all above the shear rates estimated due to bead sedimentation, suggesting that particulate analytes will not get sheared off of beads once they are bound.

2.3 Results

2.3.1 Scaling analysis provides insight into the dominant physics for each type of prototypical analyte

Bead-based analyte capture is an efficient method to separate targets of interest from complex matrices. Aside from a standalone separation method prior to traditional downstream manipulations such as polymerase chain reaction, flow cytometry and sequencing, it is often an upstream process coupled directly to an analysis method in novel assays and diagnostics. Examining the physical phenomena that govern its effectiveness can help to optimize the process for a specific application. For such purposes, we propose a framework based on scaling analysis to guide model selection and predict capture times and efficiencies for a specific application. Such a guide could help scientists and engineers select appropriate beads for their application and

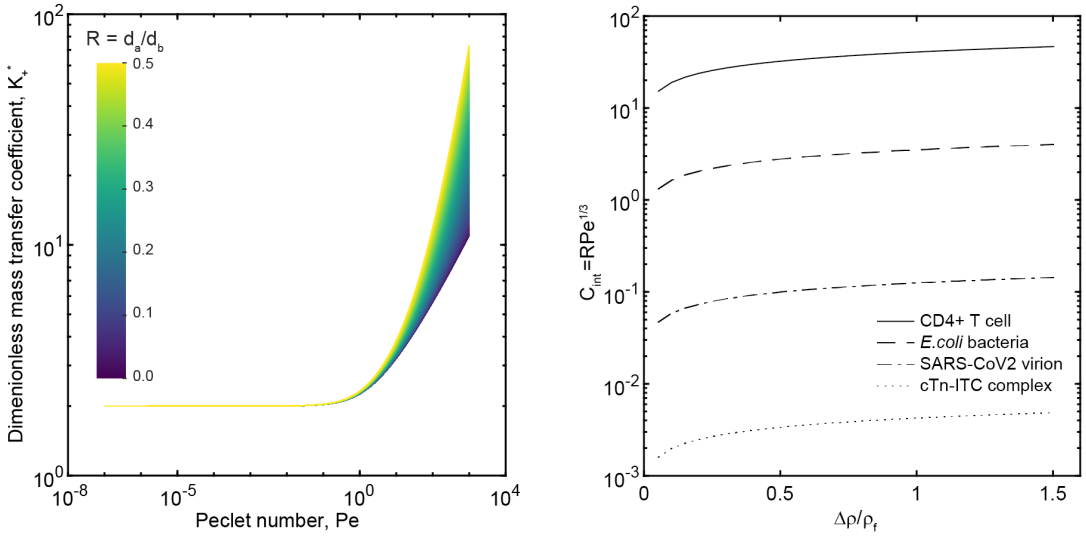

(a) (b)

Figure 2-4: **Mass transfer predictions for capture-while-settling using scaling analysis.** (a) The dimensionless mass transfer coefficient for the relevant range of Pe for bioanalytes with diffusivity 10^{-14} to 10^{-11} m/s, beads ranging in diameter from 100 nm to 20 μm and bead materials with density from 1.05 to 2.5 g/cm^3. Convective mass transport does not confer an advantage over pure diffusion until $Pe \sim 1$. The enhancement due to convection also depends on if interception is relevant, as is shown by curve parameterization by the interception parameter R. (b) The parameter C_{int} plotted by bead material for the different analytes considered, showing that interception is relevant for the transport of large analytes with low diffusivities, as is also predicted in the aerosol literature.

theoretically investigate novel assays before experimentation. In what follows, we illustrate the use of our framework to analyze analyte capture during bead settling, which sets the free stream velocity as the bead sedimentation speed ($U_0 = U_s$; Equation 2.41). However, our method is applicable to other cases – for example, when the free stream velocity is set by some external actuation – provided the assumption of creeping Stokes flow ($Re \ll 1$) is satisfied.

We first examine how capture-while-settling affects the rate of analyte transport to the surface of the bead through estimation of the capture coefficient k_+, which includes nondiffusive forms of mass transfer that are especially relevant for larger analytes. Our nondimensional capture coefficient K_+^* is plotted versus Pe in Figure 2-4a. Here, we have parameterized the curves by the interception parameter R to

illustrate when interception-based mass transport becomes influential. It is useful to think of K_+^* as a measure of mass transport enhancement over pure diffusion to a stationary bead (i.e., when $K_+^* = 2$). If $K_+^* > 2$, convection aids in mass transfer to the bead surface. Examining Figure 2-4a, convection is essentially irrelevant for mass transport until $Pe \sim 0.01$. Until this point, either the bead settles so slowly or the analyte diffuses so fast that flow does not provide an advantage. As Pe increases, the effects of convection become more evident, and at extreme Pe, flow can increase mass transport 100x compared to pure diffusion. The extent of this enhancement is modulated by R, with the highest gains found as $R \to 0.5$.

Similar to filtration literature [91], the influence of interception over convective diffusion can also be seen by examining the value of the parameter C_{int} (see Equation 2.16). In capture-while-settling, when $U_0 = U_s$, C_{int} can be further simplified to show that it has no dependence on bead size:

$$RPe^{\frac{1}{3}} = \left(\frac{d_a}{d_b}\right)\left(\frac{\Delta\rho g d_b^3}{18 D_a \mu_f}\right)^{\frac{1}{3}} \sim d_a \left(\frac{\Delta\rho g}{D_a \mu_f}\right)^{\frac{1}{3}} \tag{2.43}$$

Plotting C_{int} versus the dimensionless difference in bead and fluid density, it is clear that interception plays an increasing role as analyte size increases and analyte diffusivity decreases (Figure 2-4b). For example, C_{int} is three orders of magnitude greater for mammalian cells than for protein analytes. This reflects the disparity both in the size ($\frac{d_{CD4+Tcell}}{d_{cTnI}} \sim 10^3$) and diffusivity ($\frac{D_{CD4+Tcell}}{D_{cTnI}} \sim 10^{-3}$) between the analytes.

What insights does this analysis yield for capture-while-settling? First, for analytes such as protein antigens and virions, which are of small size and high diffusivity, convective motion by bead sedimentation does not increase mass transfer significantly over pure diffusion. For example, at the highest Pe considered for these analytes (when the bead is heaviest and largest, $\rho_b = 2.5$ g/cm^3 and $r_b = 10$ μm), $K_+^* \sim 6$ or 12, respectively. R is correspondingly low for both analytes using this bead and interception is not relevant. Significantly higher fluid flow than is found in bead settling would be required to increase K_+^*. This could be accomplished via mixing using either a vortex or a rotisserie. However, turbulent effects would likely need

to be incorporated to accurately predict the enhancement over diffusion with these methods. A previous study attempted to account for these effects [114], but modeling turbulence remains a challenge.

In the case of larger analytes such as bacteria and cells, bead convection significantly increases analyte transport to the bead surface, with an increase of nearly 100x at high Pe and R. These analytes are not transported efficiently by their own diffusion and convection provides a means to increase their transport, chiefly through increasing interception, as reflected by the value of the C_{int} for these analytes. At this end of the analyte spectrum, bead settling provides enough convection to increase mass transport, which is often limiting in applications for low diffusivity analytes. This also suggests why capture processes for larger analytes often use larger beads, which increase interception.

After estimating the reaction rate, we can compare the relative importance of each process to the overall bead-based capture rate through Da. First, it is useful to examine a general regime map to illustrate where certain processes dominate. Dividing the Da versus Pe plot into four quadrants reveals four regimes (Figure 2-5a):

I $Da \gg 1$ and $Pe \gg 1$: mass transport limited process with significant convection

II $Da \gg 1$ and $Pe \ll 1$: mass transport limited process with significant diffusion

III $Da \ll 1$ and $Pe \ll 1$: reaction limited process with significant diffusion

IV $Da \ll 1$ and $Pe \gg 1$: reaction limited process with significant convection

If a process falls squarely into one of these quadrants, capture time and efficiency prediction can be simplified significantly (i.e., Equation 2.34 for quadrant I or II; Equation 2.37 for quandrant III or IV). If in an intermediate regime, more complex models should be used (i.e., Equation 2.20).

Figure 2-5b shows this map for the capture-while-settling process, parameterized by the interception parameter R. First noticeable is the general layout of the curves, which tend to fall in the upper right (I) and lower left (III) quadrants. In quadrant I, where $Pe \gg 1$ and convection dominates, the capture process is still limited by mass

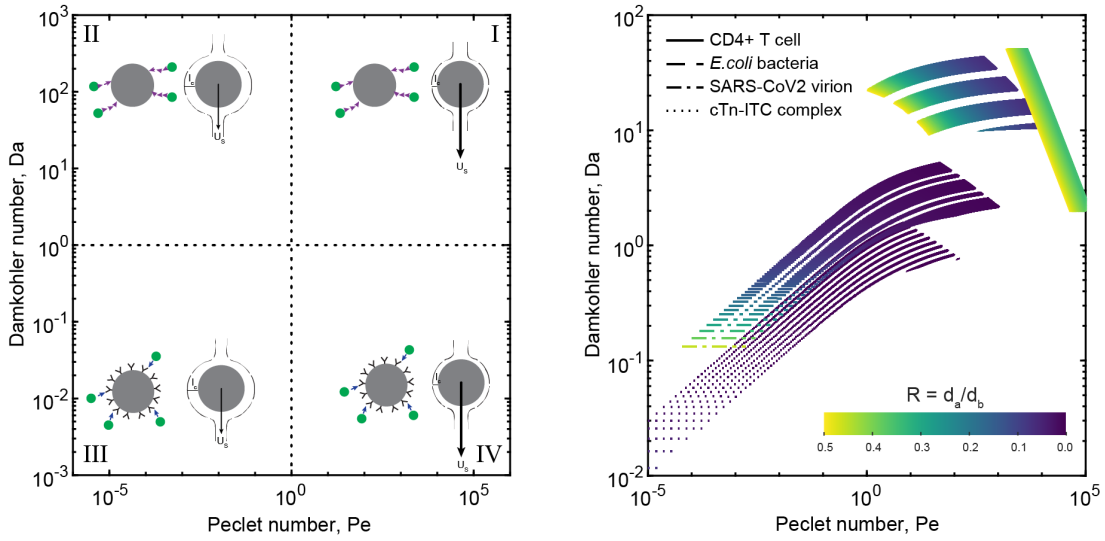

(a) (b)

Figure 2-5: **Prediction of dominant physical phenomena in bead-analyte binding.** (a) General Da versus Pe for any bead-binding process, illustrating four major regimes depending upon the values of the dimensionless parameters. In the mass transfer-limited regimes of quadrants I and II, the capture rate can be determined by Equation 2.15 and prediction of capture time can be obtained using Equation 2.34. In the reaction-limited regimes of quadrants III and IV, the capture rate can be estimated by Equation 2.18 and the capture time can be predicted by Equation 2.37. Systems which fall intermediately between these regimes can be analyzed using more complicated models such as the two compartment model (Equation 2.29) or the complete 3D convection-diffusion-reaction model (Equation 2.20). (b) Da versus Pe for analyte capture-while-settling for four different analytes, parameterized by the interception parameter R. For the flow conditions in capture-while settling, most analytes fall in a regime where neither mass transfer nor analyte-antibody reaction dominates the capture process. However, as analytes get larger and diffusivity gets smaller, the process becomes mass transfer limited.

transport despite fluid flow induced by bead convection. The different shapes of the bacteria verus mammalian cell curves are indicative of the influence of interception, which decreases the mass transport limitation for mammalian cells but is relatively insignificant for bacteria under our assumption of $R < 0.5$.

For small, highly diffusive analytes such as cTnI and SARS-CoV-2 virions, a significant portion of the curves lie in the intermediate Da and Pe regimes, indicating that neither reaction nor mass transfer dominates the capture-while-settling process. Reaction does become dominant at lower Pe (reflected in $Da < 10^{-1}$) reflecting the efficient diffusion of these analytes. In this case, a model such as Equation 2.37 could be used to predict capture time. The use of these models to predict capture are illustrated in subsequent chapters.

Given this analysis, what are the benefits of using capture-while-settling, especially in our chosen clinical application of sensing cTnI? One hypothesized advantage of capture-while-settling is that it is a passive method to increase mass transfer, which is often the limiting phenomenon in planar surface capture methods due to the growth of the concentration boundary layer in stagnant systems. It is therefore useful to compare the density of bound analytes on falling beads to that on bead arrays (such as could be found in an ELISA well) under the assumption that mass transport is limiting (Figure 2-6a). The bound analyte density on settling beads, $n_{\text{settling beads}}$, can be estimated as the analyte flux through the concentration boundary layer in the convective diffusion regime (i.e., $K_+^* \sim Pe^{\frac{1}{3}}$):

$$n_{\text{settling beads}} \sim \left(\frac{U_0 D_a^2}{d_b^2}\right)^{\frac{1}{3}} C_0 t \sim \left(\frac{\Delta \rho g D_a^2}{\mu_f}\right)^{\frac{1}{3}} C_0 t \tag{2.44}$$

The bound analyte density on the bead array on a planar surface, $n_{\text{bead-array}}$, can be estimated using the mass transport coefficient for a purely diffusive process as $k_+ \sim D/\delta_c$, where $\delta_c \sim \sqrt{D_a t}$. The total surface area of the planar bead array is $A_{plane} + n_b \pi d_b^2$, which, when normalized by A_{plane}, becomes $1 + \gamma \pi d_b^2$, where γ is the number of beads per unit planar area. Assuming the beads are regularly spaced on a grid with distance s between them, $\gamma = 1/s^2$ and the normalized area can also be

written as $[1+\pi\left(\frac{d_b}{s}\right)^2]$. For times at which $s < \delta_c$, this results in an expression for $n_{\text{bead-array}}$:

$$n_{\text{bead-array}} \sim \frac{D_a}{\sqrt{D_a t}} \frac{1}{\left[1+\pi\left(\frac{d_b}{s}\right)^2\right]} C_0 t \sim \frac{\sqrt{D_a t}}{\left[1+\pi\left(\frac{d_b}{s}\right)^2\right]} C_0 \tag{2.45}$$

The ratio between the two analyte densities becomes

$$\frac{n_{\text{settling beads}}}{n_{\text{bead-array}}} \sim \frac{\left(\frac{\Delta\rho g D_a^2}{\mu_f}\right)^{\frac{1}{3}} \left[1+\pi\left(\frac{d_b}{s}\right)^2\right]}{\sqrt{D_a}} \sqrt{t} \tag{2.46}$$

Figure 2-6b plots this ratio in Equation 2.46 for a prototypical protein analyte ($D_a \sim 10^{-11}$ m^2/s) and a capture time of $t = 10$ min. Falling spheres collect ~50-250x more analyte depending upon the difference between the bead density and the fluid density ($\Delta\rho = \rho_b - \rho_f$), which is the driving force for bead sedimentation. The ratio plateaus at the value expected for a planar, non-bead coated surface as the bead spacing increases. The gain in bound analyte comes from the replenishment of the analytes surrounding the falling bead, which sets up a constant boundary layer thickness during settling (assuming the overall analyte concentration is not significantly depleted). On the planar surface, analyte is not refreshed near the surface, leading to a layer thickness that increases with the square root of time, such that the flux decreases with time. Thus, although capture-while-settling does not lead to the mass transport enhancement seen using pumped fluid, this scaling models suggests it does provide an advantage over a purely stagnant diffusion process in a format that requires minimal instrumentation.

2.3.2 Assumptions in the current description limit its applicability, which can be extended with certain model modifications and further experimentation

Our framework provides basic insights into the physical phenomena that control capture of analytes using functionalized beads. However, our analysis applies when certain assumptions are satisfied and would be made more accurate with additional

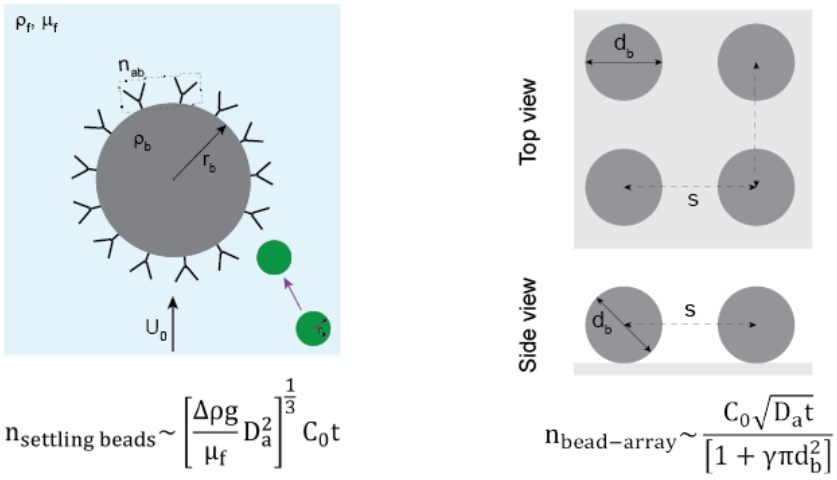

(a)

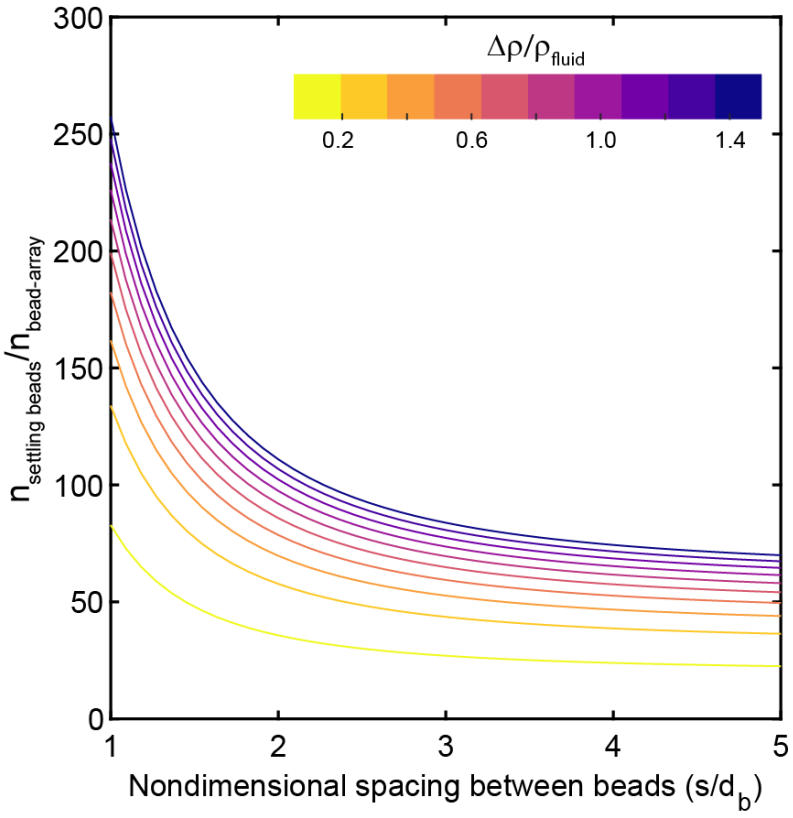

(b)

Figure 2-6: **Comparison of analyte collection using settling beads versus bead array on planar surface.** (a) Graphic illustrating settling beads versus a stagnant bead array. (b) Settling beads collect 20-100x more analyte, depending upon $\Delta\rho$, the driving force for bead sedimentation.

experimental data for certain parameters.

First, our mass transfer analysis derives coefficients for transport to a *single* bead and thus assumes that beads do not interact with one another. This criterion is satisfied when the distance between beads is at least $2\delta_v$ such that the velocity boundary layers do not interact. Given a number of beads and sample volume, and assuming beads are evenly dispersed throughout the sample, the sphere of sample fluid that a single bead occupies has a radius of $R_{sphere} = \sqrt[3]{\frac{3V_s}{4\pi n_b}}$; for the noninteracting assumption to hold, $\delta_v < R_{sphere}$. As beads become more concentrated, this assumption breaks down and mass/momentum interactions between beads would need to be considered. For example, similar to increasing the packing density of spherical arrays for filtration, when bead concentration increases, there are local increases in fluid velocity due to the flow squeezing between the space between beads [96]. Filtration models have been proposed to account for these effects and vary in their agreement with empirical results. Isolated bead models are still commonly used because capture mechanisms are near-surface phenomena. It may be warranted to incorporate these dense packing results and models to our framework to extend its applicability to the range of bead concentrations.

Secondly, the most error in our analysis likely comes from estimation of the particle on-rate, k_A. While it is known that k_A is a function of several system properties, the functional form of these dependencies is unknown, making these rates challenging to predict. Additionally, there is little empirical data on these rates available in the literature. The data that we used in our estimation was for an ICAM-1 antibody-antigen system [103, 104], which, given our assumption of using antibodies as the affinity agent, seems reasonable to use as a first order estimate. However, more studies are needed to elucidate the functional relationships between these parameters and examine the range of parameter values for different bioanalyte-affinity agent systems.

2.4 Conclusion

Towards reliable prediction of the bead-analyte capture process, this chapter presented an analysis framework that could aid in the design and selection of beads across applications. Our method relies on using nondimensional numbers to elucidate the dominating physical phenomena in a specific application and point to a suitable (simplified) model for predicting capture efficiencies. Synthesizing results from a variety of fields, our main contribution is the inclusion of mass transport and reaction phenomena for the entire range of analytes. We demonstrated our framework in the prediction of dominating phenomena for the capture-while-settling mechanism, which revealed that the rate determining process is different depending upon the target analyte.

To investigate our hypothesis that an advantages of capture-while-settling is that it permits faster capture of analytes compared to a purely diffusive process through increased mass transport, we used scaling arguments to compare the number density of captured analytes on falling beads versus that on a bead array on a planar surface. These results suggest that capture-whie-settling significantly enhances mass transfer for the same capture time, suggesting that the convection induced by the capture-while-settling process leads to advantages in analyte capture. Overall, this chapter provides a theoretical basis for bead-analyte binding and preliminary evidence that incorporating capture-while-settling in assays could decrease capture time without the use of externally-imposed flow. These contributions are valuable not only for our own work but also for the larger field of bead-based bioassays and transport phenomena.

Experimental studies examining the fraction of analytes collected by sedimenting spheres when varying the bead size, material and sample volume are needed to validate our scaling model. This was not performed in the current study. Such experiments could be relatively easy to carry out using, for example, sandwich assay measurements of protein antigens in the sample before and after capture by settling beads, or using fluorescently tagged particulate analytes to facilitate counting of analytes via microscopy. This data would complete the picture of bead-analyte capture and yield

insights into the proposed capture mechanisms.

Chapter 3

Gravity- and vibration-induced dissociation for bead-based bioassays

3.1 Introduction

To quantify bioanalytes, our proposed assay relies upon the application of a mechanical force to differentiate between beads with analyte and beads without analyte during their interaction with a functionalized sensing surface. In order to disrupt interactions between beads without analyte and the surface, the magnitude of the applied force must be greater than forces associated with nonspecific binding (NSB). However, to accurately quantify the analyte, beads with analyte must ideally remain tethered to the surface and the applied force must be less than the strength of the analyte-affinity agent interaction. This leads to a conservative criterion on the applied force in the case of a single bond tethering a bead to the surface:

$$\text{NSB} < \text{Applied force} < \text{Single analyte-affinity agent bond} \tag{3.1}$$

A single specific antibody-antigen bond is around 50 pN [112, 113, 115, 116]. Previous measurements of NSB interactions using atomic force microscopy with antibody-coated tips and BSA-coated surfaces range from 1 to 20 piconewtons (pN) [115]. However, it is unclear how many nonspecific interactions these measurements represent. Especially

in microbead interactions with planar surfaces, where contact area between the bead and the surface scales with the bead radius (see Figure 4-3b), the overall strength of NSB could be much higher than these AFM estimates.

The next three chapters detail the theoretical underpinnings and experimental work towards selection of a mechanical force that both satisfies this criterion and is applied via a method that requires minimal instrumentation beyond that which could be found in a decentralized laboratory (microscope, bench-top centrifuge, cell phone, etc). Combining non-fluidic actuation with the capture-while-settling mechanism could yield an integrated, user-friendly assay suitable for use in primary health clinics, disease screening campaigns, homes, and other decentralized settings.

In this chapter, gravity- and vibration are explored as actuation mechanisms to remove beads without analyte from the surface (Figure 3-1). In both methods, after the beads settle on to the sensing surface, the surface is inverted. The gravity-based mechanism utilizes bead weight to remove beads and requires no additional actuation beyond surface inversion. Previous assays with femtomolar sensitivity utilizing gravity-based settling have been reported for bacteria, virions and proteins [42, 43]. These assays are complicated by their readout methods and custom-made retroreflecting particles. Here, we use commercially available, larger beads in hopes of creating a sedimentation-based assay that can achieve lower detection limits without custom materials.

In the vibration method, a sinusoidal force is applied to the surface via a coin vibration motor. The moving surface induces fluid movement, which quickly decays to zero in the bulk, but produces a shear force on the bead. The shear force can be tuned through adjustment of motor movement using a simple electronic circuit. As illustrated by previous studies which have examined coin vibration motors as sample mixers [117–122], these compact devices are cheap, widely available and also found in cell phones, allowing this assay to potentially be completely performed using the tools found in a mobile phone.

Ultimately, we find that these mechanisms show promise for bioassays, but are limited by NSB, leading to suboptimal sensitivity. However, with nonfouling surfaces

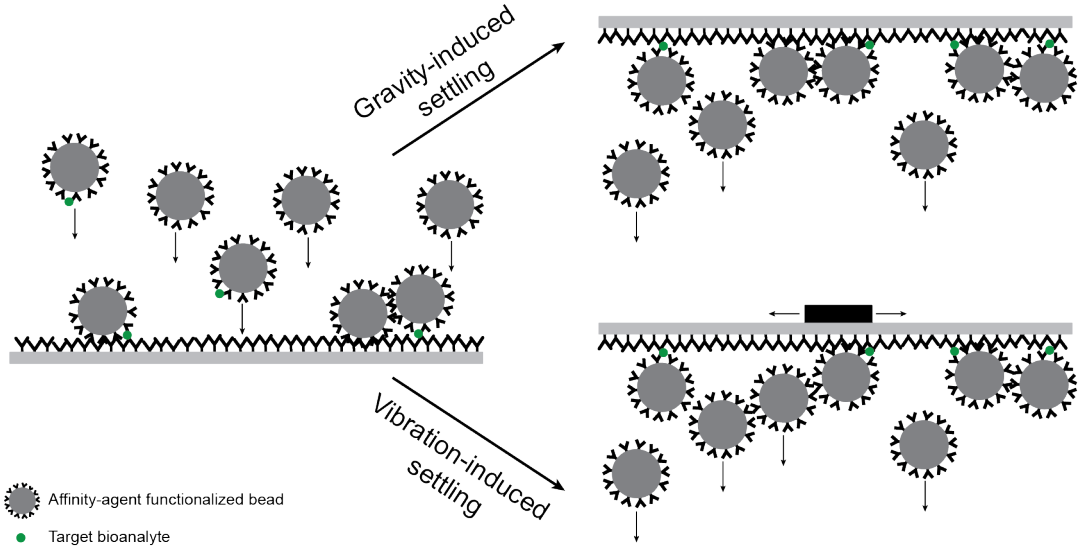

Figure 3-1: **Sedimentation-based assays utilizing actuation via gravity or vibration.** After the beads settle onto the sensing surface, the surface is inverted. In one embodiment, under influence of gravity, beads without analyte fall off of the surface (top). In another embodiment, vibration via a coin vibration motor affixed to the slide is used to induce a shear force which removes beads without analyte. In either version, beads with bound analyte remain on the surface and are counted via optical microscopy to quantify the target.

examined subsequently in Chapter 6, gravity- and vibration-induced bead settling may show efficacy and should be revisited in the future.

3.2 Materials and methods

3.2.1 Materials

Glass slides (75 x 25 x 1 millimeter [mm]), bovine serum albumin (BSA), phosphate buffered saline (PBS), Luria Bertani (LB) broth, 10 milliliter (mL) polypropylene culture tubes, 1.5 mL polypropylene microcentrifuge tubes, KimWipes and Parafilm were purchased from VWR, Inc (Radnor, PA). HybriWell sealing system chambers (6 chambers per slide, chamber dimensions 9.8 x 20 mm, 0.25 mm depth; Grace Bio-Labs), mannan from *Saccharomyces cerevisiae*, calcium chloride dihydrate ($CaCl_2{\cdot}2H_20$), ethanolamine, Tris base, sodium phosphate monobasic (NaH_2PO_4), sodium phosphate

dibasic (Na_2HPO_4), and Tween 20 were purchased from MilliporeSigma (Burlington, MA). Dynabeads M-450 Epoxy magnetic beads (herein referred to as 4.5 micron [μm] beads), ethylenediaminetetraacetic acid (EDTA) and Blocker Casein were purchased from ThermoFisher Scientific (Waltham, MA). Amine-terminated polyethylene glycol (PEG) with molecular weight of 2000 or 10000 daltons (referred to subsequently as PEG(2k) or PEG(10k), respectively) were purchased from Nanocs, Inc (New York, NY). Glass slides coated with an antifouling polymer layer and functionalized with epoxy groups (referred to subsequently as 3D epoxy slides) were purchased from PolyAn GmBH (Berlin, Germany). 10x Tris-buffered saline with 0.5% Tween 20 (TBST) was purchased from Fisher Scientific (Hampton, NH). A fusion protein affinity agent, combining the human IgG Fc portion and the carbohydrate recognition domain of mannose binding lectin (Fc-MBL) [123] was kindly provided by Michael Super of the Wyss Institute for Biologically Inspired Engineering (Boston, MA). Coin vibration motors (3 VDC, 9000 rpm) and linear 1 kiloohm potentiometers were purchase from Digi-Key Electronics (Thief River Falls, MN). Arduino Uno Rev3 microcontroller board was purchase from Arduino (Turin, Italy).

3.2.2 Coin vibration motor characterization via high-speed imaging

To quantify the motion of the slide induced by a coin vibration motor, high speed imaging was used to observe fiducial markers on glass slides during actuation. A HybriWell sealing chamber was affixed to a glass slide and fiducial marker dots were drawn on each chamber. A coin vibration motor was affixed to the glass slide between the middle two chambers, replicating the experiment geometry (Figure 3-2). An Arduino Uno microcontroller was used to control the coin vibration motor motion via pulse width modulation (PWM) under control from a potentiometer. The voltage across the potentiometer for each vibration intensity used was measured via multimeter (Fluke, Everett, WA).

While the motor was vibrating on a flat surface covered by a piece of white printing

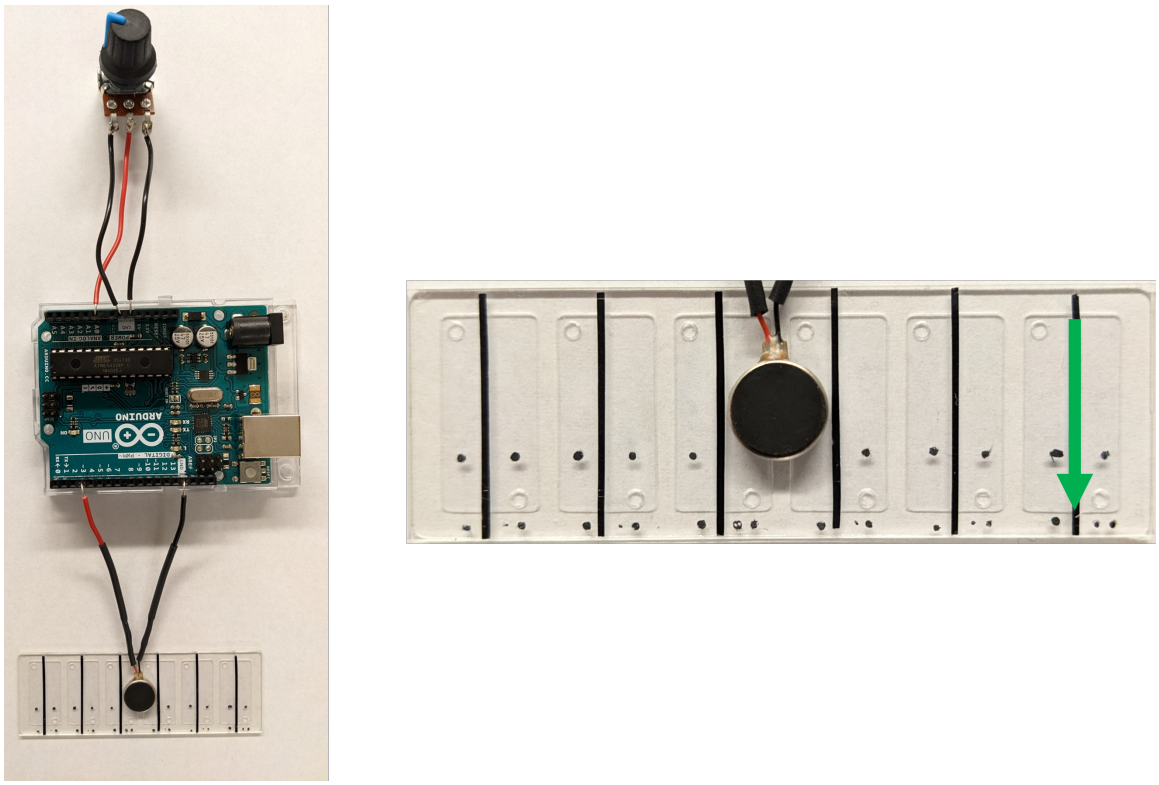

Figure 3-2: **Experimental setup for characterizing slide motion induced by coin vibration motor.** A coin vibration motor is affixed to the middle of the top side of a glass slide, which also has a HybriWell chamber adhered. Fiducial markers are drawn on the slide to aid in motion tracking. High speed imaging records the motion of the slide under different coin vibration motor vibration intensities, which is controlled via a potentiometer connected to an Arduino. In the experiments described, imaging of the chamber took place along the center vertical line of the chamber, as indicated by the green arrow.

paper, a FastCam Mini AX200 highspeed camera (Photron, Tokyo, Japan) fitted with a teleconverter and a 90 mm macro lens (both Tamron, Saitama City, Japan) was used to film fiducial markers at each chamber on the slide. Videos were taken at 5000 frames per second (fps).

Video analysis was performed using a custom Python script and the OpenCV library. Frames covering at least three revolutions of the motor were extracted. The images were binarized and the centroid x and y coordinates of the fiducial markers were determined. For each direction x(t) and y(t), a sinusoidal model of the form

$$r(t) = A\sin(\omega t + \phi) + k \tag{3.2}$$

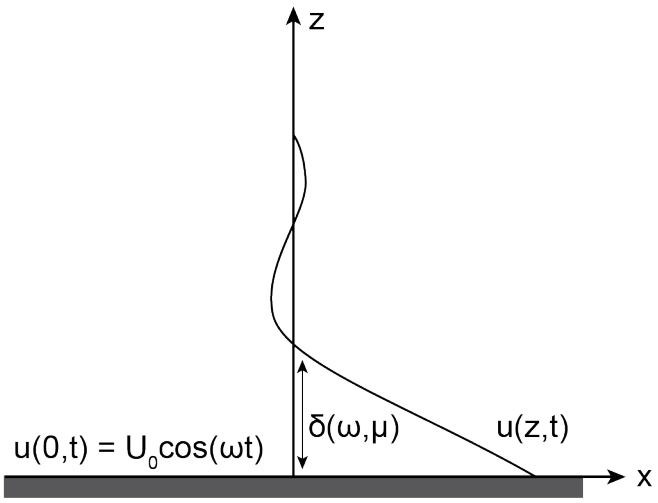

Figure 3-3: **Stokes' second problem.** A flat plate is submerged in an infinite viscous fluid and undergoes sinusoidal motion in the x direction. Friction between the plate and fluid induces motion in the in the fluid layers immediately next to the plate. This velocity profile extends into the fluid for a characteristic length δ_v, which is a function of the plate's oscillation frequency and the fluid viscosity.

was fit to the data, where A is the amplitude, ω is the angular frequency, ϕ is the phase shift and k is the offset.

3.2.3 Shear estimation from motor motion parameters

To estimate the shear force generated in the fluid chambers, results from Stoke's second problem were used [124]. Stoke's second problem derives the fluid motion induced by the one-dimensional oscillatory motion of a flat plate submerged in an infinite viscous fluid (Figure 3-3). Friction between the fluid particles and the surface of the plate sets up a flow profile $u(z,t)$ that extends into the fluid medium by a characteristic length δ_v, which is a function of the fluid dynamic viscosity μ and angular frequency ω of the oscillating plate.

The shear stress in the fluid τ, due to the oscillating motion of the plate is

$$\tau = \mu \frac{du}{dz} = \mu \dot{\gamma} \tag{3.3}$$

where u is fluid velocity and z is the spatial coordinate perpendicular to the plate. $\frac{du}{dz}$

represents the change in fluid velocity with increasing perpendicular distance from the plate, also known as the shear rate $\dot{\gamma}$. We approximate the shear rate as:

$$\dot{\gamma} \sim \frac{U_0}{\delta_v} \tag{3.4}$$

where U_0 is the peak velocity of the plate and, due to friction, the velocity of the fluid layer immediately next to the plate, and δ_v is the velocity boundary layer thickness, the distance over which the fluid velocity decays from U_0 immediately next to the plate to the bulk value (0 m/s in this case). δ_v scales as $\sqrt{\frac{2\nu}{\omega}}$, where ν is the kinematic viscosity of the fluid (equal to $\frac{\mu}{\rho}$, where ρ is the fluid density). Using Equation 3.3 and 3.4, we obtain:

$$\dot{\gamma} \sim \frac{U_0}{\sqrt{\frac{2\nu}{\omega}}} \tag{3.5}$$

$$\tau \sim \mu \frac{U_0}{\sqrt{\frac{2\nu}{\omega}}} \sim U_0 \left(\frac{\rho\mu\omega}{2}\right)^{\frac{1}{2}} \tag{3.6}$$

A scaling estimate of the shear force on a bead (F_{shear}) on the vibrating sensing surface can be found as the shear stress multiplied by the bead surface area, A_b, or

$$F_{\text{shear}} \sim \tau A_b \sim 4\pi r_b^2 U_0 \left(\frac{\rho\mu\omega}{2}\right)^{\frac{1}{2}} \tag{3.7}$$

where r_b is the bead radius. The peak velocity of the vibrating plate can be found by the equation describing its oscillatory motion, which reaches a maximum when $\cos(\omega t) = 1$:

$$u(t) = U_0 \cos(\omega t) \tag{3.8}$$

Unlike Stokes' second problem, for our case of a coin vibration motor moving a glass slide, the motion is two dimensional and the path of the fiducial marker follows a circular or elliptical path (Figure 3-4b). To estimate the peak shear force experienced by a bead, we use the maximum velocity magnitude obtained over the path in either the x or the y direction, since the maximum magnitude in either direction is obtained

when the other is zero. This can be obtained by differentiation of the fitted position versus time curves:

$$v(t) = r^{'}(t) = A\omega \cos(\omega t + \phi) \tag{3.9}$$

By comparison to Equation 3.8 above, we find $U_0 = A\omega$. Substituting this into Equation 3.7 above, we obtain a final rough scaling estimate for the peak shear force F_{shear} experienced by beads on the vibrating slide surface:

$$F_{\text{shear}} \sim 4\pi r_b^2 A\omega \left(\frac{\rho\mu\omega}{2}\right)^{\frac{1}{2}} \tag{3.10}$$

3.2.4 Investigating bead NSB on surfaces without affinity receptor

To examine the effect of surface coating on NSB between beads and surfaces, the effect of different surface densities of PEG grafted onto the bead surface was tested. 4.5 μm epoxy beads were functionalized according to a modified version of the manufacturer's protocol. Beads were incubated with PEG(2k) at a concentration that would theoretically give a surface coverage of 1x, 2x, 10x or 50x of the manufacturer's recommended coverage (200 micrograms [μg] per 4x10^8 beads, or 8 milligrams per square meter [mg/m^2]). Control beads were incubated with BSA at 1x of the manufacturer's recommended concentration. This incubation took place at room temperature for 20 hours (h) with end-over-end mixing at 6 rotations per minute (rpm). Beads were magnetically concentrated and further incubated with 50 millimolar (mM) ethanolamine or 0.1% weight per volume (w/v) BSA in 0.1 molar (M) sodium phosphate buffer for 4 h to react with any excess epoxy groups. After incubation, beads were washed three times in wash buffer (PBS with 2 mM EDTA and 0.1%(w/v) BSA), resuspended and stored at 4°C until use. The surfaces used in these initial experiments were glass or plastic slides with Hybriwell chambers. These surfaces were blocked with 1% (w/v) BSA in PBS for 1 h and washed 4 times with PBS before use.

3.2.5 Optimization of bead and sensing surface chemistry with affinity receptor

To determine the surface functionalization resulting in the lowest bead background, a series of experiments were performed to examine the effects of different nonfouling molecules, blocking agents and buffers. This process yielded an optimized protocol for bead and surface functionalization with FcMBL that was used in subsequent experiments.

The effect of adding FcMBL to the bead and the surface was examined through experiments adjusting the density of FcMBL with or without PEG of different molecular weights. 4.5 μm epoxy beads were incubated with a concentration of FcMBL corresponding to a grafting density of 0, 1 or 10 mg/m^2, in 0.1 M sodium phosphate buffer. Incubation occurred for 20 h at room temperature with end-over-end mixing at 25 rpm using a rotisserie tube mixer (ThermoFisher Scientific, Waltham, MA). After magnetic concentration, beads were incubated with PEG(2k) or PEG(10k) at a concentration corresponding to a grafting density of 10 mg/m^2 or 50 mg/m^2, respectively, in 0.1 M sodium phosphate buffer for 20 h at room temperature with end-over-end mixing at 25 rpm. Beads were subsequently incubated with 50 mM ethanolamine in 0.1 M sodium phosphate buffer for 4 h at room temperature with end-over-end mixing at 25 rpm. Beads were washed three times with wash buffer and resuspended for storage at 4°C until use.

Functionalization to make sensing surfaces followed the slide manufacturer's protocol. Hybriwell chambers were affixed to 3D epoxy slides. FcMBL was added to each chamber at a concentration corresponding to 0, 1 or 10 mg/m^2 grafting density in alkaline buffer (150 mM sodium phosphate buffer + 50 mM sodium chloride, pH 8.5) and the slide was incubated for 20 h at room temperature. To prevent evaporation, all incubations took place in a Petrie dish with a moist KimWipe and sealed with Parafilm. After FcMBL incubation, chambers were washed twice with alkaline buffer. In some trials, a solution of PEG(2k) in alkaline buffer was added to the chambers, at a concentration corresponding to a grafting density of 10 mg/m^2. Slides were

incubated for 20 h with this solution and chambers were subsequently washed twice with alkaline buffer. For all slides, to react with any residual epoxy groups on the slide surface, chambers were filled with blocking buffer (50 mM ethanolamine + 100 mM Tris base, pH 9) and incubated for 2 h at room temperature. After washing twice with PBS, the chambers were filled with 0.1% or 1% (w/v) BSA or casein in PBS to block the surface and allowed to incubate for 30 minutes (min). Chambers were subsequently washed four times with PBS + 0.05% (v/v) Tween 20. After replacing the chamber volume with PBS, the slide was stored at 4°C in a humidified Petrie dish until use.

To examine the interaction between beads and surfaces, forces were applied to the beads via inversion or vibration and the surface was imaged to quantify the number of beads that remained bound to the surface after actuation. Images were taken using a Nikon TE-2000U inverted microscope (Nikon, Melville, NY) fitted with an Andor iXon3 CCD camera (Oxford Instruments, Abingdon, UK) and using a 10x or 20x objective (corresponding to 0.64 and 0.17 mm^2 imaging area, respectively) with a 0.01 s exposure time. For each combination of bead and surface, one million beads were resuspended in 50 microliters (μL) of 1x TBST + 5 mM $CaCl_2$ (TBSTCa), injected into a chamber, and allowed to settle for 2 min, after which images across the entire vertical length of the chamber were taken (20-25 pictures in total; Figure 3-2). Though no analyte was used in these experiments, FcMBL binding is calcium-dependent [125–127] and to simulate real conditions, we utilized the buffer that would be used in an assay. The slide was then inverted and beads were allowed to settle under their own mass for 5 min. Images of residual beads followed the process outlined above. Subsequently, a coin vibration motor was affixed to the surface of the glass slide and used to apply a series of four to six vibrations at increasing intensity via potentiometer under PWM control from an Arduino microcontroller. Each vibration was applied for three minutes, after which the surface was imaged as described above.

3.2.6 Detection of mannan in a model system with FcMBL-functionalized surfaces

Using the optimal combination of FcMBL-coated beads and surfaces as determined through the aforementioned process, experiments were performed to investigate the interaction of beads and surfaces when beads were incubated with mannan. One million beads were incubated in 0.5 mL of TBSTCa buffer with 0, 1, 10 or 100 nanograms per mL (ng/mL) mannan. This incubation took place for 30 min with end-over-end mixing at 25 rpm and at room temperature. Beads were washed three times via magnetic concentration and resuspended in TBSTCa buffer. Subsequently, beads were resuspended in 50 μL of TBSTCa buffer and used in inversion/vibration experiments as described above.

3.2.7 Image analysis algorithm

To quantify the beads remaining on the surface after inversion or vibration, a custom-made MATLAB (MathWorks, Natick, MA) script was used. For each image, the script performs the following:

1. *Binarization*: Beads become white on a black background. This used the Sauvola algorithm, a local thresholding method that determines the binary value of a pixel based on a window of surrounding pixels [128]. The optimal window size for our analysis was determined by comparison of algorithm-determined bead counts to manual bead counts over a range of different residual bead counts. The chosen window of 20 x 20 pixels yielded an average error of $< 1\%$ in bead count when compared with manual counting. Black regions in the middle of the beads were turned to white using the *imfill* function.

2. *Determination of number of beads in the image*: Using *regionprops*, the area of each white bead is found and the mode of these areas is determined. Since the majority of the beads in each image are single beads, this mode area is taken as the single bead area. Using the total white area in the picture, the number of

beads in the image is determined by dividing the total white area by the mode area.

3. *Quantification*: The average bead count across the entire imaging line is found (Figure 3-2). To find the fraction of beads that remain after each actuation, the ratio of the beads remaining after each actuation to the beads in the first set of images (when the beads are first deposited, before slide inversion) is found. To examine the spatial variance in bead number, bead counts in sets of five sequential images are averaged together.

3.3 Results and discussion

3.3.1 Coin vibration motor applies shear forces with magnitudes sufficient to disrupt NSB

In order to estimate the force applied to beads via coin vibration motor, we used high speed imaging to characterize the oscillatory motion of the slide. Figure 3-4 shows example steps in the analysis process. The image processing algorithm extracts the coordinates of fiducial markers on each chamber in each video frame (Figure 3-4a, blue dot). Plotting these coordinates reveals that the motor induces 2D orbital motion, which is likely due to the motor's eccentric mass rotation (Figure 3-4b). Fitting a sinusoidal model to the x and y coordinates of the fiducial marker allows for the quantification of the motion (Figure 3-4c). Sinusoidal fits were, in general, quite robust, with $R^2 > 0.95$, demonstrating the efficacy of this image processing method.

In order to determine the magnitude and consistency of this induced motion, we characterized two of the same motors (Figure 3-5). Motor 1 was tested twice, once before use in experiments and once after ∼5 experiments worth of use. Since adhesive attached the motor to the slide and the motor was removed and repositioned multiple times during an experiment, this analysis determined if motor performance was sufficiently stable to permit use in multiple experiments. Motor 2 was tested once and compared to Motor 1 to investigate if different motors were similar in their

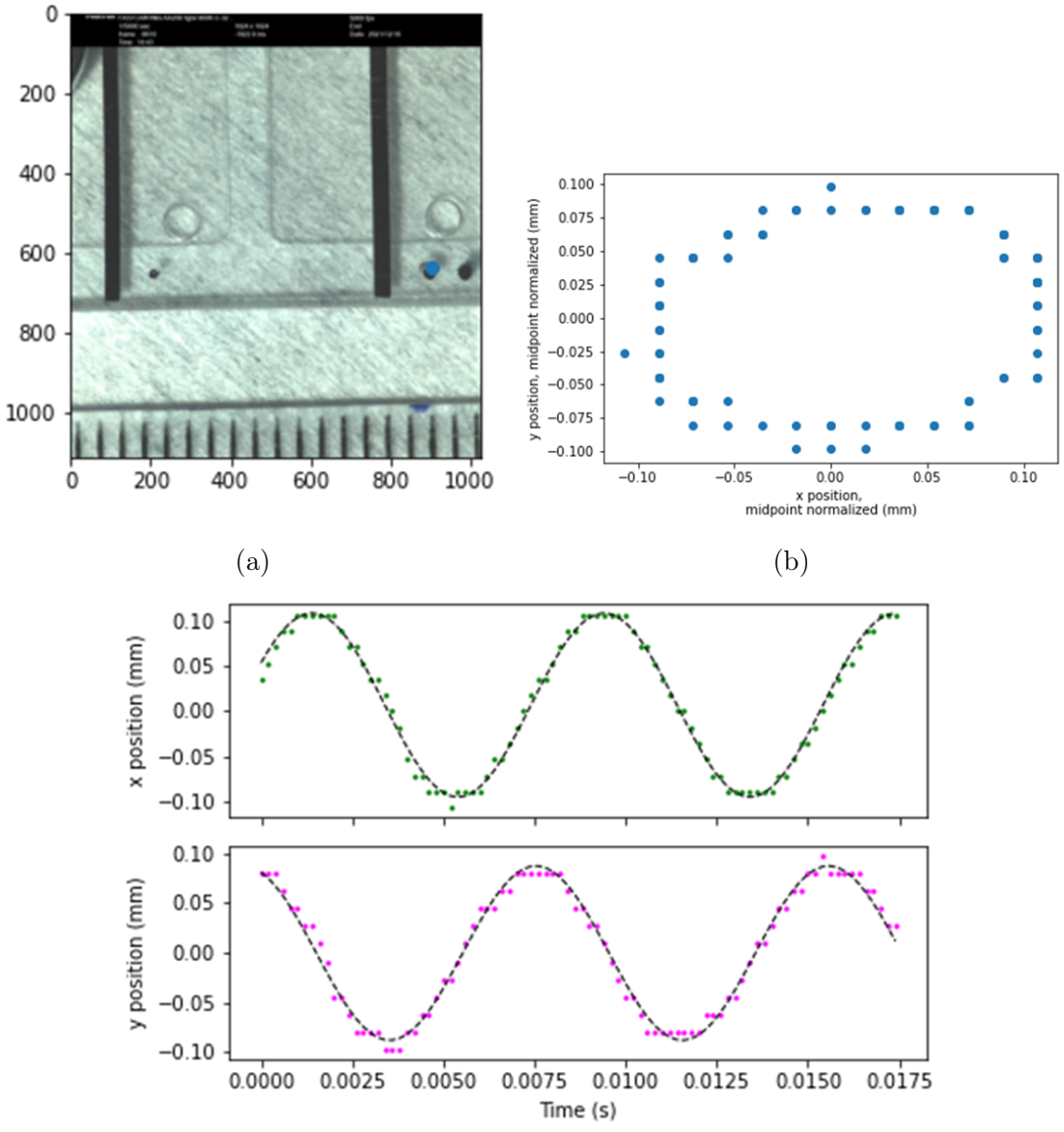

(a) (b)

(c)

Figure 3-4: **Example characterization of a coin vibration motor.** (a) For each frame, the image processing algorithm finds the fiducial marker (shown by the blue dot over the black fiducial marker). (b) The position of the fiducial marker in each frame is plotted, demonstrating the orbital motion induced by the coin vibration motor. (c) The x and y coordinates for each marker are fitted with a sinusoidal model to parameterize the marker's position versus time. Fitted parameters are subsequently used to estimate the peak shear stress induced by motor vibration.

induced motion.

Figure 3-5a plots the angular frequency ω, determined via sinusoidal curve fit, for each of the six chambers on the slide and for each iteration of motor testing, as described above. Derived parameters are also shown in Table 3.1. Estimates of δ_v are an order of magnitude smaller than half of the chamber depth (1.25x10^{-4} m), indicating minimal interactions between δ_v on each surface of the chamber and suggesting results from Stokes' second problem yield valid estimates for our purposes.

Notable within each of the three plots of Figure 3-5a is the consistency of ω across chambers. With the exception of vibration induced by 1.6 volts (V), there is less than 10% difference in ω across the chambers (maximum relative standard deviation (RSD) across the chambers is 2.9%, 4.4% and 3.5% for Motor 1 before experiments, Motor 1 after experiments and Motor 2, respectively). However, the angular frequency at 1.6 V is not consistent across the slide. At this condition, RSD in ω across the six chambers is 16% and 26% for Motor 1 after experiments and Motor 2 before experiments, respectively. During experimentation, there was an audibly noticeable change at this driving voltage, indicating that this frequency may be near the natural frequency of the motor. Motor 1 before experiments did not show this large variation in ω across the slide at 1.6 V, indicating that observations could also be due to differences in experimental setup and that care should be taken to ensure consistent motor placement.

Comparing the angular frequency between tests at each driving voltage, ω is similar for all motors. Discrepancies again arise at 1.6 V and are also present at the highest driving voltage, 2.9 V. This is close to the 3 V maximum driving voltage, where manufacturing differences between motors may be particularly amplified.

Our ultimate goal is to translate the fitted sinusoidal parameters to the maximum shear force that a 4.5 μm bead would experience at each vibration intensity. Using Equation 3.10 with the maximum fitted amplitude in either the x or y direction and the average angular frequency across the chambers at a specific driving voltage, we find that coin vibration motors are capable of generating shear stresses over the physiological range [129,130] (Figure 3-5b), with maximum differences between motors

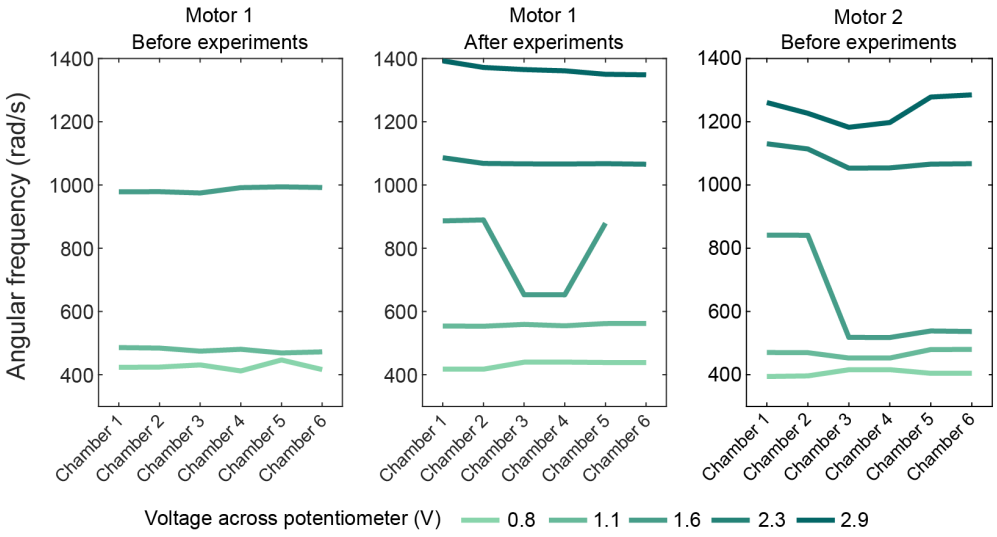

(a)

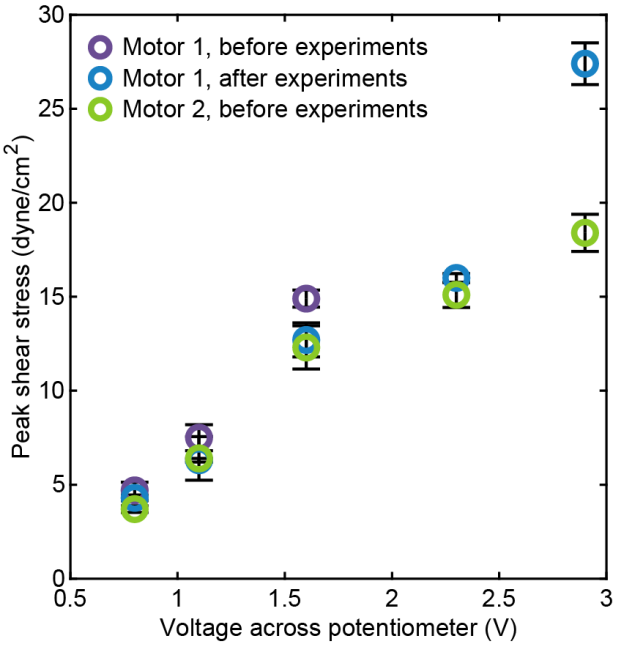

(b)

Figure 3-5: **Comparison of motion and shear induced in chambered slides by actuation using different coin vibration motors.** a) Angular frequency ω, as determined by a sinusoidal model fitted to fiducial marker coordinates, at each of six chamber locations on the slide. Lower intensities are more consistent across trials of the same motor and between motors. Motion at 1.6 V is different between motors. (b) Peak shear stress induced by fluid motion on the slide surface. Shear stress is practically linear with potentiometer voltage and, aside from actuation at the maximum operating voltage, is similar for all motors tested. This result allows us to predict the shear stress applied over the range of operating voltages. Error bars are the standard deviation of the six chambers across the slide.

Table 3.1: **Coin vibration motor motion parameters obtained through high-speed imaging and subsequent analysis.**

	Potentiometer voltage (V)	Average omega (rad/s)	Peak velocity (m/s)	Delta (m)	Peak shear rate (1/s)	Peak shear stress (dyne/cm^2)	Peak shear force on 4.5 µm bead (pN)	SD across chambers (pN)	RSD across chambers (%)
Motor 1, before use	0.8	426	0.032	6.9E-05	467	4.7	30	3	9
	1.1	478	0.048	6.5E-05	746	7.5	48	4	9
	1.6	985	0.067	4.5E-05	1491	14.9	95	3	3
Motor 1, after use	0.8	432	0.029	6.8E-05	425	4.3	27	1	4
	1.1	558	0.038	6.0E-05	629	6.3	40	1	2
	1.6	792	0.064	5.0E-05	1273	12.7	81	6	7
	2.3	1070	0.069	4.3E-05	1598	16.0	102	1	1
	2.9	1365	0.105	3.8E-05	2743	27.4	175	7	4
Motor 2, before use	0.8	405	0.026	7.0E-05	370	3.7	24	1	5
	1.1	468	0.042	6.5E-05	639	6.4	41	7	18
	1.6	632	0.072	5.6E-05	1284	12.3	78	7	9
	2.3	1081	0.065	4.3E-05	1515	15.1	96	4	4
	2.9	1238	0.074	4.0E-05	1835	18.4	117	6	5

observed near the 3 V limit. Peak shear stress varies approximately linearly with driving voltage. This characterization allows us to estimate the peak shear stress at any driving voltage. The maximum difference in shear stress when reusing a motor is 16% (for Motor 1 before and after experimentation at 1.6 V) and the maximum difference between different motors before experiments is 19% (between Motor 1 before experimentation and Motor 2 at 1.6 V).

Translating this peak shear stress to peak force experienced by a 4.5 μm bead during vibration shows that vibration-based actuation is able to generate forces theoretically capable of disrupting NSB based on previously measured values (>10 pN [112,113,115]; Table 3.1). The higher vibration intensities may be able to disrupt specific interactions between affinity agent and analyte, with generated forces greater than 100 pN. The variation in force experienced across the slide is generally <10%, suggesting that beads at any slide location will experience similar forces. This consistency is important to ensure assay robustness. Overall, our motor characterization suggests that vibration-induced shear from a coin vibration motor can generate forces high and consistent enough to disrupt parasitic NSB between beads and surfaces without the use of fluidic pumps.

Table 3.2: **Theoretical PEG graft spacings on surfaces.**

	Condition	Coating density (#/nm^2)	σ (nm^2/graft)	Separation between grafts (nm)	Brush configuration (separation < Flory radius*)?	L_0** (nm)
PEG(2k) bead testing on glass/plastic surfaces	1x	2	0.42	0.73	TRUE	11
	2x	5	0.21	0.52	TRUE	14
	10x	24	0.04	0.23	TRUE	24
	50x	118	0.01	0.10	TRUE	41
PEG(2k) with FcMBL		3	0.33	0.65	TRUE	12
PEG(10k) with FcMBL		3	0.33	0.65	TRUE	60

*Flory radius (R_F) = $a_{PEG}\left(\frac{MW_{polymer}}{MW_{PEG\ monomer}}\right)^{\frac{3}{5}}$; a_{PEG} = 0.36 nm; R_F^{PEG2k} = 3.6 nm, R_F^{PEG10k} = 9.3 nm

**Equilibrium thickness (L_0) = $a_{PEG}\left(\frac{MW_{polymer}}{MW_{PEG\ monomer}}\right)\left(\frac{{a_{PEG}}^2}{\sigma}\right)^{\frac{1}{3}}$

3.3.2 Investigating antifouling coatings establishes a foundational surface chemistry for beads and sensing surfaces

Generating robust sensing surfaces often requires additional surface functionalization with nonfouling molecules, as well as optimization of blocking agents and buffer conditions. Much of the NSB literature focuses on protein adsorption to surfaces [54, 55, 65, 131–133] and there are few reports of NSB between beads and surfaces [64, 67]. To further investigate NSB between beads and surfaces, we first performed a series of experiments that varied surface chemistry and quantified the residual beads on the surface after gravity- and vibration-induced actuation and in the absence of any analyte or functional receptor. This allowed us to estimate the strength of nonspecific interactions, as well as the most promising antifouling coating for subsequent experiments.

Our initial experiments examined the effect of PEG(2k) grafting density, backfill agent and slide material on NSB. 4.5 μm epoxy beads were functionalized with PEG(2k)

at 1x, 2x 10x or 50x the optimal coating density as specified by the manufacturer. At these conditions, the theoretical PEG(2k) grafting density suggested all were in brush layers (Table 3.2). Figure 3-6 compares results by slide and bead type. Immediately, it is apparent that glass slides are better at resisting NSB than plastic slides. A striking example is seen in comparing beads with PEG(2k) at 50x grafting density and ethanolamine backfill between the glass and plastic surfaces: applying a shear of 27 pN removed 75% of beads on the glass surface but only 38% of beads on the plastic surface, showing that the interactions between PEG(2k)-functionalized beads and plastic surfaces are stronger, despite BSA surface passivation. This observation may be partly due to the benzene ring in the backbone of the polystyrene structure, which could impart a partial negative charge to the surface and interact with partial positive charges on ethanolamine or other polarizable groups on the beads. These results caused us to cease investigation of plastic slides.

In the glass surface experiments, comparison between different backfill reagents on the bead suggests that ethanolamine or no backfill agent is preferable to BSA backfilling. However, this seems to be dependent also on the presence of PEG(2k). From all glass surface experiments, the beads backfilled with BSA (no PEG(2k)) showed the lowest residual bead binding, with nearly 87% removed under gravity-induced actuation alone (0.7 pN force), while the same actuation applied to beads with ethanolamine backfill or no backfill resulted in 25% or 35% of beads removed, respectively. However, in the presence of PEG(2k) on beads at any coating density, the fraction of BSA-backfilled beads remaining increased significantly and could not be removed even by forces exceeding 100 pN, suggesting that there is a strong interaction between the PEG(2k) molecules and the BSA on the surface. Elevated fouling due to interactions between PEG and BSA has been previously reported [65], though the mechanism behind this phenomena is unknown. The higher grafting density of PEG(2k) on the beads, which forces a certain PEG brush conformation that is less resistant to protein adsorption [131–133], could also be influential, as discussed in the next section.

Comparing ethanolamine versus no backfill reveals that while no backfill reagent

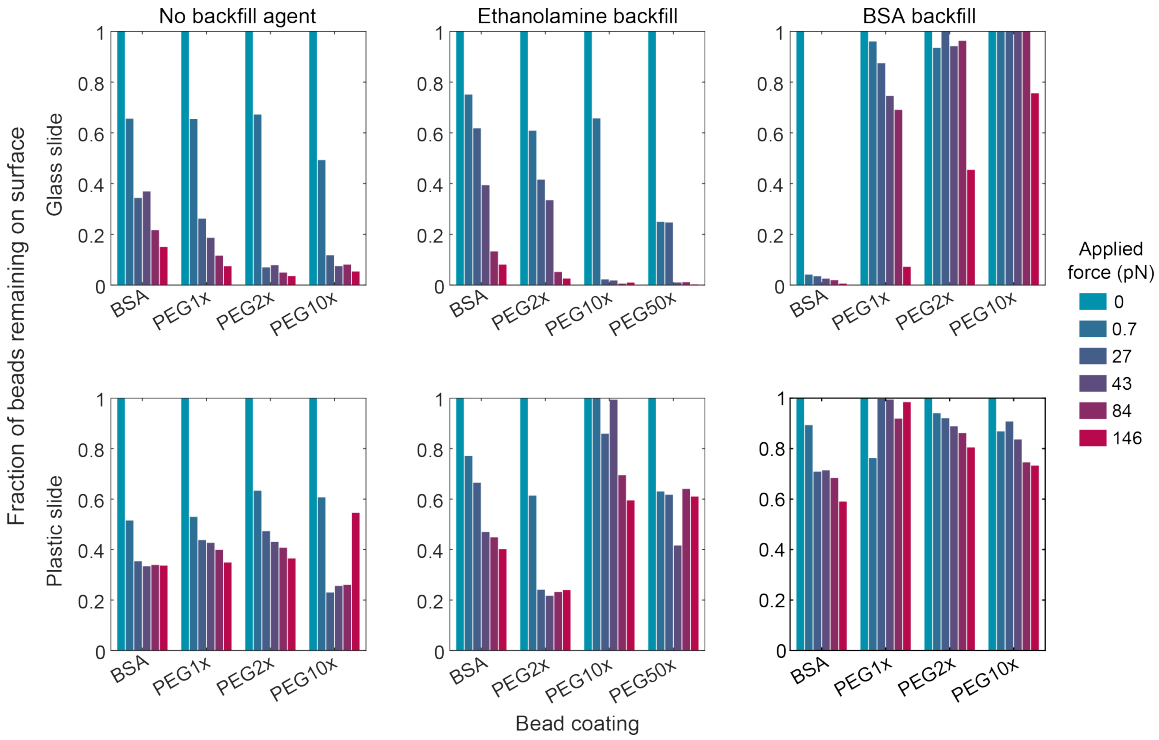

Figure 3-6: **Initial investigation of antifouling coatings for bead and sensing surfaces.** Each row represents a different slide materials, while each column represents a different backfill agent used during bead functionalization. Bars are grouped by the bead functionalization agent. BSA-passivated glass slides (top row) are superior to BSA-passivated plastic slides (bottom row) for all bead coatings tested, suggesting PEG interactions with the polystyrene backbone are strong enough to hold beads to the surface. Backfilling beads with ethanolamine, to react with any residual epoxy groups, is superior to no backfilling or BSA backfilling, suggesting that BSA interactions with PEG chains in dense brush layers may increase NSB.

leads to more beads removed at weaker actuations, the number of beads removed at each successive actuation decreases when there is no backfill, suggesting that there is a tightly held fraction of beads unamenable to removal even with applied forces exceeding 100 pN. Previous results in a magnetic pulling assay have also found different bead populations characterized by the force required for their removal [67]. By these results, such tightly held background beads could be as high as 5% of all beads (PEG(2k), 10x grafting density, no backfill beads). This is in contrast to ethanolamine-backfilled beads, which at the same PEG(2k) grafting density, only had 0.8% of beads remaining. The ethanolamine-backfilled beads seem to continually come off with increasing actuation forces, suggesting a wider distribution of bead-surface interaction forces and minimization of the maximum attractive force between the beads and the surface. Based on these screening experiments, we selected ethanolamine as our backfill reagent for subsequent functionalizations.

Additionally, increasing PEG grafting density corresponds to more beads removed at a given actuation, as would be expected by polymer brush theory [53, 56, 134], further discussed in Chapter 6, and previous results [54]. Aside from the 0.7 pN applied force, the difference between PEG(2k)-10x and PEG(2k)-50x bead grafting density was minimal.

3.3.3 Adding a model receptor to create functional surfaces requires optimization of antifouling layer and blocking agent

To determine the effects of adding a functional affinity receptor, we modified the previously determined optimal antifouling bead functionalization protocol to include a model receptor, FcMBL. FcMBL is a fusion protein made of the human IgG antibody Fc domain and the carbohydrate recognition domain (CRD) of mannose binding lectin (MBL) [123]. MBL is part of the innate immune system and acts as a calcium-dependent opsonin, binding to a range of carbohydrates found on pathogens and marking them for damage via the complement cascade [127, 135]. Originally developed

for blood cleansing purposes [123], FcMBL and one of its targets, yeast mannan, were selected as a model receptor and ligand for our sensing system to facilitate rapid screening.

Prior to addition of PEG(2k) at 10 mg/m^2 and ethanolamine, FcMBL was added to epoxy beads at 0, 1 or 10 mg/m^2 coating density. 3D epoxy surfaces were also functionalized with 0, 1 or 10 mg/m^2 FcMBL, and subsequently treated according to the manufacturer's protocol. Testing combinations of these beads and sensing surfaces revealed that increasing the FcMBL density on both surfaces resulted in the lowest bead NSB (Figure 3-7a). Notably, all combinations of bead and sensing surface after all actuations had <20% of beads remaining and this fraction decreased with increasing actuation force, presumably as more tightly held beads were removed. This suggests that the strongest interactions are absent between interactions between opposing FcMBL molecules, and between FcMBL and other coating molecules, making these interactions amenable to disruption.

The 10 mg/m^2 FcMBL bead surface and 10 mg/m^2 FcMBL sensing surface was the only surface that showed performance similar to the control at all actuations tested. For example, using 0.7 pN actuation force, 9% of beads remained when there was no FcMBL on either surface, while 3% of beads remained when both surfaces were coated with 10 mg/m^2 FcMBL. Importantly, with 10 mg/m^2 on both surfaces, the performance across replicate tests was also consistent, with standard deviation across the duplicates of 1% (as compared to 9% for the control case), suggesting repeatable performance for this condition. This was not the case for all conditions, which showed some variation between replicates (Figure 3-8). Each of the replicates was performed on the same slide suggesting that heterogeneity across the slide in, for example, epoxy group density or antifouling coating thickness, could heavily influence the residual bead background.

We additionally trialed the same set of experiments with the addition of PEG(2k) to the 3D epoxy glass surface after FcMBL incubation to determine if adding an additional antifouling molecule to the sensing surface could further decrease NSB. Results from these experiments suggest that addition of PEG to the glass sensing

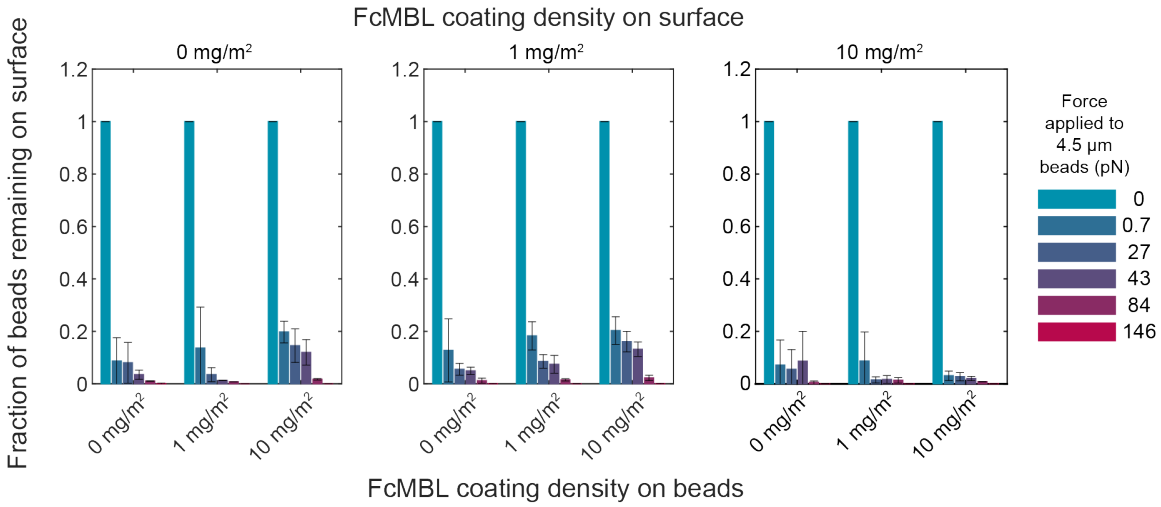

(a)

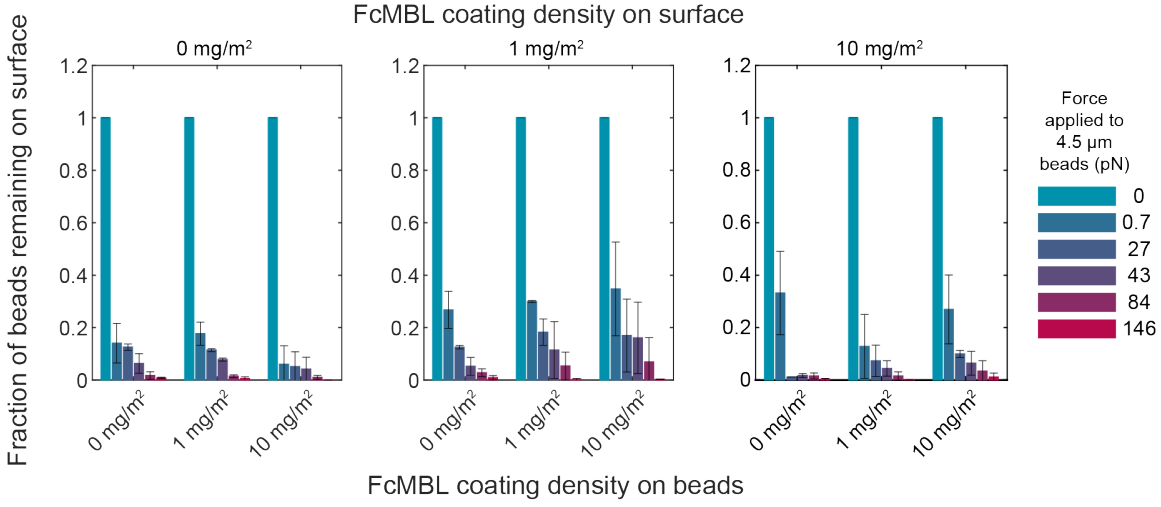

(b)

Figure 3-7: **Optimization of FcMBL and PEG coating density on beads and glass slides.** 4.5 μm Dynabeads were functionalized to achieve a theoretical FcMBL density of 0, 1 or 10 mg/m^2 and subsequently functionalized with amine-PEG(2k) at a theoretical density of 10 mg/m^2 to further promote antifouling. Glass slides were functionalized with FcMBL or with FcMBL and PEG(2k) at the same coating density used for the beads (a and b, respectively). These 18 bead-surface combinations were tested in duplicate; data shown is the average, with error bars representing the standard deviation of the duplicates. (a) The lowest and most repeatable nonspecific binding was observed when using beads with 10 mg/m^2 FcMBL and slides coated with 10 mg/m^2 FcMBL. (b) Addition of PEG(2k) to the glass surface increased the number of beads remaining on the surface, with greater variation observed between replicates.

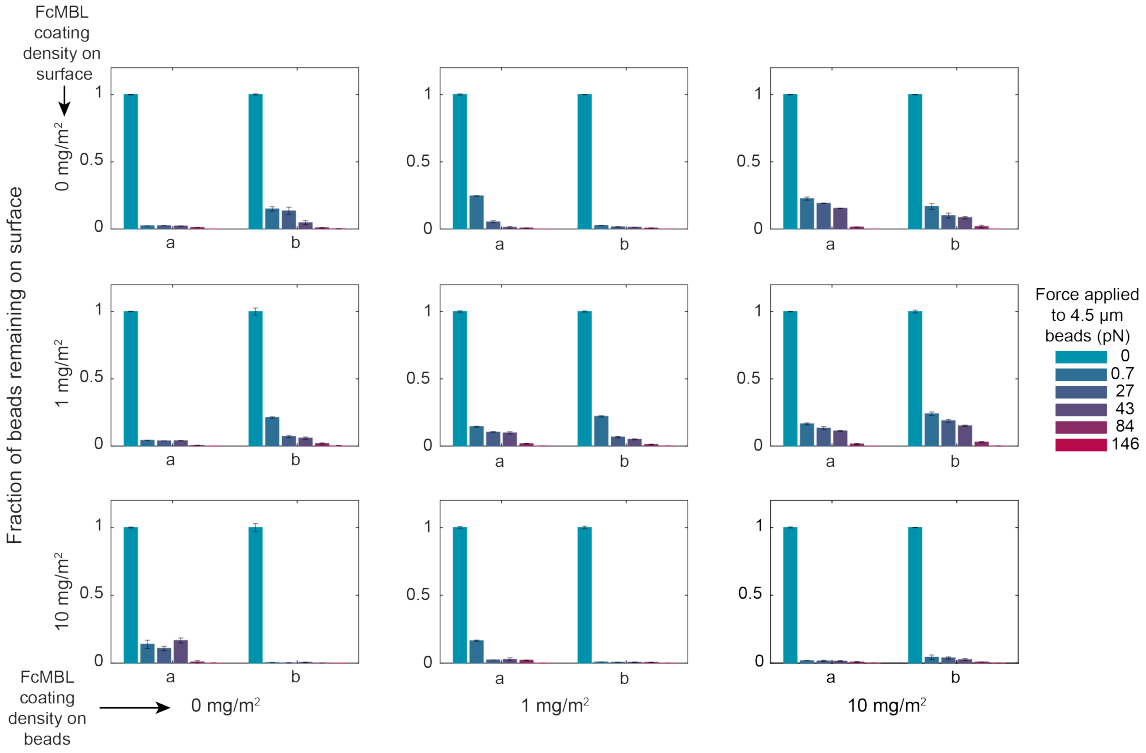

Figure 3-8: **Data from Figure 3-7a separated into individual replicate results.** Data is displayed in a matrix to show each combination of FcMBL coating density on beads and on surfaces. Many combinations show significant differences between replicates, with one chamber having higher residual beads than the other chamber for the same applied force. This suggests that the slide surface functionalization is heterogeneous, potentially due to variation in the density of functional groups or thickness of the slide coating.

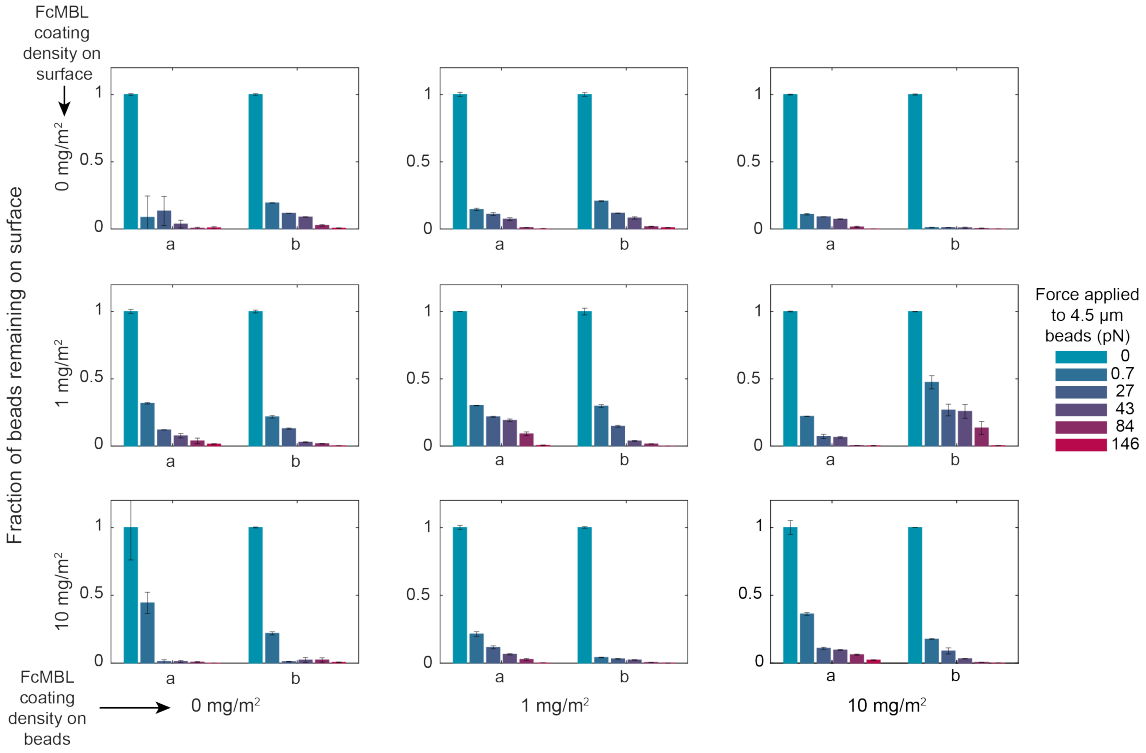

Figure 3-9: **Data from Figure 3-7b separated into individual replicate results.** Data is displayed in a matrix to show each combination of FcMBL coating density on beads and on surfaces. Many combinations show significant differences between replicates, with one chamber having higher residual beads than the other chamber for the same applied force. This suggests that the slide surface functionalization is heterogeneous, potentially due to variance in the density of functional groups or thickness of the slide coating.

surface has a detrimental effect on residual bead binding (Figure 3-7b). Comparing the 10 mg/m^2 FcMBL on both surfaces case in Figures 3-7a and 3-7b, the addition of PEG(2k) on the sensing surface increased the residual bead binding by 9x (3% of beads remaining on the surface without PEG(2k) versus 27% of beads remaining on the surface with PEG(2k), using 0.7 pN force). More variation between replicates was also observed when PEG(2k) was included on the sensing surface (Figure 3-9).

Theory and literature suggest that increasing the molecular weight of the PEG chains grafted to the surface could increase the PEG brush layer thickness and minimize NSB via steric repulsion [53–55]. To test if this was the case on our bead-surface system, we examined the residual beads remaining after actuation when beads were grafted with PEG(10k) instead of PEG(2k). We used PEG(10k) at a concentration that would theoretically result in the same number coating density as PEG(2k) (Table 3.2). In this experiment, FcMBL was present only on the sensing surface. As shown in Figure 3-10a, the fraction of beads remaining when beads were grafted with PEG(10k) was higher than when beads were grafted with FcMBL and PEG(2k). Whereas <20% of beads remained on the surface in all conditions tested with beads having FcMBL and PEG(2k), 30-40% of beads with PEG(10k) remained on the sensing surface in many cases (compare Figure 3-7a to 3-10a). This fraction did not decrease significantly until application of higher forces (>99 pN) were applied, indicating that increasing the PEG chain length increased NSB strength between beads and the FcMBL-coated sensing surface.

It is unclear why the addition of PEG to the sensing surface or the increase in PEG molecular weight increased NSB in our system. While too sparsely packed PEG layers are not able to suppress NSB [54], there is literature to suggest that too densely packed layers are also unable to suppress NSB [64, 131, 133]. Denser packing in the brush configuration ($\geq$ 5 molecules per square nanometer [64, 132]) promotes the "all-trans" PEG conformation, in which the molecules are completely planar. Less dense brush packing density promotes helical, amorphous chains. It is hypothesized that helical chains are able to better stabilize a solvation layer, due to their helical turn length scale comparable to the size of a water molecule [133]. Water molecules

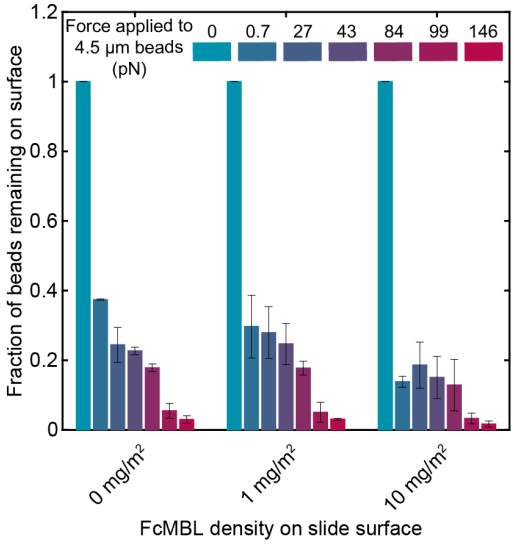

(a)

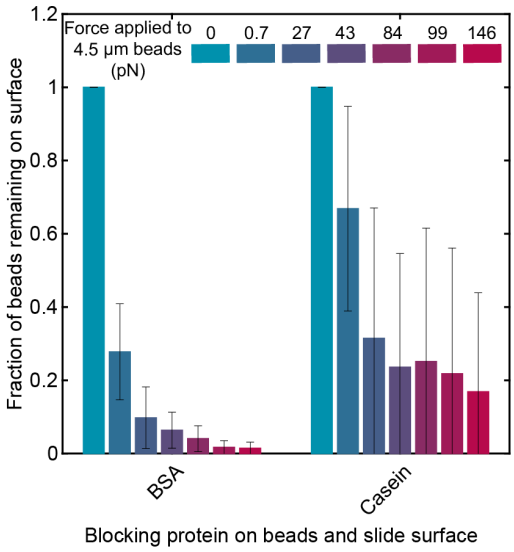

(b)

Figure 3-10: **Effect of different molecular weight PEG and blocking proteins on bead NSB on FcMBL surfaces.** a) 4.5 μm Dynabeads were functionalized with 50 mg/m^2 PEG(10k). Glass surfaces were functionalized with 0, 1 or 10 mg/m^2 FcMBL. Each bead/surface combination was tested in duplicate; error bars represent the standard deviation of the duplicate wells. Beads with PEG(10k) show higher nonspecific binding than beads with FcMBL + PEG(2k), with greater variation between replicates. (b) 4.5 μm Dynabeads were functionalized with 10 mg/m^2 FcMBL and 10 mg/m^2 PEG(2k) and blocked with either 1% (w/v) BSA or casein. Glass surfaces were functionalized with 10 mg/m^2 FcMBL and blocked with either 1% (w/v) BSA or casein. Experiments using beads and surfaces with the same blocking protein were performed in duplicate.

do not fit as easily in the planar "all-trans" forest, resulting in a less stable water layer and decreased resistance to fouling. Much of the evidence for PEG conformation and fouling comes from studies of protein adsorption to surfaces, but there is at least one report of PEG conformation potentially influencing microsphere adhesion [64]. Some of our grafts theoretically exceeded or were close to this packing limit (Table 3.2), suggesting that PEG conformation could play a role in our system as well.

Finally, using the optimal bead and sensing surface chemistry identified through the exploration above (beads with 10 mg/m^2 FcMBL + 10 mg/m^2 PEG(2k) and surface with 10 mg/m^2 FcMBL), we examined the effect of different blocking proteins on the suppression of NSB. Commonly used in the engineering of functional biomedical surfaces, blocking agents adsorb to remaining exposed surface area to prevent NSB at those locations. Many blocking agents have been identified and used in the literature for sensing surfaces [52, 136, 137], but two of the most widely used and economical are BSA and casein. BSA is a 66 kilodalton (kDa) protein [52] while casein contains a heterogeneous mixture of peptides ranging in molecular weight from <10 kDa to over 60 kDa [138]. This heterogeneity is hypothesized to contribute to casein's superior blocking ability over BSA for some applications [139].

When we tested the ability of these blocking agents to suppress bead binding to the sensing surface, we found BSA to be the better blocking agent (Figure 3-10b). BSA-treated surfaces not only showed a lower fraction of beads remaining after all actuations, but also more repeatable performance across the replicates. As casein is extracted from bovine milk, which contains carbohydrates that MBL is known to bind [140], residual sugar content in casein could contribute to this increased NSB. In general, optimal blocking agents are application specific and screening these agents is an important step in assay development.

In summary, from this evaluation of bead and sensing surface chemistries, we identified that beads with FcMBL at 10 mg/m^2 and PEG(2k) at 10 mg/m^2 and sensing surfaces with FcMBL at 10 mg/m^2, both blocked with BSA, minimizes NSB, with 3% of beads remaining after an application of 0.7 pN and <1% of beads remaining after applying a force of 99 pN. Neither increasing PEG molecular weight nor grafting

PEG on the sensing surface provided further advantage, potentially due to interactions between opposing PEG chains and the conformation of PEG chains. This bead-surface combination was selected to move forward in experiments investigating gravity- or vibration-induced dissociation.

3.3.4 Inversion and vibration mechanisms can differentiate between mannan concentrations, but sensitivity is limited by bead background

To determine the efficacy of the proposed actuation method in a bead-based assay, we incubated FcMBL-functionalized beads with different concentrations of mannan, applied them to a FcMBL-functionalized sensing surface and quantified the fraction of beads remaining after actuations of increasing force. Mannan is a carbohydrate target of FcMBL, of 40 kDa average molecular weight [141], and is present on the surface of many pathogens [135]. It was hypothesized that the fraction of beads remaining on the surface should increase with increasing mannan concentration. As mannan concentration increases, the amount of mannan sandwiched between a bead and the sensing surface increases, translating into greater force required to remove beads and a greater fraction of beads remaining on the surface for the same applied force.

Figure 3-11a shows the results from the initial experiment and verifies this hypothesis. As mannan concentration increases from 0 to 100 ng/mL, the fraction of beads remaining on the surface at each applied force is greater. The largest difference between mannan concentrations is seen using forces $<$84 pN; above this force, the fraction of beads remaining is similar, suggesting forces higher than this remove beads indiscriminately and are too strong to differentiate between mannan concentrations. This force cutoff is unique to the FcMBL-mannan interaction and would be different for other analytes. The range of relevant forces over which sensing can occur will vary by the strength of the specific affinity receptor-ligand interaction used in each assay.

Noticeable, however, is the large background of beads that remains even with the optimized surface chemistry in the 0 ng/mL condition. After 0.7, 27 and 43 pN

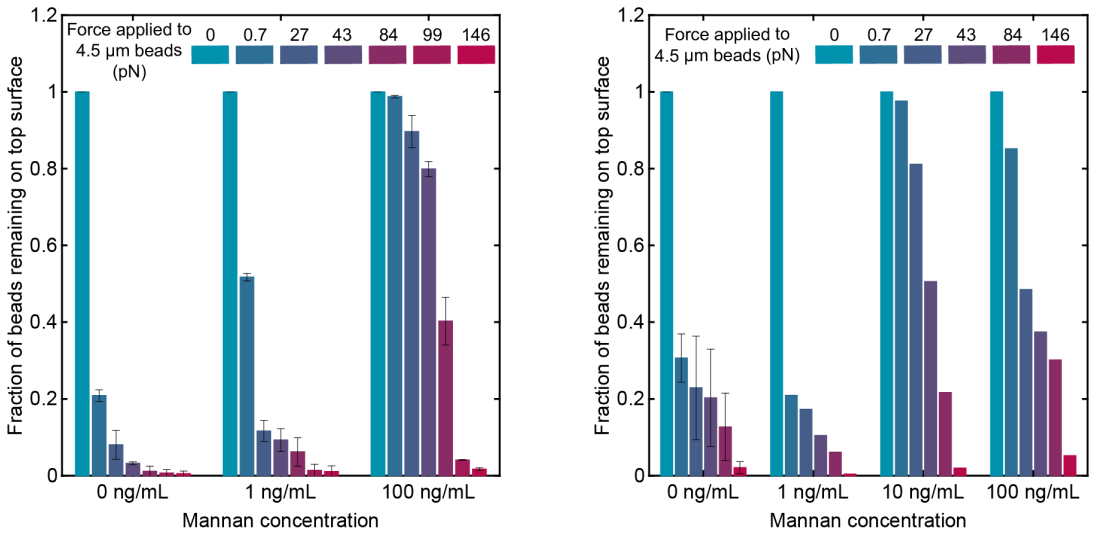

(a) (b)

Figure 3-11: **Demonstration of mannan sensing in gravity- or vibration-induced sedimentation assay using optimized bead and glass surface chemistry.** FcMBL-functionalized 4.5 μm beads were incubated at 1 million beads/mL for 30 min with yeast mannan at various concentrations (as shown on the x-axis). (a) Initial experiment with 0, 1 or 100 ng/mL of mannan suggests that gravity-induced sedimentation or vibration-induced sedimentation can differentiate between different concentrations. Lower forces (<84 pN) are better for differentiation; higher forces remove beads indiscriminately. Error bars represent the standard deviation of duplicate measurements. (b) Experiment with 0, 1, 10 or 100 ng/mL of mannan, using glass slides from a new lot. 0 ng/mL condition was performed in triplicate with error bars representing the standard deviation of the replicates, while the other conditions were performed in singlet. This trial show less robust performance, with much greater variation between replicates and higher bead background, which makes differentiation between mannan concentrations difficult.

applied force respectively, 20%, 8% and 3% of beads remain on the surface in the control condition, while 50%, 12% and 9% of beads remain on the surface in the 1 ng/mL condition. While concentrations between 0 and 1 ng/mL were not tested in this trial, the small difference in beads remaining between these two concentrations could lead to challenges in differentiating concentrations less than 1 ng/mL with the current surface chemistry. Comparison of these 0 ng/mL results to the results with optimal surface chemistry in Figure 3-7a also suggest heterogeneity in surface coating and/or functionalization from slide to slide, as the Figure 3-7a results had 3.1%, 2.7% and 2.0% of beads remaining after applying a force of 0.7, 27 and 43 pN, respectively.

To examine the assay performance with a greater range of mannan concentrations and using a different 3D epoxy slide lot, we performed the same experiment using 0, 1, 10 or 100 ng/mL of mannan. All trials were on the same slide, but the 0 ng/mL condition was performed in triplicate, while the 1, 10 or 100 ng/mL were performed in singlet (Figure 3-11b). Results from this experiment were more mixed than in the initial experiment. For one, the bead background in the control 0 ng/mL condition was consistently higher after all applied forces, and did not fall under 20% beads remaining until a force of 84 pN was applied, indicating stronger bead-surface interactions. This is in contrast to the previous experiment in Figure 3-11a and, since the same beads were used in each experiment, suggests slide-to-slide and lot-to-lot variation could be a major source of variability in assay performance.

Additionally, due to this large bead background, this experiment was not able to differentiate between 0 ng/mL and 1 ng/mL or between 10 ng/mL and 100 ng/mL. The trend was reversed from the hypothesis, with a greater fraction of beads remaining after each applied force for 10 ng/mL when compared to 100 ng/mL. Heterogenous surface chemistry could play a role here, but it also could be that the assay is reaching saturation at these higher concentrations (i.e., the beads are covered with the maximum amount of mannan at 10 ng/mL, leading to the inability to differentiate between mannan concentrations above this, a phenomena known as the hook effect [142]).

Also noticeable in the control condition are the large error bars, especially in comparison to the 0 ng/mL condition in the initial trial in Figure 3-11a. To examine

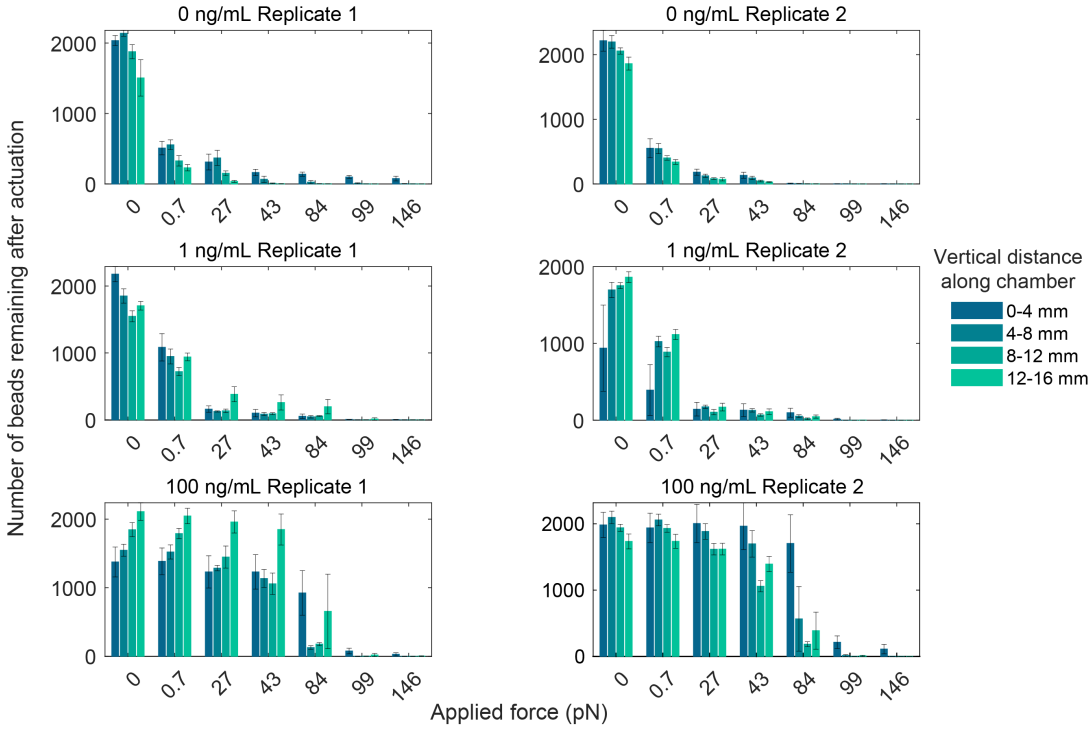

Figure 3-12: **Spatial variation in number of residual beads across the vertical length of chamber during initial mannan experiment.** Data from Figure 3-11a was separated by replicate and show variable residual bead count across the slide. Error bars represent the standard deviation of the five images included for the particular location.

the source of this variability, for both assay trials, we looked at the spatial heterogeneity across each of the chamber replicates. We averaged the number of beads per field of view (FOV) over each set of 5 sequential images at each applied force. Results are shown in Figure 3-12 and suggest heterogeneity not only between replicates but between different areas of individual chambers. The middle of the slide (4-8 mm and 8-12 mm vertical distance) seems to be relatively consistent, while there can be large differences between the beginning (0-4 mm) and end (12-16 mm) of the chamber (for example, in Figure 3-12, 100 ng/mL, Replicate 1). There is also a difference between slide lots; comparison between the 0 ng/mL replicates in Figure 3-12 with the replicates in Figure 3-13 show that more beads remain on the slide in the second assay trial, especially at the beginning of the chamber.

Differences along the vertical length of the chamber again suggest that functionalization is not consistent across the slide. The glass slides arrive from the manufacturer with two layers. The first is an antifouling polymer layer, in the range of 10-50 nm (per personal communication). The identity of this polymer is unknown. The second is epoxy derivatization of this polymer layer for reaction with biomolecules. Heterogeneity could arise in either layer. If the layer thickness is not consistent across the slide, there could be sparsely covered or thinner areas, which would not be able to physically block the van der Waals attraction between the bead and the slide surface as effectively and potentially lead to areas of increased bead binding (see Chapter 6 for additional discussion of this). If the epoxy derivatization of the antifouling layer is not consistent, the subsequent FcMBL functionalization performed in our lab would result in a heterogeneous coating of FcMBL across the surface. Process variability in either of these steps would cause difference between slides in the same lot and across different lots. Without knowledge of the functionalization process, it is challenging to attribute our observations to one of these effects. However, our observations highlight the requirement of reliable and robust surface chemistry as the foundation to a sensitive assay.

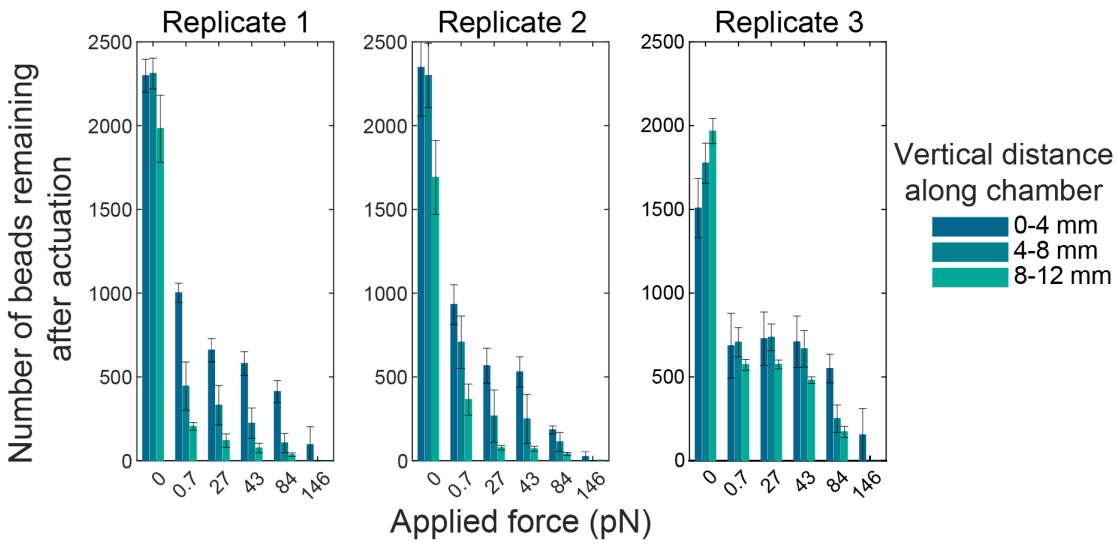

Figure 3-13: **Spatial variation in number of residual beads across vertical length of chamber during follow-up mannan experiment.** Data from Figure 3-11b was separated by replicate, demonstrating that anomalies are generally seen towards the top edge and middle bottom of the chamber. Compared to the 0 ng/mL replicates in Figure 3-12, these chambers have a higher bead background at most applied forces, suggesting variation between slide lots. Error bars represent the standard deviation of the five images included for the particular location.

3.4 Conclusion

In this chapter, we explored the efficacy of using gravity- and/or vibration-induced settling of beads after interaction with a functionalized sensing surface, in differentiating between bioanalyte concentrations. Using 4.5 μm beads, gravity and vibration via coin vibration motor can apply forces to beads from 0.7 to 146 pN, covering the reported range of nonspecific and specific binding interactions. A screen of surface functionalization led to selection of a bead and sensing surface combination that minimized residual bead binding for a model affinity agent, FcMBL. Using this bead-surface system, we showed initial evidence that gravity- and vibration-induced settling of beads is able to differentiate between mannan concentrations over a range of forces less than $<$84 pN. This illustrates the importance of matching the actuation force to the interaction force between affinity receptor and ligand in order to leave specific interactions intact.

However, our explorations also revealed the limitations that surface chemistry imposes on assay sensitivity. Repeated trials of our optimal surface chemistry without any mannan present showed that bead background can range from 3 – 30% for the same applied force and the same beads, suggesting that most heterogeneity in performance comes from the sensing surface itself. Due to the multiple layers on the slide, there are several possible sources of heterogeneity. One of the most consequential is a variation in antifouling coating thickness, which modulates the van der Waals force between the bead and surface; modeling this interaction and investigating strategies to minimize it are the subject of Chapter 6. Because of this variability in performance, we decided to investigate other actuation mechanisms. However, with improvements in surface chemistry, gravity- and vibration-induced assays could be promising as a bead-based sandwich assay for decentralized settings, due to the minimal manipulation required in order to perform the assay.

Chapter 4

Bead-based assays using on microsphere rolling: the integrated rolling microsphere assay (iRMA)

4.1 Introduction

Previous bead-based affinity assays have utilized fluid flow to promote rolling across a functionalized surface. By tuning the flow rate, the shear force on the beads can be controlled such that weakly-held, nonspecifically bound beads are washed away while beads with analyte remain stably tethered on the surface (see Chapter 1). A disadvantage of these platforms is that they rely on fluidic actuation, which requires precisely controlled pumps to start and maintain the flow field to ensure accurate results. This instrumentation requirement can limit the translation of these devices to decentralized settings

Another method to achieve bead rolling is to incline the surface at an angle to promote gravity-driven motion. An assay architecture using this concept is shown in Figure 4-1. We call this concept the integrated rolling microsphere assay (iRMA). Beads capture analyte as they settle through the sample solution onto an affinity

Mary Strawser, Krithika Ramchander, Chun Man Chow and Rohit Karnik contributed to the ideation of the platform discussed in this chapter

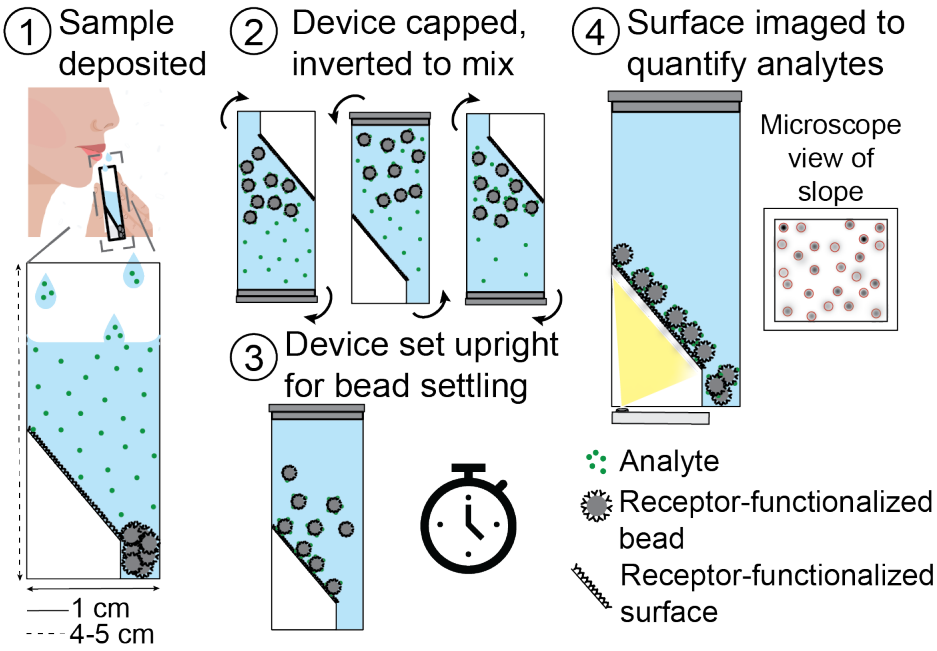

Figure 4-1: **The integrated rolling microsphere assay (iRMA).** A liquid sample is deposited into the cuvette-like device, which contains functionalized beads. After capping, the device is inverted several times to suspend the beads and is set upright to allow beads to settle. During settling, the beads contact a sloped surface and roll down the surface under the influence of gravity. Analyte-bound beads stably tether to the surface, creating a sandwich complex between the beads and the functionalized surface. Beads without analyte continue to roll off of the slope. The slope is imaged to count the number of beads that remain on the surface and quantify the number of analytes present in the original sample.

agent-functionalized inclined surface. As they roll down the surface, beads with analyte are selectively tethered by the affinity agents, which arrests their motion, while beads without analyte continue to roll down the surface. Tethered beads are counted via low-power digital microscopy and image analysis to quantify the number of analytes in the sample.

To differentiate between analyte bound and unbound beads, iRMA uses natural driving forces, the strength of which can be tuned through selection of bead size, bead material and slope inclination angle. In this way, the assay can be modified to accommodate specific receptor-ligand pairs with a range of binding forces. These parameters can also control the "washing" strength to ensure minimal nonspecific binding (NSB), which is detrimental to assay limit of detection (LOD). Overall, using

gravity, iRMA has the potential to realize highly sensitive diagnosis with the ease-of-use of lateral flow immunoassays.

Motivated by the COVID-19 pandemic, iRMA was initially ideated for whole virion sensing and, in this chapter, we outline the theoretical model that validates the iRMA concept for this application. This includes an integrated model accounting for the three major physical processes in iRMA: (1) analyte capture during bead settling; (2) bead rolling on an inclined plane; and (3) stable tethering of virion-bound beads to the sloped surface (Figure 4-2). These modeling results allowed us to gain insight into potential device designs and select a commercially available bead to test. Next, we highlight experiments which examined ability of beads to roll down an inclined surface, towards experimental validation of the iRMA concept. These experiments illustrate that NSB during bead rolling is a major barrier to the implementation of this assay concept and extensive optimization of surface chemistry would be required to minimize NSB. This caused us to pivot towards other non-fluidic assay concepts, though we note that surface modifications discussed in Chapter 6 could decrease NSB and make the iRMA format more promising.

4.2 Model of the major physical processes involved iRMA

Separate analytical model modules were implemented in MATLAB (MathWorks, Natick, MA) for each of the three physical processes involved in iRMA (Figure 4-2). We outline the theory behind the implemented models below. Model variables, their units and their values are shown in Table 4.1. Analyte-specific values are shown in Table 4.2.

Bead-analyte binding during settling

The capture of particulate analytes, such as virions, by functionalized beads involves mass transport of the analytes to the surface of the sedimenting microspheres, followed

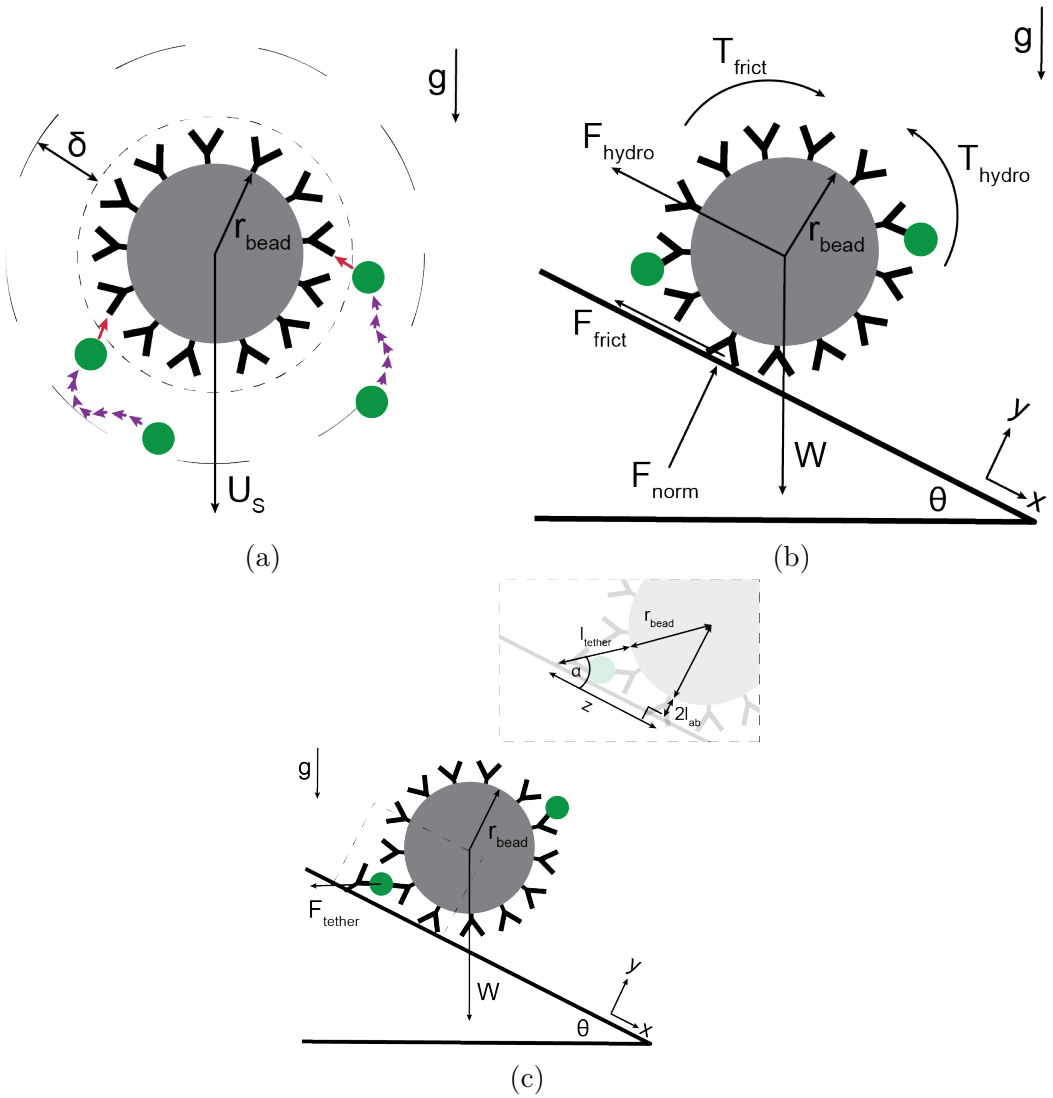

Figure 4-2: **Major physical processes involved in iRMA.** Green circles represent analytes. a) Analyte capture by sedimenting microspheres by mass transfer to the bead surface through the boundary layer δ (purple arrows) and binding to the receptors (pink arrows). (b) Microsphere rolling down a sloped surface influenced by hydrodynamics and friction with the surface. (c) Stable tethering of analyte-bound beads to the inclined surface via analyte sandwiched between receptors on the sloped surface and the bead.

by analyte binding to the receptors on the functionalized beads (Figure 4-2a). In order to predict the time to bind a certain fraction of analytes from the sample, we use a resistance model formulation outlined in Chapter 2 (see Equation 2.39). We neglect the off-rate and surface saturation considerations for the current calculation.

Given a desired captured analyte fraction ($f_{capture}$), the amount of analytes remaining in solution can be expressed as $\frac{C_{\text{inf}}t}{C_{\text{inf},0}} = 1 - f_{bound}$ and Equation 2.39 can be solved for the time required to bind this fraction ($t_{f_{capture}}$):

$$t_{f_{capture}} = -ln\left(1 - f_{capture}\right)\left(\frac{V_s R_{tot}}{n_b A_b}\right) \tag{4.1}$$

where R_{tot} is the total resistance (Equation 2.39), n_b is the number of beads ($n_b = C_b V_s$) and A_b is the single bead surface area ($A_b = 4\pi r_b^2$). For modeling the iRMA assay, we set $f_{capture} = 0.25$ and loop through each bead size and density combination to calculate $t_{f_{capture}}$.

Bead rolling down inclined plane

Using a model derived for microspheres rolling down an inclined plane in Stokes flow conditions [143–145], we consider beads with bound analytes as spheres with asperities $\delta_a = d_a + 2l_{ab}$ (the diameter of the analyte + two times the length of the antibody). We use this model to estimate the constant rolling velocity of the sphere on a given sloped surface of incline angle θ (Figure 4-2b).

The net weight of the bead when submerged in the sample is $W = \frac{4}{3}\pi r_b^3 \Delta\rho g$, where $\Delta\rho = \rho_b - \rho_s$, the difference between the density of the bead material and the density of the fluid sample. This weight is resolved into two components due to the inclined plane, a tangential component in the x direction ($W_t = W sin(\theta)$) and normal component in the y direction ($W_n = W cos(\theta)$). Under conditions of steady rolling velocity u and angular frequency ω, these components are balanced by forces and torques resulting from the viscous drag on the sphere and the interaction of the sphere

with the sloped surface:

$$W_n = F_n \tag{4.2}$$

$$W_t = 6\pi\mu r_b \left(uF_t + r_b\omega F_r\right) + F_{frict} \tag{4.3}$$

$$\mu_f r_b W_n = 8\pi\mu r_b^2 \left(uT_t + r_b\omega T_r\right) \tag{4.4}$$

where F_n is the normal force of the inclined plane on the bead, μ is the dynamic viscosity of the liquid sample, F_{frict} is the frictional force between the sphere and the inclined plane ($F_{frict} = \mu_f W_n$), μ_f is the empirical coefficient of friction between the plane and the sphere, and F_t, F_r, T_t and T_r are resistance functions relating the motion of the sphere to the hydrodynamic force and torque. F_t, F_r, T_t and T_r are functions of the gap between the sphere and the surface due to the sphere's surface asperities [143, 145]:

$$F_t \sim -\frac{8}{15} ln\left(\zeta\right) + 0.9588 \tag{4.5}$$

$$F_r \sim \frac{2}{15} ln\left(\zeta\right) + 0.2526 \tag{4.6}$$

$$T_t \sim \frac{1}{10} ln\left(\zeta\right) + 0.1895 \tag{4.7}$$

$$T_r \sim -\frac{2}{5} ln\left(\zeta\right) + 0.3817 \tag{4.8}$$

where $\zeta = \delta_a / r_{bead}$. Equation 4.3 states that the tangential component of the sphere weight is balanced by the hydrodynamic force due to drag as well as the force of friction between the sphere and the surface. Equation 4.4 balances the torque due to frictional contact between the sphere and the surface with the hydrodynamic torque.

We express the above force and torque balance in dimensionless form by scaling the translational velocity and angular velocity by the sphere sedimentation velocity

($U_s = \left(\frac{2}{9}\right) \frac{\Delta \rho g r_b^2}{\mu}$) and the inclination angle θ:

$$U = \frac{u}{U_s \sin\theta} \tag{4.9}$$

$$\Omega = \frac{r_b \omega}{U_s \sin\theta} \tag{4.10}$$

which results in the following nondimensional versions of Equations 4.3 and 4.4:

$$1 = (UF_t + \Omega F_r) + \mu_f \cot\theta \tag{4.11}$$

$$\mu_f \cot\theta = \frac{4}{3}(UT_t + \Omega T_r) \tag{4.12}$$

We assume that the sphere is rolling without slipping, which is the case when μ_f is sufficiently high [145]. This requires that the translational and rotational velocities be equal ($r_b\omega = u$), resulting in a single equation [145]:

$$U = \Omega = \frac{1}{F_t + F_r + \frac{3}{4}(T_t + T_r)} \tag{4.13}$$

When made dimensional, this equation results in an analytical expression for the translational velocity of a sphere with asperities of size δ_a rolling down a surface inclined at θ:

$$u = \frac{U_s}{F_t + F_r + \frac{3}{4}(T_t + T_r)} \tag{4.14}$$

To model the iRMA assay for a given analyte, the above equation is solved for each combination of bead radius and material, and slope angle. Using this translational velocity, we calculate the time required for the sphere to roll a distance of 5 mm. We note that this rolling length is a design parameter and would ultimately need to be selected based on a balance between assay sensitivity (longer rolling allows the sphere surface to be sampled for analytes more times) and NSB (longer rolling also allows more opportunities for a sphere without analyte to bind nonspecifically).

Table 4.1: **Parameters and their values used in iRMA theoretical model.**

Parameter	Description	Units	Value	Reference
ρ_f	Fluid sample density	g/cm^3	1.0	
μ	Fluid sample viscosity	Pa*s	1x10^{-3}	
T	Temperature	K	298	
g	Gravitational acceleration	m/s^2	9.8	
k_B	Boltzmann constant	J/K	1.38x10^{-23}	
n_A	Avogadro's number	#/mole	6.022x10^{23}	
V_s	Fluid sample volume	mL	1.0	
ρ_b	Bead density	g/cm^3	0.5 - 2.5	
r_b	Bead radius	μm	0.1 - 10	
C_b	Bead concentration	#/mL	1x10^6	
n_{ab}	Coating density of antibodies on beads	#/μm^2	10^4	[89, 106]
l_{ab}	Antibody length	nm	10	[146, 147]
MW_{ab}	Antibody molecular weight	g/mole	1.5x10^5	[146]
C_{ab}	Antibody cost	\$/g	4.5x10^6	Abcam website
θ	Slope surface angle	°	20-80	
F_{tether}	Maximum tethering force	pN	50	[113, 115]
$f_{capture}$	Target analyte capture fraction	—	0.25	
t_{target}	Target maximum assay time	min	30	

Table 4.2: **Analyte properties used in iRMA theoretical model.**

Analyte	Parameter	Description	Units	Value	Reference
SARS-CoV-2 virion	d_a	Virion diameter	nm	100	[110]
	D_a	Virion diffusivity	m^2/s	5x10^{-12}	[88]
	k_A	Virion on-rate	m/s	Low: 4x10^{-7} High: 5.9x10^{-6}	[103]

Stable analyte-bound bead tethering to sloped surface

For beads with analyte to remain stuck to the slope for quantification, the molecular sandwich that forms between the antibody on the slope surface must be of sufficient strength to balance the bead mass. This leads to a practical limit on r_b and ρ_b that can be tethered for a specific analyte and θ.

Considering static tethering, a force and torque balance about the sphere-surface contact point results in the following equations (Figure 4-2c):

$$\Sigma F_x = -F_{tether}\cos\alpha + W\sin(\theta) - F_{frict} = 0 \tag{4.15}$$

$$\Sigma F_y = F_{norm} - W\cos\theta - F_{tether}\sin\alpha = 0 \tag{4.16}$$

$$(\Sigma T_z)_A = F_{tether}\sin\alpha z - W\sin\theta r_b = 0 \tag{4.17}$$

where F_{tether} is the force of the molecular, antibody-analyte tether, α is the angle between the tether and the sloped surface, W is the weight of the sphere ($W = \frac{4}{3}\pi r_b^3 \Delta\rho g$), θ is the slope angle, F_{frict} is the frictional force between the sphere and the inclined plane, and z is the distance between the contact point of the sphere with the surface and surface tether. Solving the torque balance of Equation 4.17 yields an expression for F_{tether} required for a given bead size and material and slope angle:

$$F_{tether} = W\left(\frac{\sin\theta}{\sin\alpha}\right)\left(\frac{r_b}{z}\right) \tag{4.18}$$

The kinematics of the tether and the bead give geometrical expressions that allow us to solve Equation 4.18 explicitly:

$$\begin{aligned}(r_b + 2l_{ab})^2 + z^2 = (l_{tether} + r_b)^2 \rightarrow z &= \sqrt{(r_b + l_{tether})^2 + (r_b + 2l_{ab})^2} \\ &\approx \sqrt{(r_b + l_{tether})^2 + r_b^2}\end{aligned} \tag{4.19}$$

$$\frac{zr_b}{r_b + l_{tether}}F_{tether} = r_b W\sin\theta \rightarrow F_{tether} = \frac{4}{3}\frac{\pi r_b^3 \Delta\rho g\sin\theta}{\left[1 - \frac{r_b^2}{(l_{tether}+r_b)^2}\right]^{\frac{1}{2}}} \tag{4.20}$$

where $l_{tether} = 2l_{ab} + d_a$, the length of the sandwich tether. Equation 4.18 was solved

for each combination of bead size and material, and incline angle θ to determine F_{tether}. To determine if this bead and slope combination would be valid for an iRMA assay, F_{tether} is compared to the single antibody-antigen binding force found in literature (50 pN [112, 113, 115]). Only those r_b and ρ_b combinations with $F_{tether} \leq 50$ pN were considered as potential options for iRMA.

Model algorithm

For each combination of ρ_b, r_b, and θ, the following algorithm is carried out:

- Determine if the bead can stably tether on the slope surface. If yes, the next calculations are performed. If no, the algorithm is stopped here.
- Calculate the translational rolling velocity of the sphere on the slope and the time required for the bead to roll 5 mm.
- Calculate the time required for $f_{capture} = 0.25$ via bead sedimentation. Combined with the settling speed, this time is used to calculate the required height of the device.
- Add the times from steps 2 and 3 to determine the minimum total assay time for the combination. This set of assays is restricted to a final set of bead and slope combinations by down selecting only those assays which have a total time less than thirty minutes.

This analysis yields a set of potential bead and slope combinations valid for iRMA, which is further examined to find ideal assays that have minimal cost and use commercially available materials.

Additional model considerations

The majority of the assay consumable cost will come from the antibody coating of the beads. To estimate this cost, we use the surface area of the bead ($A_b = 4\pi r_b^2$), number of beads per assay (n_b), maximum reported antibody coating density (n_{ab}), the molecular weight of an IgG antibody (MW_{IgG}) and the cost per gram (\$/g) of

monoclonal antibody (C_{mAb}), as found in vendor catalogs. We chose monoclonal antibodies because they are generally better affinity agents, though they are more expensive than polyclonal antibodies. Using these parameters, we calculate the bead antibody coating cost per assay (Figure 4-3a):

$$\text{Cost} = \frac{V_s C_{bead} A_{bead} n_{ab} MW_{IgG} C_{mAb}}{n_A} \tag{4.21}$$

where n_A is Avogadro's number.

Another aspect to consider is the contact area of the sphere with the sloped surface, which will influence the assay sensitivity and the length of the slope. Assuming the bead rolls randomly, sampling the entire bead surface, to ensure that any bound analyte has the chance to interact with the sloped surface, will require a certain number of rolls based on the instantaneous contact area. Accommodating at least this number of rolls determines the minimum length of the slope. Sampling the entire surface more than once can increase the sensitivity of the assay by maximizing the chances for a bound analyte to contact the slope. This is a balancing act however, because the probability of nonspecific interactions also increases with increasing slope length. The contact area is a spherical cap that is determined by r_b, l_{ab} and $d_{analyte}$, and can be determined by the equations shown in Figure 4-3b.

From Figure 4-3b, one sees that the fraction of the bead surface area in contact with the slope decreases as bead radius increases. This translates into more rolls (and longer slope length) required for larger beads.

4.3 Methods

4.3.1 Materials

Silica beads (20 micron [μm] diameter, nonporous), Luria Bertani (LB) broth, biotin-protein A conjugate, HybridWell sealing system (9.8 x 20 x 0.25 millimeter [mm] chamber size; Grace Bio-Labs) and calcium chloride dihydrate ($CaCl_2 \cdot 2H_2O$) were purchased from MiliporeSigma (Burlington, MA). *Escherichia coli* (*E.coli*) K-12

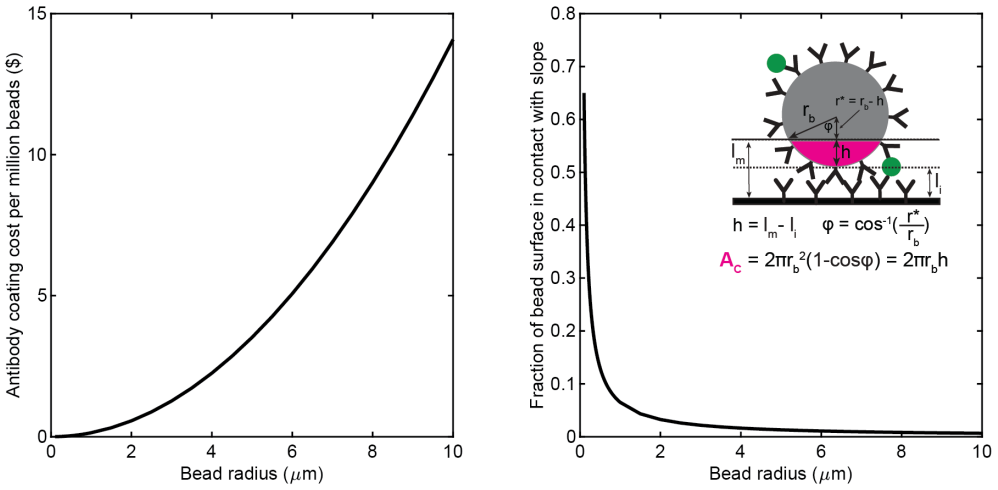

(a) (b)

Figure 4-3: **Additional considerations around bead size for iRMA.** (a) Antibody cost per million beads drives the total cost of the assay, with coating cost increasing as r_b increases. (b) Fraction of bead area instantaneously in contact with the slope during rolling decreases with increasing r_b. This translates into further rolling to sample the entire bead surface for larger beads. The contact area is determined by length of the analyte and the antibody, which can be lengthened via PEG or other linkers, to increase the contact area.

Alexa Fluor 488 bioparticles and Syto9 green fluorescent nucleic acid stain were purchased from ThermoFisher Scientific (Waltham, MA). Streptavidin was purchased from New England Biolabs (Ipswich, MA). *E.coli* MG1655 was purchased from the American Type Culture Collection (ATCC; Manassas, VA). Soda lime glass beads (10-30 μm diameter) and streptavidin-coated silica microspheres (5 μm diameter) were purchased from PolySciences (Warrington, PA). Biotin-LC-bovine serum albumin (BSA) conjugate, BSA, glass microscope slides (75 x 25 x 1 mm) and phosphate buffered saline (PBS) were purchased from VWR (Radnor, PA). 10x Tris-buffered saline + 0.5% volume/volume (v/v) Tween 20 (TBST) was purchased from Fisher Scientific (Hampton, NH). Epoxy-functionalized silica beads (15 μm diameter, nonporous) were purchased from Creative Diagnostics (Shirley, NY).

4.3.2 Inclined-plane rolling experiments without analyte using different size and material beads

To investigate rolling of beads on inclined surfaces without any analyte, borosilicate glass beads and silica beads were functionalized as described below. All incubation steps included end-over-end mixing at 5 rpm and occurred at room temperature. In between incubation steps for each layer, centrifugation was used to separate the beads from the supernatant. The volume for each incubation step was 0.75 milliliter (mL) for borosilicate glass beads and 1 mL for silica beads and all steps occurred in PBS.

Briefly, a desired mass of (non-functionalized) glass beads was dispensed and resuspended in PBS containing biotin-BSA conjugate at a concentration corresponding to a coating density of 25 milligram per square meter (mg/m^2) to functionalize the beads with biotin. Incubation occurred for 30 min. Beads were then incubated with streptavidin at a concentration corresponding to a surface coating density of 2.5 mg/m^2 for 30 min. The next layer was created by incubation with biotin-protein A conjugate at a concentration corresponding to 5 mg/m^2 for 30 min. The final functional layer was created by incubation with FcMBL for 30 min at a concentration corresponding to a surface coating density of 1 mg/m^2 to functionalize the beads with FcMBL via

protein A-Fc interactions. After this final layer, beads were blocked via incubation in PBS + 0.1% (w/v) BSA for 30 min. Beads were then washed three times with PBS via centrifugation before storage at 4 degrees Celcius (°C).

Glass slides were functionalized using the same sequential coating process as above. Chambers were created on the glass slide via affixing Hybriwell chambered adhesives and each chamber was functionalized according to the above protocol using a volume of 50 microliters (μL) per chamber.

To examine the rolling behavior of beads on these surfaces, 0.5 mg of beads was deposited in a chamber port. The ports were covered with an adhesive plug and the slide was set on a cardboard stand that fixed the slide at either 60° or 80° (Figure 4-4). Rolling was filmed using a USB microscope (Celestron, Torrance, CA) and allowed to proceed for 10 min, after which two sets of images of the surfaces were taken using a microscope (TE2000U, Nikon, Melville, NY). One set of four images was taken at 20x in the middle of the chamber and used in an image analysis algorithm to quantify the number density of residual beads left on the surface after rolling. Another set of sixteen images was taken at 10x to stitch together for a visual comparison of beads left in the chamber between conditions.

The rolling protocol for 5 μm silica beads differed slightly due to these beads' slower rolling velocity. After bead deposition in the chamber, slide arrangement on the inclined stand and USB microscope filming, the beads were allowed to roll down the slide surface for 14 hours (h) overnight. Microscope images were taken after this longer period.

4.3.3 Inclined plane rolling experiments with *E.coli*

To examine the effect of analyte presence on bead rolling down an inclined plane, we used 20 μm FcMBL-functionalized silica beads and glass slides. Though we simulated the iRMA assay for virions, we used bacteria to examine rolling to minimize safety concerns. Two different types of bacteria were used: (1) Alexa Fluor 488 labeled *E.coli* BioParticles, which are heat inactivated *E.coli* K12 that have been stained with fluorophore by the manufacturer and retain their immunogenicity for phagocytosis

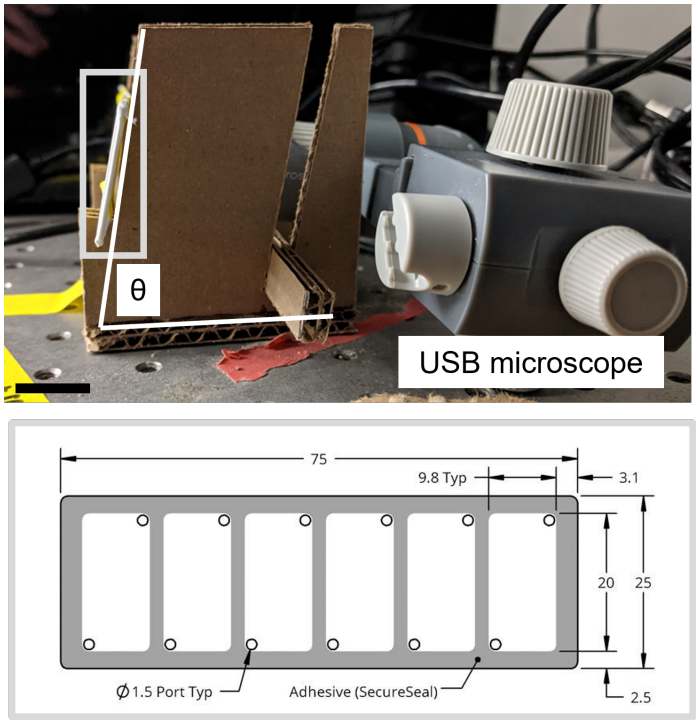

Figure 4-4: **Experimental setup to test bead rolling on incline.** A slide holder, fabricated out of cardboard, held the slide at an angle θ. A USB microscope was focused on the slide surface and filmed the beads as they traveled down the slide surface (top). Scale bar in lower left corner is 10 mm. The slide had separate chambers created by an adhesive seal and each bead/surface combination used one chamber (geometry shown in bottom gray box, with dimensions in mm, from the manufacturer).

and other studies, or (2) live *E.coli* MG1655 grown in our lab and stained with Syto9 green fluorescent nucleic acid stain.

Preparation of live *E.coli* MG1655 occurred as follows. Primary cultures of *E.coli* K12 were grown from glycerol stocks in 5 mL of LB broth overnight with shaking at 37°C. 0.5 mL of this primary culture was introduced into 4.5 mL fresh LB broth for secondary culture and grown until log phase, as assayed by OD600 using a UV/Vis spectrophotometer (Cary UV/Vis, Agilent, Santa Clara, CA). Using the OD600 value, 10^8 bacteria were removed, washed three times via centrifugation in PBS at 3000 rpm for 10 min, and stained with Syto9 at 1:1000 in PBS for 30 min and protected from light. Bacteria were subsequently washed three times with PBS via centrifugation using the same conditions as above, to remove residual dye.

For bead capture of either type of *E.coli*, 500,000 FcMBL-functionalized 20 μm silica beads were mixed with 5x10^8 bacteria in TBST + 5 millimolar (mM) $CaCl_2$ (TBSTCa) in 500 μL total volume in 1.5 mL centrifuge tubes. Tubes were hand-inverted for 40 min to promote binding of bacteria to the beads and to recapitulate what might happen in an iRMA assay. After incubation, beads were allowed to settle to the bottom of the tube, the supernatant was removed and replaced with 500 μL TBSTCa. This process was repeated three times to wash the bead-bacteria conjugates, which were finally resuspended in 250 μL TBSTCa. 5 μL of this resuspension ($\sim$10000 beads) was deposited into 100 μL TBSTCa in a 96 well plate. Four images of these beads at 20x were taken via microscopy, with each field of view imaged in brightfield (0.01 s exposure time) and using a fluorescent FITC filter (1 s exposure time with gain of 5). Additionally, 25 μL of the 250 μL suspension was deposited into a chamber on a functionalized glass slide and followed the previously outlined protocol to examine bead rolling on a 60° or 80° incline.

Finally, to test the effect of covalent modification on bacteria capture efficiency and the overall iRMA assay, we functionalized 15 μm epoxy-coated, nonporous silica beads with FcMBL. We also functionalized separate sets of these beads with BSA or PEG(2k) as controls. Functionalization took place in 0.1 molar (M) sodium phosphate buffer. Briefly, BSA, PEG(2k) or FcMBL were added to beads at a concentration

corresponding to 8 mg/m^2 surface density. Beads were incubated for 20 h at room temperature with end-over-end mixing. After concentration by centrifugation, beads were resuspended in sodium phosphate buffer with 50 mM ethanolamine and incubated for 4 h. Beads were then washed three times with PBS + 0.1% (w/v) BSA + 2 mM EDTA and resuspended in this wash buffer for storage at 4°C. iRMA experiments using these beads and *E.coli* MG1655 followed the same protocol as used for glass and silica beads.

4.3.4 Image analysis for residual beads

A custom script was implemented in MATLAB to count the number of beads in 20x images of each chamber. Briefly, this script performed the following operations on each image:

1. Background adjustment to increase the contrast and make the background lighter using *imadjust* function with [low$_{in}$ high$_{in}$] as [0 0.45]

2. Bead detection and quantification using *imfindcircles* function with radius range [19 30] pixels and object polarity as dark

Using the scale of the images and image size, the bead count was transformed into a residual bead density (in number per square mm [#/mm^2]), which was averaged across images to determine a mean residual bead density for each condition tested.

4.4 Results and discussion

4.4.1 Slope angle places a practical limit on the bead size and material combinations valid for iRMA assay

The iRMA method relies on counting beads stuck to a sloped surface by the sandwich formed between analyte on affinity-agent functionalized beads and the affinity agent on the surface. Stable tethering of analyte-bound beads requires that the static force from gravity acting on the bead (a function of θ, r_b, ρ_b and l_{tether}) to be less than the force of

a single affinity agent-analyte bond. For antibody-antigen interactions, AFM studies indicate that this is around 50 pN [113, 115]. Though it is likely that, for particulate analytes, multiple bonds will form between analyte and the surfaces resulting in a tethering force that is greater than 50 pN, using the single antigen-antibody value represents the weakest, worst case scenario and also enforces a safety factor on our analysis.

Figure 4-5 shows the maximum angle that can stably tether a bead, with curves parameterized by $\Delta\rho$, which sets the buoyant force on the bead. Curves start out horizontal at 80°, the maximum slope angle simulated and for which the tethering force required is maximum. This shows that stable tethers can be formed for all angles simulated. For each $\Delta\rho$, there exists a r_b at which the maximum θ decreases because the tethering force is greater than the antibody-antigen force. The value of r_b at this transition increases with $\Delta\rho$, showing the influence of buoyant force on the tethering force. For SARS-CoV-2 virions, valid tethers form in 96% of the 137340 assays simulated.

As the force required to tether the beads, and the rolling velocity, scales with θ, higher incline angles are favorable to prevent NSB but also require greater F_{tether}, which limits the combinations of bead size and materials that can be used. In examination of Equation 4.20, one finds that increasing l_{tether} decreases the required tethering force. l_{tether} is a function of the analyte diameter, so smaller analytes are at a geometric disadvantage. Experimentally, to increase the range of θ on which beads could stably tether when bound to smaller analytes, the tether length could be extended by using polymer spacers, such as those made of polyethylene glycol (PEG).

4.4.2 Valid iRMA assays favor larger, heavier beads, which translates to higher cost

A target for decentralized assays is to have test results returned within the length of a normal patient appointment [148], estimated to be ∼30 min at maximum. To determine iRMA architectures that would satisfy this requirement, we looked at

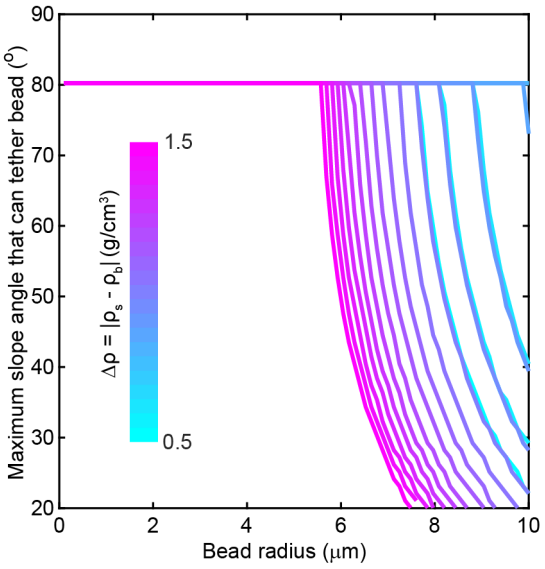

Figure 4-5: **Tethering force limits the bead size and material combinations that can be used in iRMA.** The maximum incline that can hold an analyte-bound bead stably on the slope depends on $l_{tether} = d_a + 2l_{ab}$, r_b and ρ_b. As r_b and ρ_b increase, the maximum slope that can hold the bead decreases. Using larger, heavier beads and higher inclines is advantageous for decreasing assay time.

the library of valid assays generated by the model and further restricted our list to those with a total assay time of $\leq$30 min. From the original set of 137340 assays, enforcing this time criterium returned 4376 assays for virions (3.2% of total assays), demonstrating the promise of our iRMA concept. The fastest of these assays, for each valid combination of r_b and ρ_b are plotted in Figure 4-6. While there are assays under 30 min for most ρ_b, it is clear from these figures that iRMA favors beads >4 μm in diameter, illustrating the effect of radius on both analyte capture time and bead rolling time (both inversely proportional to r_b^2).

The common shape of the curves in Figure 4-6 arises from the stable tethering requirement. Fastest total assay time decreases with increasing r_b until a certain value. These assays in this area of the curves utilize the largest slope θ simulated, 80°. At the r_b when 80° can no longer stably tether the bead, the max slope θ decreases, leading to a decrease in rolling velocity, an increase in rolling time and a change in curve trend to increasing total assay time with increasing radius. This means that, for each

ρ_b, there is a optimal r_b which leads to the minimal possible total assay time (the inflection point in the plots of Figure 4-6) and this r_b increases with decreasing ρ_b.

One major uncertainty in the modeling is the value of the analyte on-rate k_A, during analyte capture, which was estimated using experimental results of nanoparticle docking on antibody-coated surfaces at different shear rates [103]. k_A is a function of the intrinsic antibody-analyte binding kinetics, as well as several parameters that can be controlled by the functionalization process, including n_{ab}. To illustrate the influence of this parameter on iRMA, we used two different on rates in our modeling: low k_A (using an antigen/antibody density product of $2.5/\mu m^4$, an experimental point on published curves; Figure 4-6a) or a high k_A (using extrapolated values based on literature-reported spike antigen density values [110], and published k_A versus density product curves; Figure 4-6b). The high k_A is one order of magnitude greater than the low k_A. As would be expected, there are more valid assays for the higher k_A (4376 versus 12276 for virions, for low and high k_A, respectively) as it decreases the analyte capture time. For the same r_b and ρ_b combination, the higher k_A can result in overall assay times that are several minutes faster. Higher k_A also permits smaller r_b to be used in the iRMA assay with our imposed criteria, which has other important implications discussed below. Further studies on the exact antibody-antigen interaction, as well as greater understanding of the multivalent nature of particle capture, are needed to make more precise predictions of assay time.

Though the fastest iRMA assays utilize larger beads, there are several additional considerations to weigh. The first is the contact area between the rolling bead and the sloped surface, which is a function r_b, and the gap between the bead and the surface, which depends on the antibody and analyte size (Figure 4-3b). This contact area influences the required slope length, as a bead with less instantaneous contact area will have to roll for a longer time to sample the entire surface for bound analytes. Larger beads have greater contact area but also larger overall surface area to sample, resulting in a lower fraction of the total bead surface area instantaneously in contact with the sloped surface. This required more rolls and a longer sloped surface. Larger contact area also means greater NSB.

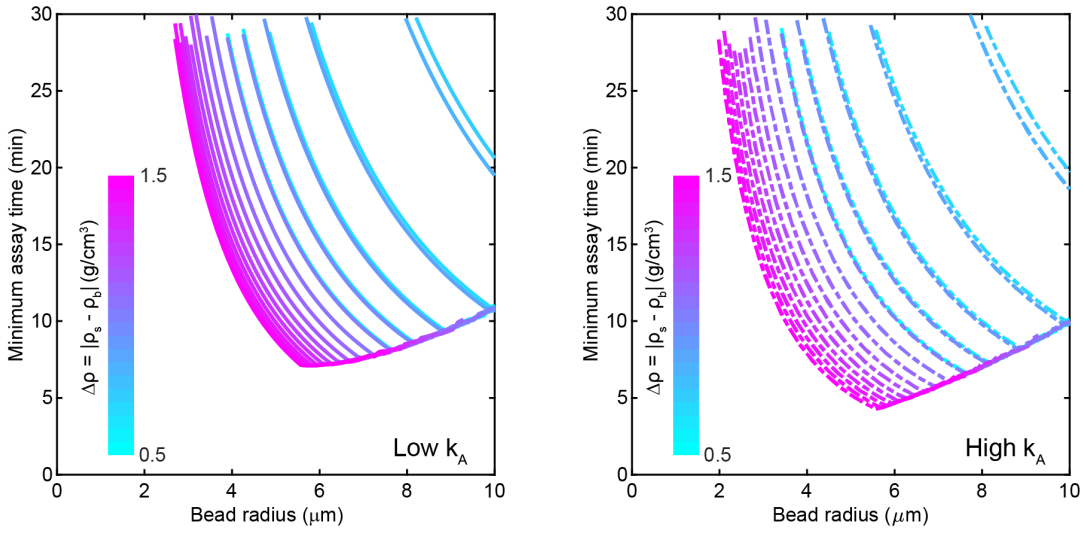

(a) (b)

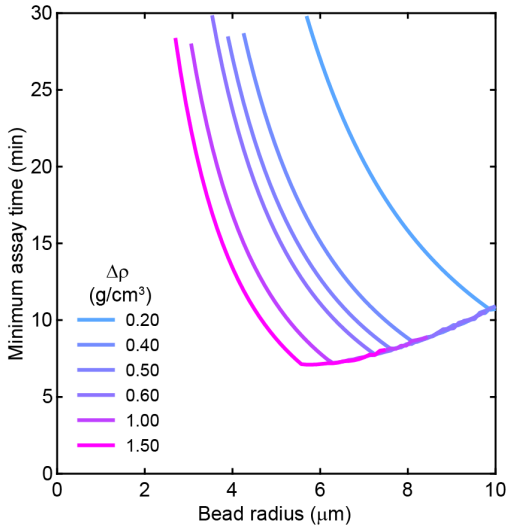

(c)

Figure 4-6: **Model predictions of bead size and material combinations that yield the fastest total iRMA time for virion detection.** The assay time is heavily dependent upon the analyte binding time, which is influenced by our estimate of k_A. Comparison of valid assays using low estimate of k_A (a) and valid assays using high estimate of k_A (b) demonstrates this dependence. (c) Valid assays using commercially available bead materials and low k_A suggesting multiple bead size and material combinations show efficacy for iRMA.

Table 4.3: **Fastest iRMA assays for virions using silica beads (ρ_b =2.0g/cm^3) and with a cost of $<$ \$5.**

Bead radius (μm)	Slope angle (°)	Total assay time (min)	Minimum device height (cm)
3.5	45	27	1.4
3.5	80	21	1.4
5.5	45	11	1.4
5.5	80	9	1.4

The other consideration is the antibody coating cost for the beads, which is the major cost for the assay (Figure 4-3a) and scales with r_b^2, as shown in Equation 4.21. Another ideal for decentralized assays is that they are cost-effective. For public health campaigns, resource constrained settings and home-use applications, a device cost of $<$ \$5 could likely be tolerated. For iRMA utilizing 1 million beads, this translates to assays utilizing $r_b < 6\ \mu m$. Our modeling assumed that assays using 1 million beads as a starting point, because this ensured a bead:analyte ratio of 100 (10^6 beads with 10^4 virions, a target LOD for SARS-CoV-2 diagnostics), but more or less beads could be used. Determining the optimal number of beads depends on both the target sensitivity, assay time and assay cost. For example, increasing the number of beads would lead to increased assay cost, but decreased binding time.

Taking all of these aspects into consideration, as well as further restricting the bead options to those materials that are commercially available (as show in Figure 4-6c), we list the fastest assays assuming low k_A with an antibody coating cost of $<$ \$5 and a total time of $<$30 min in Table 4.3, which show that our model predicts total assay times of less than 10 - 20 min for virions. We choose silica as the bead material, due to its high biocompatibility and wide variety of surface functionalizations and bead sizes available commercially. We also list two different options for slope angle, since this has implications for device design. Larger θ translates into a taller device and necessary confinement of beads during the sedimentation process, since the projected area of higher θ surfaces provides less area on which beads can settle. Overall, our modeling theoretically validates iRMA as a low-instrumentation platform that is rapid and cost-effective.

4.4.3 Experimental testing of bead rolling demonstrates the need for surface coating optimization

Guided by the results of the analytic model, we first performed experiments to examine the extent of NSB between functionalized beads and surfaces to determine if beads would roll without analyte present. We used polydisperse soda lime glass beads (r_b =5-15 μm, ρ_{bead} = 2.5 g/cm^3) and glass microscope slides, both functionalized as described above. Beads were deposited into chambers on these glass slides and the slide was inclined at a specific angle while the surface was filmed by a USB microscope. Slides were subsequently imaged via inverted microscope to analyze the beads that remained on the slope after rolling.

Figure 4-7 shows the last frame from the USB camera videos of the bead rolling process for nine bead-surface combinations in two different buffers. Bare surfaces had no functionalization, passivated surfaces had the first three layers in the coating process but no functional ligand, and FcMBL surfaces had all four layers of the coating process including the functional FcMBL layer. As MBL-analyte binding is calcium-dependent [149], the experiment was performed in two different buffers to examine the effect of adding calcium and detergent on rolling and residual binding. At an 80° incline, the required tethering force for a 20 μm bead is 380 piconewton (pN) and the instantaneous fraction of a 20 μm sphere surface area in contact with the surface during rolling is 0.0065.

These images show that the coating process decreases NSB, as the conditions with either bare beads and/or bare surfaces have the largest residual bead count regardless of buffer. This suggests that the force of NSB interactions is extremely strong between beads and surfaces and could be due to electrostatic effects, as bare glass surfaces are known to carry negative surface charges in physiological buffers [150], as well as long-range van der Waals forces, discussed in depth in Chapter 6.

Quantification of the residual bead density on these surfaces puts numbers to the observed differences (Figure 4-8). Bare surfaces in any combination have the largest residual bead density, and, aside from two conditions, the presence of detergent

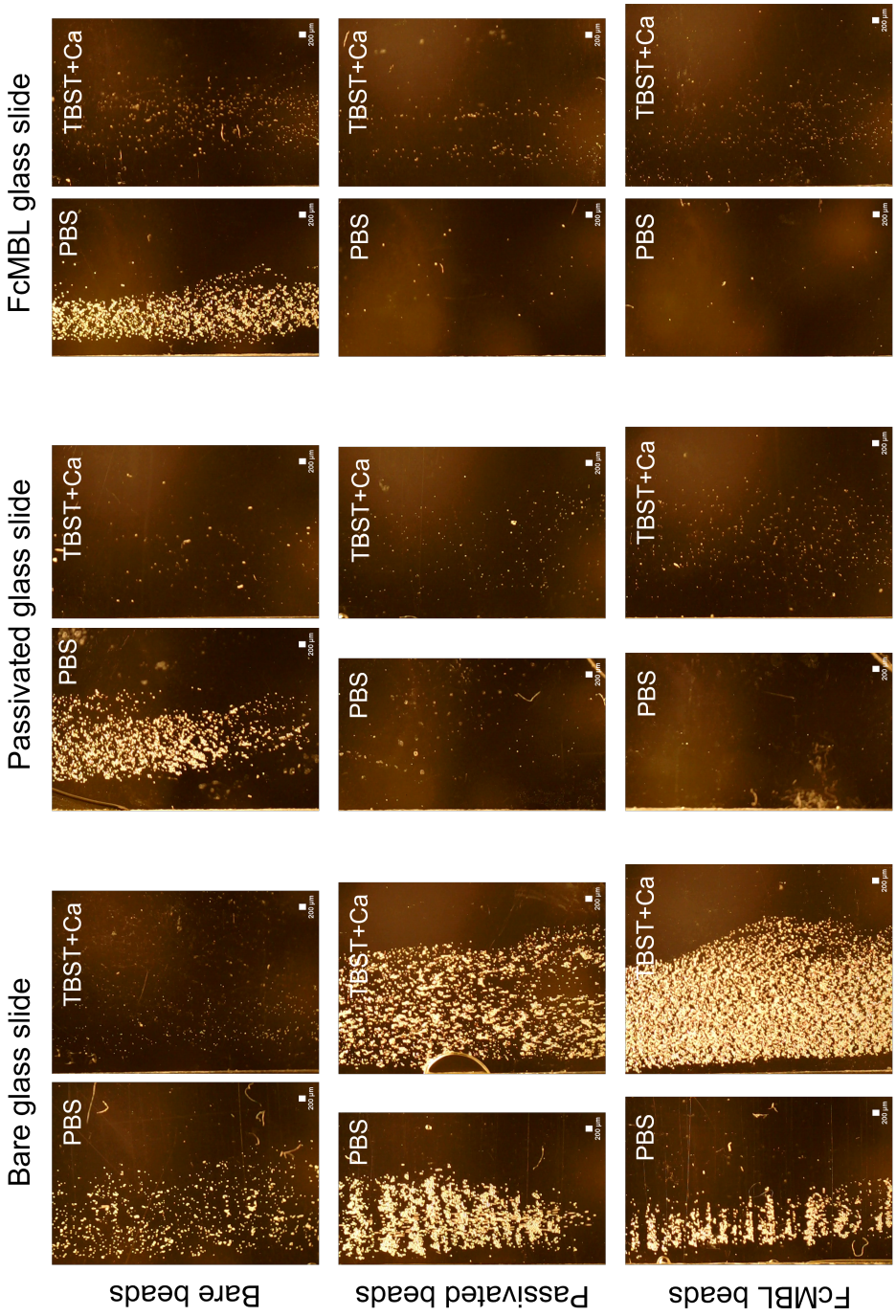

Figure 4-7: **Effect of surface coating on borosilicate bead rolling on glass slide surfaces.** Surfaces were either left bare or functionalized via a multistep coating process. Passivated surfaces had three layers, with biotin-Protein A as the last layer, and FcMBL surfaces had an additional FcMBL layer. The residual beads on the surface allow us to grossly see which surfaces interact the strongest and show high NSB. Bare surfaces have the highest NSB, which is decreased by the presence of the layers. In general, TBSTCa buffer also decreases NSB, presumably because of the presence of Tween 20 detergent, which disrupts NSB.

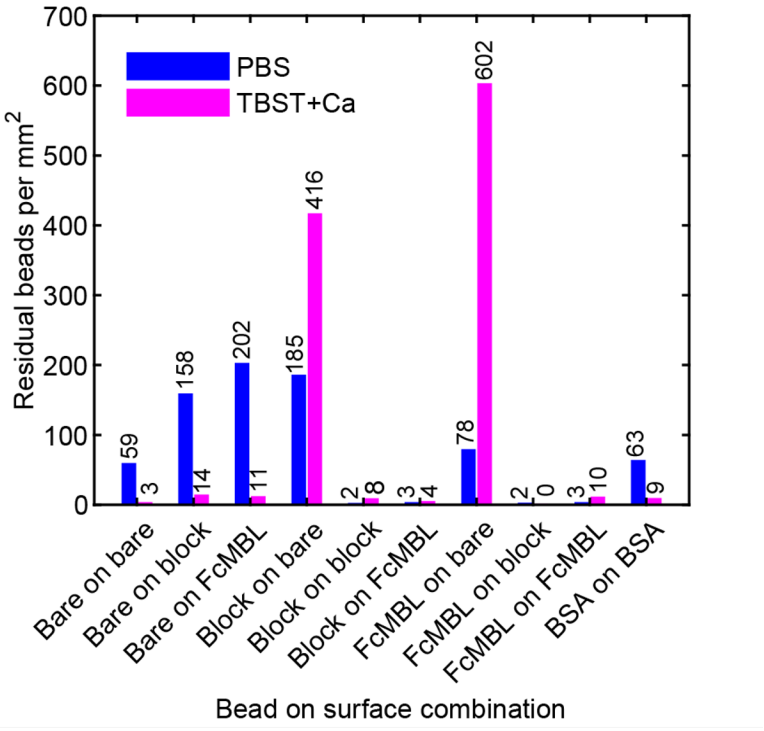

Figure 4-8: **Quantification of residual glass beads left after rolling on differently coated surfaces, expressed as an areal density.** Aside from blocked beads on a bare surface or FcMBL beads on a bare surface, TBSTCa buffer has lower residual bead area density, suggesting that the presence of a detergent significantly influences the extent of NSB. FcMBL does require Ca^{+2} for binding, which may be behind the large residual bead count in the FcMBL beads on bare surface condition. However, the low residual binding between FcMBL beads and FcMBL surfaces suggests that there are minimal self-interactions between opposing FcMBL molecules.

seems to decrease NSB in general. The two conditions with the largest bead density ($>300/mm^2$) are blocked beads on a bare glass surface and FcMBL beads on a bare glass surface, both when in TBSTCa buffer. The main difference between the two buffers is the presence of calcium, which is known to increase adhesion of cells to culture surfaces through cell surface proteins, and the presence of Tween 20, which is an NSB disruptor. Interestingly, when the surfaces are reversed (bare beads on a blocked glass surface or bare beads on a FcMBL glass surface), the experiments in PBS buffer had the higher bead background. This suggests that a phenomena involving the glass of the inclined surface with bead coating molecules is at play.

Encouragingly, the residual bead density in the FcMBL beads on FcMBL slide experiment was one of the lowest observed in the entire experiment set and even lower than the BSA-blocked surface in PBS. The residual density is slightly higher in TBSTCa buffer, potentially attributable to the FcMBL acquiring its functional, calcium-dependent form. This low background is promising, suggesting that opposing FcMBL molecules on bead and slide surfaces interact minimally, which is advantageous for high sensitivity assays.

We repeated the same experiment using 20 μm silica beads (ρ_{bead} = 2.0 g/cm^3) and only in TBSTCa buffer, which is the working buffer for an assays utilizing FcMBL. These silica beads were functionalized using the same coating process as was used for the glass beads. The force required to tether a 20 μm silica bead on an 80° slope is 254 pN. Figure 4-9 shows that, similar to the experiments with glass beads, there were more residual silica beads on bare glass slides, again indicting the high strength of NSB in the absence of any coating molecules. These residual densities were higher than those in the equivalent conditions using glass beads, potentially due to the lower ρ_b of silica beads. Conditions with FcMBL on beads had more residual beads, but the FcMBL bead on FcMBL surface condition had a residual density comparable to the same condition with glass beads, again suggesting that interactions between opposing FcMBL molecules is minimal.

Finally, we performed an additional experiment with passivated 5 μm silica beads and coated glass slides. The tethering force for these beads on an 80° incline is 4.2x10^{-4} pN, significantly lower than the larger beads previously trialed. Additionally, the smaller size of the bead leads to a greater fraction of the bead surface instantaneously in contact with the sloped surface (0.026). Considering both of these aspects, in the absence of optimized surfaces for minimization of NSB, one may expect that many more beads to stick to the surface as compared to the previous trials. This is indeed our observation as shown both macroscopically in the last frame of the USB microscope videos and at higher magnifications (Figure 4-10). Furthermore, these beads are stably bound to the surface, as the stitched images were taken after the slide remained inclined at 80° for 14 h. These results suggest that, without optimization of

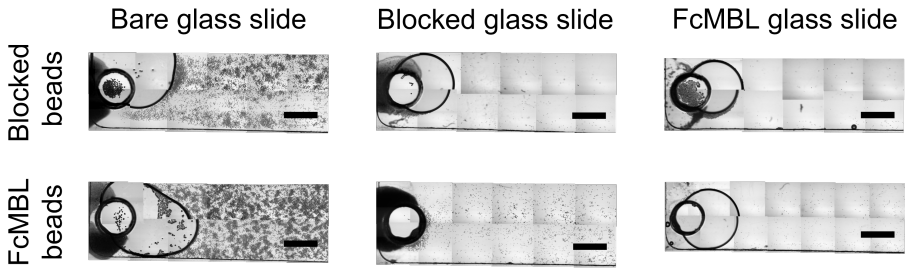

(a)

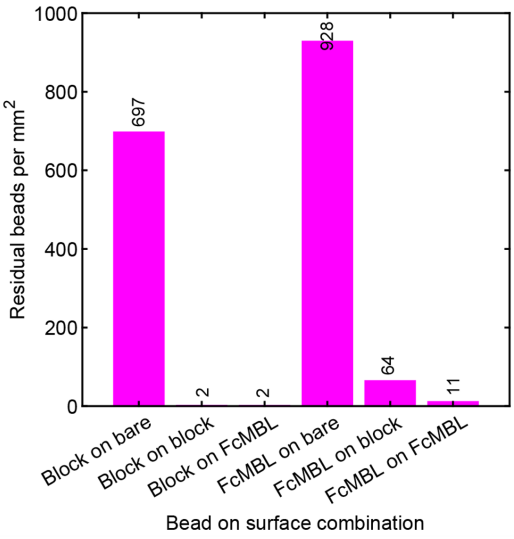

(b)

Figure 4-9: **Residual 20 μm silica beads left on coated glass surfaces after rolling on 80° inclined surface in TBSTCa buffer.** (a) Stitched microscope images illustrating, at a macro level, the residual bead density. Scale bars are 1.5 mm. (b) Quantified residual bead density for different bead and surface combinations. Similar to borosilicate glass beads, the most residual beads occur in the blocked beads on bare surface and FcMBL beads on bare surfaces conditions.

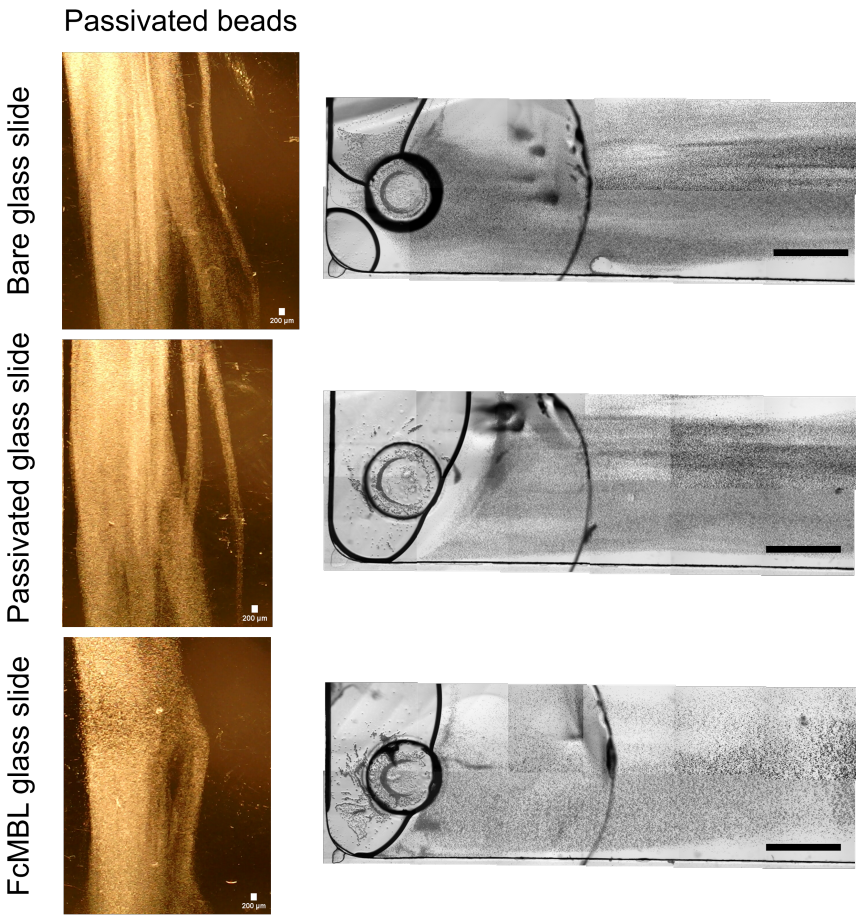

Figure 4-10: **Residual 5 μm silica beads left on coated glass surfaces after rolling on 80° inclined surface in TBSTCa buffer**. Final frames of USB videos after 10 min of rolling (left) and corresponding microscope images after 14 h of slide incline (right), both demonstrate high NSB.

surface coatings, iRMA using smaller beads is limited by NSB. Because of this, we turned our focus to iRMA demonstration using larger beads, whose mass could help minimize NSB. NSB is revisited in depth in Chapter 6.

4.4.4 Surface functionalization and commercial bead quality limit application of iRMA

We sought to demonstrate the iRMA assay with 20 μm silica beads. As our initial target analyte, we chose *E.coli*, to which FcMBL is known to bind [125,126] and which is safer to handle in the lab. We used two types of *E.coli* which were stained with

green fluorescent dyes to facilitate visualization and quantification of bacteria: (1) *E.coli* BioParticles, which are inactivated fluorescently-stained bacteria, and (2) live *E.coli* MG1655 stained with Syto9 nucleic acid stain.

We first incubated beads with bacteria at a 1:100 bead:bacteria ratio for 40 min with end-over-end mixing by hand. Figure 4-11a shows microscope images of the beads after the incubation period, with *E.coli* in green. The control condition had no bacteria. When incubated with *E.coli* bioparticles or live *E.coli*, the beads bind bacteria, as indicated by the green fluorescent dots on the beads and suggesting that there is some FcMBL on the beads. However, the fraction of total bacteria captured in either case is extremely low ($\ll 1\%$) and does not agree with binding model predictions. This discrepancy indicates that either model parameters are not accurately capturing these conditions, which is possible given the uncertainty in k_A, or that the bead coating process is not efficient.

The control beads and the beads incubated with *E.coli* MG1655 were subsequently deposited into chambers on an FcMBL-functionalized glass slide and allowed to roll down the slide when inclined at either 60° or 80°. Figure 4-11b shows the residual beads on the surface of the slide for each bead condition and incline angle. Interestingly, the beads that remain on the surface in the *E.coli* MG1655 condition do not appear to have any *E.coli* cells associated with them, as illustrated by the lack of fluorescent green dots associated with the beads. This suggests that either the beads are nonspecifically bound to the surface or held to the surface via cell fragments or secretory products from the bacteria, which can bind FcMBL [125, 126]. When residual bead density is quantified (Figure 4-11c), there are more residual beads on the surface in the bacteria conditions. This difference is more pronounced when using a sloped surface of 60°, suggesting that the increase in required F_{tether} between 60° and 80° (223 or 254 pN, respectively) cannot be provided by the molecular tethers between whole bacteria or bacterial products and FcMBL. Overall, while suggesting some efficacy, this experiment is inconclusive and suggests that bead surface chemistry is limiting.

To trial beads with a base coating that would allow for covalent modification (as opposed coating processing with an initial BSA-biotin layer, which relies on

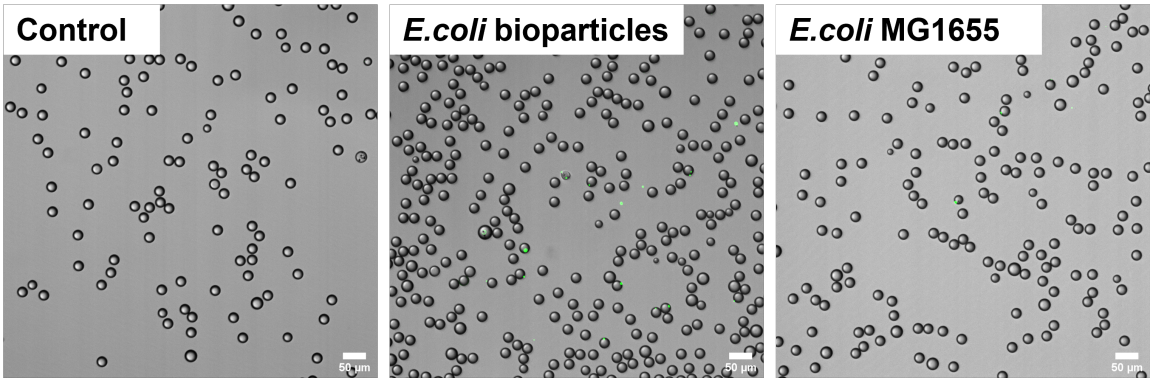

(a)

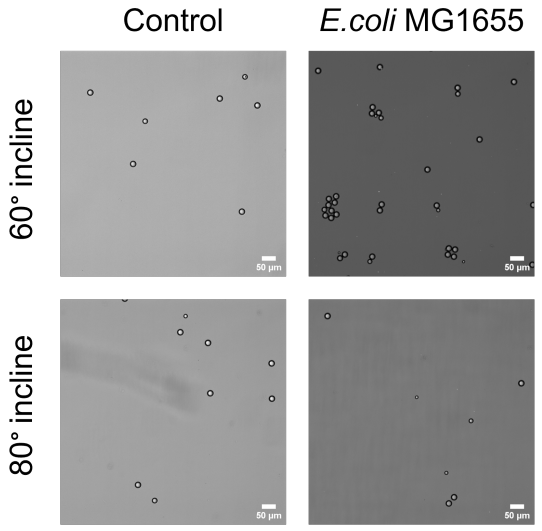

(b)

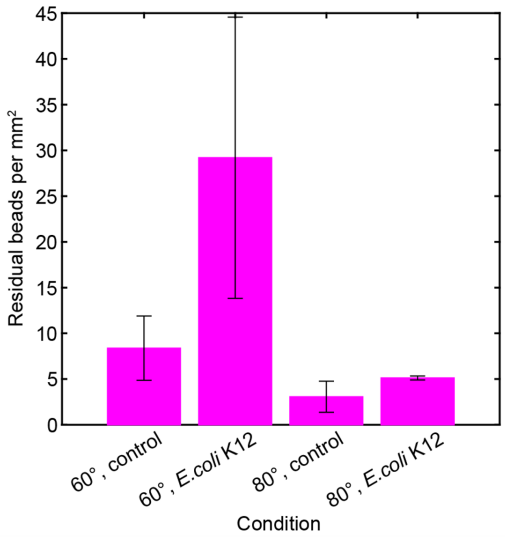

(c)

Figure 4-11: **Trial of 20μm FcMBL-coated beads in iRMA with *E.coli*.** (a) Beads were incubated with green fluorescent *E.coli* bacteria for 40 minutes via end-over-end hand mixing and imaged to quantify the number of bacteria that were captured. Functionalized beads bound very few bacteria, suggesting challenges with the coating process and/or the incubation. (b) Microscope images of residual beads, previously incubated with or without *E.coli*, on FcMBL-functonalized glass surfaces. By visual inspection, there are no beads in the *E.coli* condition that appear to be tethered by *E.coli* cells, suggesting the residual beads are kept on the surface by NSB or other interactions. (c) Quantification of residual beads in (b) at each incline angle. Error bars represent the standard deviation of images from two replicate chambers. There does seem to be some difference between control beads and beads incubated with *E.coli* in each incline condition, suggesting that this method of *E.coli* detection might have merit, if the level of residual beads in the control condition, which sets the sensitivity, can be lowered further.

adsorption), we used nonporous silica beads with a 7.5 μm radius and epoxy coating. Epoxy groups react with amine or sulfhydrl groups in a one-step reaction to produce biofunctionalized surfaces. We reacted these beads with either BSA or PEG(2k) (for control beads) or FcMBL (for functional beads) and used them in an experiment with *E.coli* MG1655 similar to what was performed with 20 μm silica beads. Figure 4-12 shows the results of this experiment and illustrates challenges in using these beads. First, despite repeated washing of bacteria after Syto9 staining, beads seem to take up residual dye during bacteria incubation (Figure 4-12a). This is either due to reaction of residual epoxy groups with the dye on the bead surface or adsorption of dye molecules to the bead surface and masks the binding of fluorescently-dyed bacteria to the beads. Furthermore, when these beads are placed on an FcMBL-functionalized surface and inclined at 80° for rolling, it seems they shatter or fragment (Figure 4-12b). This seems to happen in all conditions and makes quantification of residual beads difficult. The source of fragmentation is unclear, as the beads were not vortexed or otherwise intensely disturbed before deposition into chambers.

This experiment illustrates how bead quality limits the realization of iRMA. Regularly–stocked, pre–functionalized beads generally have a maximum size of <10 μm and beads larger than that are available on a custom-ordered basis. This limited selection and, as shown by our results, unoptimal quality of custom beads, restricts the realization of iRMA, despite theoretical results that suggest its promise. In-house synthesized beads are an option to overcome this and could be explored in the future.

4.5 Conclusion

In this chapter, we explored the theoretical underpinnings of iRMA, an assay architecture that utilizes gravity to drive sphere rolling down an inclined plane and quantifies analytes through the number of beads that remain on the surface via analyte-affinity agent sandwiches. An analytical model of the major physical processes in iRMA applied to virion sensing suggests that the assay could return a result in <30 min and with a cost of < \$5 using beads that are 11 μm in diameter. The most time-intensive

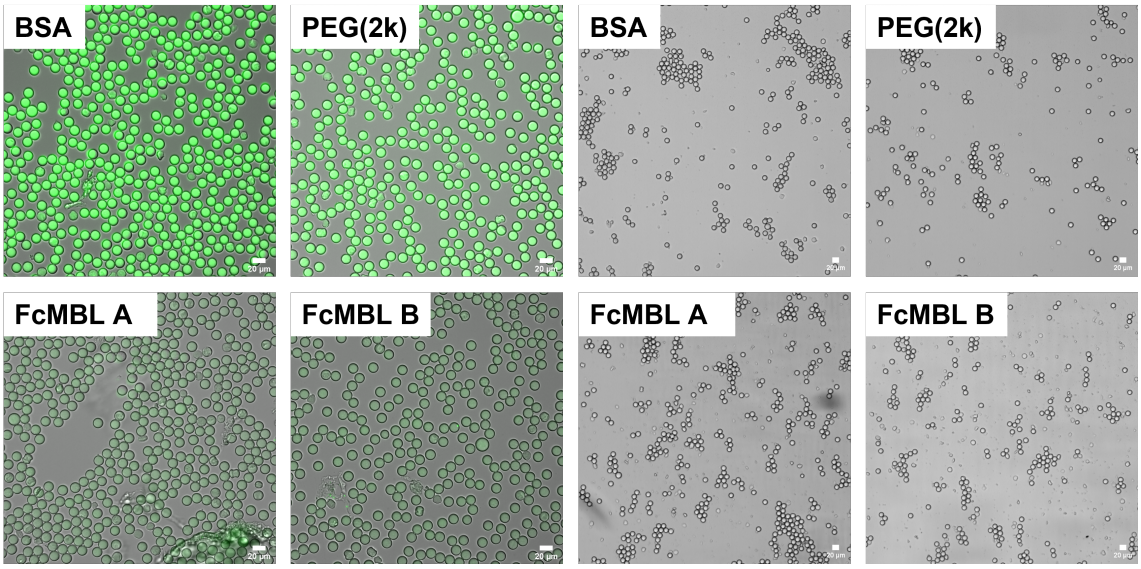

(a) (b)

Figure 4-12: **Trial of iRMA assay with functionalized 15 μm silica beads on FcMBL-functionalized glass surfaces inclined at 80°.** (a) Beads after incubation with *E.coli*. Despite repeated washing of the bacteria after staining, these beads bind the dye, making them fluorescent green during microscopy and masking bound bacteria. (b) Residual beads on FcMBL-coated glass slides inclined at 80°. The quality of the beads limits the assay, as beads seem to have shattered and broken apart, masking any differences between the conditions and making quantification challenging.

process in iRMA is the analyte capture, suggesting that optimization of that process via efficient and facile surface chemistry or using a greater bead concentration, could minimize the overall assay time. These optimizations, however, are not without their trade-offs, including potential increases in assay cost, and would need to be weighed accordingly for each application.

We experimentally characterized the rolling of beads on surfaces. A major question was how NSB would influence rolling and tethering, as it was not accounted for in the model. Promisingly, our initial results with large FcMBL-coated glass or silica beads on FcMBL-coated glass slides showed little background when inclined at 80°, suggesting that the interactions between opposing FcMBL molecules did not cause significant NSB. Results with 5 μm beads were, however, much less promising and indicate that NSB between beads and surfaces precludes small beads from rolling.

Two different experiments were undertaken to demonstrate the iRMA assay with FcMBL surfaces and *E.coli*. The first utilized 20 μm silica spheres functionalized via a multistep coating process. Though this experiment showed a difference between the control and experimental conditions, the capture efficiency of *E.coli* was extremely low and it was unclear what caused the residual bead tethering in the experimental condition. To determine if covalent functionalization helped with these challenges, the second experiment utilized epoxy-coated, 15 μm silica beads. Unfortunately, iRMA was also unable to be demonstrated using these beads due to quality issues. These experiments illustrate the difficulty of realizing iRMA without a steady, robust supply of larger beads, despite theoretical validation, and caused us to focus on other methods of actuation. It is possible that the promise of iRMA could be realized with nonfouling surface coatings, as discussed in Chapter 6. Given the advantages for decentralized testing, it would be warranted to revisit iRMA with such coatings in the future.

THIS PAGE INTENTIONALLY LEFT BLANK

Chapter 5

Bioanalyte sensing by observation of bead diffusion

5.1 Introduction

Our original assay concept centered upon inducing bead movement by external actuation methods. Naturally occurring phenomena can also influence bead-surface interactions. If able to be quantified via microscopy, colorimetry or other methods, these phenomena can serve as a signal for bead-analyte binding for analyte quantification. An inherent advantage to these mechanisms is that they do not require external actuation or instrumentation, which decrease assay complexity, minimize sources of error, and lead to a more user-friendly assay, an attribute especially appealing for decentralized settings.

One such phenomenon is diffusion, or Brownian motion, which is the random thermal motion of beads due to collisions with surrounding molecules. Observing and quantifying a bead's motion over time via mean squared displacement (MSD) yields information about physical influences on the bead's motion (Figure 5-1a). In the absence of other influences, particle motion is linear with time (Figure 5-1b, blue square). The slope of this line is the particle's diffusivity (D), which is related to the temperature (T), medium viscosity (μ_f) and bead radius (r_b) through the

Stokes-Einstein relation:

$$D = \frac{k_B T}{6\pi\mu_f r_b} \tag{5.1}$$

where k_B is the Boltzmann constant. If other physical processes influence the particle, the shape of this curve changes. Positive curvature indicates the presence of fluid flow or drift (Figure 5-1b, green square), while negative curvature demonstrates confinement by some force (Figure 5-1b, red square). Depending on the interaction with the surface, particles can also show a mix of these phenomena. For example, a particle can be transiently confined, wherein its motion is restricted temporarily, but can revert to random diffusion when the particle acquires enough energy to overcome confinement.

MSD is not the only quantification measure that can be derived from watching bead interactions with a surface. Recording bead-surface interaction dynamics during an observation window yields a rich set of data that can be quantified through other metrics. This data could be useful not only for bioassays but also for examining the spatial and temporal nature of bead-surface interactions.

In the context of a bioassay, observing the motion of affinity agent-functionalized beads on an affinity agent-functionalized sensing surface can yield information about analyte concentration. When an analyte is sandwiched between the receptors on the bead and the surface, the bead's motion changes due to the interaction imposed by this molecular tether. Quantification of a bead's motion through video microscopy allows for differentiation between analyte concentrations, as bead movement changes in proportion to the interaction between the bead and the surface. Hundreds of beads can be monitored in a single field of view, allowing for sufficient statistical power to quantify the analyte with sensitivity largely determined by the affinity of the receptor on the bead and sensing surface, and dynamic range based on the analyte concentration at which bead motion cannot be detected. Assays utilizing this diffusion-based sensing mechanism could yield a direct quantification of analyte concentration that requires no extra instrumentation beyond a low-powered microscope.

As outlined in Chapter 1, other groups have described bioanalyte quantification based on bead diffusion in a number of different platforms, demonstrating this

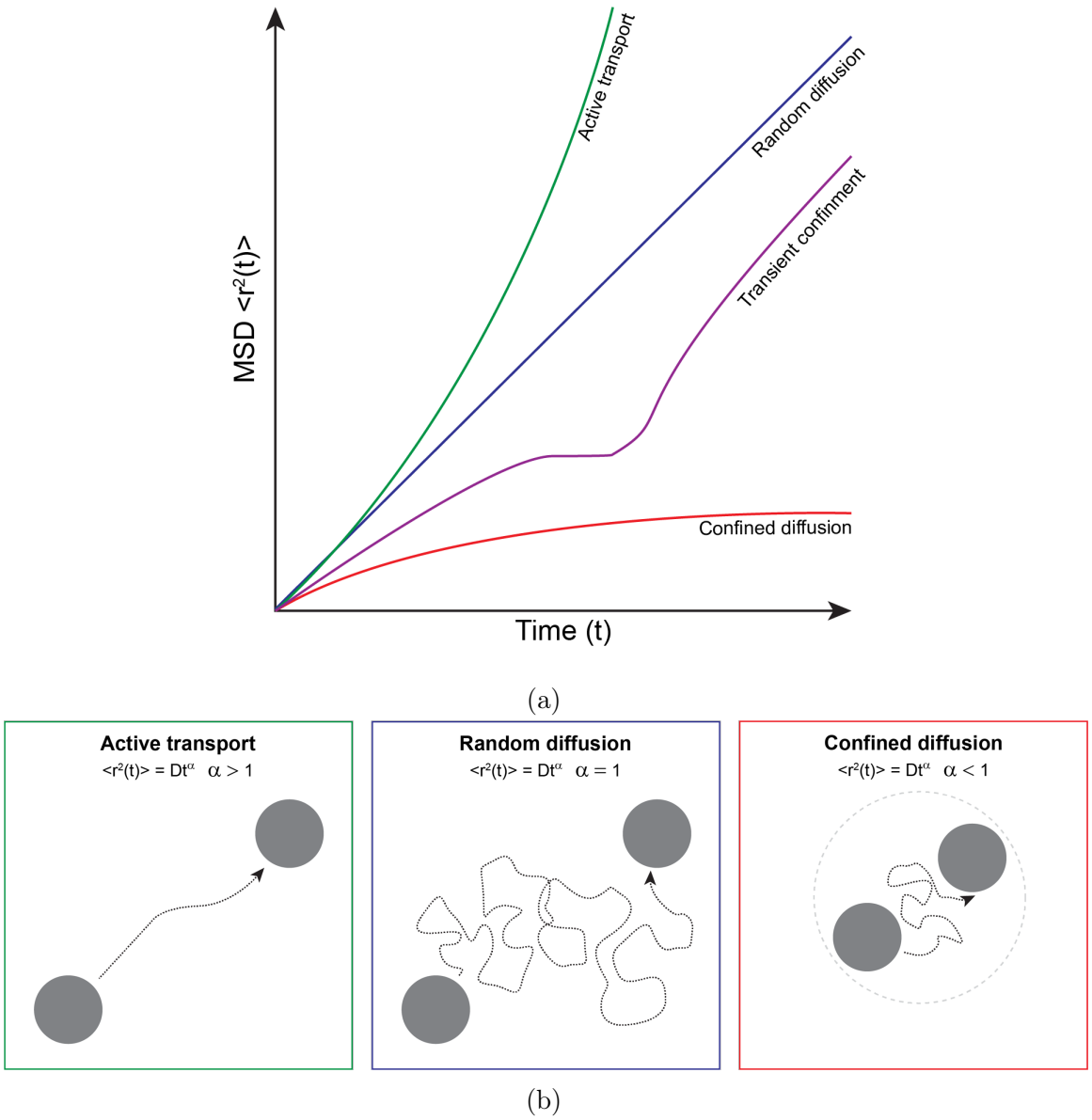

Figure 5-1: **Different types of diffusion as reflected by mean squared displacement (MSD) versus time.** MSD is a measure of the distance traveled by a diffusing entity and different types of diffusion or transport can be differentiated based on the shape of their MSD versus time curve. (a) All three major mechanisms depend on the diffusion coefficient and vary in their dependency on time. (b) In active transport, when the particle's motion is influenced by both diffusion and fluid motion, the curvature is positive and the exponent on the time is greater than one (green square). In free diffusion, when the particle is unhindered by other interactions, MSD is linear with time and the slope of this line is the diffusion coefficient (blue square). In confined diffusion, when the particle's motion is constrained by interactions with other entities, the curvature is negative and the exponent on time is less than one (red square).

mechanism's potential [44, 45, 47–50]. Our work builds on these reports and further extends them to larger beads for easier visualization and describes additional sensing surface actuations that could increase sensitivity. Additionally, our exploration to moves towards an integrated bioassay utilizing sensing based on diffusive bead motion and the capture-while-settling mechanism, a platform which requires little manual manipulation and simple computer-enabled microscopy suitable for decentralized testing.

This chapter discusses the experiments and analyses performed to determine the merits of bead-based bioassays based on the thermal motion of beads on a surface. We utilize a model affinity agent-analyte system, FcMBL and mannan, to investigate the effects of bead concentration, nonfouling coatings and sensing surface manipulation on assay sensitivity. Finally, we outline the different metrics that can be used to quantify bead motion, and show initial evidence that the integrated capture-while-settling and diffusive motion sensing system shows feasibility for bioanalyte quantification. The results of these investigations are used to inform the design of a clinically relevant assay, discussed subsequently in Chapter 7.

5.2 Materials and methods

5.2.1 Materials

Bovine serum albumin (BSA), phosphate buffered saline (PBS), KimWipes and Parafilm were purchased from VWR, Inc (Radnor, PA). HybriWell sealing system chambers (6 chambers per slide, chamber dimensions 9.8 x 20 millimeter [mm], 0.25 mm depth; Grace Bio-Labs), ProPlate multiwell chambers (16 x 6 mm diameter wells; Grace Bio-Labs), mannan from *Saccharomyces cerevisiae*, calcium chloride dibasic ($CaCl_2{\cdot}2H_20$), ethanolamine, Tris base, sodium phosphate monobasic (NaH_2PO_4), sodium phosphate dibasic (Na_2HPO_4) and Tween 20 were purchased from Millipore-Sigma (Burlington, MA). Dynabeads M-450 Epoxy and Dynabeads M-270 Epoxy magnetic beads (hereafter referred to 4.5 micron [μm] and 2.8 μm beads, respectively)

and ethylenediaminetetraacetic acid (EDTA) purchased from ThermoFisher Scientific (Waltham, MA). Amine-terminated polyethylene glycol (PEG) with molecular weight of 2000 and 10000 daltons (subsequently referred to as PEG(2k) or PEG(10k), respectively) were purchased from Nanocs, Inc (New York, NY). Glass slides coated with an antifouling polymer layer and functionalized with epoxy groups (subsequently referred to as 3D epoxy slides) were purchased from PolyAn GmBH (Berlin, Germany). 10x Tris-buffered saline with 0.5% Tween-20 (TBST; Boston BioProducts) was purchased from Fisher Scientific (Hampton, NH). A fusion protein affinity agent combining the human IgG Fc portion and the carbohydrate recognition domain of mannose binding lectin (Fc-MBL) [123] was kindly provided by Michael Super of the Wyss Institute for Biologically Inspired Engineering (Boston, MA, USA).

5.2.2 Surface functionalization

Sensing surfaces were created by functionalization of 3D epoxy slides with FcMBL at a density of 10 milligram per square meter (mg/m^2), according to the manufacturer's protocol and previously outlined in Chapter 3. For initial experiments, chambers on slides were created using the Hybriwell sealing system. For the capture-while-settling experiments, wells on slides were created using the ProPlate multiwell system.

4.5 μm beads were functionalized according to previous optimizations in combination with the manufacturer's recommended protocol. Incubation steps took place at room temperature and with mixing in reciprocating mode on a rotisserie mixer at 30 rotations per minute (rpm), unless otherwise noted. Briefly, beads were incubated for 20 hours (h) with 0.1 molar (M) sodium phosphate buffer (pH 7.4) with FcMBL at a concentration to coat beads with 10 mg/m^2. After magnetic concentration, beads were resuspended with PEG(2k) or PEG(10k) in 0.1 M sodium phosphate buffer for a coating density of 10 mg/m^2 or 50 mg/m^2, respectively, and incubated for 20 h. Beads were magnetically concentrated, resuspended in 50 millimolar (mM) ethanolamine in 0.1 M sodium phosphate buffer and incubated for four hours. Finally, beads were washed three times for five minutes (min) with wash buffer (PBS + 2 mM EDTA + 0.1% weight per volume [w/v] BSA). Beads were counted and stored at 4°C until use.

5.2.3 Diffusion experiments using mannan-FcMBL model system in the HybriWell chambers

Initial experiments used rotisserie mixing during bead-mannan binding. Mannan was diluted at 0, 0.005, 0.01, 0.05, 0.1, 1, 10 or 100 nanograms per milliliter (ng/mL) in 1x TBST + 5 mM $CaCl_2$ (TBSTCa). 500 microliters (μL) of mannan solution were added to 10^6 or 10^5 beads in a 1.5 milliliter (mL) microcentrifuge tube and incubated for 30 min with end-over-end mixing at 25 rpm. Beads were magnetically concentrated and washed in TBSTCa. Washing conditions varied between no washes (simple magnetic concentration and supernatant aspiration) to three washes.

After any washing, beads were resuspended in 50 μL of TBSTCa and injected into a chamber on the FcMBL-functionalized slide. Chamber port holes were sealed using tape to prevent evaporation. Using a Nikon TE-2000U inverted microscope fitted with an Andor iXon3 CCD camera (Oxford Instruments, Abingdon, UK), twenty images were taken along the length of the chamber at 10x magnification with 0.01 second (s) exposure time. At every five images, a video of the beads on the surface was taken at 20x magnification (300 frames at 5 or 10 hertz [Hz] with 0.01 s exposure time), resulting in four videos at different regular spacings along the slide length (Figure 5-2a).

In some experiments, additional manipulations of the slide were performed. The slide was inverted such that gravity could act on weakly-held beads to remove them from the surface. In this case, imaging and filming of the "inverted orientation" were performed using the same process and parameters as described above and started 5 min after slide inversion to allow beads to settle.

5.2.4 Capture-while-settling experiment using mannan-FcMBL model system in ProPlate wells

ProPlate wells were clipped to an Epoxy 3D slide (Figure 5-2b) and the slide surface was functionalized with FcMBL at 10 mg/m^2, as previously described. The number of beads and volume of mannan solution were chosen based on the geometry of the well.

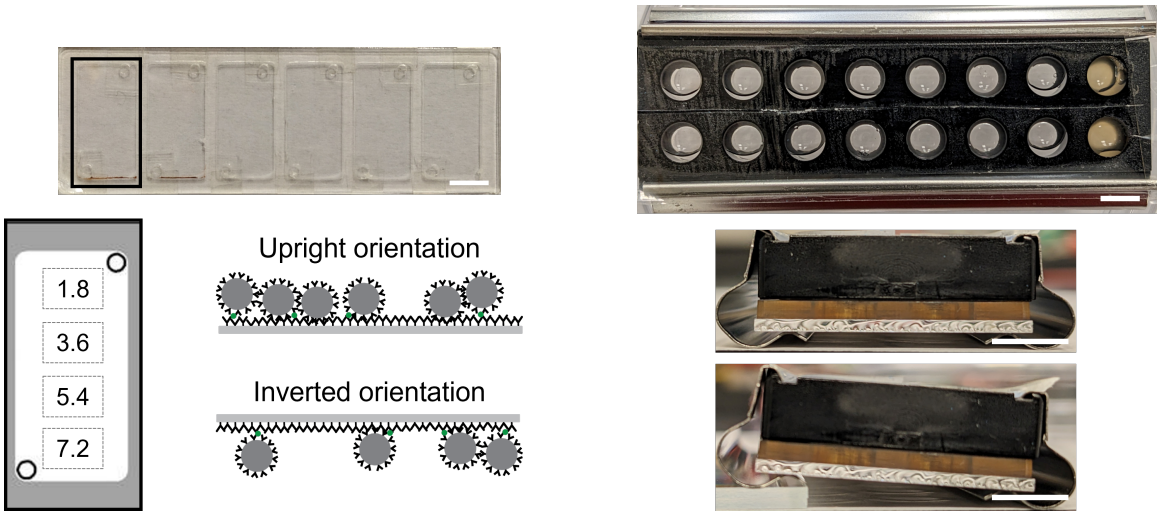

(a) (b)

Figure 5-2: **Slide partitioning and orientations used in diffusion experiments.** (a) Chambered slide created by affixing HybriWell gasket to a glass slide, creating six chambers per slide each holding 50 μL and with dimensions of 9.8x20 mm (top, scale bar is 10 mm). Boxes with dotted lines indicate the location where videos were filmed along the length of the chamber, corresponding to the 1.8, 3.6, 5.4 and 7.2 mm measured from the top edge of the chamber (bottom, left). Beads in the chambered slide were filmed with the slide in two orientations (bottom, right). In the upright orientation, the slide remained underneath the beads. In the inverted orientation, the slide was flipped, so that it was on top of the beads, to promote bead settling under gravity. (b) Well slide created by clamping ProPlate scaffolding to a glass slide, creating a slide with 16x6 mm diameter wells. Each well can hold 200 μL (top). The ProPlate scaffolding consists of a Delrin well plate and a silicone gasket, which is clamped to a glass slide via stainless steel clips (middle). White scale bars on all images are 6 mm.

Briefly, 1.78x10^5 FcMBL-functionalized 4.5 μm beads in 7 μL of TBSTCa was initially deposited into the well. 173 μL of mannan solution in TBSTCa was subsequently added to the well and pipetted up and down three times to mix. In a 6 mm-diameter well, this corresponds to a fluid column height of 6 mm. With a 4.5 μm bead settling speed of 5.52x10^{-6} m/s (bead density of 1.5 grams per cubic centimeter [g/cm^3]), it takes ~20 min for a bead at the top of the fluid to settle to the surface. Videos at three different random points in the well were taken using the previously described conditions.

5.2.5 Image and video analysis algorithms

Custom MATLAB (MathWorks, Natick, MA) scripts were developed to quantify bead number and bead motion. This algorithm builds on the image processing algorithm and the parameters selected through optimization discussed in Chapter 3.

Video analysis took place in two steps, which are briefly outlined below:

1. Raw data extraction

    - For each frame in the video, the algorithm binarizes the image using the Sauvola local thresholding algorithm [128] with an optimized window of 20 x 20 pixels and inverts the image so that the beads are white on a black background.
    - After clearing any beads that exist on the borders so that their area is not used in calculations (*imclearborder* function), the area and centroid coordinates of each white blob is determined via the *regionprops* function.
    - From the list of blob areas, the mode area is determined and assumed to be the area of a single bead, since these are the most numerous in any video.
    - White areas are separated into single beads or clumped beads by comparison to the single bead area and a threshold (i.e., if the area is 0.90 to 1.10 times the mode area, the area is assumed to represent a single bead)

- Beads in the current frame are matched to beads in the previous frame by finding the minimum 2D Euclidean distance between centroids via the *pdist2* function. The Euclidean distance d between two centroids $c_1 = (x_1, y_1)$ and $c_2 = (x_2, y_2)$ is defined as:

$$d = \sqrt{(x_1 - x_2)^2 + (y_1 - y_2)^2} \tag{5.2}$$

- Invalid beads or clumps, those areas which are characterized as single beads in one frame but disappear in the next frame due to joining a clump, are discarded by enforcing that the maximum distance between the same bead in subsequent frames is less than the bead radius.

- Centroid coordinates are corrected for drift due to bulk fluid motion or instrumentation drift. This was performed by assuming that the velocity observed for each particle, $v_i(t)$, is a combination of the diffusive velocity and the drift velocity [151]:

$$v_i(t) = v_{i,\text{drift}}(t) + v_{i,\text{diffusive}}(t) \tag{5.3}$$

We assume that the same drift velocity influences all particles, whereas the diffusive motion depends on the particle. When the average velocity $\langle v(t) \rangle$ over all N(t) particles is found, the diffusive contribution sums to zero the diffusive motion is uncorrelated between particles, i.e.:

$$\langle v(t) \rangle = \frac{1}{N(t)} \sum_i v_{i,\text{drift}}(t) + v_{i,\text{diffusive}}(t) = \langle v_{i,\text{drift}}(t) \rangle \tag{5.4}$$

This holds for the velocity in both the x and y directions. To determine the bead displacement due to the drift in a certain frame, the drift velocity

in each direction can be integrated to the current time of the frame [151]:

$$x_{\text{drift}}(t) = \int_0^{t'} \langle v_x(t') \rangle dt' \tag{5.5}$$

$$y_{\text{drift}}(t) = \int_0^{t'} \langle v_y(t') \rangle dt' \tag{5.6}$$

This displacement is subtracted from the corresponding component of the centroid of every bead in the frame. This yields a set of 2D matched, drift-corrected centroid coordinates for each bead or clump p at each frame time t:

$$r_p(t) = [x_p(t), y_p(t)] \tag{5.7}$$

- The total white area, mode area and set of centroids for beads and clumps in each frame are saved for analysis in the next step.

2. Data analysis and quantification of MSD and other metrics

   - The total number of beads, single bead count, clumped bead count and fraction of beads that are clumped are determined for each video using the mode area and total white area found in the raw data extraction process.

   - Using the matched centroids for each single bead or clump in a video, MSD at each observation time t is determined. MSD is a measure of the distance a bead has moved after a specific time interval (Figure 5-3) and is hypothesized to be indicative of the concentration of the analyte in our assay. For a video with a frames taken at frame rate r (in Hertz [Hz]), the minimum time between two frames is $\tau_{\text{min}} = \frac{1}{r}$ and the maximum time between two frames is $\tau_{\text{max}} = \frac{a-1}{r}$. This gives possible time intervals of $t = n\tau_{\text{min}}$ where $n = 1$ to $(a-1)$. For example, for a video with 300 frames taken at 10 Hz, frames corresponding to $t = 0.1$ s would be frames 1 and 2, frames 2 and 3, frames 4 and 5, and so on, while $t = 0.5$ s would correspond to frames 1 and 6, frames 2 and 7, and so on. The maximum time would be $t = 29.9$ s between frame 1 and frame 300. Thus, for a set of 2D coordinates

representing a single bead or clump p, the time-averaged MSD for a specific time interval is [152–154]

$$\mathrm{MSD}_{p,x}(t = n\tau_{min}) = \frac{1}{a-n}\sum_{i=1}^{a-n}[x_p\,(t_i + n\tau_{min}) - x_p\,(t_i)]^2 \tag{5.8}$$

$$\mathrm{MSD}_{p,y}(t = n\tau_{min}) = \frac{1}{a-n}\sum_{i=1}^{a-n}[y_p\,(t_i + n\tau_{min}) - y_p\,(t_i)]^2 \tag{5.9}$$

$$\mathrm{MSD}_{p}(t) = \mathrm{MSD}_{p,x}(t) + \mathrm{MSD}_{p,y}(t) \tag{5.10}$$

Notice that for a specific time interval t, there are $a - n$ observations of that time interval over the video. This means that more measurements can be extracted for a shorter t than for a longer t and an increasing uncertainty in MSD measurements for longer t (standard deviation for a specific t scales as $\frac{1}{\sqrt{a-n}}$). For example, the time-average above uses 299 observations for $t = 1\tau$ but uses 100 observations for $\tau = 200\tau$. In practice, this leads to using time intervals that cover 1/3 to 1/2 of the total video for quantification and analysis [152–154].

- For the entire set of beads N_p in a given video, the ensemble average MSD for a given time is calculated as the average of the individual bead MSD for that time interval [152–154], i.e.:

$$\mathrm{MSD}_{ens}(t) = \frac{1}{N_p}\sum_{p=1}^{N_p}\mathrm{MSD}_{p}(t) \tag{5.11}$$

- For each individual bead in a video, two parameters were calculated based on the bead trajectory over the observation time, each of which are a slightly different measurement of bead motion during observation (Figure 5-4)

  – The radius of the circle that encloses positions in all frames is calculated by finding the centroid of all (x, y) positions and computing the radius of the circle that would enclose these points (the "enclosing radius")

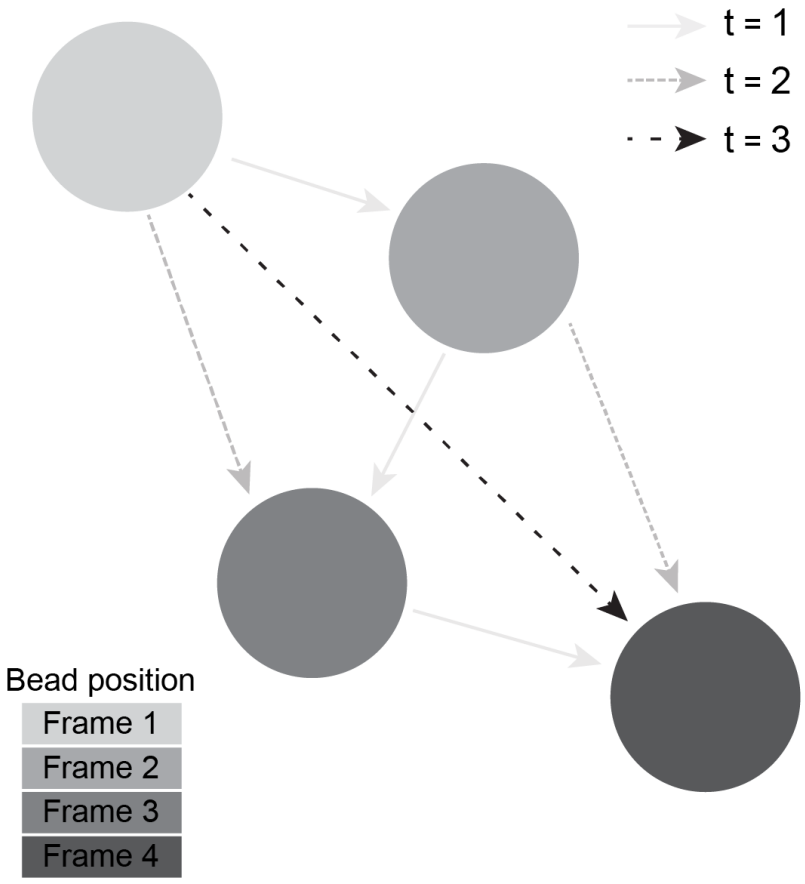

Figure 5-3: **Using particle positions to calculate MSD from video frames.** In each frame, the particle's centroid x and y coordinate are recorded. For a specific time t, the MSD is calculated as the distance traveled in all possible intervals of length t over all video frames. For example, for the particle illustrated above in four frames, there are three MSD trajectories for $t = 1$ between the positions in the first and second frame, the second and the third frame and the third and the fourth frame. For $t = 2$, there are two trajectories between positions in the first and the third frame and the second and the fourth frame. For $t = 3$, there is one trajectory between positions in the first and the fourth frame. Following this pattern, for a total observation of a frames, there are $a - 1$ MSD measures for $t = 1$ and one MSD measure for $t = a - 1$. This has implications for the accuracy of the MSD; as t increases, the standard deviation in MSD also increases. In practice, this results in using $1/3$ to $1/2$ of the observation window for quantification and analysis.

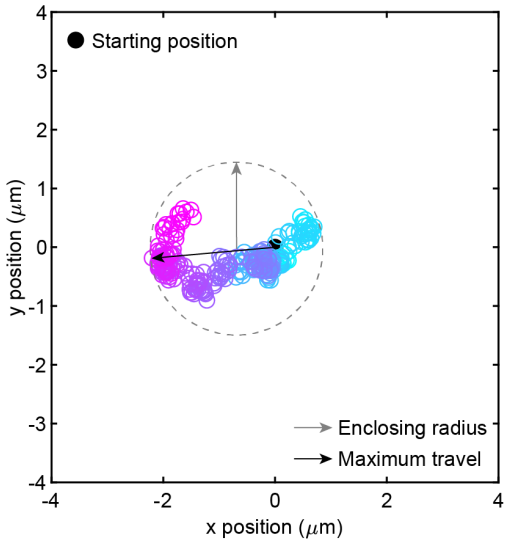

Figure 5-4: **Example of trajectory geometry metrics calculated for each bead.** The enclosing radius is calculated by finding the centroid of all (x, y) points during the video and finding the minimum radius of the circle that encloses all of those point (gray arrow). The maximum travel is the maximum distance the bead moved away from its starting point (black arrow).

  - The maximum travel from the starting position is calculated by finding the maximum distance between the starting position and all other bead positions by Euclidean distance (the "maximum travel")

- For each individual bead or clump, a linear model $y = mx + b$ is fit to the MSD versus time data after excluding the first two seconds worth of data and using half of the total frames. This calculation utilizes the *polyfit* function and returns slope and intercept for each bead.

5.3 Results and discussion

5.3.1 Quantifying bioanalytes via bead diffusive motion depends upon increased bead-surface interactions as analyte concentration increases

Observing diffusive motion of beads on a surface is a simple method to quantify analyte concentration as it arises naturally from thermal gradients and can be observed via microscopy. In combination with the capture-while-settling mechanism utilizing large beads, we hypothesize that diffusion-based sensing could provide a sensitive, simple platform for bioanalysis particularly suited for the low infrastructure requirements of decentralized settings.

How is bead diffusive behavior used to measure bioanalyte concentration? The motion of a bead on a surface is influenced by analyte sandwiches that form between analytes bound to the bead and the affinity agent on the surface. The formation of these molecular tethers is a function of both the bound analyte density on the beads as well as the contact area between the bead and the surface, the surface density of the affinity receptors and the analyte-affinity receptor bond kinetics. Predicting how the bound analyte density and bead properties influences tether formation can yield insights into the bead motion patterns that may be observed during an experiment. Below, we go through this analysis using the model mannan-FcMBL system.

First, the theory outlined in Chapter 2 can be used to predict the bound-analyte bead surface density after a settling time t. Using the on-rate for mannan-MBL ($k_{on}^{3D} \sim 7\text{x}10^4 \frac{1}{Ms}$ [155]), the maximum FcMBL functionalization density ($n_{ab} \sim \frac{10^{16}}{m^2}$ [106]) and k_+ estimated using the Peclet number and dimensionless mass capture coefficient from the correlation in Equation 2.12, we find that the Damkohler number is ~ 1. This means that both reaction and mass transport must be considered when predicting analyte capture. For simplicity, we use a settling time of 5 minutes (before equilibrium and receptor off-rates must be considered; $t_{eq} \sim \frac{1}{k_{off}^{3D}}$ [106], $k_{off}^{3D} \sim 10^{-3} s^{-1}$ [155]) and the resistance model (Equation 2.39) to predict the fraction of analytes captured

(F_{capture}) using beads of different size:

$$F_{\text{capture}} \approx 1 - \exp\left(-\frac{n_b A_b}{V_s}\frac{k_{on}^{3D} n_{ab}}{1+\frac{k_{on}^{3D} n_{ab}}{k_+}}t\right) \tag{5.12}$$

Assuming each bead binds the same number of mannan molecules and for a given initial mannan concentration C_0 in a sample of volume V_s, we estimate the bead-bound mannan density n_{mannan} on a single bead (in $\#/\text{m}^2$) as

$$n_{\text{mannan}} = \frac{F_{\text{capture}} C_0 V_s}{n_b A_b} \tag{5.13}$$

The number of mannan molecules in the contact area between the bead and the surface is then $A_c n_{\text{mannan}}$, where A_c is the contact area between the bead and the surface, for which we assume that the bead-surface separation is two times the length of the FcMBL molecule (estimated as the length of an IgG molecule, $L_{IgG} \sim 10$ nm [146, 147, 156]):

$$A_c = 2\pi r_b \left(2L_{IgG}\right) \tag{5.14}$$

For an illustration of this A_c calculation [102, 156], refer to Figure 4-3b.

Table 5.1 presents the results of this calculation for three different mannan concentrations and two different bead sizes, and Figure 5-5 presents a graphic representation of the tethering process. As mannan concentration increases, more mannan molecules are found in the contact area between any size bead and the surface. This forms the basis for our hypothesis that increasing analyte concentration will be quantifiable through changes in bead diffusive motion due to tethering.

Next, due to the dependence of A_c on bead size, larger beads have a geometric advantage over smaller beads. For the same concentration of beads in the sample (in the case presented in Table 5.1, 1 million/mL), though the bound mannan density is greater for smaller beads, the contact area of 4.5 μm beads is 1.6x greater than that of 2.8 μm beads which translates to ~1.5x more analytes in the contact area for these larger beads. Since the probability of bead tethering is proportional to the number of analyte molecules in A_c, the chances of a 4.5 μm bead tethering after 5 minutes of

Table 5.1: **Calculation illustrating effect of mannan concentration on tethered analytes on contact area between bead and surface.**

		2.8 µm diameter	4.5 µm diameter
	Bead-surface contact area (µm^2)	0.088	0.141
Mannan molecules in contact area after incubation* with indicated concentration	0.05 ng/mL	0.043	0.065
	1 ng/mL	0.86	1.33
	100 ng/mL	8.6	133

*5 minute incubation in 500 µL with 10^6 beads

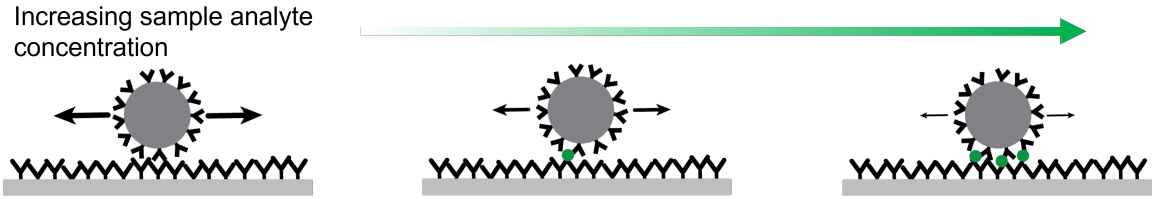

Figure 5-5: **Influence of analyte density in the bead-sensing surface contact area on bead diffusive motion**. As the sample analyte concentration, and the resulting analyte density captured on the bead, increases, more analyte sandwiches are formed between the bead and the surface. The greater the number of analyte sandwiches, the more confined the bead motion becomes (as indicated by the length and weight of the black arrows).

incubation with any mannan concentration is greater than for 2.8 μm beads.

While it may seem that increasing bead size is always advantageous for these assays, it is worth considering several other ways in which bead size could influence the assay. For one, diffusivity scales with the inverse of the bead radius (Equation 5.1), which translates to 2.8 μm beads moving 1.6x faster and sampling of the entire bead surface for bound analyte occurring in a shorter amount of time. Fewer tethers may also be needed to produce a noticeable difference in bead motion for smaller beads due to their lower inertia. Because of this, differences in bead motion may be more obvious when observing smaller beads, provided the microscope optics for quantification can resolve these changes. Additionally, the larger bead-surface contact area as r_b increases also increases the chance of NSB. On the other hand, for the capture-while-settling mechanism, sedimentation velocity scales as r_b^2, yielding 2.5x faster speed for 4.5 μm beads as compared to 2.8 μm beads of the same material. This has real implications for total assay time when using the capture-while-settling mechanism.

At some concentrations in Table 5.1, there is, on average, less than one mannan molecule in the contact area. For robust signal generation, a bead-bound analyte should always be within the instantaneous bead-surface contact area. However, if there is a fractional molecule within the contact area, potential tethers can only form during a fraction of the observation time, which has several implications for assay sensitivity. For one, the observation time must be of sufficient length to observe constrained motion, or a sufficiently large number of beads must be monitored to observe bound beads since the fraction of bound beads will be smaller. Assuming one tether can cause a noticeable change in bead motion, the longevity of this sandwich-constrained motion is on the order of k_{off}^{3D-1}, which is several minutes in the worst-case scenario. The more influential aspect is that the fraction of beads capable of constrained motion at any given time must be greater than the fraction of beads nonspecifically in the no analyte condition in order to produce a signal above the background. It is therefore useful to determine the analyte concentration at which there would always be one analyte molecule in contact with the surface; below this concentration, signals may be

noisy and undistinguishable from background depending on the extent of NSB. From the data in Table 5.1 for our model mannan-FcMBL assay and taking the probability of sandwich formation for an analyte in the contact area as 1, this is predicted to be around 1 ng/mL for both bead sizes. This concentration can be decreased by increasing the number of analytes captured per bead, for example by decreasing the number of beads, decreasing the sample volume or increasing the settling time. These modifications need to be balanced with other trade-offs when designing for a specific application.

5.3.2 Diffusion-based sensing can differentiate between different analyte concentrations in a model system

We performed experiments with the mannan-FcMBL model system to validate the use of bead diffusion as a signal for bioanalyte concentration. Our initial experiment used one million FcMBL-PEG(2k)-functionalized 4.5 μm beads and mannan concentrations from 0-100 ng/mL. Results show that mannan concentrations can be differentiated by the ensemble average MSD (Figure 5-6a) and validate our hypothesis (as well as agree with previous studies [44, 45, 47–50]) that increasing bioanalyte concentration decreases bead movement. The lowest concentration that can be differentiated from 0 ng/mL is 0.1 ng/mL, which, using the range of molecular weights reported for mannan (4-130 kilodalton [141]), suggests at least pM sensitivity.

Examining the individual bead time average MSD versus time curves, which are averaged into the ensemble for each mannan concentration, yields insight into the majority bead motion at each mannan concentration and how the motion changes with mannan concentration (Figure 5-6b). For example, for the 0 ng/mL condition, 44% of the beads freely diffuse (defined as the fraction of beads having >0.1 square micron [μm^2] MSD at $t = 15$ s), as shown by MSD curves that are mostly linear with time. An active transport process seems to be influencing the motion of one or two beads, despite the chamber being sealed during the experiment and drift velocity correction in the image processing algorithm. This could be due to locally induced effects such

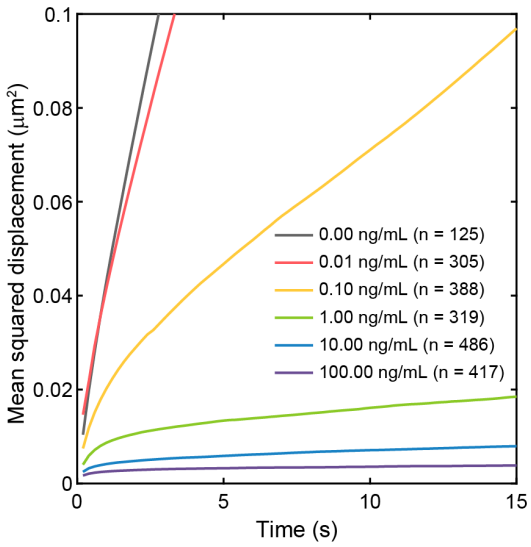

(a)

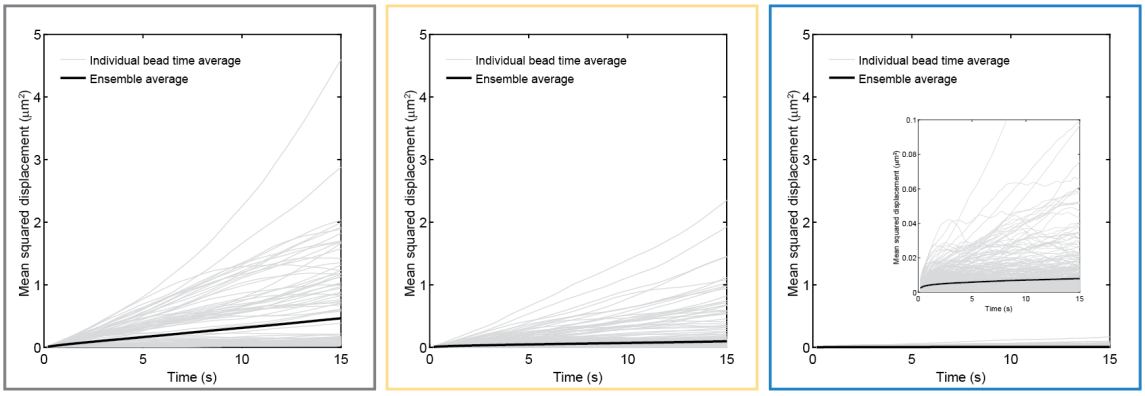

(b)

Figure 5-6: **Detection of mannan using 4.5 μm FcMBL-coated beads and sensing surface.** (a) Mannan concentrations can be differentiated by the ensemble average MSD, which is an average measure of distance traveled over all beads observed. This metric suggests that we can reliably detect 0.10 ng/mL, which translates to 0.75 to 2.5 pM sensitivity [141], a level relevant for many bioassays. (b) Individual bead time average MSDs for 0.00, 0.10 and 10.00 ng/mL mannan conditions (left, center, right, respectively) show how free diffusion decreases with increasing mannan concentration. The black line in each plot is the ensemble average MSD in (a).

as surface topography or heating from microscope illumination, and warrants future examination.

In the 0.1 ng/mL condition, 16% of beads are freely diffusing (Figure 5-6b, yellow box). The ensemble MSD has a shallower slope than the 0 ng/mL condition, indicative of the smaller fraction of beads that are freely diffusing. On the other hand, the individual bead time averages for the 10 ng/mL condition look markedly different (Figure 5-6b, blue box). The majority of beads in this condition show confined diffusion with minimal motion. Only 0.2% of beads show free diffusion, yielding an ensemble average curve that suggests the majority of beads are confined by analyte tethers. Overall, this shows that the change the ensemble MSD as analyte concentration increases is caused by a decrease in the fraction of beads exhibiting free diffusion due to tethering via analyte sandwiches.

Our analysis method of filming beads yields data that can be mined to examine other bead behaviors, including revealing the frame-by-frame motion of individual beads. Figure 5-7 shows trajectories over the complete 300 frame video for six individual beads from the 0.00 ng/mL condition (gray box) in Figure 5-6b. These beads illustrate different bead motions during interaction with the sensing surface, including completely confined diffusion (left column), temporary confinement (middle column) and free diffusion (third column). Though not performed in this study, analyzing these trajectories further could yield insights into the nature and strength of confinement on the sensing surface. In the 0.00 ng/mL condition, this corresponds to the background nonspecific binding (NSB), which controls assay sensitivity and is the subject of Chapter 6.

5.3.3 Filming location and slide manipulation influences assay sensitivity

Our model mannan-FcMBL assay utilized chambered FcMBL-coated glass slides, which were created using a Hybriwell chambered gaskets. For each mannan concentration, videos were taken along the length of the chamber (see Figure 5-2a) and compared to

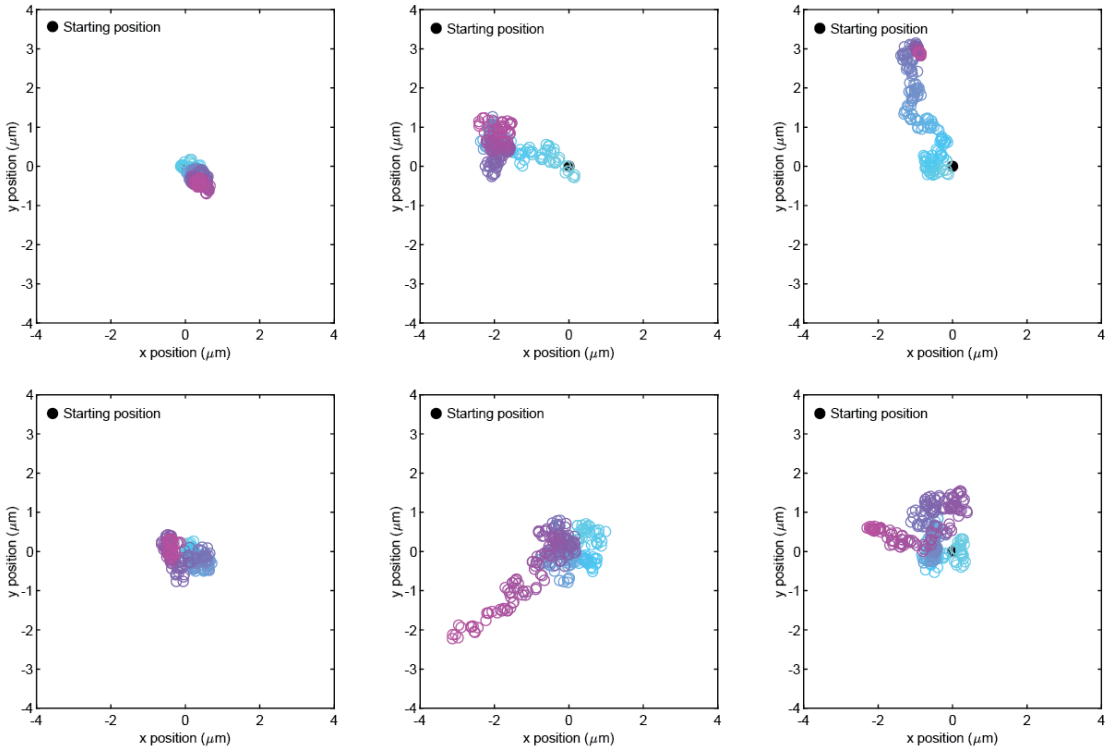

Figure 5-7: **Example individual bead trajectories in 0.00 ng/mL mannan condition.** Examples of individual bead trajectories from Figure 5-6b (left gray box) over the 300 frame video, illustrating the range of bead motions. Beads with low MSD show confined diffusion (left column), while freely diffusing beads have high MSD (right column). Intermediate MSD can arise from beads that are temporarily confined (middle column). Colors represent observation time, going from blue at the beginning of observation to magenta at the end of observation, with each circle representing the centroid position in one frame.

evaluate if location along the chamber influenced assay performance. Ideally, with a uniformly coated sensing surface, assay sensitivity would not depend upon the video location. This analysis was motivated by our previous results in Chapter 3 which showed variation along the chamber.

Figure 5-8 shows ensemble MSD versus time plots for the mannan-FcMBL assay using one million FcMBL-PEG(2k) coated 4.5 μm beads at different video locations along the chamber. The distance along the chamber is indicated by the measurement above each column and is referenced from the top chamber edge (see Figure 5-2a). The first column of plots corresponds to the normal assay orientation, with the slide underneath the beads, and the 1.8 mm panel in this row is the same data shown in Figure 5-6a. From this column, it is evident that video location influences assay sensitivity. In the 7.2 mm location, the 0.01 ng/mL ensemble MSD is clearly distinguishable from the 0.00 ng/mL measure, whereas at the 1.8 and 3.6 mm locations, these two lines overlap. Additionally, in the 5.4 mm video, the 0.01 ng/mL MSD is greater than the 0.00 ng/mL. This could result from either there not being enough tethers to confine bead motion to be distinguishable from free bead motion using our microscopy settings or due to FcMBL not having sufficient affinity to restrain bead motion to an observable extent. Experiments discussed in a subsequent section suggest which is the causative mechanism.

Notably, though the magnitude is differs by location, the MSD for 0.10 ng/mL and greater concentrations mainly follows the expected trend, with increasing concentration lowering ensemble MSD. The differing MSD magnitude for the same mannan concentration in each chamber location suggests that the sensing surface is somewhat heterogeneous. This may be caused by local changes in topography due to defects in the underlying, antifouling 3D polymer coating. Though the coating process is not disclosed, the manufacturer quotes the antifouling coating layer thickness at 10-100 nanometer (nm; personal communication). As investigated in Chapter 6, increasing the separation distance between the bead and the glass surface helps to mitigate the physical aspects of NSB. Local differences in the coating thickness could therefore lead to different slide areas being more prone to NSB than others, which would manifest

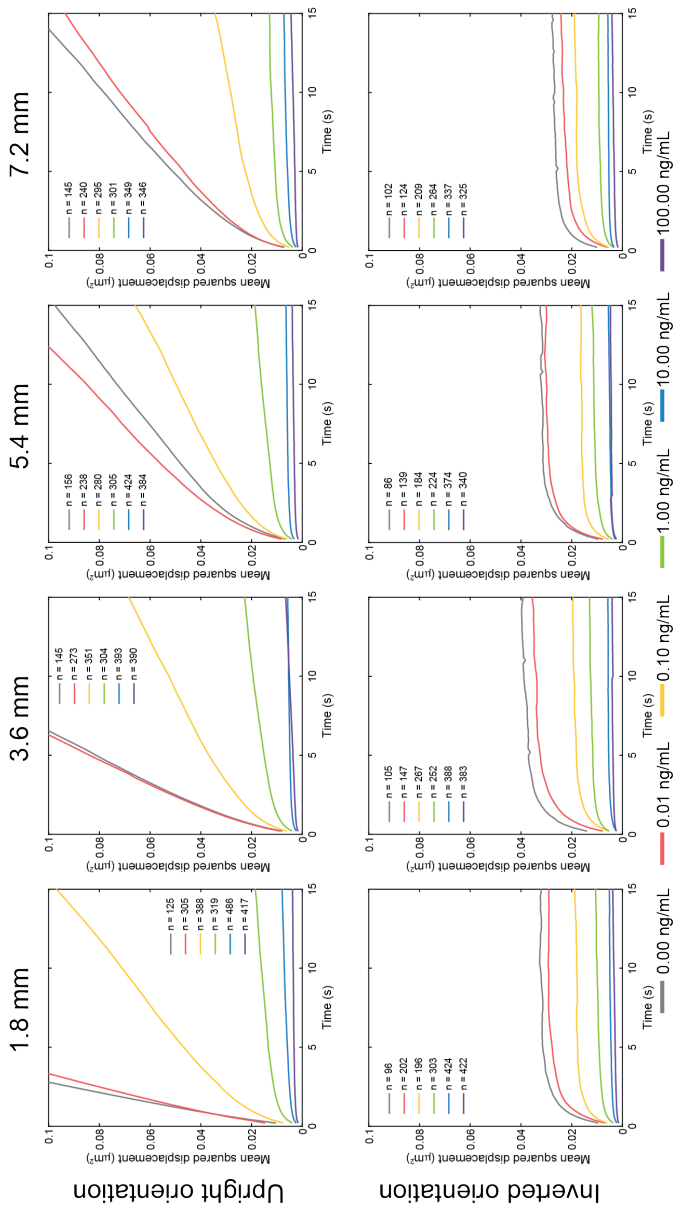

Figure 5-8: **Effect of observation location and slide manipulation on ensemble average MSD during mannan sensing experiments with one million, 4.5 μm PEG(2k), FcMBL-coated beads.** The first row are results when the sensing surface is in its original upright position, below the beads, and shows that the magnitude of the MSD for a particular mannan concentration generally decreases as the observation location is further from the injection port. The second row shows results when the sensing surface is inverted, above the beads. For a particular mannan concentration, MSD magnitude is similar and can be used to differentiation between all mannan concentrations at all locations. Inverting the slide helps to remove beads that weakly interact with the surface, thereby decreasing the background and increasing the assay sensitivity.

in more beads stuck at that location and a lower ensemble MSD. This highlights the crucial nature of having a robust, uniform sensing surface to maximum assay sensitivity and repeatability.

We also investigated if different slide manipulations would influence assay performance. In one version, we combined the settling-under-gravity mechanism with diffusion-based sensing: the slide was inverted to allow weakly-held beads to fall off under their own weight and the beads remaining on the surface were filmed. The second column in Figure 5-8 shows the ensemble average MSD versus time for this inverted slide orientation. This version of the assay shows consistent sensitivity, with the 0.01 ng/mL MSD curve distinguishable from the 0.00 ng/mL curve in all four locations. Additionally, the magnitude of bead motion for each mannan concentration is more consistent across the slide, suggesting that most of the variation in MSD magnitude comes from freely-diffusing beads. Overall, these results show that using gravity to remove freely diffusing and weakly bound beads decreases background and reveals constrained residual bead motion that is proportional to analyte concentration.

While this inverted orientation shows better performance than the upright orientation, from a user experience perspective, it introduces a manual step that could introduce error into the assay process. The slide must be inverted carefully so as to not drop or otherwise strongly disturb the beads on the surface. It also introduces complications for device design, as any air introduced into the device could result in bubbles that displace beads as they travel to the sensing surface after slide inversion. Due to these factors, though we continued inversion in subsequent experiments, we did not pursue it further for assay demonstration using a clinically relevant analyte (Chapter 7).

5.3.4 Bead concentration and antifouling coating are influential factors for assay sensitivity

We repeated the assay described in Figure 5-6 using the same procedure but different bead conditions in order to examine the influence of PEG antifouling coatings and

bead concentration on assay performance.

Effect of PEG molecular weight (MW) and brush thickness

Previous studies suggest that thicker PEG layers on beads are better at resisting fouling, though most of these studies examined proteins adsorbing to beads [54, 55]. One study examining bead-surface interactions found that there was an optimal PEG molecular weight for NSB mitigation, beyond which performance decreased [64]. We tested the influence of the PEG antifouling layer on 4.5 μm beads by comparing coating with FcMBL-PEG(2k) and FcMBL-PEG(10k). At the conditions used during bead functionalization, the theoretical length of the PEG brush coating is 12 and 60 nm, for PEG(2k) and PEG(10k) respectively (Table 3.2).

Figure 5-9 shows ensemble MSD versus time for an experiment using 1 million FcMBL-PEG(10k) beads. Compared to the same slide orientation in Figure 5-8, it is evident that assays using PEG(10k) beads have similar sensitivity to assays using PEG(2k), and also show inconsistent MSD for 0.00 ng/mL and 0.01 ng/mL along the length of the chamber. In the locations at which MSD follows the expected trend (3.6 mm and 7.2 mm), the separation between the 0.00 ng/mL and 0.01 ng/mL MSD curves is greater, suggesting that the thicker PEG(10k) brush may mitigate NSB binding better than PEG(2k). However, it is difficult to draw conclusions given the other two locations show poorer performance. Notable, however, is that the magnitude of MSD curves for concentrations >0.01 ng/mL is relatively similar to the corresponding locations in Figure 5-8, suggesting that PEG size has less of an influence on bead motion than the local surface conditions.

In the inverted orientation (Figure 5-9, second row), similar trends in MSD magnitude are observed, with the 0.00 ng/mL condition MSD plateauing between 0.02 and 0.04 μm^2 whether PEG(2k) or PEG(10k) is used. However, the sensitivity of the assay in this orientation is less consistent along the chamber with PEG(10k) beads. Comparing Figure 5-8 and Figure 5-9, there is only one location that shows the expected MSD versus time trend for increasing mannan concentration in the PEG(10k) case (1.8 mm), whereas all locations show the expected trend when using PEG(2k).

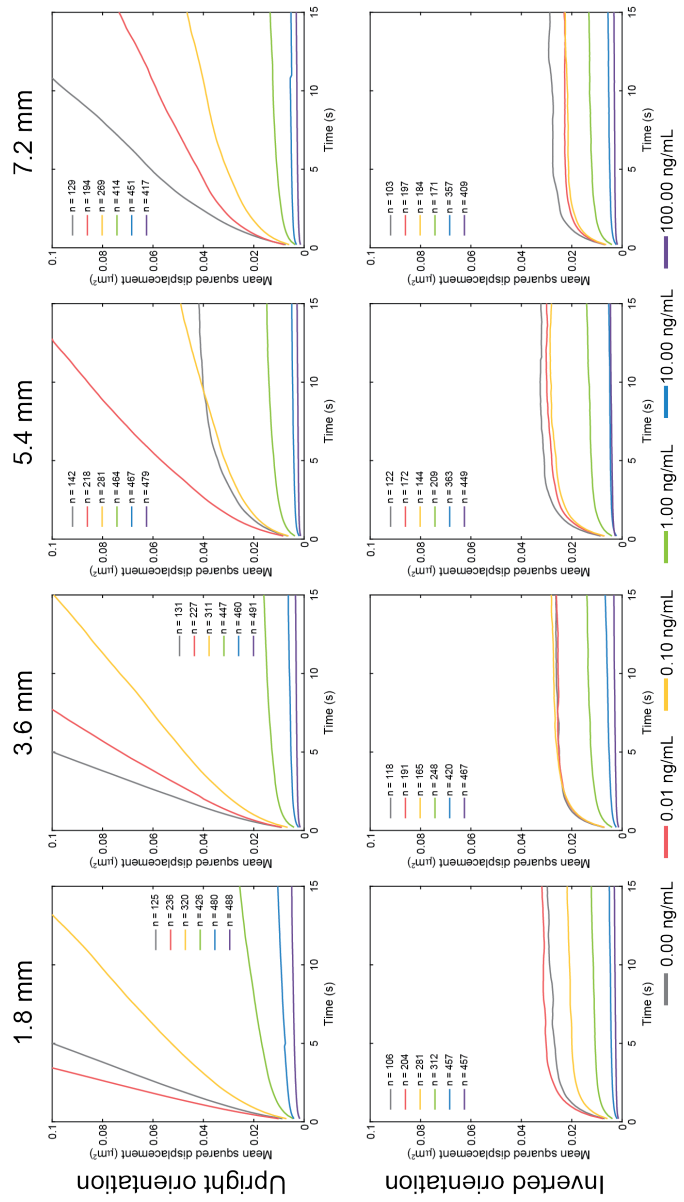

Figure 5-9: **Effect of observation location and slide manipulation on ensemble average MSD during mannan sensing experiments with one million, 4.5 μm PEG(10k), FcMBL-coated beads.** Slide in the upright orientation (first row) and in the inverted orientation (second row)

Using PEG(10k) seems to especially result in less distinguishable motion between 0.01 and 0.1 ng/mL conditions. The thickness of the PEG brush might be at play here, as the predicted brush thickness for PEG(10k) is greater than the length of FcMBL (estimated to be on the order of an IgG antibody, ∼10 nm [146, 147]). The estimated length of the PEG(2k) brush is around the length of the FcMBL and may leave more sites accessible for binding.

Taken together, utilizing PEG(10k) does not seem to impart appreciable improvements to the assay and seems to hinder its performance in some cases. These results are similar to those reported in the aforementioned study on PEG molecular weight in bead-surface interactions [64], which found optimal PEG antifouling effects when using MWs from 2-5 kDa.

Effect of bead concentration

Modulating bead concentration during analyte capture controls the number of bound analytes per bead, which changes the number of analytes in the bead-surface contact area and subsequently controls bead motion. To examine the effect of bead concentration, we used 10x less beads in the same capture conditions. Theory predicts ∼1.25x more analytes per bead when using 100,000 beads than when using one million beads.

Results using 100,000 FcMBL-PEG(2k) beads are shown in Figure 5-10. In the upright orientation, two out of three video locations have clear separation between the 0.00 ng/mL and 0.01 ng/mL MSD curves. This suggests that the number of analytes per bead controls assay sensitivity; if the FcMBL affinity was more influential, we would expect to see curves similar to those in Figure 5-8. Results also suggest that there is a larger fraction of beads that are confined when using 100,000 beads compared with 1 million beads, which follows from beads having a higher bound mannan density when less beads are used.

However, in the inverted orientation, using 100,000 beads results in a less sensitive assay than when using 1 million beads, with 0.01 and 0.1 ng/mL being indistinguishable from 0.00 ng/mL in some cases. The magnitude of the overall constrained motion is smaller when using less beads, with all curves plateauing at 0.2 μm^2 MSD or lower

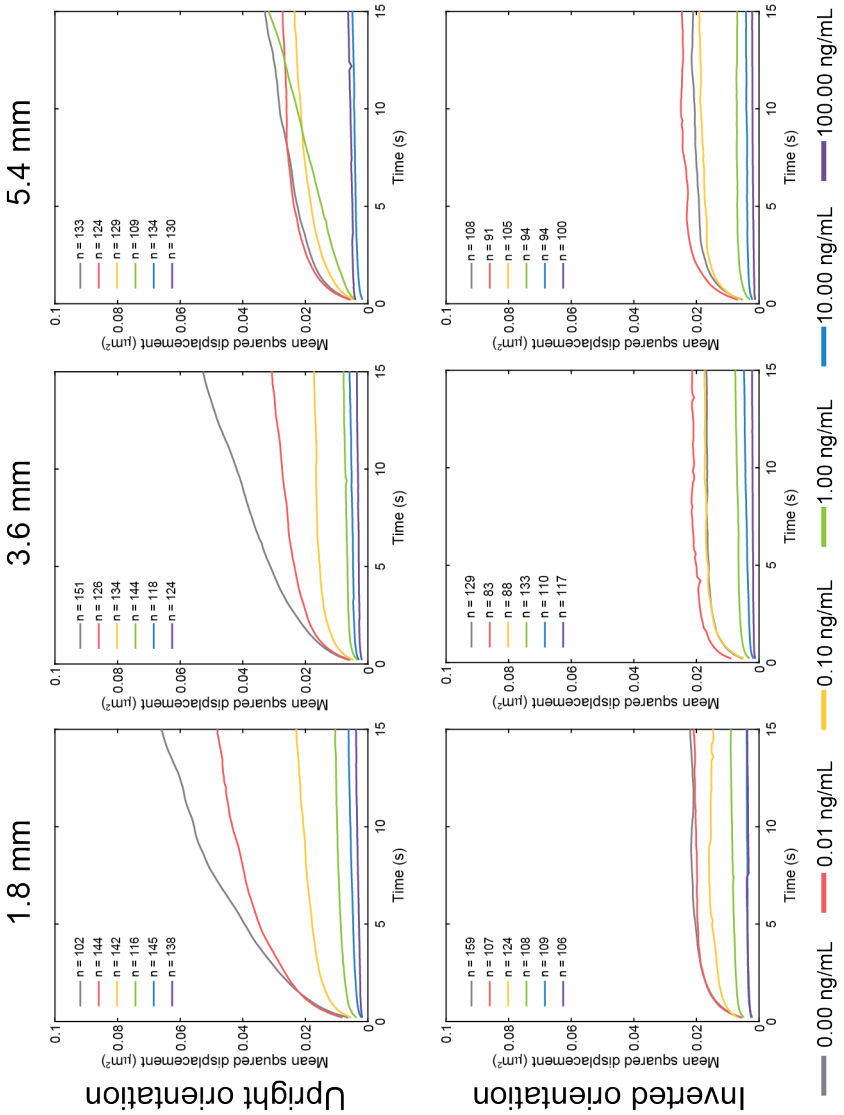

Figure 5-10: **Effect of observation location and slide manipulation on ensemble average MSD during mannan sensing experiments with one hundred thousand, 4.5 μm PEG(2k), FcMBL-coated beads.**

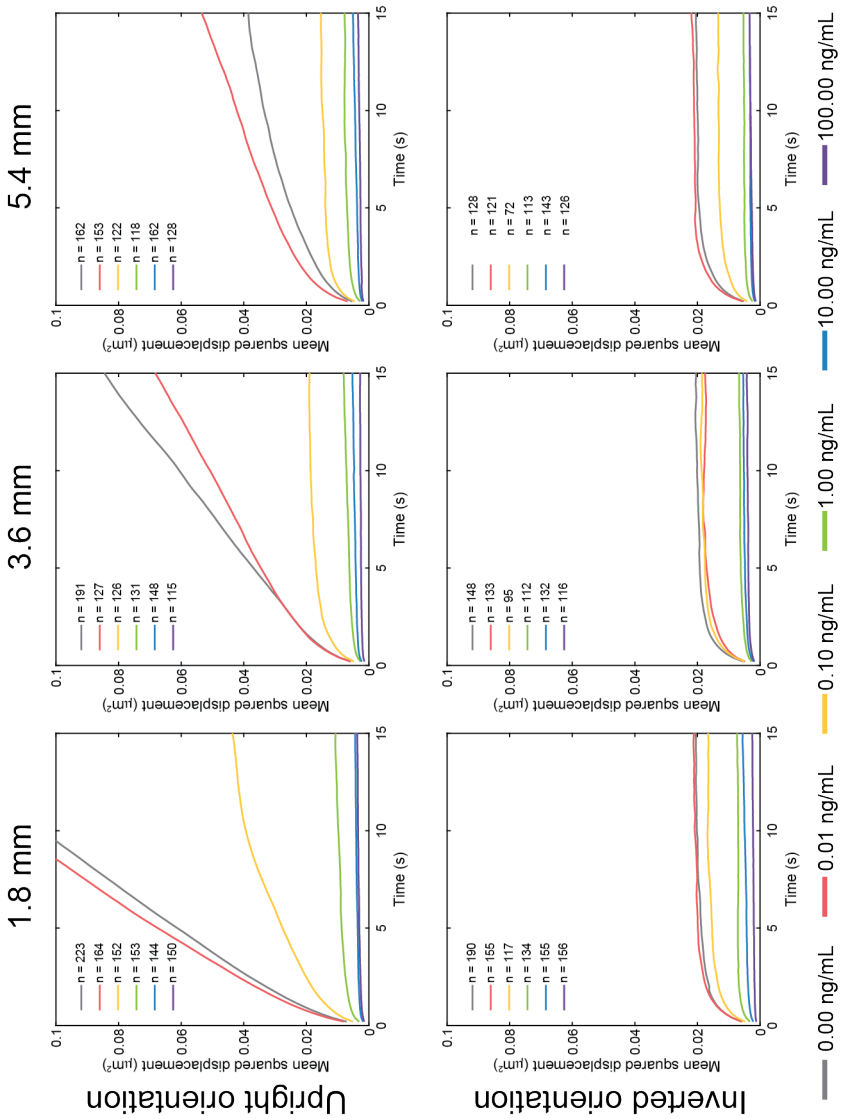

Figure 5-11: **Effect of observation location and slide manipulation on ensemble average MSD during mannan sensing experiments with one hundred thousand, 4.5 μm PEG(10k), FcMBL-coated beads.**

(as opposed to the more spread-out behavior seen with 1 million beads in Figure 5-8). This could be a direct result of higher bound analyte density per bead in the 100,000 bead case, which would result in more constrained motion and more tightly held beads remaining on the surface after slide inversion, than in the 1 million bead condition for the same mannan concentration. An experiment with 100,000 FcMBL-PEG(10k) beads was less conclusive, showing anomalous performance across all locations in both the upright and inverted orientation (Figure 5-11).

Overall, these experiments suggest that there is minimum number of tethers required to noticeably constrain the motion of a single bead and obtaining this minimum can be modulated by the bead concentration. Tuning bead concentration will, therefore, be crucial for obtaining an assay with optimized sensitivity.

5.3.5 Different measures of bead motion yield more sensitive metrics for analyte concentration

Though we have thus far presented the experimental data in terms of MSD, video microscopy yields data that can be analyzed in multiple ways, some of which may be more sensitive for quantification than MSD. In what follows, we present several alternate metrics and discuss their efficacy for a quantitative bead-based diffusion assay. Unless otherwise mentioned, we use the data presented in Figure 5-6 (1 million, 4.5 μm Fc-MBL-PEG(2k) beads at the 1.8 mm location with the slide in the upright orientation) to illustrate these metrics. Because of limited replicates, we do not calculate limit of detection (LOD) by these metrics here, but show their potential. We do explore calculating LOD by these metrics in the clinically relevant assay discussed in Chapter 7.

Bead count-based: Fraction of single beads by concentration

The previously-presented MSD versus time plots included data from only single beads and the number of single beads n that made up the ensemble average for each concentration is included in each plot. Examination of these numbers shows that the

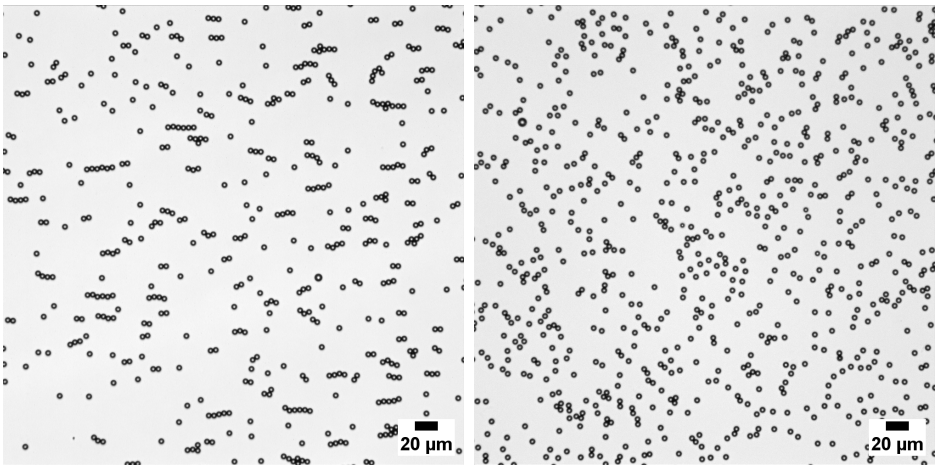

(a) (b)

Figure 5-12: **Bead clumping differs with mannan concentration.** a) In the 0.00 ng/mL mannan condition, beads are observed to clump or chain partly due to the tendency of bends agglomerate during free diffusion or due to bead-bead interactions. (b) In the 10.00 ng/mL mannan condition, beads remain single and stuck to the surface.

number of single beads generally increases with increasing concentration for both slide orientations.

Images also reveal that increasing the mannan concentration decreased the number of beads in clumps (Figure 5-12) One contributing factor is that freely diffusing beads tend to clump over time. In lower mannan concentration conditions, where there are more beads that move freely, more clumping is observed with time. This is an important consideration to take into account in assay design, as waiting too long to start bead observation could lead to filtering out of fast-moving beads in image analysis due to clumping. This could be mitigated by tuning bead concentration and the time at which the bead-surface interactions are observed, or by observing bead motion as beads settle to the surface.

Based on this observation, we tried using the fraction of beads that are free and the fraction of beads that are clumped as a quantification metric. However, none of these plots yielded a trend with concentration in this set of experiments. This metric is revisited in Chapter 7.

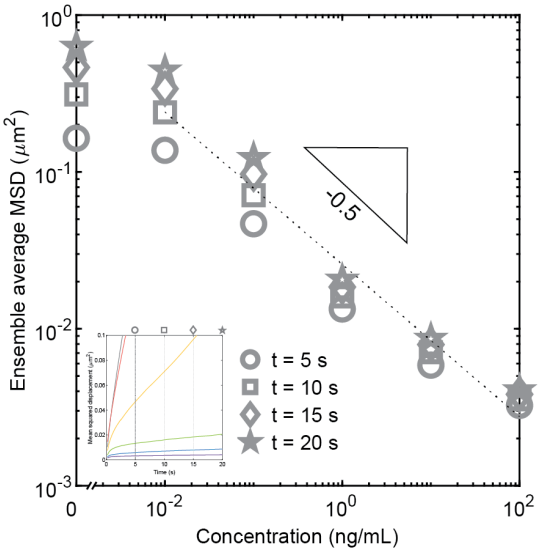

Figure 5-13: **MSD at different times can differentiate between mannan concentrations.** For each mannan concentration in Figure 5-6a, ensemble average MSD at 5, 10, 15 and 20 s is plotted. On this log-log plot, the slope of this relationship is -0.5, suggesting an MSD $\sim$concentration$^{-\frac{1}{2}}$. Higher concentrations have similar MSD values at the times examined, whereas lower concentrations show more spread. This plot reinforces the sensitivity of $\sim$0.1 ng/mL, as the linear relationship breaks down between the 0.00 and 0.01 ng/mL concentrations.

MSD-based: Evaluating MSD at different time intervals

MSD is a measure of how far beads travel after a specific time interval and decreases as analyte concentration increases and there are more tethered beads. For each mannan concentration, the ensemble MSD value at different times was extracted from the curves in Figure 5-6a and plotted in Figure 5-13, resulting in a linear relationship on a log-log scale for concentrations 0.01 – 100 ng/mL with a slope of roughly 0.5. This relationship holds for MSD extracted at various times from 5 – 20 s. For concentrations >0.1 ng/mL, the MSD at each time shows less spread, evident of the consistent constrained motion which already plateaus at 5 s. For concentrations less than 0.1 ng/mL, there is more spread in the MSD at each time, indicative of more freely-diffusing motion and the variability that this imparts in the average measure. The aforementioned estimated sensitivity of the assay is clear from this plot, as the linear relationship breaks down between 0.00 ng/mL and 0.01 ng/mL.

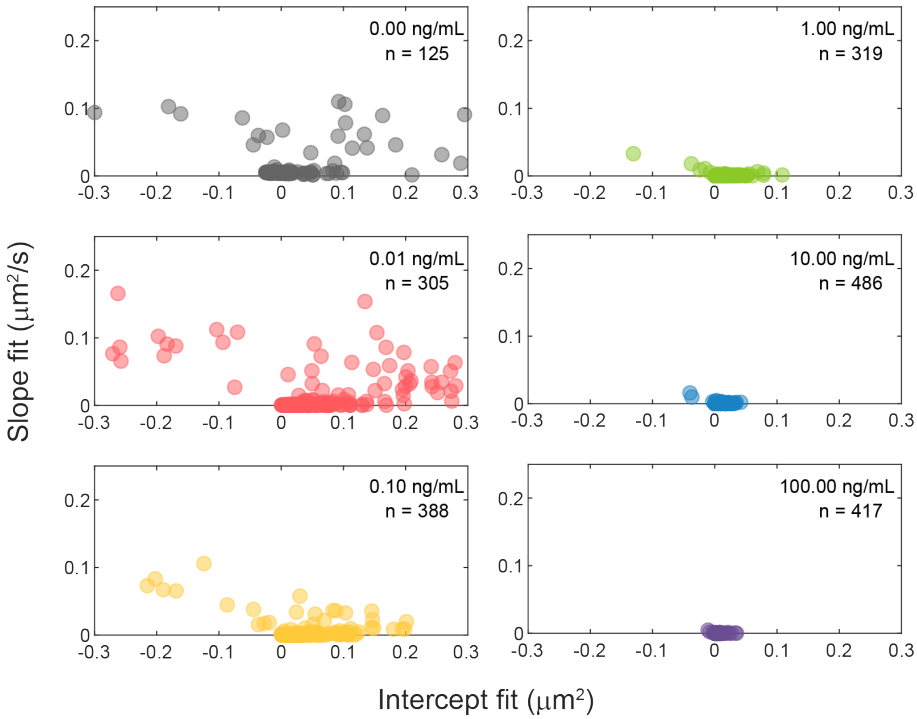

Figure 5-14: **Concentration differentiation based on fitting linear models to MSD curves in the experiment shown in Figure 5-6.** For each bead in each concentration, a linear model in the form of $y = mx + b$ was fitted to the MSD versus time curve. The fitted slope and intercept for each bead, plotted for each concentration, shows the spread of the two parameters, both of which tend towards zero as mannan concentration increases and reflect an increase in the stuck or confined behavior of beads when greater amount of analyte is present.

MSD-based: Fitting linear models to individual bead time average MSD curves to yield slopes and intercepts characteristic of bead motion

After excluding the first two seconds of data, a linear model in the form of $y = mx + b$ is fit to each individual bead time average MSD curve in each concentration. This results in a fitted slope (the diffusivity [μm^2/s]) and intercept (μm^2) for each bead. The rationale behind this metric comes from observations of the individual bead MSD time average plots, in which the shape for some beads indicates a free diffusion region at small time intervals, followed by a constrained/tethered diffusion region at longer times (i.e., there is a shoulder region).

When these fitted parameters are plotted for each bead by concentration, several observations can be made (Figure 5-14). First, as the mannan concentration increases,

both the slope and the intercept tend towards zero, indicating the increasing stuck nature of beads. Second, in the lower concentration conditions, some beads have negative intercepts, which could result if there is active transport (as opposed to thermal diffusion alone). Though our image processing algorithm removes motion by bulk fluid motion or instrument drift, it does not account for local active transport, which would influence beads on an individual level and could make the algorithm more computationally intensive. One method of correcting for this motion could be to fit each individual bead MSD versus time curve with an equation including a quadratic term which accounts for active transport, and subsequently subtracting this term. We have not implemented this in the current analysis and despite the presence of some actively transported beads (less than 5% of total observed beads), using sufficient beads allows for mean metrics that are not heavily influenced by the presence of these few outliers. However, this is an area that warrants future investigation from both an experimental and algorithmic perspective.

This fitted slope and intercept for each bead can be used in several ways to quantify concentration. First, when the mean slope and mean intercept for each concentration are plotted against each other, a roughly linear relationship is observed (Figure 5-15a). The 0.00 ng/mL is an outlier from this trend due to the average slope being negative, which suggests more beads influenced by local active transport in this condition. Unfortunately, aside from the example shown, other locations did not show a relationship between these two average measures.

As noted in the above discussion about Figure 5-14, as mannan concentration increases, both the slope and intercept of each individual bead tends towards (0, 0), making this a natural choice as a reference point on which to base a metric. For each (intercept, slope) pair, the Euclidean distance from the (0, 0) reference point was calculated and subsequently averaged over all beads. When this average metric is plotted versus concentration, a power law relationship is revealed (Figure 5-15b). For the 1 million FcMBL-PEG(2k) bead experiment, all video locations, as well as those in the inverted orientation, show this trend (Figure 5-15c), even if the MSD versus time plot did not follow the expected trend. The power law has a slightly different

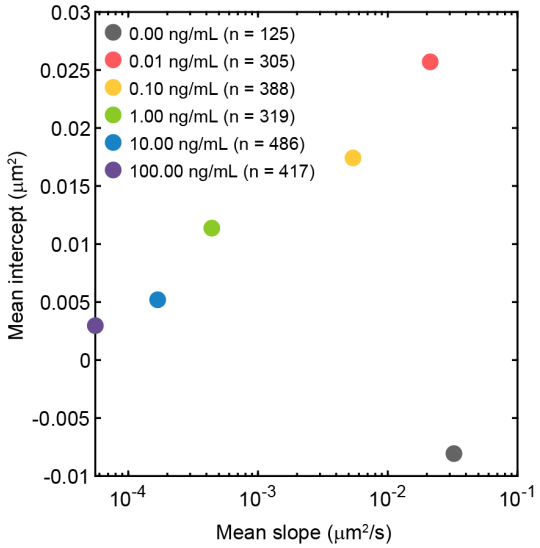

(a)

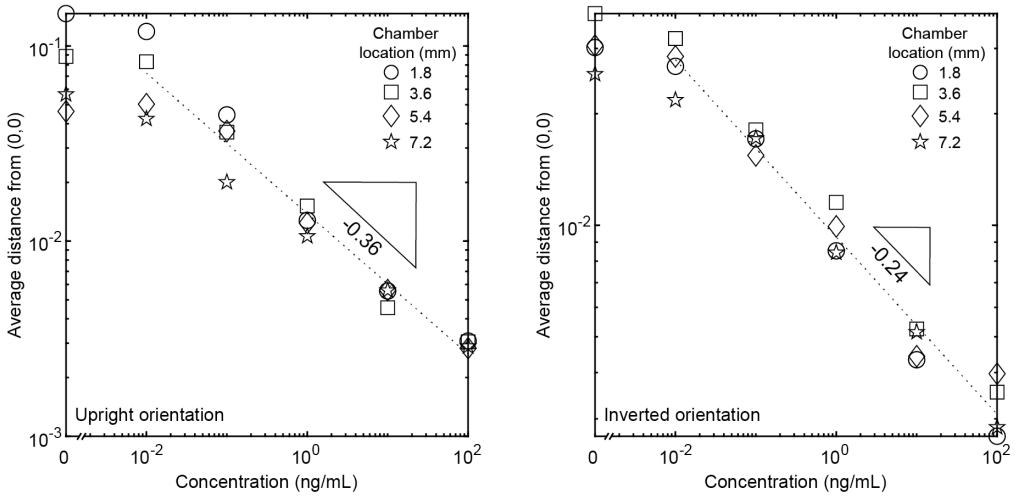

(b) (c)

Figure 5-15: **Fitted slope-intercept quantification metrics for experiment in Figures 5-6.** (a) Mean intercept versus mean slope parameterized by concentration. The relationship between the two fitted mean parameters is roughly linear on a semilog plot, but the 0.00 ng/mL differs from this trend, due to the mean intercept being negative. Negative intercepts could be caused by beads showing active transport; though our algorithm subtracts out common drift, local factors could influence bead motion. (b and c) Average distance of points from (0,0) versus concentration. From the 2D plot in Figure 5-14, the Euclidean distance from (0,0) was calculated. When the average of this distance parameter is plotted versus concentration on a loglog plot, a linear relationship is revealed. This linearity holds when the slide is in both the upright (b) or inverted (c) position and for all video locations in the chamber.

exponent for the upright and inverted slide orientation, potentially indicative of a difference in the motion shown by the majority of beads in each slide orientation.

Bead trajectory-based: Using the geometry of bead positions during the video

As shown in Figure 5-4, the trajectory of each individual bead can be evaluated by extracting its coordinates in each video frame. Several different methods can be used to quantify the extent of this trajectory and may be a method to quantify concentration, since the trajectory of beads becomes more confined with increasing mannan concentration.

When the enclosing radius is plotted in a histogram for each concentration, it is clear that this metric decreases with increasing concentration, matching the previous observation that more beads become confined with increasing mannan concentration (Figure 5-16a). There are a few outlier beads in each concentration, which show greater enclosing radius than the majority, as shown by the right-skewed tail of the distribution. When the mean enclosing radius is plotted against the concentration (Figure 5-16b), an approximately linear relationship is revealed, suggesting that, with additional replicates, this metric may be suitable for concentration quantification.

Another method of quantifying the bead trajectories is to determine the maximum travel of the bead, which is the maximum distance between the starting position and the position of the bead throughout the observation period. When plotted in a histogram for each concentration, this parameter shows a similar distribution as the enclosing radius, but with a magnitude that is slightly greater (Figure 5-17a). Plotting the mean maximum travel against the concentration (Figure 5-17b) again shows an approximately linear relationship that warrants exploration in experiments with additional replicates.

What is the subtle difference between these two measures? Enclosing radius is a measure of the entirety of the bead motion, whereas the maximum travel represents the furthest extent of bead travel. The difference in the two measures is most evident for beads that are temporarily confined; such a bead may move significantly at some

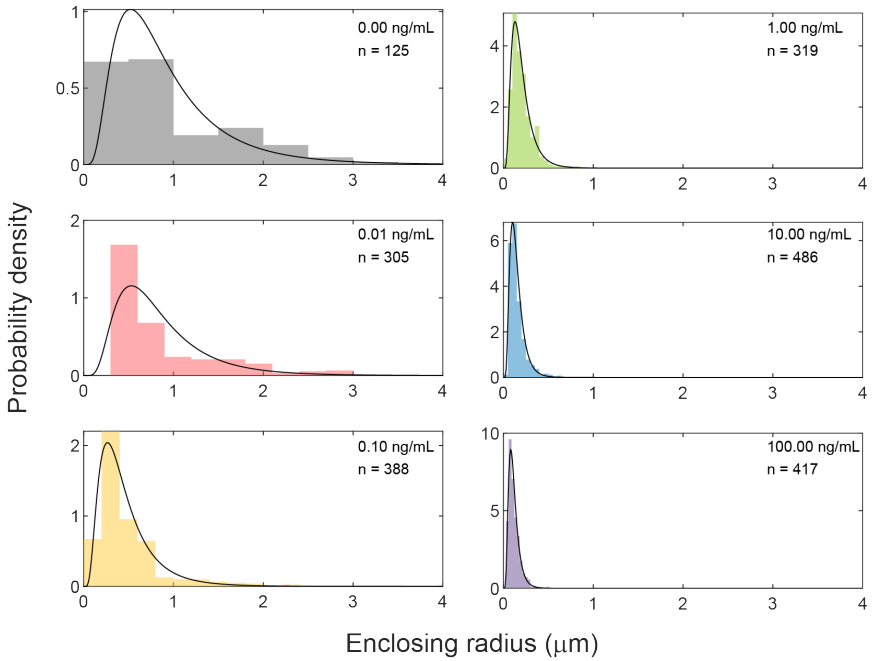

(a)

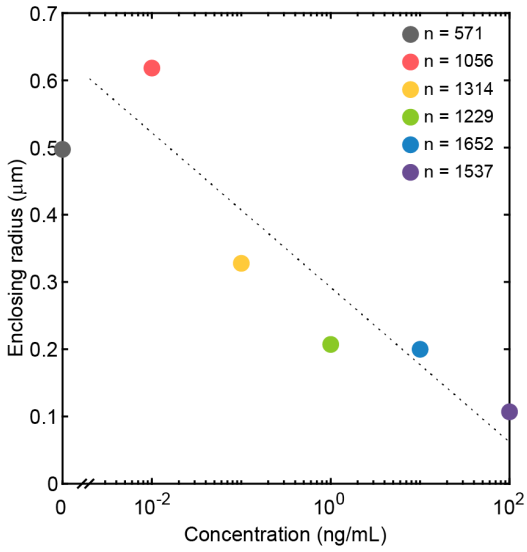

(b)

Figure 5-16: **Concentration differentiation based on enclosing radius of bead trajectories, from the experiment shown in Figure 5-6.** (a) For each bead in each concentration, the radius of the circle which encloses all positions over the frames is plotted in a histogram. It is evident that the average and standard deviation of this radius decreases as mannan concentration increases. Black lines are lognormal distribution fits to the data. (b) Plotting the average enclosing radius versus mannan concentration reveals an approximately linear relationship on a semilog plot.

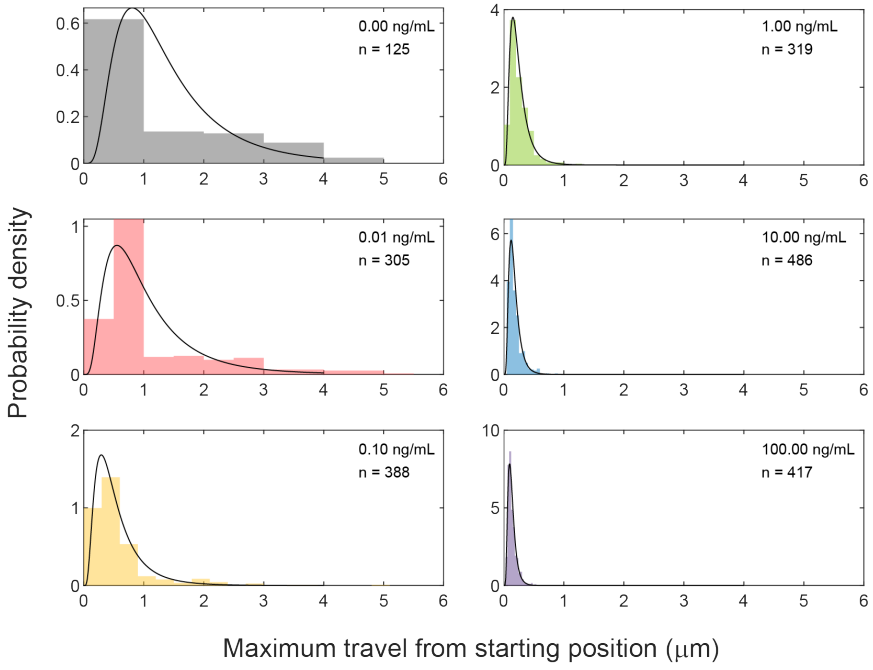

(a)

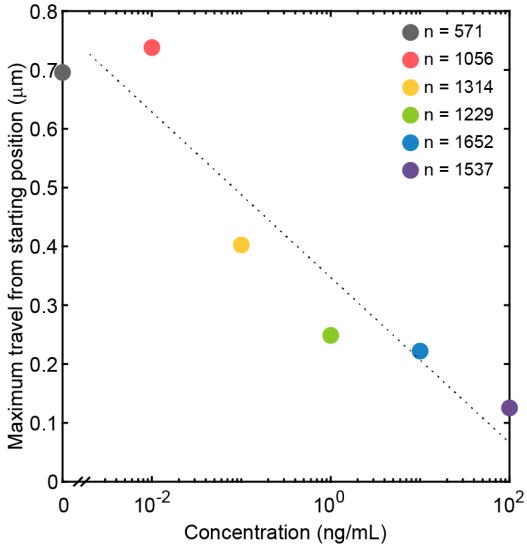

(b)

Figure 5-17: **Concentration differentiation based on maximum travel of beads from their starting position, from the experiment shown in Figure 5-6.** (a) The maximum travel reflects the extent the bead movement beyond its starting position and could be different from the enclosing radius, especially for beads that were temporarily confined. Histograms reveal that this parameter has a similar distribution as the enclosing radius, but has greater overall values. The maximum travel also decreases with increasing mannan concentration. Black lines are lognormal distribution fits to the data. (b) Plotting the average maximum travel versus mannan concentration from (a) reveals an approximately linear relationship on a semilog scale.

point during the observation period but get stuck in a position that is closer to the starting point. In this case, the maximum travel would reflect this translation but the enclosing radius might not capture the extent of the bead's motion.

5.3.6 Integrated capture-while-settling + diffusion assay with the FcMBL-mannan model system suggests efficacy of the platform as a decentralized bioanalytical tool

To demonstrate the potential of combining capture-while-settling with bead diffusion quantification as an integrated bioassay, we used wells on glass slide as miniature devices in which the entire assay can be performed (Figure 5-2b). FcMBL-PEG(2k)-functionalized 4.5 μm beads settle through a 6 mm column of buffer with a certain mannan concentration and land on a FcMBL-functionalized surface. The bead motion on this surface was monitored via video microscopy as in the previous experiments with the chambered slide. Based on the capture model described initially in this section, using a concentration of one million beads/mL, this should result in 8% of mannan molecules bound in the 20 min settling period.

Figure 5-18a shows the results of this initial experiment, which validate that the integrated assay can differentiate between different mannan concentrations. Quantifying bead motion by MSD suggests this format has ~10x less sensitivity than the chambered slide format previously presented, as the 1.00 ng/mL curve is the first curve that can be readily distinguished from the 0.00 ng/mL condition. 1.00 ng/mL is the concentration around which there is predicted to be 1 mannan molecule per instantaneous contact area. Signals from concentrations below this could be subject to time fluctuations in tethering due to an analyte being present in the bead-surface contact area only a fraction of the observation time. Increasing the signal from beads at lower mannan concentrations could be accomplished by using a lower bead concentration, a longer capture time or a higher affinity antibody. The first two aspects are easier to modify through changes in the assay procedure.

To examine if decreasing bead concentration could increase assay sensitivity, we

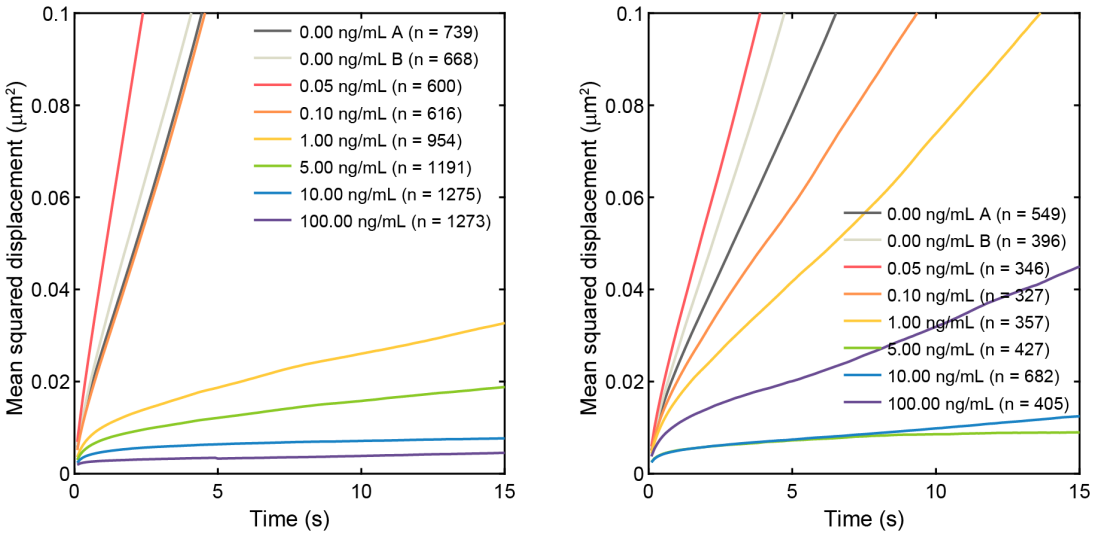

(a) (b)

Figure 5-18: **Integrated capture-while-settling and bead diffusion assay using the FcMBL-mannan model system.** (a) Settling experiment utilizing 1 million beads/mL shows efficacy but with ∼10x less sensitivity compared to the chambered assay. MSD curves of 0.05 and 0.10 ng/mL are indistinguishable from the 0.00 ng/mL condition, suggesting that not enough analytes are bound on a per bead basis to effectively tether the bead at these two lower concentrations, which agrees with theoretical calculations. (b) Using 100,000 beads/mL leads to better differentiation at lower concentrations.

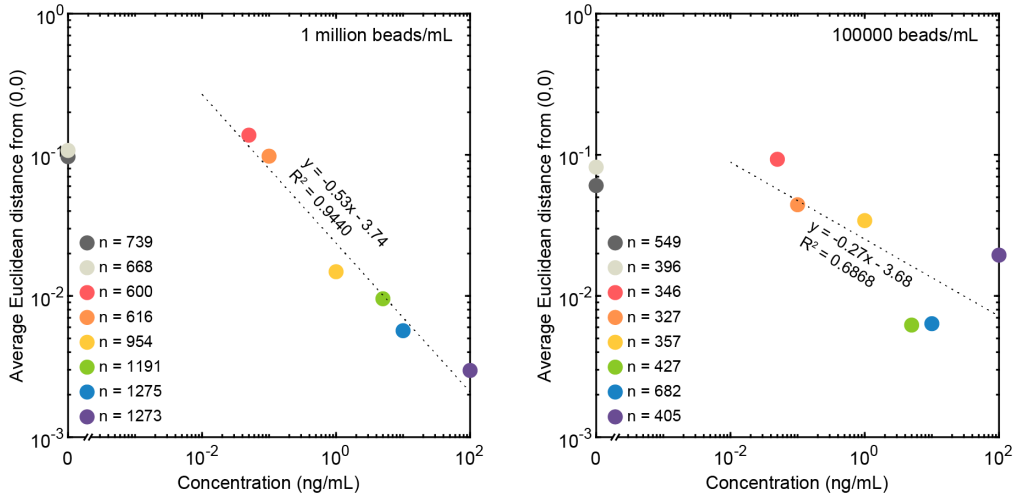

(a) (b)

Figure 5-19: **Quantification metrics applied to FcMBL-mannan integrated assay.** Average Euclidean distance from (0,0) datum for slope/intercept fits from 1 million/mL (a) and 100k/mL (b) experiment.

also performed an experiment with a bead concentration of 100,000/mL. The MSD versus time plot in Figure 5-18b shows that using this lower bead concentration results in 0.1 ng/mL being the lowest concentration distinguishable from 0.00 ng/mL. The higher concentrations are less distinguishable in this experiment, suggesting a trade-off between bead concentration and dynamic range. However, the results at higher mannan concentrations are also anomalous, making it difficult to draw conclusions about observed trends at these conditions. These results provide further evidence that assay sensitivity is controlled mainly by bound analyte density and suggest that assay conditions (incubation time and bead concentration, among others) should be finely tuned to attain the highest sensitivity.

When the average slope-intercept Euclidean distance from (0,0) for all beads in a concentration trial is plotted versus the concentration, a power law relationship is observed in both iterations (Figures 5-19a and 5-19b), with a more robust correlation observed in the 1 million/mL bead experiment (correlation coefficient >0.9). The lowest concentrations in this condition follow this trend and can be differentiated from one another, suggesting that this metric may be more sensitive for quantification.

Duplicate 0.00 ng/mL blank conditions were included in each assay iteration to examine the consistency of bead background and NSB across different wells on the same sensing surface. Duplicates in the 1 million bead/mL condition were consistent, as shown by the similar metric values for both replicates in Figure 5-19a. Duplicates in the 100,000 bead/mL condition show more difference. As the beads used in each experiment were the same, the sensing surface is likely to be the cause of these discrepancies. The same slide was used for both experiments, with the 1 million beads/mL and the 100,000 beads/mL experiments taking place in the upper and lower row of eight wells, respectively (Figure 5-2b). Heterogeneity in the sensing surface seems to contributing heavily to background signal and NSB, an observation which again points to the importance of sensing surface chemistry on assay performance.

Overall, these experiments preliminarily validate that the capture-while-settling mechanism can be integrated with bead diffusion sensing to create a standalone assay capable of quantifying mannan concentration. The experiments presented here indicate a sensitivity of at least 1 ng/mL mannan, which could be further improved through tuning assay conditions to increase bound analyte surface density and sensing surface chemistry.

Sensing surface chemistry is often a bottleneck for optimized assay performance. The glass slides currently used in our experiments come pre-functionalized with epoxy groups on a 10-100 nm-thick antifouling polymer coating. Variations in the thickness of this polymer coating and/or epoxy group chemistry could heavily influence assay repeatability and NSB across the slide. Additionally, slide storage conditions could influence the homogeneity of these coatings across the surface. A slide functionalization process established in-house could result in more robust sensing surfaces; however, these investigations were beyond the scope of our current study. It is clear that understanding NSB is crucial to optimizing this assay and selecting mitigation strategies. Our observations from experiments described in this section motivate our theoretical exploration of bead-surface interactions and experiments conducted to characterize the ability of different surface coatings to mitigate NSB, presented in Chapter 6.

Further characterization of local effects that influence bead motion, but are not

due to the surface, are also warranted. A major contributing factor is the local thermal environment, since bead diffusion is proportional to temperature. Heating from microscope illumination during video recording could elevate the temperature in the observation area, leading to increased bead motion. Heating of the fluid could occur quite rapidly due to the small fluid volumes handled in the chambers or wells. Though the chambers and wells were closed to the atmosphere in these experiments to prevent bulk fluid motion, thermal gradients could lead to thermally-induced fluid flow, which could result in local active bead transport. Correcting bead coordinates individually would remove these velocity components but would also be more algorithmically intense, especially when observing large (>1000) bead populations. Future development of the assay should include investigations of thermal homogeneity across the sensing surface and testing the efficacy of individual bead coordinate correction.

5.4 Conclusion

Using a model mannan-FcMBL system, we first validated bead diffusion on a FcMBL-functionalized surface as a quantifiable signal indicative of analyte concentration. Experiments confirm our hypothesis that beads become more constrained in their motion as mannan concentration (and therefore, bound mannnan density on beads) increases. In the chambered format with an upright slide orientation, the assay has a sensitivity of at least 0.1 ng/mL using 1 million FcMBL-PEG(2k) functionalized beads. Based on the range of mannan molecular weights in the literature [141], this is equivalent to at least single pM sensitivity, which is a relevant limit of detection for many bioanalytes. Inverting the slide to remove weakly bound beads reveals constrained bead motion that is proportional to mannan concentration, yielding an assay format that has 10x lower limit of detection but is more sensitive to human error due to manual slide inversion.

Experiments varying the bead concentration suggest that assay sensitivity is determined by bound mannan density as opposed to FcMBL affinity for mannan, as

using a smaller number of beads increased assay limit of detection. Increasing the PEG brush thickness on the bead by incorporating a PEG of higher MW had less of an effect on assay performance. Video location along the chamber also influenced assay sensitivity, emphasizing the importance of a homogenously coated surface on assay repeatability.

Different quantification metrics beyond MSD versus time were explored to investigate if certain measures could differentiate bead motion with greater sensitivity. Of these, the average distance from $(0, 0)$ and geometric measures of bead trajectory show the most promise, with correlations that can be fit by power law or linear models and can differentiate between lower mannan concentrations in some instances. There are many additional metric combinations that could quantify analyte concentration, including combinations of greater than two parameters, and exploration of this space would be warranted during clinical assay development. It is also possible that machine learning techniques could aid in analysis.

Finally, we combined the capture-while-settling mechanism with bead diffusion to test the ability of this integrated format as a stand-alone bioassay without fluidic actuation and utilizing minimal handling steps. Our results in a well format using 1 million beads/mL show that this integrated assay is able to differentiate between mannan concentrations. MSD curves suggest this assay has a slightly elevated limit of detection as compared to the chambered assay. Metrics based on fitted MSD slope and intercept were able to differentiate mannan concentrations robustly, again indicating the efficacy of this parameter for concentration differentiation. Parameters based on bead trajectory geometry were also efficacious. Results for an experiment utilizing 100,000 beads were less conclusive at higher concentrations, but agreed with previous results from chambered slide experiments suggesting that bound analyte density controls assay sensitivity, as 0.1 ng/mL was able to be differentiated from 0.00 ng/mL using this bead concentration. Results from both experiments reiterate the importance of a homogeneous sensing surface on assay repeatability and sensitivity.

Our demonstration of an integrated assay using capture-while-settling and bead motion quantification represents a significant step towards realization of a high-

sensitivity, minimally instrumented bioassay suitable for decentralized settings. The results presented in this chapter builds on previous reports of bead diffusion-based assays [44, 45, 47–50] while significantly differentiating our concept from these previous studies, which utilize off-slide bead-analyte capture, fluidic pumping and microwell-bead confinement. Our results form the basis for investigations into mitigating NSB for increased assay sensitivity (Chapter 6) and for development and demonstration of an assay for a clinically relevant biomarker (Chapter 7).

THIS PAGE INTENTIONALLY LEFT BLANK

Chapter 6

Surface coatings towards minimized nonspecific binding for high sensitivity bioassays

6.1 Introduction

The main barrier to realizing high sensitivity assays is nonspecific binding (NSB). In the context of our assay architecture, NSB occurs due to nonspecific physical and/or chemical interactions between beads and the sensing surface, which causes beads without bound analyte to contribute to the signal (Figure 6-1). This decreases the number of specific interactions that can be reliably detected and increases limit of detection (LOD). In some cases, NSB increases the assay LOD to a level which lacks any clinical or other utility.

The challenge, then, is to decrease NSB to a level that allows for analyte to be quantified at or below the lowest relevant concentration. Understanding the strength of these interactions is crucial to designing surfaces that resist NSB. As highlighted in

Xiaoyu Chen from Professor Xuanhe Zhao's group in the MIT Department of Mechanical Engineering contributed to the experiments investigating hydrogel and polymeric surface coatings to mitigate NSB, described in this chapter.

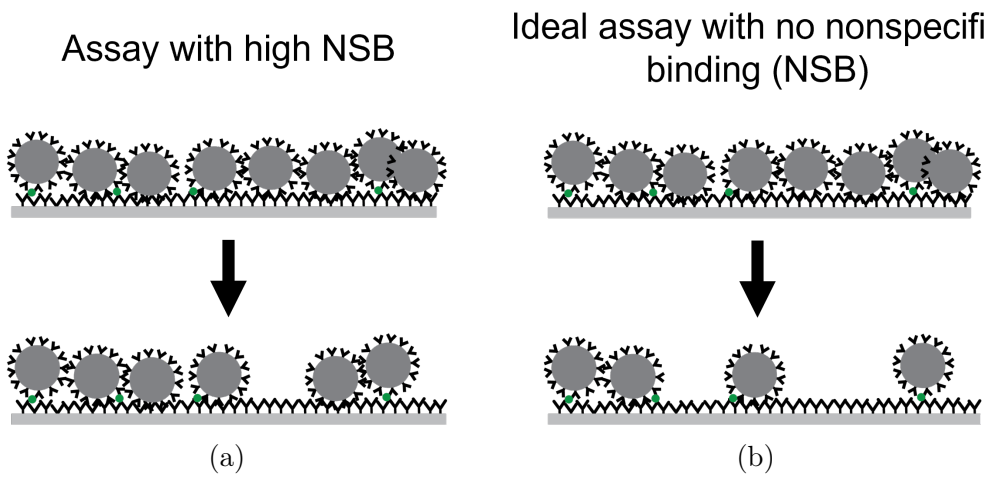

Figure 6-1: **The effect of nonspecific binding (NSB) on bead-based assay sensitivity.** (a) When NSB is high, beads without bound analyte interact with the surface in similar ways as beads with bound analyte and confound the signal. This leads to an increased bead background and limit of detection, decreasing assay utility. (b) When NSB is mitigated, beads without bound analyte are removed or interact with the surface in such a way that they are distinguishable from beads with bound analyte. This decreased bead background allow beads with bound analyte to be accurately and reliably quantified, leading to increased sensitivity.

the introduction, AFM characterization of NSB forces between different molecules and antigen/antibody pairs estimates NSB magnitude to be between 1 – 10 pN [113, 115] but these estimates depend heavily on the identity of the molecules, the geometry and the materials used in the investigation. Few studies have examined NSB forces between beads and surfaces [64, 67], which is inherently different than the interactions between single molecules, due to the large contact area between the bead and the sensing surface, which promotes multivalent binding. Indeed, our results in previous sections show that a fraction of beads without bound analyte can remain adhered to the surface even when perturbed by forces in excess of 100 pN. This is despite bead surfaces being functionalized with hydrophilic, nonfouling molecules, which is a method used in the literature to minimize NSB [64].

This chapter explores the physical basis of NSB towards designing bead and sensing surfaces that can resist these interactions. We first explore the theory behind physical NSB mechanisms to estimate the attractive forces involved when a bead is

nonspecifically bound to a surface. We simulate the addition of different antifouling treatments to determine their theoretical mitigating effect on these attractive forces. To validate model results, we experimentally test these coating materials to identify the most promising strategy for our bead-surface system. Finally, we present results showing the potential of zwitterionic (ZI) coatings to decrease NSB in our bead motion assay and increase the FcMBL-mannan model assay sensitivity. This exploration lays the groundwork for strategies that could be implemented in a clinically relevant assay in samples with high fouling potential.

6.2 Physical theory for nonspecific binding

To investigate the main physical forces involved in NSB between beads and surfaces, we use the basic geometry illustrated in Figure 6-2. A bead of radius R is separated by distance D from the top of a flat surface, both of which are submerged in a liquid medium. The bead is made of material b with relative permittivity ε_b and index of refraction n_b, the surface is made of material s with relative permittivity ε_s and index of refraction n_s, and the medium is of substance m with relative permittivity ε_m and index of refraction n_m. All components are at temperature T. We examine the force between the bead and the surface as D varies; when the overall force is negative, the interaction is attractive, and when the force is positive, the interaction is repulsive. To minimize NSB, we would like to identify strategies in which this interaction force is repulsive (negative) over all D.

In the most basic case, the total force between the bead and the surface (F_{total} (D)) is sum of the van der Waals (vdW) force (F_{vdW}) and the electrostatic force (F_{ES}):

$$F_{total}(D) = F_{vdW}(D) + F_{ES}(D) \tag{6.1}$$

F_{vdW} results from dispersion interactions at the atomic level, which arise from induction of charge polarization in one atom due to the instantaneous dipoles in a neighboring atom [59]. In macroscale structures, such as beads and surfaces, the instantaneous

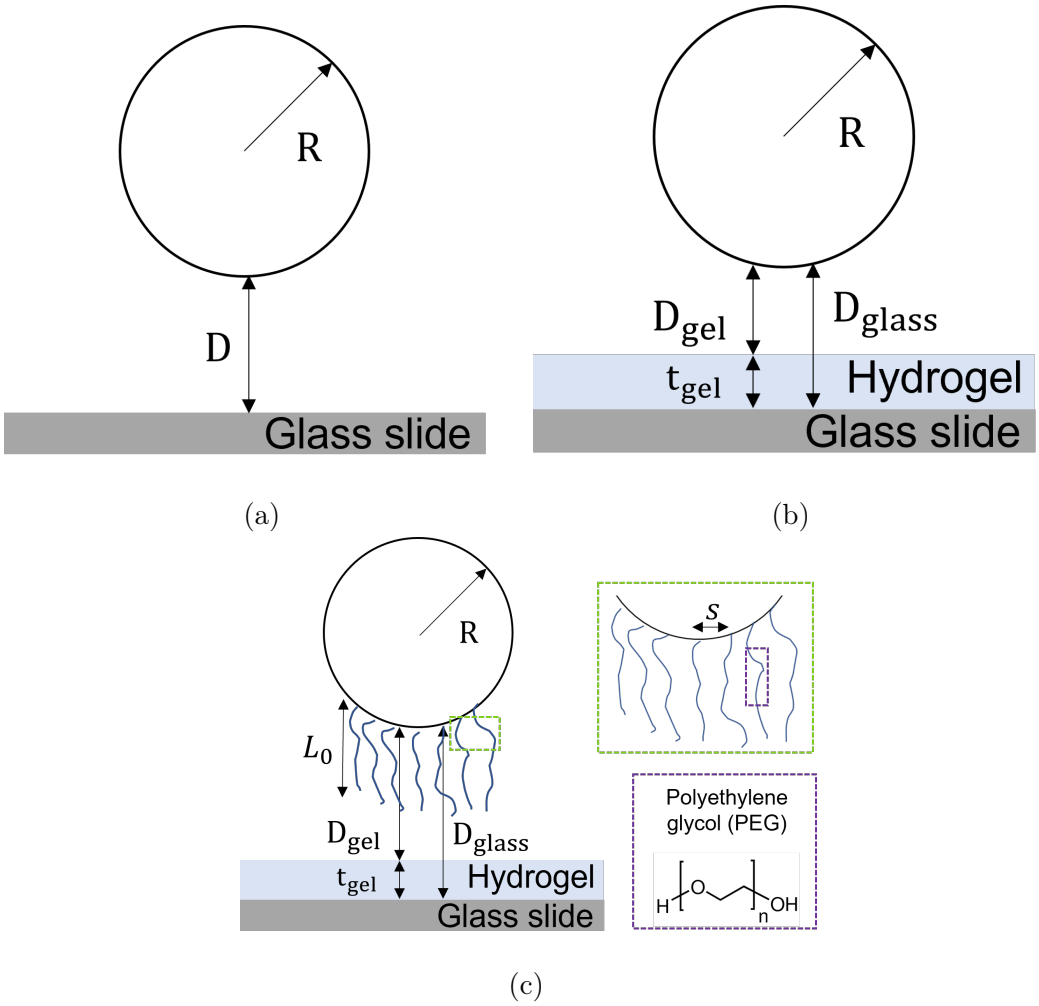

Figure 6-2: **Geometry for modeling the physical basis and mitigation strategies for nonspecific binding.** (a) In the most basic case, a microsphere of radius R and material b and a surface of material s are submerged in medium having relative permittivity ε_m and index of refraction ε_m. The distance from the surface of the sphere to the surface is D. The main force between the bead and the surface is the van der Waals force (F_{vdW}), which is a function of the Hamaker constant A, D and R. (b) A hydrogel of thickness t_{gel} is coated on the surface. This adds another surface which interacts with the bead through a van der Waals interaction, but this interaction is weaker due to lower Hamaker constant. The hydrogel also physically increases the distance between the bead and the glass surface, leading to overall lower attractive force. (c) The bead is grafted with polymer chains of equilibrium length L_0, which is determined by the spacing between polymer chain grafts s. These polymer chains impart a repulsive force between the bead and the surface upon chain compression.

dipole from one atom can affect all other neighboring atoms, resulting in forces that can be significant. F_{ES} comes from surface charges on the flat surface and the bead [57]. We neglect this force in our analysis, since we consider neutral surfaces or surfaces coated with neutral polymer brushes, and its relevance is negligible beyond the Debye length (λ_D):

$$\lambda_D = \frac{1}{\kappa} = \left(\frac{\varepsilon_r \varepsilon_0 k_B T}{e^2 \sum_i c_i z_i^2} \right)^{\frac{1}{2}} \tag{6.2}$$

where ε_r is the relatively permittivity, ε_0 is the permittivity of a vaccum, k_B is the Boltmann constant, e is the elementary charge, c_i is the concentration of ion i and z_i is the valency of ion i. In physiological buffer, λ_D ~0.7 nanometer (nm). The nature of F_{ES} is highly dependent upon the surface charge density, which is not precisely known for our system. Thus, our analysis considers only F_{vdW} (Figure 6-2a):

$$F_{total}(D) = F_{vdw}(D) \tag{6.3}$$

When the distance between the bead and the surface is small ($D \ll r_b$), F_{vdW} takes the following form:

$$F_{vdW}(D) = -\frac{A r_b}{6D^2} \tag{6.4}$$

where A is the Hamaker constant (in joules [J]), which characterizes the strength of dispersion forces between macroscopic bodies [59]. Lifshitz theory, a continuum theory, can be used to calculate A for a multi-material macroscopic system based upon the permittivity and index of refraction of the bulk materials [59]. According to this theory, the A is the sum of a zero-frequency term and the frequency dependent term:

$$A = A_{\nu=0} + A_{\nu>0} \tag{6.5}$$

The zero-frequency term is the result of Keesom and Debye forces, which result from interactions between permanent dipoles and permanent and induced dipoles, respectively. The frequency-dependent term comes from interactions between induced dipoles, called the London dispersion force. At $D = 0$, these terms can be calculated

as [68]

$$A_{\nu=0} = \frac{3k_BT}{4}\frac{\varepsilon_b - \varepsilon_m}{\varepsilon_b + \varepsilon_m}\frac{\varepsilon_s - \varepsilon_m}{\varepsilon_s + \varepsilon_m} \tag{6.6}$$

$$A_{\nu>0} = \frac{3h\nu_e}{8\sqrt{2}}\frac{(n_b^2 - n_m^2)(n_s^2 - n_m^2)}{(n_b^2 + n_m^2)^{\frac{1}{2}}(n_s^2 + n_m^2)^{\frac{1}{2}}\left[(n_b^2 + n_m^2)^{\frac{1}{2}} + (n_s^2 + n_m^2)^{\frac{1}{2}}\right]} \tag{6.7}$$

The magnitude of the Hamaker constant varies with D. The frequency dependent term decays with distance from the surface due to retardation effects [59], which result from dipole directional changes during the time it takes the reflected field to return to the atom:

$$A_{\nu>0}(D) = \frac{A_{\nu>0}(0)}{1 + \frac{14D}{100}} \tag{6.8}$$

where D is in nanometers (nm). The zero-frequency term is reduced in the presence of electrolytes, which screen the electric fields that polarize dipoles. The distance over which this screening occurs is equal to the Debye length and the term decays exponentially with increasing surface separation according to

$$A_{\nu=0}(D) = A_{\nu=0}(0)e^{-\kappa D} \tag{6.9}$$

Combining these two effects together, we obtain the total Hamaker constant A:

$$A(D) = \frac{A_{\nu>0}(0)}{1 + \frac{14D}{100}} + A_{\nu=0}(0)e^{-\kappa D} \tag{6.10}$$

where the zero separation distance values are given by Equations 6.6 and 6.7 above.

We investigated two modifications to the basic setup depicted in Figure 6-2. In the first, a hydrogel of thickness t_{gel} coats the surface (Figure 6-2b). The addition of the hydrogel introduces an additional F_{vdW} between the bead and the hydrogel surface [157]:

$$F_{total}(D) = F_{vdW,surf}(D) + F_{vdW,gel}(D) \tag{6.11}$$

where $F_{vdW,surf}$ is the vdW force between the bead and the solid supporting surface of material s and $F_{vdW,gel}$ is the vdW force between the bead and the hydrogel surface.

Each of the forces is calculated according to Equation 6.4 with Hamaker constants A_{surf} and A_{gel}, respectively, calculated by Equation 6.10. When calculating their contributions, we measure D from the outer most surface and the separation distance from the bead to the original surface is modified due to t_{gel}:

$$D = \begin{cases} D + t_{gel} & \text{bead - support surface} \\ D & \text{bead - gel surface} \end{cases} \tag{6.12}$$

which modifies Equation 6.11

$$F_{total}(D) = F_{vdW,surf}(D + t_{gel}) + F_{vdW,gel}(D) \tag{6.13}$$

In the second modification, we introduce a polymer brush grafted to the surface of the bead with equilibrium length L_0, which, when compressed, induces a repulsive force between the bead and the surface, called the steric repulsion force (F_{PSR}; Figure 6-2c) [53, 56]. The literature on grafted polymer brushes is robust, with many different theories and experimental results for specific conditions [53]. For our purposes of gaining insight into the potential NSB mitigation mechanisms, we use the simplest deGennes theory, which takes the monomer concentration to be uniform throughout the brush layer [58]. L_0 is determined by a balance between the osmotic force and the elastic force resulting in

$$L_0 = Na\left(\frac{a^2}{s^2}\right)^{\frac{1}{3}} \tag{6.14}$$

where N is the number of monomers in the polymer chain, calculated as the ratio between the molecular weight of the polymer and the molecular weight of the monomer ($MW_{polymer}/MW_{monomer}$), a is the monomer length, and s is the distance between polymer grafts.

When compared to the Flory radius (R_F) of the chain, given by $R_F = N^{\frac{3}{5}}a$ in a good solvent [134], s determines the conformation of the chain on the surface of the bead. If $s < R_F$, the polymers are grafted close enough that steric effects force them into a brush configuration. In the opposite case, when $s > R_F$, there is enough space

between polymer grafts that the grafts can collapse into themselves and form blobs on the surface of the bead, a configuration known as the mushroom configuration. Grafted polymers should be in the brush configuration for optimal antifouling effects and the above criterion sets an upper bound on s in order to realize these effects [54, 55, 64, 66].

The pressure between a brush-coated bead and a flat surface is [158]

$$P_{PSR}(D) = \frac{k_B T}{2s^3}\left[\left(\frac{L_0}{D}\right)^{\frac{9}{4}} - \left(\frac{D}{L_0}\right)^{\frac{3}{4}}\right] \tag{6.15}$$

which can be integrated over the bead-surface contact area to yield the force

$$F_{PSR}(D) = \frac{4\pi R k_B T L_0}{35s^3}\left[7\left(\frac{L_0}{D}\right)^{\frac{5}{4}} - 5\left(\frac{D}{L_0}\right)^{\frac{7}{4}} - 12\right] \tag{6.16}$$

When combined with the other force components, the total force between a polymer brush-coated bead and a hydrogel coated surface is

$$F_{total}(D) = F_{vdW,surf}(D + t_{gel}) + F_{vdW,gel}(D) + F_{PSR}(D) \tag{6.17}$$

Using these equations, we modeled three different situations:

1. Bare bead interacting with a bare glass surface using Equation 6.3

2. Bare bead interacting with a hydrogel-coated glass surface using Equation 6.11 with different t_{gel}

3. Polymer brush-coated beads, with PEG polymers of different molecular weight and grafting densities, interacting with a hydrogel-coated glass surface using Equation 6.17

Material properties used in the model are shown in Table 6.1 and calculated Hamaker constants at zero separation are shown in Table 6.2.

Table 6.1: **Material properties used in calculations to predict forces between surfaces and beads.**

Material	Index of refraction	Relative permittivity
Water [68]	1.33	78.3
Glass [68]	1.52	6.9
10% PEG gel [159]	1.35	71.5
Silica [68]	1.43	3.8

Table 6.2: **Hamaker constants for different bead-surface systems at zero bead-surface separation.** These constants were calculated using the material properties in Table 6.1 and using Equations 6.6 and 6.7. Systems in rows 1 and 2 were used in modeling; System in row 3 is shown for comparison.

System materials			
Bead material	Surface material	Medium	Hamaker constant A (J)
Silica	Glass	PBS buffer	7.4×10^{-21}
Silica	10% PEG hydrogel	PBS buffer	6.8×10^{-22}
10% PEG hydrogel	10% PEG hydrogel	PBS buffer	1.2×10^{-22}

6.3 Materials and methods

6.3.1 Materials

Glass slides (75 x 25 x 1 millimeter [mm]), bovine serum albumin (BSA), phosphate buffered saline (PBS), 1.5 mL polypropylene microcentrifuge tubes, KimWipes and Parafilm were purchased from VWR, Inc (Radnor, PA). Mannan from *Saccharomyces cerevisiae*, calcium chloride dibasic ($CaCl_2 \cdot 2H_20$), ethanolamine, Tris base, sodium phosphate monobasic (NaH_2PO_4), sodium phosphate dibasic (Na_2HPO_4), Tween 20, 2-[(methacryloyloxy)ethyl] dimethyl-(2-sulfopropy)ammonium hydroxide, N,N'-methylenebisacrylamide, 2-Hydroxy-4'-(2-hydroxyethoxy)-2-methylpropiophenone, (trimethoxy silyl) propyl methacrylate (TMPSM), 1-ethyl-3-[3-dimethylaminopropyl] carbodiimide hydrochloride (EDC) and N-hydroxysuccinimide (NHS) were purchased from MilliporeSigma (Burlington, MA). Dynabeads M-270 and M-450 epoxy magnetic beads (herein referred to as 2.8 and 4.5 micron [μm] beads, respectively), molecular biology grade agarose and ethylenediaminetetraacetic acid (EDTA) were purchased from ThermoFisher Scientific (Waltham, MA). Amine-terminated polyethylene glycol (PEG)

with molecular weight of 2000 or 10000 daltons (referred to subsquently as PEG(2k) or PEG(10k), respectively) were purchased from Nanocs, Inc (New York, NY). 10x Tris-buffered saline with 0.5% Tween 20 (TBST) was purchased from Fisher Scientific (Hampton, NH). A fusion protein affinity agent, combining the human IgG Fc portion and the carbohydrate recognition domain of mannose binding lectin (Fc-MBL) [123] was kindly provided by Michael Super of the Wyss Institute for Biologically Inspired Engineering (Boston, MA).

6.3.2 Evaluation of NSB mitigation using coated surface and PEG-functionalized beads

To experimentally investigate NSB on different surfaces, we examined the diffusive movement of two different bead sizes with two different size PEG grafts on nine different surfaces. Additionally, we conducted the experiments in two different buffers to examine the effects of detergent on NSB.

Beads were coated with PEG(2k) or PEG(10k) using optimized procedures based on the manufacturer's recommended protocol for epoxy chemistry. 4.5 μm beads were incubated with PEG(2k) or PEG(10k) in 0.1 molar (M) sodium phosphate buffer at a concentration for 10 milligrams per square meter (mg/m^2) or 50 mg/m^2 coating density, respectively. Incubation occurred at room temperature for 20 hours (h) with end-over-end mixing at 30 revolutions per minute (rpm) in reciprocating mode. After concentration, beads were resuspended in 50 millimolar (mM) ethanolamine in 0.1 M sodium phosphate buffer and incubated for four hours using the previous mixing conditions. After ethanolamine incubation, beads were concentrated, resuspended in wash buffer (PBS + 2 mM EDTA + 0.1% weight per volume (w/v) BSA) and incubated for 5 minutes (min) with end-over-end mixing. This washing step was performed three times and subsequently, beads were resuspended in wash buffer for storage at 4 degrees Celsius (°C) until use.

2.8 μm beads were incubated with PEG(2k) or PEG(10k) in 0.1 M sodium phosphate buffer at a concentration for 13 mg/m^2 or 65 mg/m^2 coating density,

Table 6.3: **Theoretical PEG graft characteristics used in experiments.**

			2.8 μm beads			4.5 μm beads		
PEG molecular weight (g/mole)	Polymer degree N^{+}	R_F* (nm)	Mass density (mg/m^2)	Density on bead (#/m^2)	Graft spacing (nm)	Mass density (mg/m^2)	Density on bead (#/nm^2)	Graft spacing (nm)
2000	45	3.5	13	3.91	0.57	10	3.01	0.65
10000	227	9.3	65	3.91	0.57	50	3.01	0.65

$^{+}$ $\mathrm{MW_{PEG\ monomer}}$ = 44 g/mol [64]
* Assuming polymer is in a good solvent [134]; a = 0.358 nm [64]

respectively. Incubation occurred at 37°C for 24 h with end-over-end mixing at 30 rpm. After incubation, beads were washed four times with PBS + 0.1% (w/v) BSA and resuspended in the same buffer for storage at 4ºC until use. Theoretical calculations of PEG brush characteristics for both bead sizes are presented in Table 6.3.

Nine different surfaces were fabricated to test the effect of surface coating on NSB between beads and surfaces. Five of nine surfaces used glass slides as the supporting surface and the remaining four used polystyrene Petrie dishes. Description and details about the fabrication of these surfaces are as follows:

- *Bare glass* is a glass slide which was washed three times with ethanol and dried prior to the experiment.

- *BSA* is BSA physisorbed to a glass slide. Glass surfaces were treated with 1% (w/v) BSA in PBS for 30 min at room temperature and subsequently washed 3x with PBS

- *Fluorosilane* involved glass slides were washed with deionized (DI) water for 30 min and were subsequently washed with ethanol for 30 min with sonication. After slides were fully dried, they were treated with oxygen plasma for 30 minutes. 0.2 weight % (wt.%) 1H,1H,2H,2H-perfluorooctyltriethoxysilane in hexane was added to the top of the slides and reacted for 6 h. Slides were subsequently washed with hexane and ethanol and allowed to dry prior to use.

- *Zwitterionic (ZI) coating* is a thin coating of [2-(methacryloyloxy)ethyl] dimethyl-

(2-sulfopropyl)ammonium hydroxide on a glass slide. Glass slides were washed first with DI water for 30 min and were subsequently washed with ethanol for 30 min with sonication. After drying, the slides were treated with oxygen plasma for 30 min. 3 wt.% (trimethoxy silyl)propyl methacrylate (TMPSM) in ethanol was added to the top of the glass slide and allowed to react for 3 hours, after which slides were washed with water and ethanol and fully dried. A mold was placed on top of the slide and an aqeuous solution of 4 wt.% [2-(methacryloyloxy)ethyl] dimethyl-(2-sulfopropyl)ammonium hydroxide, 0.008 wt.% N'N'-methylenebisacrylamide and 0.08 wt.% 2-hydroxy-4'-(2-hydroxyethoxy)-2-methylpropiophenone was added into the mold. Another glass slide was placed of on top of the mold to seal the chamber. Polymerization occurred under 365 nm UV irradiation for four hours. After this reaction, the slide was washed with DI water and stored in wet state until use.

- *Agarose* refers to 1 millimeter-thick gels of various weight percentages (0.5, 1.0, 2.0 or 4.0%) of agarose in 15 mm Petrie dishes. The desired amount of agarose was dispersed in PBS and heated to dissolve. A volume of molten agarose sufficient for 1 mm thick gels was poured into the Petrie dish and allowed to solidify.

Experiments with all bead, surface and buffer combinations followed the same general protocol. Beads were suspended at 1 million per milliliter (mL) in PBS or PBS + Tween 20 0.05% (v/v) (PBST). 200 microliters (μL) of beads was pipetted onto each surface, which was submerged (in the case of surfaces based on the glass slide) or covered (for agarose hydrogels) with the corresponding buffer. Beads were allowed to settle on to the surface and subsequently, video microscopy was used to record the movement of the beads on the surface using a TE2000U inverted microscope (Nikon, Melville, NY) fitted with an Andor iXon3 CCD camera (Oxford Instruments, Abingdon, UK). For both bead sizes, videos were taken for 300 frames at 10 Hz and 0.01s exposure time. For 4.5 um beads, videos were taken at 20x magnification and for 2.8 um beads, videos were taken at both 20x and 40x magnification.

6.3.3 FcMBL-mannan assay on ZI coatings

ZI coatings were synthesized on glass slides as previously described with the addition of 0.1 wt.% acrylic acid monomer to the aqueous reaction mixture to decorate the ZI coating with carboxyl groups for covalent modification. After polymerization of the coating, silicone isolator wells were placed on top of the surface to functionalize discrete areas. In these wells, an aqueous solution of 2 wt.% EDC, 1 wt.% NHS and 0.066 mg/mL FcMBL was added and reacted for 2 hours. Following the reaction, the chamber was rinsed with DI water and stored in the wet state until use.

To test the model mannan-FcMBL assay using ZI-coated glass surfaces, one million 4.5 μm beads previously functionalized with 10 mg/m^2 FcMBL were incubated with 0, 0.05 or 1 ng/mL of mannan in 500 μL TBSTCa for 30 min with end-over-end mixing at 25 rpm. After capture, the beads were concentrated and resuspended in 400 μL TBSTCa. 200 μL of the resuspension was deposited into the silicone isolator well and the beads were allowed to settle onto the ZI-FcMBL surface for 2 min. Videos of six different random areas of the well were taken at 20x for 300 frames using 10 Hz sampling.

6.3.4 Video analysis

Bead diffusive behavior was analyzed using a custom-made MATLAB (MathWorks, Natick, MA) script utilizing functions from the Image Processing Toolbox, as previously described in Chapter 5.

6.4 Results and discussion

6.4.1 F_{vdW} is long-range and attracts beads to the surface even at large separation distances

In the context of our assay, NSB arises due to interactions between the beads and the sensing surface. These interactions can be physical or chemical in nature, and

understanding their magnitude and dependencies on modifiable parameters is crucial for design of nonfouling surfaces. To understand the physical interactions that lead to NSB, we focused on F_{vdW} that develops between surfaces due to instantaneous dipoles from the random movement of electrons in atoms.

Figure 6-3a plots F_{total} between a glass surface and two different sizes of silica beads in PBS. Recalling that an attractive force has a negative magnitude, this graph shows that F_{vdW} is a long-range, highly nonlinear attractive force. At small separation distances (<5 nm), F_{vdW} is hundreds to thousands of times greater than the bead weight under gravity (0.17 and 0.70 pN for 2.8 μm and 4.5 μm beads of density 1.5 g/cm^3, respectively). Our previous results, that beads can remain stuck to the surface even with disruptive forces in excess of 100 pN, make sense in light of this modeling. As shown in the inset plot, the force remains attractive for both bead sizes even at separations of greater than 20 nm and does not fall below -1 pN until a distance of 35 and 44 nm, for 2.8 μm beads and 4.5 μm bead, respectively.

The length of an IgG molecule is around 10 nm [146, 147], so an antibody-functionalized bead that lands on an antibody-functionalized surface will be maximally separated by ~20 nm (assuming that the antibodies behave as rigid extensions). In such a system, which approximates that found in our assay, the above analysis indicates that, without any mitigating treatment, F_{vdW} will attract the beads to the surface and effectively prevent them from moving.

6.4.2 Surface coatings could help to mitigate NSB via increasing the separation distance, decreasing the Hamaker constant and introducing a repulsive force

Examining the parameters on which F_{vdW} depends lead to insights on physical methods that could decrease this attractive force. Equation 6.4 shows that F_{vdW} is linearly dependent on the size of the bead and the Hamaker constant, as well as inversely proportional to D^2. As shown in Figure 6-3a, the magnitude of the attractive force between 2.8 μm beads and the glass surface is smaller than between 4.5 μm beads and

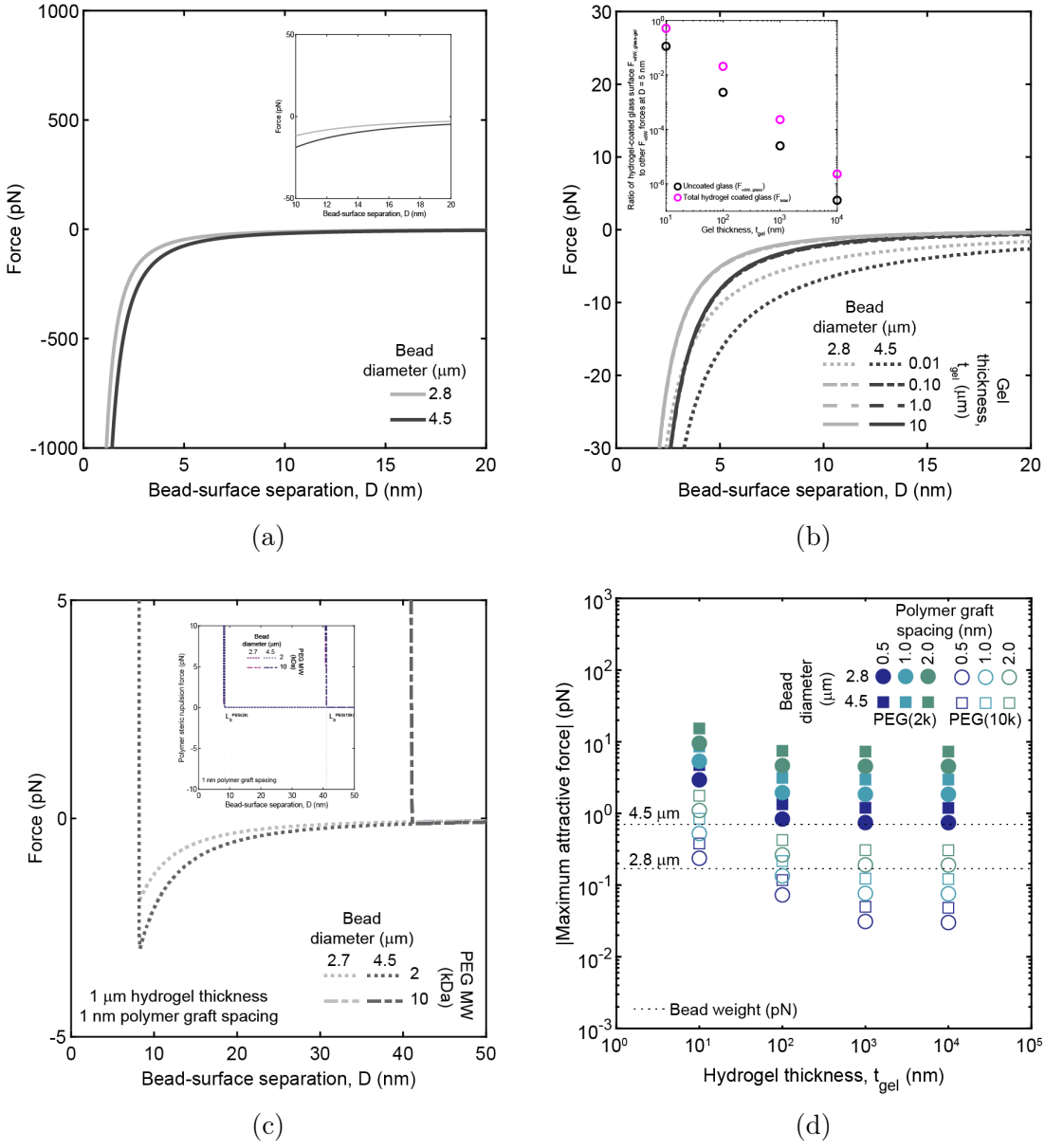

Figure 6-3: **Modeling of physical causes of and mitigation strategies for NSB.** (a) When considering $D > \lambda_D$, the major cause of NSB is the van der Waals force (F_{vdW}). This overall attractive interaction decays slowly, with 10-20 pN of attractive force still existing when the bead is 10 nm away from the surface. (b) Coating the surface physically increases the distance between the surfaces, which decreases the attractive force at least 10 fold. The strength of NSB mitigation increases with increasing t_{gel}. (c) Grafting polymer brushes to the bead further decreases the attraction due to the repulsive force that develops upon brush compression. At the conditions shown in the panel, the force is decreased 200x from the glass-bead only system in (a). The PSR force alone (inset) is zero until the brush contacts the surface at $D = L_0$, at which point it is completely repulsive. (d) The maximum attractive force between a polymer-coated bead and a hydrogel coated glass slide, illustrating the combined effects of a physical hydrogel barrier and PSR on the overall force.

the surface. However for our system, decreasing bead size may require higher-powered microscopy, which would increase the cost and complexity of the system. Additionally, the settling speed of spheres depends on R^2 and utilizing smaller beads would increase the time required to capture analytes during bead settling. We therefore focused on strategies that can lower F_{vdW} through modulation of the Hamaker constant and the separation distance.

As shown in Equations 6.6 and 6.7, the Hamaker constant is a function of the difference between the refractive index and the relative permittivity of the materials used in the system. Systems with materials that have similar properties have lower Hamaker constants. For bioassays, the buffer is usually aqueous in nature, as this ensures the stability and viability of analytes. To decrease F_{vdW} in bead-based bioassays, it is therefore advantageous to use surface materials that are water-based.

Hydrogels are appealing materials for surfaces due to their high water content, their biocompatibility and their organic polymer backbone, which make them amenable to functionalization. Table 6.2 compares the Hamaker constants for different bead-surface-medium systems and Table 6.1 presents the values of the material properties used in calculations. Replacing the surface with a 10% PEG hydrogel decreases the Hamaker constant by nearly an order of magnitude, while using both a surface and a bead made of hydrogel results in almost a two order of magnitude reduction in Hamaker constant. This illustrates the efficacy of using similar materials to modulate F_{vdW} via the Hamaker constant.

Our current assay uses commercially available polymer-coated iron magnetic beads [160], though exploration of other bead materials could be warranted in the future. Because of this, we focus on changing the properties of the sensing surface. One complication with using pure hydrogel sensing surfaces is their fragility, which makes them difficult to use solely as a surface in a device. A more practical method would be to coat a rigid material with a hydrogel. Though this introduces two vdW forces (one between the rigid glass surface and the bead and the other between the coating and the bead), it also enforces a minimum physical distance of t_{gel} between the bead and the rigid surface. For the same D between the bead and the top surface, compared to

the unmitigated $F_{vdw,surf}$, $F_{vdW,glass-gel}$ is decreased by a factor of $\frac{D^2}{\left(D+t_{gel}\right)^2}$ (Figure 6-3b, inset, black circles) and is only a fraction of F_{total} from the composite gel-glass surface (Figure 6-3b, inset, pink circles). The hydrogel surface closest to the bead contributes force proportional to the bead-gel Hamaker constant, which is nearly 10x lower than the bead-glass Hamaker constant.

The combined effect of this modification is a reduction of at least ∼50x in F_{total} (Figure 6-3b). Coating glass surfaces with $t_{gel} \sim$ 100–1000 nm shows the most reduction, after which the contribution from the glass surface is negligible. The hydrogel surface exerts an attractive force of 10s of pN on the beads, a magnitude that is ∼ 10-100x the weight of the beads and could be disrupted by sufficient actuation (such as vibration). However, this also risks disrupting single antibody-antigen bonds (∼50 pN). Therefore, while hydrogel coatings significantly reduce nonspecific attractive forces, further modifications are necessary to decrease NSB.

In addition to coating the sensing surface, the bead surfaces can be modified to include antifouling polymer brushes which help to further mitigate NSB via steric repulsion. For biomedical applications, PEG is the polymer most investigated for antifouling, due to its biocompatibility, hydrophilicity, and electric neutrality [161]. When grafted at sufficient density, polymer chains extend from the bead surface at length L_0, which is also determined by the molecular weight (MW) of the polymer and monomer size (see Equation 6.14). As beads approach the surface, the brushes make contact at $D = L_0$ and build up a steric repulsive force as they resist compression (Equation 6.14). As shown in the inset of Figure 6-3c, this force is zero until brush-surface contact at $D = L_0$ and turns purely repulsive with high magnitude at $D < L_0$.

When combined with a hydrogel-coated slide, beads with brush coatings experience minimized attractive forces. An example situation is shown in Figure 6-3c for a glass slide with a 1 μm hydrogel coating and beads with PEG of MW 2 or 10 kilodalton grafted with 1 nm between chains. In this system, the maximum attractive force experienced by the beads is now > -5 pN, which is less than a typical antibody-antigen bond. The effect of using brush-coated beads is to effectively truncate attractive forces at L_0, with this effect occurring at larger D as brush length is increased.

To illustrate the combined effect of polymer and hydrogel coatings, the absolute value of the maximum attractive force experienced between the PEG-coated bead and the hydrogel-coated glass surface is plotted in Figure 6-3d. The weight of the beads is also plotted for reference as dotted lines, to show which combinations yield attractive forces less than the bead mass. For both bead sizes, PEG(10k) brushes yield maximum attractive forces that are lower than the bead mass at most t_{gel}. Increasing the t_{gel} or decreasing the polymer graft spacing increases this mitigating effect by both increasing the separation from the glass surface and increasing L_0, which increases the separation distance at which the polymer brush makes contact with the surface. This model predicts that PEG(2k) cannot effectively reduce attractive forces at any graft spacing, reflecting that L_0 for PEG(2k) does contact the gel surface at a separation distance when the attractive forces are sufficiently low.

Overall, this theoretical analysis suggests that the major physical force for NSB, $F_{vdW,surf}$, can be effectively decreased by including coatings on either the glass surface and/or the bead. This combination can decrease the overall attractive force on the bead by three orders of magnitude. Our model does not take into account the chemical components of NSB, which acts in parallel to the forces considered here. Chemical interactions involved in NSB are complex and not well understood, making modeling of these phenomena challenging [52]. Nonetheless, our modeling results suggest relatively simple methods could decrease the physical forces of NSB in a bead-sensing surface system.

6.4.3 Experiments varying hydrogel coating, PEG brushes, bead size and buffer validate model predictions on mitigation of NSB

To test the predictions from our physical model of NSB, we performed a series of experiments in which the motion of PEG-coated beads was observed during their interaction with various surfaces. Though not considered in our model, we also varied the buffer in which the beads and the surface interacted to evaluate how a detergent

affects bead motion. We quantified these effects through calculating the mean squared displacement (MSD) of beads in contact with coated surfaces. We first present plots of this metric for a visual comparison (Figures 6-4, 6-5 and 6-6) and then present a quantitative summary with discussion of the observations (Figure 6-7).

Figure 6-4 shows MSD versus time plots for experiments with coated and uncoated glass slides and 4.5 μm beads coated with either PEG(2k) or PEG(10k). As expected, beads get stuck to bare glass surfaces (Figure 6-4b). Coating the surface with a 1 mm, 2% agarose gel helps to preserve bead movement, but the majority of the beads still remain stuck (Figure 6-4d). Increasing the PEG MW on the beads allows more beads to freely diffuse than the lower MW PEG (Figure 6-4f). These three observations are in line with model predictions.

Figure 6-5 shows MSD versus time plots for experiments that compare the effects of gel molecular identity, buffer and bead size on NSB. Figure 6-5a is the same as Figure 6-4d and is included in this series for comparison. Changing the polymer coating, from a thick agarose gel to a ZI polymer coating, leads to a substantial increase the in the number of beads freely diffusing on the surface (Figure 6-5d). A number of beads in this condition have MSD traces that start off increasing linearly and then level out horizontally, indicative of confined diffusion and likely related to topographical variations in the coating thickness.

Including Tween 20 in the PBS buffer further increases the fraction of beads that retain their motion, with the majority of beads showing MSD >0.2 μm^2 (Figure 6-5f). Confined diffusion is also observed in this experiment. Finally, decreasing the bead size from 4.5 μm to 2.8 μm causes nearly all beads to remain untethered and travel faster than 4.5 μm beads (Figure 6-6d). The slope of the ensemble average MSD is 2x greater for the 2.8 μm beads as compared to the 4.5 μm beads, 25% greater than the expected ratio of their free diffusivities based on the Einstein relationship (Equation 5.1) and illustrative of the influence of the surface on bead diffusion.

Figure 6-7 presents the summary of all experiments on NSB between beads and surfaces as the fraction of beads that are stuck (<0.1 μm^2) at 15 s of observation time for 2.8 μm beads (Figure 6-7a) and 4.5 μm beads (Figure 6-7b). Though experiments

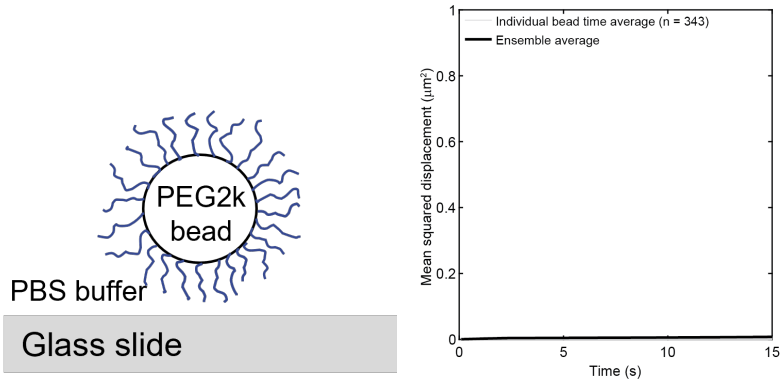

(a) (b)

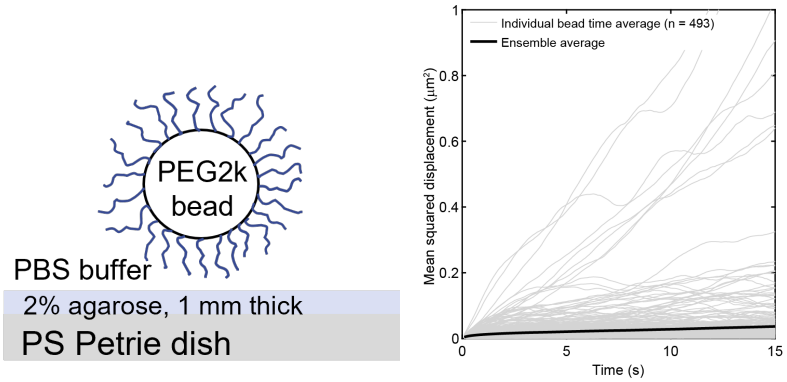

(c) (d)

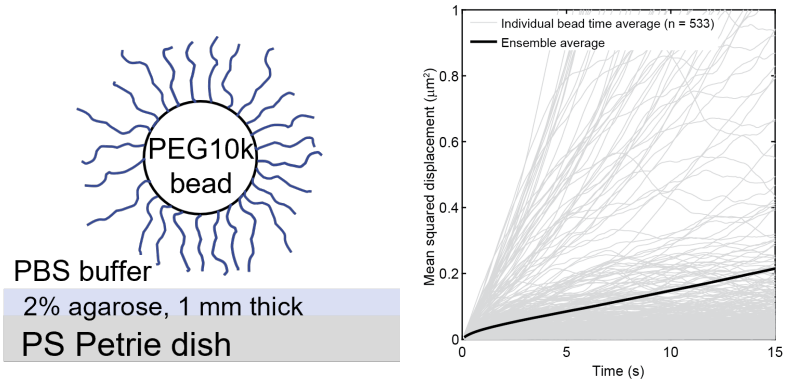

(e) (f)

Figure 6-4: **Effect of surface coating and PEG MW on nonspecific binding between 4.5 μm, PEG(2k)-coated beads and support surfaces in PBS.** (a, b) Without any mitigation, PEG(2k)-coated beads stick to bare glass slides. (c, d) When coated with 1 mm-thick, 2% agarose gel, more PEG(2k)-coated beads retain free motion. (e, f) Using a PEG(10k) coating results in a larger fraction of beads retaining their free motion, as is predicted by the physical model.

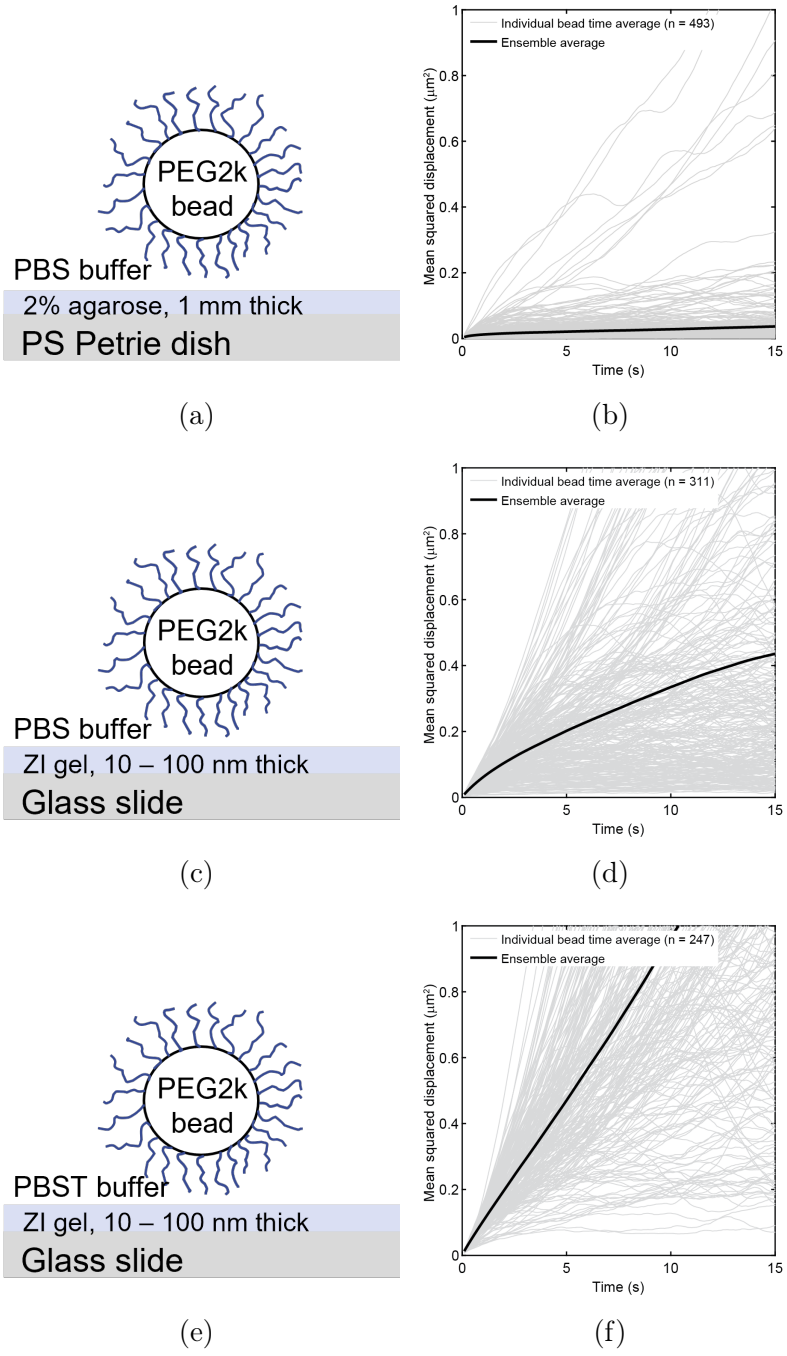

Figure 6-5: **Effect of gel type and buffer on NSB between PEG(2k)-coated beads and support surfaces.** (a, b) Coating surfaces with 2% agarose allows more 4.5 μm beads to move, but there are still many beads that show confined motion. (c, d) Coating the surface with a zwitterionic (ZI) polymer significantly increases the fraction of 4.5 μm beads that retain free motion. There are also a number of beads that diffuse quite freely initially and then become confined, which is hypothesized to be caused by nonuniformities in the coating. (e, f) Using PBST buffer instead of PBS results in nearly all 4.5 μm beads freely diffusing, suggesting the chemical nature of NSB may be more consequential than the physical aspects.

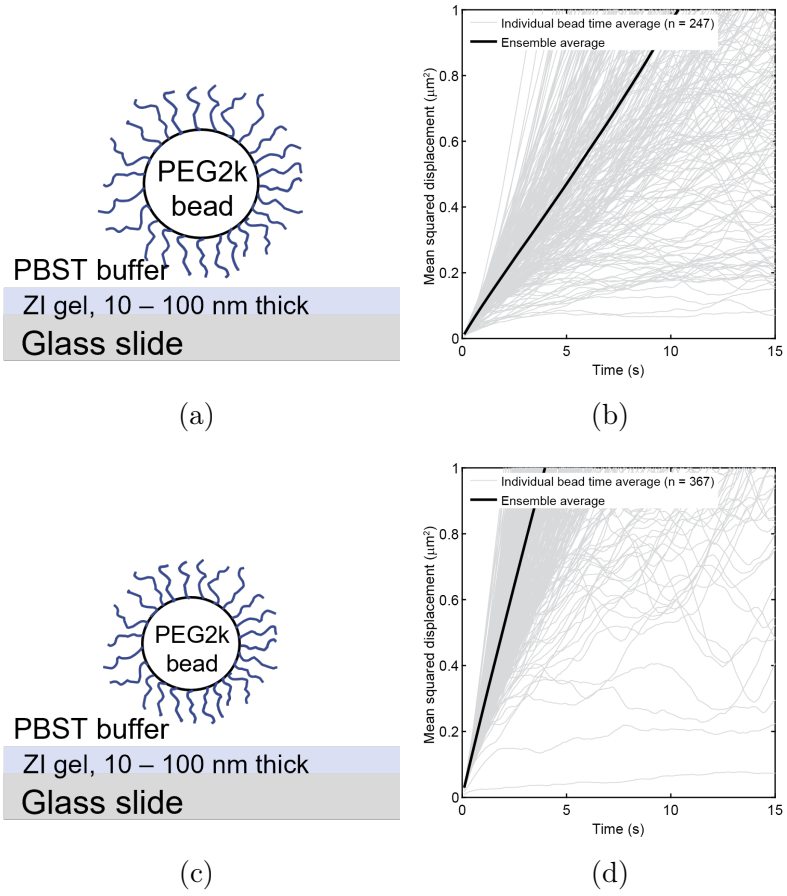

Figure 6-6: **Effect of bead size on NSB between PEG(2k)-coated beads and support surfaces in PBST.** Larger beads have smaller MSD magnitude (b) than smaller beads (d), with nearly all small beads showing free diffusion.

were only performed in singlet, a few trends are evident from these plots. For one, while coating the rigid surface generally decreases NSB, the molecular nature of the polymer coating matters. For example, for coatings on the molecular scale (∼10 nm), ZI polymer coatings perform better than the physisorbed BSA coating or the fluorosilane coating. Hydrophilic materials have shown consistent robust performance in NSB mitigation [61, 161]; BSA and ZI polymers both render the glass surface hydrophilic, while fluorosilanes have hydrophobic regions that could promote attractive interactions.

Studies have suggested that the basis for the increased antifouling effect of ZI coatings comes from the solvation layer held next to the gel via electrostatic interactions with the charged groups on the polymer chains [60, 61]. While ZI polymers are overall

neutral in charge, they possess groups with both negative and positive charges, which interact with molecules in solution. The electrostatic nature of these interactions holds water molecules more strongly than the physisorbed water molecules on other molecules, such as BSA. This may partly explain the increased performance of ZI over BSA, PEG gels and agarose gels, the latter of which were much thicker than the ZI coating.

Second, the effect of PEG MW on bead-surface NSB is unclear from these experiments. For example, on agarose surfaces in PBS, increasing the PEG MW slightly decreased NSB of 4.5 μm beads, but increased or retained NSB of 2.8 μm beads. Previous studies on the fouling resistance of PEG brush coatings present results opposite to this, showing that increasing PEG MW increases antifouling, though these studies examined NSB in the context protein adsorption to PEG brushes on beads and not bead-surface NSB [54, 55]. Results from a previous study of bead-surface NSB identified an optimal PEG MW range for NSB, above and below which NSB was worse [64]. The authors of the study postulated that the existence of this optimal range could be due in part to the PEG brush conformation, which can be further subdivided in to "all-trans" or "helical" forms. The helical conformer exhibits slight coils, the spacing between which can accommodate a water molecule. On the other hand, the planar form all-trans conformers creates a high-density brush that can be more challenging for water molecules to penetrate. This difference in solvation of the brush layer is hypothesized to make helical brushes more resistant to NSB than all-trans brushes [131–133]. Therefore, NSB resistance requires PEG molecules that are densely packed, but not too densely packed, leading to the criteria that 0.5 nm $< s < R_F$ to obtain the full antifouling effects of a PEG brush layer [64]. Though we did not measure the PEG grafting density on our beads, theoretical calculations indicate that graft spacings could have been around this range, suggesting PEG conformation may play a role in our observations.

However, both PEG sizes were grafted at the same theoretical density suggesting that additional effects are likely at play. One study examined the effect of compression on protein adsorption to PEG layers of different MW and found differential results

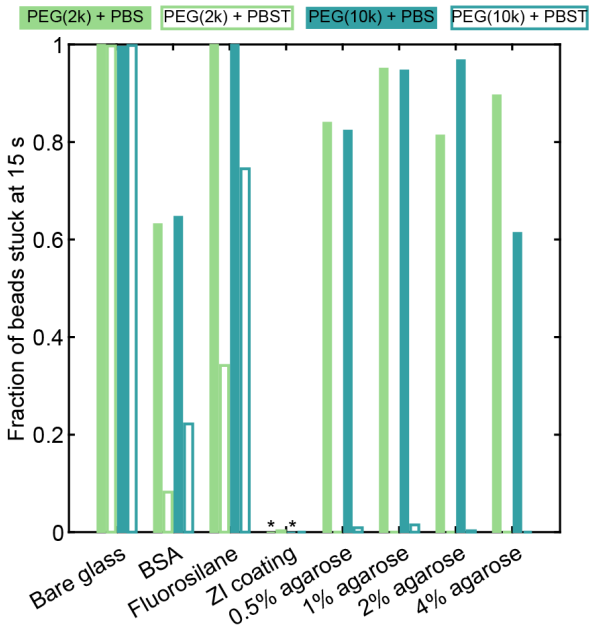

(a)

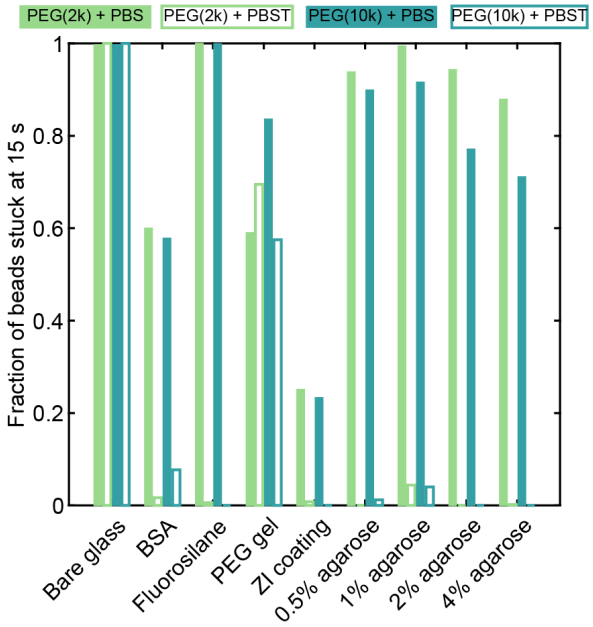

(b)

Figure 6-7: **Summary of NSB experiments, highlighting the effect of PEG size, bead size, buffer and surface coating on the number of beads that are stuck during the observation period.** Each plot is for a different bead size, 2.8 μm diameter (a) or 4.5 μm diameter (b). For both beads, the ZI coating in PBST buffer mitigates NSB to the greatest extent, suggesting that NSB is a complex interplay between both physical and chemical aspects of the surface.

based on PEG MW. Importantly, the authors measured attraction between a protein-functionalized tip and PEG brushes grafted on a lipid bilayer at probe-PEG separation distances greater than the Debye length, indicating that the attractive forces were due to PEG-protein interactions (and not interactions with the electric double layer) [65]. These attractive interactions increased in strength with increasing PEG MW, which was also observed in previous experiments with BSA. Several reasons for this behavior were hypothesized, including the distribution of hydrophilic and hydrophobic regions in different PEG brush conformations and interconversion between these conformations. Though our coatings were polymer- or polysaccharide-based, from these previous results, our results also show that the molecular nature of the coating can influence the extent of PEG layer fouling resistance. In general, this area is not well studied and further investigations are warranted to untangle the effects of PEG MW and grafting density on brush fouling resistance, especially in the context of bead-surface systems.

Though bead size affected the MSD magnitude (Figure 6-6), the overall effect of bead size on NSB was less pronounced. There were less stuck 2.8 μm, PEG(2k) beads than 4.5 μm, PEG(2k) beads on corresponding agarose surfaces, but for BSA, the fraction of beads stuck was similar for both bead sizes. This suggests a modest effect of bead size on overall NSB. Though using smaller beads in a bead diffusion assay may carry other advantages (such as faster and further free diffusion over a defined observation time), the tradeoffs between bead size, motion sensing resolution and device operation time need to be considered during assay design.

Finally, adding detergent to the buffer had the greatest impact on decreasing NSB of beads to surfaces, with experiments in PBST having no stuck beads or a much smaller fraction of stuck beads than seen in the corresponding experiments using PBS. This observation holds for any of the coated glass surfaces for beads of both sizes and coated with PEG of both MW. Non-ionic detergents such as Tween 20 are routinely included in buffers for sandwich assays to minimize NSB and block surfaces through the disruption of hydrophobic interactions [136, 137]. This marked decrease (>90% in some cases) in stuck beads when Tween 20 is included suggests that the majority of the NSB observed in our experiments with coated surfaces is due to chemical interactions,

presumably hydrophobic interactions. Interestingly, the addition of Tween 20 did not decrease NSB on pure glass surfaces, perhaps reflecting a shift of the dominant NSB interactions from physical or electrostatic to chemical upon coating glass surfaces.

Overall, our results suggest that NSB is influenced by both physical interactions and the molecular makeup of the surfaces. NSB can be partly mitigated by minimizing vdW forces via surface coatings and PEG grafts on beads, but the majority of NSB seems to come from chemical interactions. Interactions between surface molecules can be challenging to model, which has led to a relative dearth of theoretical investigations on the topic. Most studies on NSB are empirical in nature. Our experiments were not performed in replicate and replication is required to draw robust conclusions. Nonetheless, our experiments point to the need for additional studies on NSB in order to better understand the mechanisms involved.

6.4.4 FcMBL-mannan assay utilizing FcMBL-functionalized ZI coatings shows decreased NSB and preliminary increased sensitivity

To test if using a ZI-coated glass slide would allow for an enhanced sensitivity mannan assay, we used EDC-NHS chemistry to functionalize ZI coatings with FcMBL at 100 mg/m^2 density. This increased density was used to ensure that functionalization was not limited by the ligand concentration, as we were unsure of the penetration of the ZI gel by FcMBL. We then performed the assay with 1 million FcMBL and PEG(2k) modified 4.5 μm beads as previously described.

Figure 6-8 shows results of this assay with mannan concentrations of 0.00, 0.05 and 1.00 ng/mL, which can be successfully differentiated by MSD at all times (Figure 6-8a). Our results add to previous studies which have utilized ZI coatings and gels to enhance sensitivity of bioassays [62, 63]. Though this was a single replicate, this suggests a 2x increase in sensitivity over experiments utilizing other polymer surfaces, as outlined in Chapter 5. Notably, the MSD magnitude in the 0.00 ng/mL condition is decreased from that exhibited in experiments with PEG; the ensemble average MSD

in the black panel of Figure 6-8b is 1 μm^2 at 10s, while in Figure 6-6a, it is 0.25 μm^2. This is likely due in part to the added interactions between FcMBL molecules on the bead and ZI surface, which could slow the motion of freely diffusing beads.

The change in MSD between 0.00 ng/mL and the two other concentrations is lower than what was seen with the 3D epoxy slides in Chapter 5. This could reflect a reduction in NSB between the beads and the surface, with bead movement now reflective of only the specific interactions between mannan and FcMBL. Replicates are needed to determine the resolution at which individual specific interactions can be resolved, especially given that the difference in MSD between 1.5 orders of magnitude of mannan concentration is < 0.1 μm^2 at 15s.

The individual bead traces in Figure 6-8b provide a visual comparison of the effect of mannan concentration on MSD in this experiment. A greater fraction of beads retain movement in all three concentrations as compared to the same mannan conditions in previous experiments (see Chapter 5, Figure 5-6). For example, 20% of beads are stuck in the 0.00 ng/mL condition on the ZI coated surface, while 56% of the beads are stuck in the same concentration on the 3D epoxy slides used in Chapter 5, evidence that the ZI gel affects NSB. The bead traces in the 0.05 ng/mL condition look similar to the 0.00 ng/mL, reflecting the small change seen in the ensemble averages in Figure 6-8a. Diffusion confinement by increased mannan concentration is clearly evident in the 1.00 ng/mL condition. Interestingly, all three conditions have multiple beads that show temporary diffusion, beads that start off moving freely but then become confined. This is similar to what was seen in experiments without FcMBL (Figure 6-5) and could be due to heterogeneous FcMBL functionalization across the surface or heterogeneous surface topography of the ZI coating. Notably, this was the first time we attempted the ZI polymer coating and EDC-NHS functionalization of the glass surface in silicone gaskets and the process was not optimized. At certain points in the coating process, fluid was leaking from the wells, causing periods in which the surface was not submerged. Further investigation of the functionalized ZI surfaces would include establishing the optimal receptor concentration during functionalization and controls during the coating process to ensure consistency.

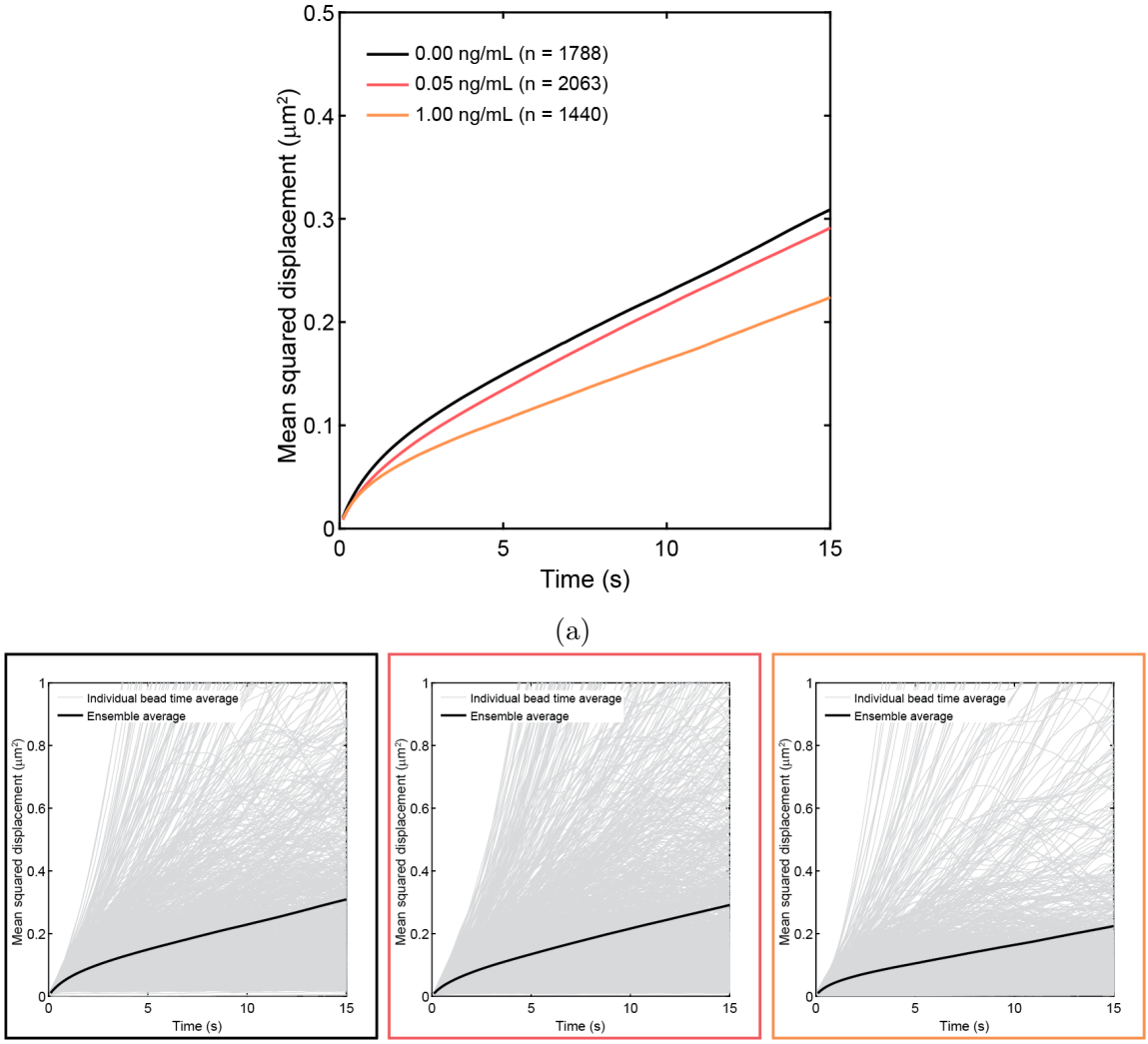

Figure 6-8: **Mannan detection using 4.5 μm FcMBL-PEG(2k) beads on FcMBL-functionalized ZI surface.** Beads were incubated for 30 minutes with 0.00, 0.05 or 1 ng/mL mannan, allowed to settle on a FcMBL-ZI surface in a silicone gasket and observed via video microscopy. (a) The assay using ZI gel surfaces is successful in differentiating mannan concentrations. However, the magnitude of the MSD is much lower than what is seen in Figure 6-5f. This could be due FcMBL functionalization or suboptimal surface coating process. (b) Individual bead MSD versus time plots for beads in each concentration in panel (a). Increasing mannan concentration increases the number of beads that are stuck. There are a number of beads in each concentration that start freely moving but then become confined. This could be due to heterogeneous FcMBL functionalization across the surface or due to heterogeneities in the coating topography, both of which warrant additional investigation and optimization.

6.5 Conclusion

In bioassays, NSB has a major effect on sensitivity and must be sufficiently mitigated to ensure assay robustness. There have been few experimental studies on NSB binding between functionalized beads and surfaces, and even fewer theoretical studies on the physical mechanisms behind NSB. Bead-surface NSB is inherently different from protein-surface NSB due to the greater physical size of the entities involved and the potential for multivalent interactions. Given the ubiquity of bead-based bioassays, there is a need to examine NSB in these geometries to establish design guidelines.

In this chapter, we theoretically modeled the major physical forces that contribute to NSB. Through a combination of surface coatings and the addition of PEG brushes to the bead surface, our model suggests that the vdW attractive force can be decreased ~1000x. Experimental results utilizing different surface coatings, bead sizes, PEG MW and buffers lend support to our model predictions, but also suggest that chemical interactions between surfaces heavily influence NSB. These interactions are harder to model than physical interactions, but it is clear that additional studies are warranted to unravel their effects.

Finally, we showed initial demonstration of sensitivity increase through NSB reduction using our model FcMBL assay on an FcMBL functionalized ZI coating on a glass slide. Using this surface increased assay sensitivity compared to the 3D epoxy surfaces utilized in Chapter 5. Further replication and optimization is needed to confirm and expand this result. Overall, our results suggest that ZI-coatings can successfully retain bead motion and could help enhance sensitivity in bead diffusion assays.

THIS PAGE INTENTIONALLY LEFT BLANK

Chapter 7

Detection of cardiac troponin I by intergrated bead settling and diffusion assay

7.1 Introduction

Current sandwich assays, a commonly used diagnostic method in decentralized settings, generally fall into two categories. High sensitivity assays (i.e., ELISA, dELISA, Luminex; see Chapter 1) can detect analytes at concentrations as low as attomolar, but take hours to return a result and involve specialized instrumentation and analysis methods that increases their cost. On the other hand, the user-friendly lateral flow assay (LFA) returns results in under 20 minutes but suffers from increased sensitivity. Neither assay format delivers on the ASSURED criteria (affordable, sensitive, specific, user-friendly, rapid and robust) for point-of-care (POC) diagnostics specified by the WHO [148, 162], leaving a gap in affinity assays suitable for decentralized bioanalysis. Recognizing the transport gains inherent at small scale, the microfluidics community has created solutions that combine the advantages of these categories (high sensitivity, rapid, low cost) but translating these devices remains a challenge often due to usability aspects, as controlling microfluidics often involves bulky instrumentation and metered

pumping. As a result, decentralized bioanalysis continues to suffer.

Inspired by the testing concerns brought forth during the height of the COVID-19 pandemic [9], our integrated assay concept focuses on user-friendliness towards creating a sensitive platform suitable for use in settings from rural health clinics without the resources for specialized instrumentation and skill sets, to public health screening campaigns in parking lots, where the temporary nature of the setting necessitates high throughput screening and precludes investment in permanent infrastructure. Previous theoretical and experimental results on a model system presented in Chapters 2 and 5, respectively, suggest that combining capture-while-settling and analysis by bead diffusion can quantify analytes at picomolar sensitivity in standalone format. In this chapter, we more formally combine the two processes for quantification of cardiac troponin I (cTnI), to demonstrate our platform's clinical relevance

As an established protein biomarker for cardiac injury [109, 163], cTnI is routinely monitored in a variety of settings including emergency rooms, clinics and critical care units. In undamaged tissue, cTnI is part of the actin-myosin complex which controls muscle contraction. Upon muscle injury, cTnI is released into the bloodstream. Elevated cTnI concentration measured either once or temporally is indicative of a range of conditions including heart attack (acute myocardial infarction), chronic heart failure or myocarditis, making cTnI diagnostics crucial for triaging and treating life-threatening conditions [164, 165]. This is reflected by the inclusion of cTnI diagnostics on the WHO's List of Essential Diagnostics [2]. Due to the severity of associated conditions, timely testing of cTnI is crucial, with ideal time to result in under 30 minutes. Additionally, due to the global epidemiological shift in major causes of death from infectious to chronic diseases [166], cTnI sensing will have continued relevance as a biomarker and increasing access to cTnI testing in settings which are not served by current assays will be essential to sustaining and improving health outcomes.

Quantification of cTnI occurs via immunoassay, the current formats of which are appropriate for commercial or hospital-based laboratories or POC settings. The majority of cTnI in the bloodstream is found in secondary or tertiary complexes with cardiac troponin T (cTnT) or both cTnT and cardiac troponin C (cTnC), respectively

[167]. For this reason, standard assays generally detect one of the complexed forms to ensure accuracy. In the laboratory setting, fluorescent sandwich assays are performed in an automated, high-throughput manner on specialized instruments which can return a result in 20-30 minutes and have limits of detection (LODs) in the single picogram per milliter (pg/mL) range [168]. This current performance is the result of years of research and development, which has improved sensitivity 1000x since the 1990s [164]. Despite their sensitivity, the size and resources required for these laboratory instruments makes them impractical for decentralized use. For POC applications, there are a number of handheld or benchtop instruments available, some of which return results in under 15 minutes but with lower sensitivity ($\sim$ 50 pg/mL) and throughput [169, 170]. The cost and maintenance requirements of this dedicated instrumentation restricts the use of these POC assays to bedsides in critical care or emergency departments. For reasons unknown, there are currently no cTnI LFAs approved for use in the United States, leaving a gap in cTnI diagnostics for decentralized settings and an opportunity for technology innovation. The clinically relevant cutoff for cardiac diagnoses based on cTnI is based on a reference population and is measured for each platform during regulatory testing, but generally is on the order of 0.010 nanograms per milliliter (ng/mL) [164, 168].

In this chapter, we demonstrate the ability of our combined bead settling and diffusion assay to quantify cTnI at clinically relevant levels in a prototype device format that requires a single manual mixing step. Through experiments and analysis, we show that multiple metrics based on bead diffusion yield LODs 5-25x higher than current POC devices but on a comparable timescale and in a format that is high-throughput, massively distributable and more user-friendly. We highlight strategies to that could improve our assay's analytical performance towards establishing our platform as a direct alternate to POC devices. Overall, based on the ease-of-use and current performance, our results demonstrate that cTnI can be quantified using a standalone, mostly passive device format, laying the foundation for use of our assay in decentralized bioanalysis for our selected analyte and extending to others as well.

7.2 Materials and methods

7.2.1 Materials

Monoclonal mouse anti-human antibodies specific to either cTnI or the tertiary cardiac troponin complex (Table 7.1) were purchased from Hytest (Turku, Finland) or from Medix Biochemica (St. Louis, MO). cTnI-free serum and recombinant tertiary cardiac troponin complex were purchased from Hytest. Bovine serum albumin (BSA), phosphate buffered saline (PBS), KimWipes and Parafilm were purchased from VWR, Inc (Radnor, PA). HybriWell sealing system chambers (6 chambers per slide, chamber dimensions 9.8 x 20 millimeter [mm], 0.25 mm depth; Grace Bio-Labs), ProPlate multiwell chambers (16 x 6 mm diameter wells; Grace Bio-Labs), calcium chloride dibasic ($CaCl_2{\cdot}2H_20$), ethanolamine, Tris base, sodium phosphate monobasic (NaH_2PO_4), sodium phosphate dibasic (Na_2HPO_4), polyclonal mouse IgG from serum and Tween 20 were purchased from MilliporeSigma (Burlington, MA). Dynabeads M-450 Epoxy magnetic beads (hereafter referred to 4.5 micron [μm] beads), Zeba spin desalting columns (7000 Dalton molecular weight cutoff) and ethylenediaminetetraacetic acid (EDTA) were purchased from ThermoFisher Scientific (Waltham, MA). Antibody diluent/HAMA blocker was purchased from Abcam (Cambridge, UK). Amine-terminated polyethylene glycol (PEG) with molecular weight of 2000 (subsequently referred to as PEG(2k)) was purchased from Nanocs, Inc (New York, NY). Glass slides coated with an antifouling polymer layer and derivatized with epoxy groups (subsequently referred to as 3D epoxy slides) were purchased from PolyAn GmBH (Berlin, Germany). 10x Tris-buffered saline with 0.5% Tween-20 (TBST; Boston BioProducts) was purchased from Fisher Scientific (Hampton, NH).

We note that the tertiary cardiac complex is the source of cTnI in our experiments. As previously mentioned, this molecule contains cTnI and two other subunits in a 1:1:1 ratio [109]. The majority of cTnI has been found to exist in blood in the complexed form [167]. The tertiary complex concentration is provided in units of cTnI from the manufacturer. This stock concentration was used in the calculation of concentrations used in assays and we report performance metrics in cTnI concentration.

Table 7.1: **Monoclonal antibodies to human cTnI or cTn complex screened for use in assay.**

Antibody	Vendor	Epitope (amino acid #)	Species	Isotype	Immunogen	kD (nM)
560	Hytest	83-93	Mouse	IgG1	cTn-complex	not provided
19C7	Hytest	40-50	Mouse	IgG2b	Free cTnI	not provided
20C6	Hytest	N/A	Mouse	IgG2b	cTn-complex	not provided
9705	Medix Biochemica	21-30	Mouse	IgG1	not provided	0.064
9707	Medix Biochemica	190-195	Mouse	IgG1	not provided	0.003

7.2.2 Functionalization of beads and surfaces with cTnI-specific antibodies

To remove azide and other additives that could react with functional groups, antibodies were desalted using Zeba spin columns prior to functionalization and according to the manufacturer's protocol. Desalted antibodies were aliquoted and stored at 4°C, as recommended by the manufacturer.

4.5 μm beads were functionalized according to previous optimizations in combination with the manufacturer's recommended protocol. Incubation steps took place at room temperature and in reciprocating mode on a rotisserie mixer at 30 rotations per minute (rpm), unless otherwise noted. Briefly, beads were incubated for 20 hours (h) with 0.1 molar (M) sodium phosphate buffer (pH 7.4) containing antibody at a concentration to theoretically coat beads with 10 milligrams per square meter (mg/m^2). In some conditions, after magnetic concentration, beads were resuspended with PEG(2k) in sodium phosphate buffer at a concentration for a coating density of 10 mg/m^2 and incubated for 20 h. After coating beads with antibody or antibody + PEG(2k), beads were magnetically concentrated, resuspended in 50 millimolar (mM) ethanolamine in 0.1 M sodium phosphate buffer and incubated for 4 h. Finally, beads were washed three times for five minutes (min) with wash buffer (PBS + 2 mM EDTA + 0.1% weight per volume [w/v] BSA), counted and stored at 4°C until use.

Sensing surfaces were created by functionalization of 3D epoxy slides according to the manufacturer's protocol. A Hybriwell sealing gasket or ProPlate multiwell scaffold was attached to the slide. 50 microliters (μL) of antibody at a concentration for 10 mg/m^2 coating density in alkaline buffer (150 mM sodium phosphate buffer + 50 mM sodium chloride, pH 8.5) was added to each chamber or well and the slide was incubated for 20 h at room temperature. To prevent evaporation, all incubations took place in a Petrie dish with a moist KimWipe and sealed with Parafilm. After antibody incubation, chambers were washed twice with alkaline buffer. To react with residual epoxy groups on the slide surface, chambers or wells were filled with 50 μL blocking buffer (50 mM ethanolamine + 100 mM Tris base, pH 9) and incubated for 2 h at room temperature. After washing twice with alkaline buffer, the chambers or wells were filled with 50 μL of 1% (w/v) BSA in PBS and incubated for 30 min to block the surface. Chambers or wells were subsequently washed four times with PBS + 0.05% (v/v) Tween 20. The chamber or well was filled with PBST and the slide was stored at 4°C in a humidified Petrie dish until use.

7.2.3 Selection and screening of antibody pairs

To determine which antibody pairs preserved free movement of beads on the sensing surface when no cTnI is present, 1 million antibody-functionalized 4.5 μm beads were resuspended in 500 μL of either PBS + 0.05% (v/v) Tween 20 (PBST) or 1x TBST + 5 mM $CaCl_2$ (TBSTCa) and incubated for 30 minutes with end-over-end mixing at 30 rpm. After three washes with buffer, beads were resuspended in 50 μL of the same buffer and injected into a Hybriwell chamber on an antibody-functionalized slide. Chamber ports were sealed and bead motion was recorded via video microscopy at 20x magnfication (12 Hertz [Hz], 0.01 second [s] exposure time and 30 s total length) using a Nikon TE-2000U inverted microscope (Nikon, Melville, NY) fitted with an Andor iXon3 CCD camera (Oxford Instruments, Abingdon, UK). Four videos were taken along the length of the chamber to examine the variation in bead movement with slide location. Thirteen combinations of bead, surface and buffer were trialed; combinations are shown in Table 7.2. Capture antibody refers to the antibody on the

bead surface and detection antibody refers to the antibody on the slide surface.

7.2.4 Integrated assay in buffer and serum

To examine the efficacy of an integrated assay combining capture-while-settling and bead diffusion, two antibody pairs were tested using slides fitted with Proplate wells. cTnI was diluted in the buffer corresponding to each antibody pair in three dilution series:

- Trial 1: 0, 0.001, 0.005, 0.010, 0.050, 0.1, 1 and 10 ng/mL, tested in singlet on a six month old slide

- Trial 2: 0, 0.005, 0.050, and 0.500 ng/mL, tested in duplicate on a six month old slide

- Trial 3: 0, 0.001, 0.010, 0.100 and 1.00 ng/mL, tested in triplicate on a six month old or one week old slide

Slides fitted with Proplate wells and previously functionalized with antibody were emptied of their storage buffer and 5 μL of buffer, containing either 178500 or 17850 antibody-functionalized beads, were deposited into the well. 175 uL of cTnI in buffer was subsequently added to the wells and mixed by pipetting up and down three times. Bead concentrations in these wells were therefore 1 million per milliliter (mL) or 100,000/mL, respectively.

Wells were sealed with tape to prevent evaporation and beads were allowed to settle to the sensing surface for 20 min, after which bead movement on the surface of the slide was recorded using video microscopy at the previously described conditions. Five or six videos were taken at random locations on the slide.

The same experiment was also performed in cTnI-free serum using conditions in trial two to determine the efficacy of cTnI sensing in a clinically relevant matrix.

7.2.5 Troubleshooting serum interference

A series of experiments were undertaken to shed light on serum interference by removing or minimizing serum components through pretreatment. Experiments were conducted using beads at a concentration of 1 million/mL and in Proplate wells, using the procedure and video microscopy analysis as previously described. Serum was prepared differently for each condition, which was assayed in duplicate for the 9705/20C6 pair, unless otherwise noted:

- *Buffer*: Settling in buffer using previously described procedure.
- *Nonfat*: Fat was separated from serum using centrifugation at 3000 rpm for 15 min. A pipet was inserted below the resulting top fat layer and the serum was removed to another tube for subsequent experimentation.
- *Diluted serum*: Serum was diluted 10x in the buffer corresponding to each antibody pair.
- *Diluted serum in buffer + 1% (w/v) BSA*: Serum was diluted 10x in the buffer corresponding to each antibody pair. The buffer additionally contained 1 % (w/v) BSA.
- *0.1 % Tween 20*: Tween 20 was directly added to serum at a concentration of 0.1 % (v/v).
- *Off-slide incubation*: Beads were incubated in serum in a microcentrifuge tube for 30 min, washed 3x with buffer and resuspended in buffer prior to deposition in the well.
- *Preadsorbed serum*: Serum was incubated for 1 h with 9705 antibody at 50 ng/mL to adsorb residual cTnI prior to use in the assay. This condition was tested in singlet.
- *Mouse IgG preadsorbed serum*: Serum was incubated with 0.7 grams per liter of polyclonal mouse IgG for 30 min with end-over-end mixing at 30 rpm prior to use in assay [171]. This condition was tested in singlet.

- *Commercial blocker*: Serum was diluted 1:10 in antibody diluent/HAMA blocker and incubated for 30 min with end-over-end mixing at 30 rpm prior to use in assay. This condition was tested in singlet.

Additionally, to determine if serum fouled through interaction with the antibodies, several conditions were trialed with different non-antibody functionalized surfaces. In one series, Hybriwell-chambered glass slides were coated with BSA (1% (w/v) incubation for 30 min, followed by 3x wash with PBS). One million, PEG(2k)-functionalized 4.5 μm beads were suspended in 50 μL of PBS or serum and injected into a chamber. This condition was tested in singlet and bead motion was observed using video microscopy at the previously described conditions.

7.2.6 Demonstration of assay in diluted serum

Using 9705 + PEG(2k)-functionalized beads and 20C6-functionalized surface, the performance of the integrated assay was examined in 10x diluted serum in TBST + 5 mM $CaCl_2$ + 1% (w/v) BSA. Cardiac troponin complex was diluted in cTnI-free serum. Immediately prior to testing, 50 μL of serum was added to 450 μL of buffer and vortexed to mix. Proplate wells were emptied of storage buffer and 5 μL of beads in buffer (containing 178500 beads) were added to the well. 175 μL of diluted serum was added to the well and mixed by pipetting up and down three times. Wells were sealed with tape to prevent evaporation and beads were allowed to settle onto the surface for 20 min. Bead motion was observed using 20x video microscopy (12 Hz, 0.01 s, 30 s observation period) at five or six random locations on the sensing surface. The undiluted cTnI concentration series used were:

- Trial 1: 0, 0.050, 0.500 and 5.000 ng/mL, tested in quadruplicate
- Trial 2: 0, 0.050, 0.500, 5.000 and 50.000 ng/mL, tested in triplicate
- Trial 3: 0, 0.050, 0.200, 0.600, 5.000, 50.000, 500.000, and 2000.00, testing in quadruplicate

7.2.7 Image analysis

Analysis of videos was performed using a custom MATLAB (Mathworks, Natick, MA) script using functions from the Image Processing Toolbox and previously outlined in Chapter 5.

7.2.8 Determination of limit of detection

Metrics highlighted in Chapter 5 were examined for their ability to quantify cTnI, including:

- Mean squared displacement (MSD) at different observation times
- Geometry parameters characterizing the bead trajectories including the enclosing radius and the maximum travel from the starting position
- Euclidean distance of the fitted slope/intercept pairs from the (0,0) datum
- Fraction of single or clumped beads

Limits of detection (LODs) for the assay were calculated based on each metric. For each metric, a dose-response curve was constructed by plotting the mean metric value of the replicate measurements versus the concentration on a semilog plot. For trials one and two, curves were fit with a linear model. For trial three, curves were fit with a four parameter logistic (4PL) model:

$$y = D + \frac{A - D}{1 + (\frac{x}{C})^B} \tag{7.1}$$

For all trials, the LOD was estimated using the fitted curves by finding the concentration value corresponding to the mean of the blank replicate samples plus or minus three times the standard deviation of the blank replicate samples (depending on the metric trend), as is a common method of estimating LOD in analytical methods [23, 24, 48, 172].

7.3 Results and discussion

7.3.1 Paired antibody testing reveals robust antibody pairs for the assay and highlights the need of empirical pair testing early in the development process

Non-competitive sandwich immunoassays require two different antibodies, a capture antibody and a detection antibody, for antigen detection so that antibodies are not competing for the same epitope. Before using any analyte in the assay, these antibodies must be screened for interactions to ensure they do not interact with each other and lead to false positive signals in the absence of any analyte [173]. There is currently no accurate way to predict antibody interactions, so this exploration must be performed empirically for each assay. In our case, we monitored the motion of antibody-coated beads on antibody-coated surfaces to ensure beads move freely when there is no cTnI present.

We trialed seven different bead-surface pairs with antibodies which were selected based on recommendations from two different vendors, who manufacture reagents used in commercially available cTnI platforms, as well as antibody pairs reported in bioassay literature [174, 175]. Two different conditions were trialed. In the first base case, beads functionalized with only antibody and in PBST buffer were used. In the second case, beads functionalized with antibody and PEG(2k) in TBSTCa buffer were used. PEG(2k) was added to make the bead surface more hydrophilic and potentially decrease nonspecific binding (NSB), as was found to be efficacious in the FcMBL-mannan system. TBSTCa buffer was used to keep the cardiac troponin complex intact, as the formation of the complex is dependent upon the presence of calcium and the majority of cTnI is found in the complexed form [167].

Pairs tested and results are shown in Table 7.2. Example mean squared displacement (MSD) versus time plots, illustrating antibody pairs that showed efficacy and a few pairs that did not, are shown in Figure 7-1. Despite using manufacturer recommended combinations, only two out of 13 conditions trialed preserved free diffusion

Table 7.2: **Results of cTnI antibody pair screening in the absence of analyte.** The desired result is preserved bead motion, indicating that capture and detection antibodies do not interact and cause false positive results. Red cells represent pairs that confined bead motion, while green cells represent pairs that preserved motion.

Capture antibody	Detection antibody	Beads with PEG(2k), TBSTCa buffer	Beads w/o PEG(2k), PBST buffer
20C6	560		
19C7	560		
560	20C6		
9705	20C6		N/A
19C7	20C6		
9705	9707		
560	9707		

and these pairs used antibodies from different vendors. The buffer and the presence of PEG(2k) on the beads made a difference, as exemplified by the 560 capture/9707 detection pair, which preserved bead movement in PBST but not in TBSTCa buffer with PEG(2k) on the bead surface.

This analysis highlights the importance of antibody screening early in the assay development process to ensure selection of the antibody pair with the lowest NSB and high assay sensitivity. Though not evident in our experiments, even simple modifications such as switching antibody orientation, can make a difference (i.e., antibody A as capture and B as detection versus B as capture and A as detection) [173]. The underlying reasons as to why some antibody pairs show interferences and others do not are not well studied or understood and further investigation is warranted to uncover potential general design guidelines that could aid in antibody selection without extensive empirical efforts.

Of the antibody pairs that show efficacy, 9705 capture and 20C6 detection showed the most consistent motion across the slide (Figure 7-1a,) with slightly greater motion observed at the top of the chamber, similar to observations in the FcMBL-mannan experiments (see Chapter 5). Both antibodies in this pair recognize the cardiac troponin complex. On the other hand, 560 capture and 9707 detection showed more variation across chamber locations and also $\sim \frac{1}{3}$ lower overall MSD. One antibody

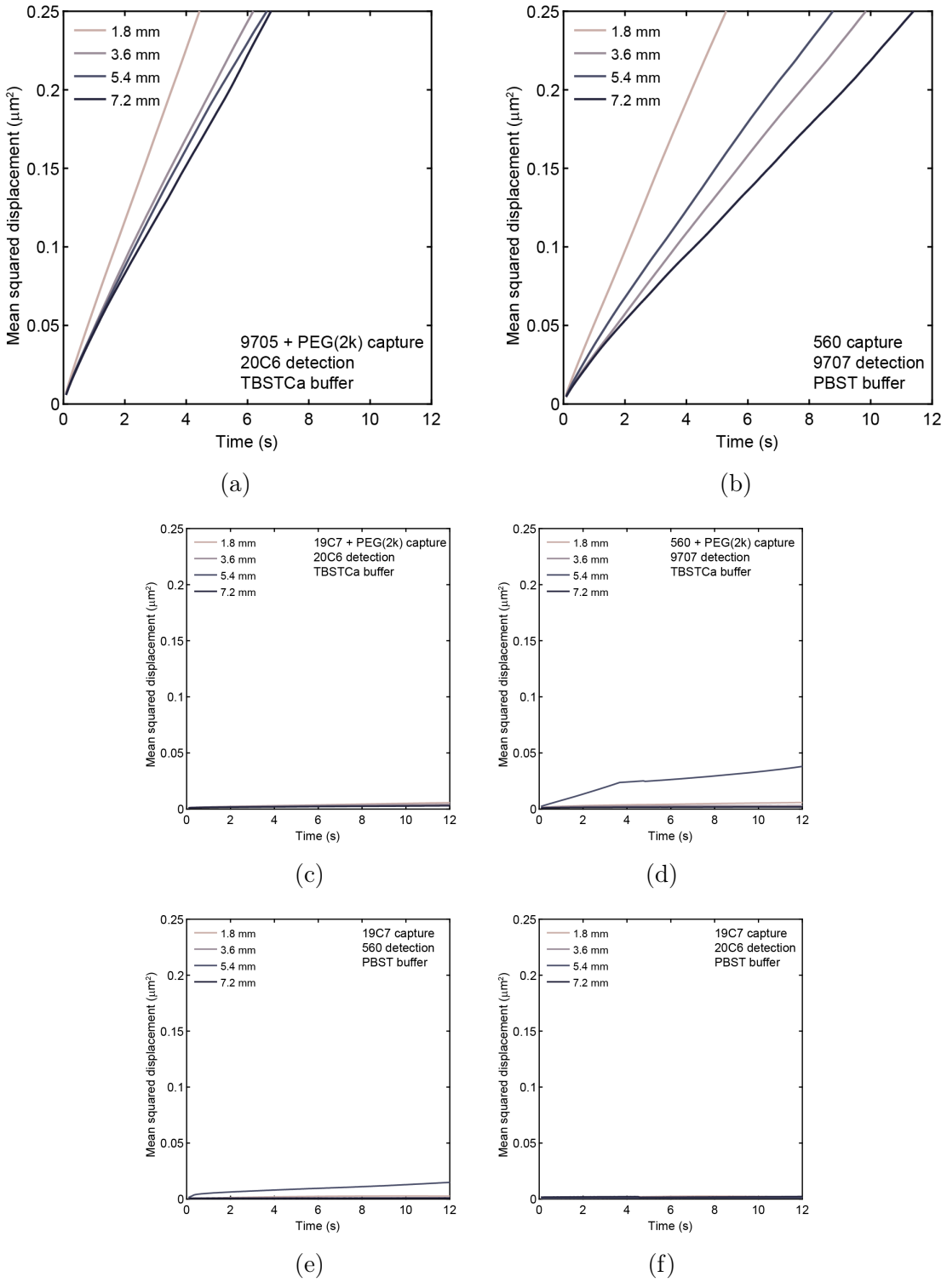

Figure 7-1: **Example ensemble average MSD versus time plots from cTnI antibody screening.** Antibody pairs were screened to determine which combinations preserved bead movement in the absence of cTnI. (a,b) Examples of pairs which retained motion. (c-f) Examples of pairs which constrained motion. Capture antibody, PEG(2k) presence on bead, detection antibody and buffer are indicated on each plot.

in this pair, 9707, recognizes the cardiac troponin complex; the manufacturer does not disclose if 560 recognizes the complex, but comparison of epitope specificity of this antibody with other commercially available antibodies suggests that it does not recognize the complex. Recognition of the complex is important for robust cTnI detection and having one antibody that recognizes the complex is sufficient, as long as the other antibody recognizes an epitope of cTnI that is exposed when the antigen is complexed. Based on these considerations, both efficacious pairs should be able to sense complexed cTnI and were taken ahead for experiments examining cTnI detection.

7.3.2 cTnI can be detected by integrated assay in buffer

Towards the goal of demonstrating cTnI quantification in a standalone device incorporating capture-while-settling and bead diffusion, we used a simple prototype device to demonstrate our concept (Figure 7-2a). The sample is transferred to a well that already contains functionalized beads. Pipette mixing is used to disperse the beads in the sample, after which the beads are left to settle onto the sensing surface. After a designated amount of settling time, video microscopy is used to observe and record bead interactions with the surface and these interactions are subsequently quantified by multiple metrics. We wish to highlight the simplicity of this process, which involves a single manual transfer and mixing step, an ease-of-use profile that is suitable for decentralized settings. In future device iterations, it is envisioned that the sample could be directly deposited into the device and manually mixed by inverting the device several times, removing the sample transfer step completely.

Our prototype device is in the form of well scaffolding affixed to a functionalized slide (Figure 7-2b). The wells are 6 millimeters (mm) in diameter and our total sample volume of 180 μL creates a 6 mm-tall fluid column. Using the settling speed of our 4.5 μm, 1.5 grams per cubic centimeter material density beads ($U_s = 5.5$ μm/s), this translates to a settling time of ~20 min. By the theory outlined in Chapter 2, utilizing the resistance model (Equation 2.39; Da ~0.54) with 9705 antibody on-rate ($k_{on}^{3D} = 7x10^{-5}M^{-1}s^{-1}$), maximum antibody density on the beads ($n_{ab} \sim 10^{16}/m^2$), capture coefficient found by Equations 2.1 and 2.15 ($k_+ = 2.2x10^{-05}$ m/s) and a bead

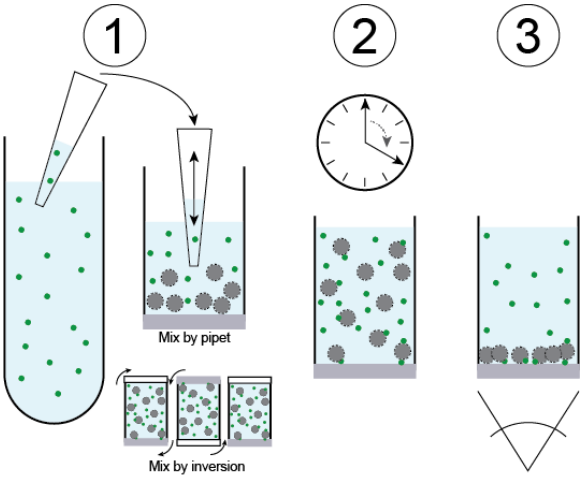

(a)

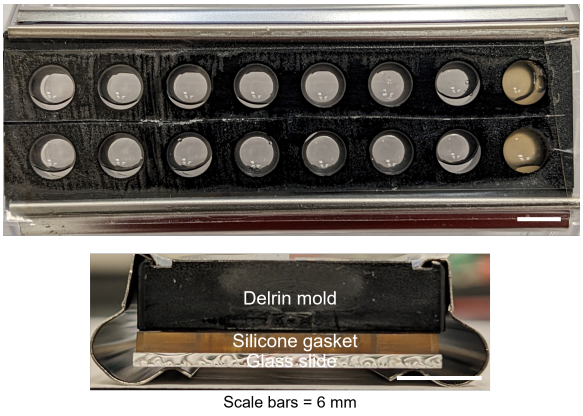

(b)

Figure 7-2: **Prototype integrated assay.** (a) The assay is performed in three steps: (1) sample is transferred to the device and mixed with beads already in the device either via pipetting up and down several times or via manual inversion of the device; (2) the device is left undisturbed and beads are allowed to settle to the surface in an amount of time based on the fluid volume and bead settling speed; and (3) bead interaction with the surface is observed and recorded by video microscopy and subsequently quantified by various metrics to reveal analyte concentration. (b) Prototypical device used in integrated assay trials consists of a Delrin well scaffold on a functionalized glass slide.

concentration of 1 million/mL, we estimate that 44% of cTnI molecules should be captured in this time.

Figure 7-3 shows results from the initial integrated assay trial in buffer for both antibody pairs and demonstrates that combining capture-while-settling and diffusion-based analysis shows efficacy for cTnI sensing. Comparison of the top and bottom plots for each antibody pair shows that bead concentration heavily influences assay performance, with lower cTnI concentration MSD curves overlapping more when using 10x less beads than in the bottom row, 1 million beads/mL condition. By theoretical calculations, using 100,000 beads/mL results in ∼1.3x more analytes per bead than when using 1 million beads/mL. Higher bound analyte density is predicted to result in more consistent signals, which was the case in the model FcMBL-mannan assays. The current results show the opposite trend, that increasing bead concentration results in better concentration differentiation. A potential contributor to this observation is that, due to faster moving beads preferentially forming clumps, which are removed during image analysis, freely diffusing beads are effectively filtered out and do not contribute to the MSD signal. This may leave a background of beads that move similarly in lower concentration samples and lead to less difference in MSD between concentrations, since, as shown previously, differentiation between concentrations heavily depends upon observing freely diffusing beads. At lower bead concentrations, sampling enough beads to get above this background population becomes more crucial and perhaps was not adequately performed in this trial. Overall, these results highlight the crucial nature of selecting bead concentration to ensure maximum sensitivity in bead motion sensing.

Comparison between the two pairs in the 1 million bead/mL condition shows that the 9705/20C6 pair performs more robustly, with the expected MSD trend by concentration evident (Figure 7-3c). Though this experiment was performed in singlet, the separation between the 0.000 ng/mL curve and the 0.001 ng/mL curve suggest that this sensing method could have extremely high sensitivity. The 560/9707 pair shows more separation of lower cTnI concentrations, but the 0.000 ng/mL condition has lower MSD than the first two concentrations trialed, suggesting lower overall

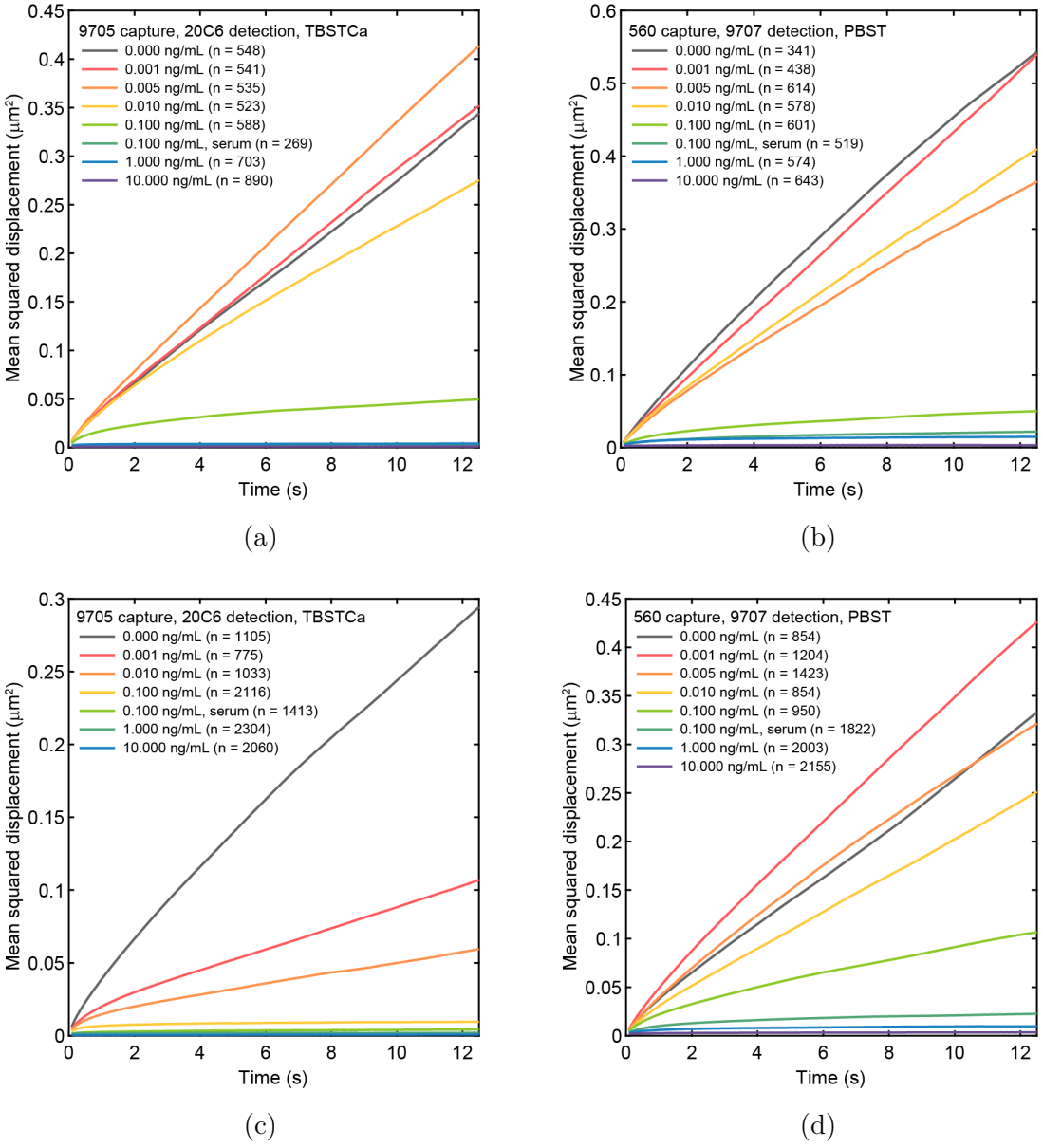

Figure 7-3: **Initial detection of cTnI by integrated assay in buffer**. Both antibody pairs were tested in prototype devices that perform the standalone assay. Single trials of the assay were performed with using (a,b) 100,000 beads/mL, and (c,d) 1 million beads/mL, showing that bead concentration affects assay performance. For each line in each plot, the number of beads analyzed to determine the mean value is indicated by 'n='.

sensitivity. Differences in antibody affinity are likely at play here. Based on the higher suggested sensitivity of the 9705/20C6 pair, we moved forward with this pair in further replicate testing. We note, however, that exploring the efficacy of the 560/9707 pair is warranted in the future, especially because the maximum MSD magnitude is higher than the 9705/20C6 pair, which could lead to an assay with greater dynamic range.

Notably, we also included 0.100 ng/mL cTnI in serum condition in this experiment. Compared to the same 0.100 ng/mL cTnI concentration in buffer, serum reduced the MSD signal from this concentration by nearly 10x. As 0.000 ng/mL in serum condition was not included in this experiment, it is unclear if this represents total serum fouling of the system or if this is truly the signal from cTnI in serum. However, it suggests that serum has high potential to foul our assay and overcoming this effect will be crucial for clinical relevance.

7.3.3 cTnI can be quantified by various metrics, but performance is limited by slide variability

To estimate the LOD of our integrated assay, we performed replicate experiments using the 9705/20C6 antibody pair in TBSTCa buffer. Since our previous results point to sensing surface chemistry being a major source of variation, we incorporated different conditions to examine differences across and between slides. In these trials, we prioritized analyzing this variation over increasing the number of concentrations tested per replicate; since there are sixteen wells on one slide, to examine variation across a single slide, we could test a maximum of 5 concentrations in triplicate. All experiments used beads from the same functionalized stock, so variability in our results are indicative of sensing surface variation. We additionally calculated LOD using several different metrics, as first presented in Chapter 5, to examine which metrics are most sensitive for cTnI quantification.

Results from this replicate analysis are shown in Figure 7-4. By visual comparison, it is immediately clear that there is a difference in MSD magnitude within and across slides. For example, trial 1, performed in duplicate on an older slide, shows MSD

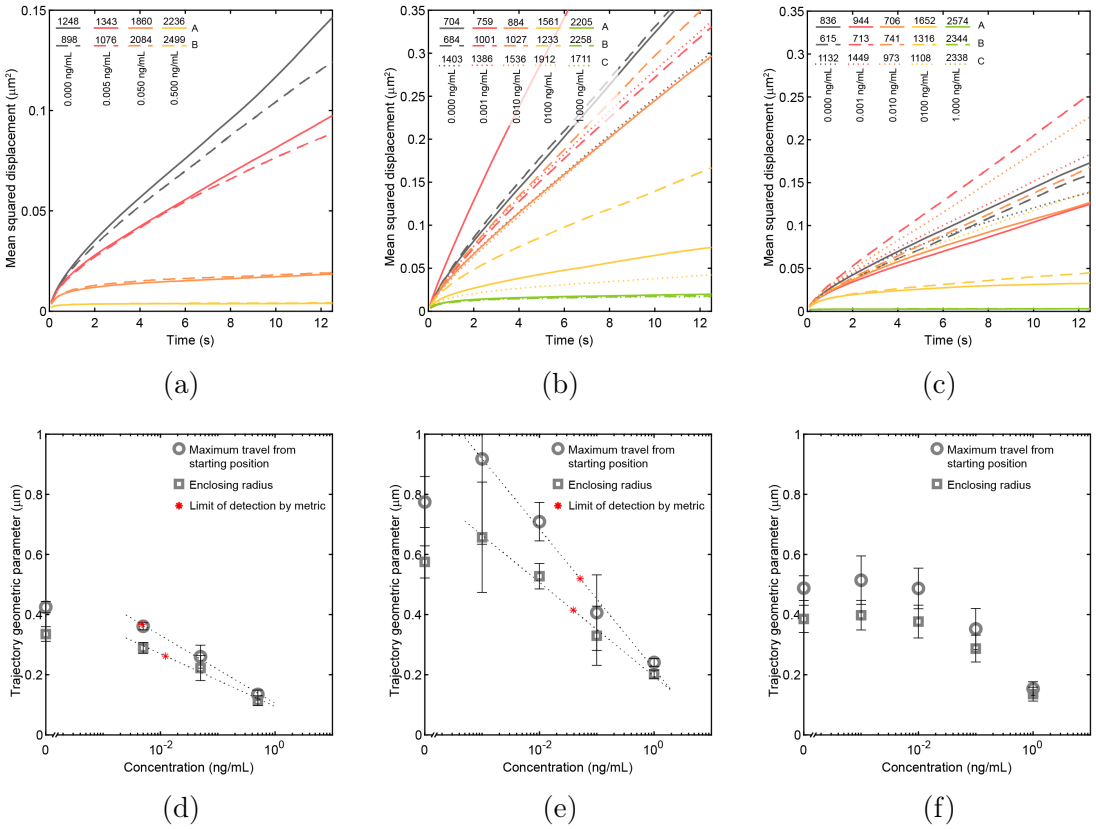

Figure 7-4: **Demonstration of cTnI sensing in buffer with replicate integrated assays on different slides.** (a-c) Ensemble average MSD and (d-f) dose-response curve for geometry metrics, illustrating the difference in assay sensitivity by slide. Plots in the first, second and third column represent trial 1, 2 and 3, respectively. Trials in first and second column were performed on slides that were 6 months old. The trial in third column used a slide that was one week old. Error bars represent the standard deviation of the replicate measurements. For each curve in MSD versus time plots, the number of beads analyzed to determine the mean value is indicated by the number over the corresponding line style in the legend.

curves that are nearly on top of one another, while trial 2 (triplicate, older slide) shows more variability. Though the concentrations tested are not the same for each experiment, the variability can be examined by the relative standard deviation (RSD) between replicate MSD measurement at different times for a single concentration. We choose the second highest concentration in each trial, because nearly all beads are stuck in the highest concentration tested. Results are shown in Table 7.3. Though MSD RSD increases with time due to sampling considerations discussed in Chapter 5 [154], comparing RSD across slides illustrates the differences between and within lots: there is at least 10x difference in RSD between slides from the same lot (trials 1 and 2) and at least 12x difference in RSD between slides from different lots (trials 1 and 3), even at early times. This comparison also illustrates the variation across a single slide, as the slide used in trial 1 yielded much more consistent results (low RSD at all times) compared to the slides in the other two trials.

In another illustration of slide variation, when comparing the maximum overall magnitude of MSD, trial 1 is an outlier, with maximum MSD magnitude of $\sim$0.15 μm^2, compared to 0.35 μm^2 and 0.25 μm^2 for trials 2 and 3, respectively. Trials 1 and 2 were performed on slides whose packaging was opened six months prior to use and it is likely that epoxy groups on the surface degraded during this time even with optimal storage conditions. However, the $\sim$2x higher maximum MSD between these trials again points to random slide to slide variation within the same lot. Of note, trial 2 and 3 replicated the well layout exactly (i.e., trial 2, replicate A, 0.000 ng/mL well was the same well location as trial 3, replicate A, 0.000 ng/mL well) for an exact location comparison.

This variability manifests in estimated assay LODs (Table 7.4). Trial 1, which is well fit by a linear model, has LODs $<$0.010 ng/mL by multiple metrics, while trial 2 suffered from larger variation between replicates at most concentrations, giving slightly higher LODs. LODs for trial three were not calculated. cTnI quantification by geometry metrics shows the most efficacy and dose-response curves for these metrics are shown in Figure 7-4c-f, where the variability between replicates within a slide and across slides is visually evident.

Table 7.3: **Relative standard deviation between MSD measurements in assay replicates at the second highest concentration tested.** For trial 1, this concentration is 0.05 ng/mL. For trials 2 and 3, this is 0.1 ng/mL. Trial 1 and 2 used slides from the same lot.

Time (s)	Trial 1	Trial 2	Trial 3
5	5	57	60
10	4	65	75
15	0.01	11	86
20	2	13	94

Overall, these results suggest that our integrated assay potentially has LODs 1-2x higher than commercially available POC assays, which suggests clinical utility. However, the large variation in results within and between slides is concerning and limits the applicability of our assay. Some variation is expected between slide lots due to natural process variation, but more concerning is the disparate results on the same slide or between slides from the same lot. Differences on the same slide could be due to spatial variation during the coating, derivatization and/or functionalization process. We took precautions to apply the same reagents to the slide at the same conditions in attempt to minimize variation in covalent modification. Coating and derivatization are performed by the manufacturer. It is possible that coating thickness or epoxy derivatization of the coating is variable across the slide, which could lead to some areas having thicker coatings or higher epoxy group density and subsequently, differential binding. This could be further examined using atomic force microscopy or ellipsometry. Without specific knowledge of these manufacturing processes, it is difficult to pinpoint causes to mitigate. In-house produced slide coatings, potentially using zwitterionic gels, could help mitigate this variation. Including standardized reference beads could also help. The seemingly random variation observed in these experiments may be hard to control and surface chemistry needs to be further investigated in order to establish our assay as an alternative to current POC assays for decentralized settings.

Table 7.4: **Estimated cTnI assay LOD (ng/mL) using 9705/20C6 antibody pair in TBSTCa buffer and different slides.**

	Trial 1		Trial 2	
	LOD	R^2	LOD	R^2
MSD at 5s	0.005	0.998	0.025	0.997
Maximum travel	0.005	0.996	0.051	0.972
Enclosing radius	0.012	0.982	0.042	0.985
Slope-intercept distance	0.003	0.965	0.028	0.965
Diffusivity	0.005	0.811	0.049	0.911
Clumped fraction	0.399	0.929	0.579	0.987

7.3.4 Serum components compromise assay performance

Towards demonstration of our assay in a clinically relevant matrix, we trialed the 9705/20C6 antibody pair in cTnI-free serum using the same procedure as was used in experiments with buffer. Serum is a complex matrix of proteins, fats and ions, all of which can foul surfaces and decrease performance. During assay development, it is important to examine and minimize interferences from these components to achieve the highest possible sensitivity.

Results are shown in Figure 7-5, with both trials on the same slide. Serum fouls surfaces to such an extent that all beads stick and no concentration differentiation is possible. Previously noted trends in single bead count increasing with increasing analyte concentration are not observed here, lending further evidence that beads are nonspecifically stuck to the sensing surface due to serum components.

In hopes of gaining insight into components causing fouling, a series of experiments were performed to minimize certain serum components. Eight different pretreatments were performed and compared to buffer in their ability to preserve bead motion when no cTnI is present. Of these eight treatments, seven showed no improvement over serum (Figure 7-6). The off-slide incubation condition was included to ascertain if fouling components bound to the bead and the results confirm this, indicating that separate incubation in serum does not mitigate the fouling effect.

Subsequent trials with PEG(2k)-coated beads on BSA surfaces in serum preserved bead motion and point to a component interacting with antibodies on the surfaces (data

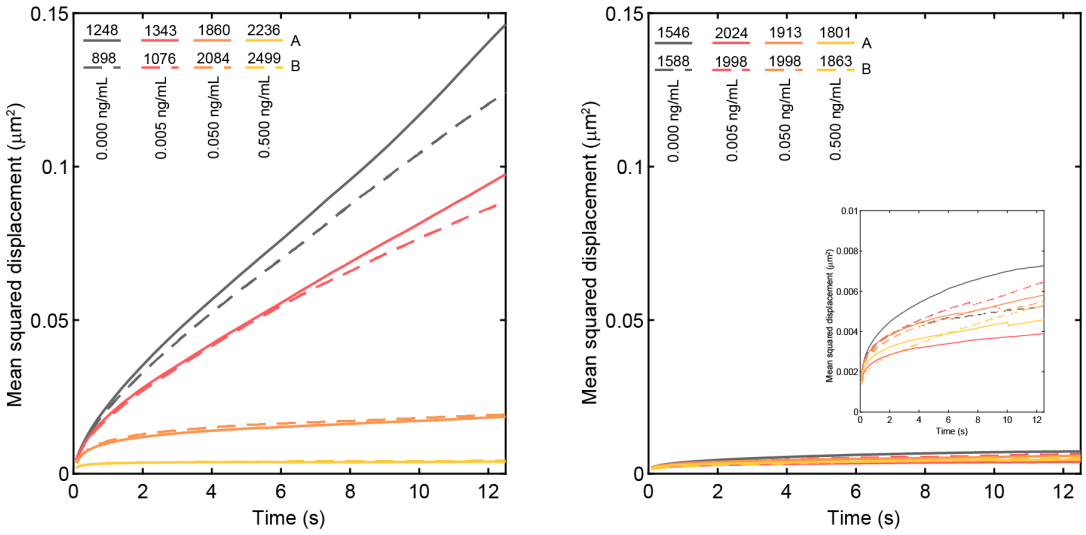

(a) (b)

Figure 7-5: **Comparison between integrated assay in buffer and assay in 100% serum.** (a) Trial one in buffer (same as Figure 7-4a) showing bead movement allows for cTnI concentration differentiation in buffer. (b) Serum components foul the surfaces leading to stuck beads that produce no signal. For each curve, the number of beads analyzed to determine the mean value is indicated by the number above the line legend.

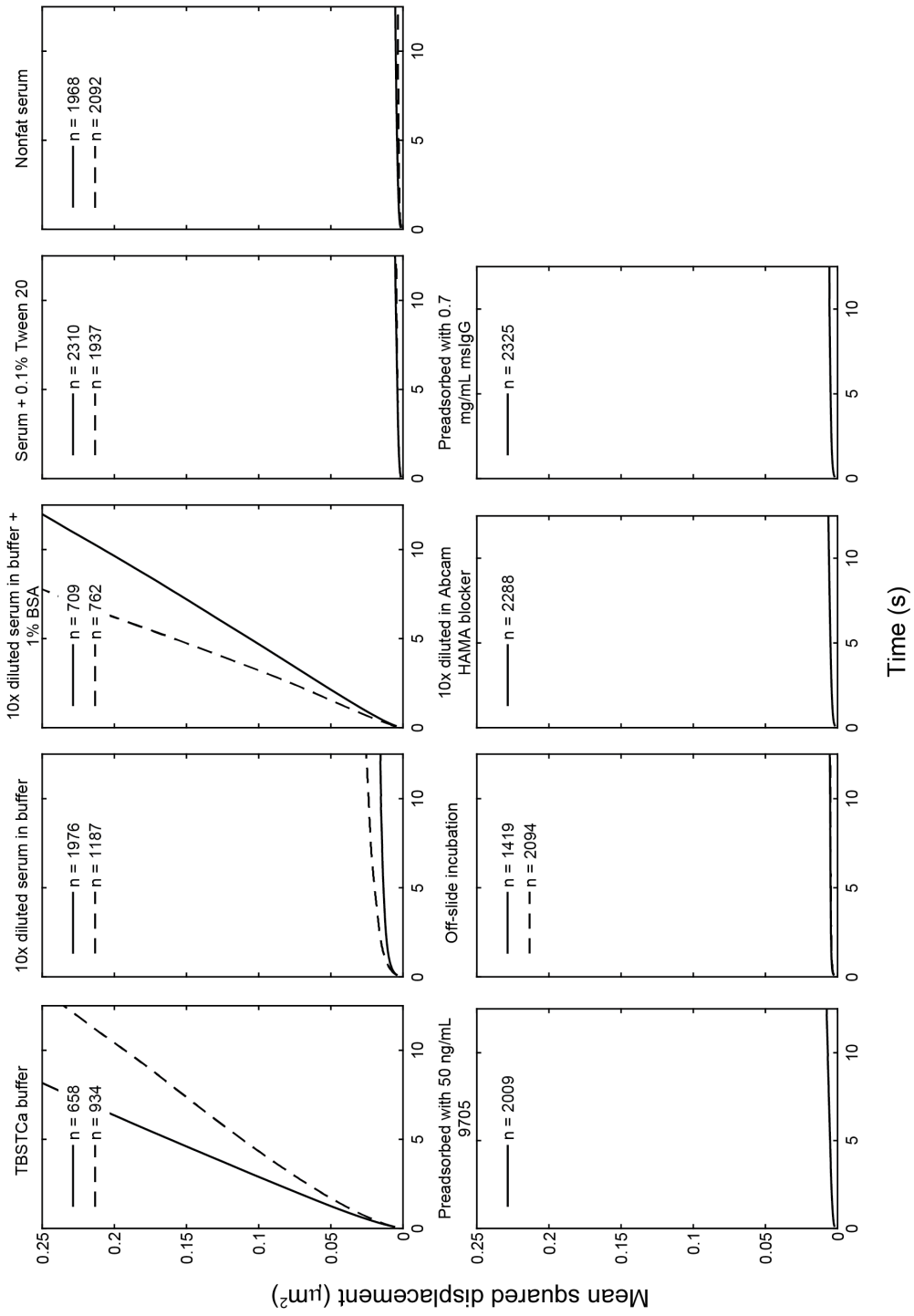

Figure 7-6: **Selective minimization of serum components to determine fouling component(s)**. Each trial used serum treated to remove or minimize one or several components and tested the ability of this altered matrix to preserve bead movement when no cTnI is present. The only treatment that retained bead motion similar to buffer is 10x diluted serum in TBSTCa + 1% (w) BSA (first and third panel, top row, respectively). For each curve, the number of beads analyzed to determine the mean value is indicated by 'n='.

not shown). Literature review of common interferences in immunoassays revealed that naturally occurring human anti-mouse antibodies (HAMA), which occur in up to 40% of the population, can bridge capture and detection antibodies, which are often made in mouse, and result in high background [176–179]. These antibodies have been found to specifically confound the signal in cTnI immunoassays [180]. Methods previously used to mitigate HAMA interference, including dilution in commercially available blocking solution and treatment with polyclonal mouse IgG to adsorb HAMA [171], did not prove efficacious in our hands, suggesting that other serum components may be at play.

We therefore moved forward with the single treatment that preserved bead motion, serum diluted 10x in buffer + 1% (w/v) BSA. This condition was originally included as a treatment mimicking ELISA diluents, which commonly include 1-5% of a blocking agent [181]. A number of different protein and polymer blocking agents have been reported for ELISA and the optimal agent must be determined empirically for each target.

7.3.5 Integrated assay in diluted serum shows LODs on par with previous generation high sensitivity assays

Figure 7-7 shows two trials of the integrated cTnI assay using 10x diluted serum in TBSTCa + 1% (w/v) BSA as the matrix. Similar to replicate assays performed in buffer, we prioritized examination of variation across a single slide. In MSD versus time plots, both sets of individual replicates of the assay show the expected decrease in MSD with increasing cTnI concentration, though the replicate curves of the same concentration show some variation, especially at lower concentrations. Though these trials were performed on slides from different lots, the maximum MSD magnitude is similar, unlike the trials in buffer. It may be that by preserving bead movement through blocking of NSB, BSA also increases assay repeatability.

Interestingly, in comparing the orange and yellow curves in both trials, there is a gap between the MSD curves for 0.500 and 5.000 ng/mL. This gap occurs in all

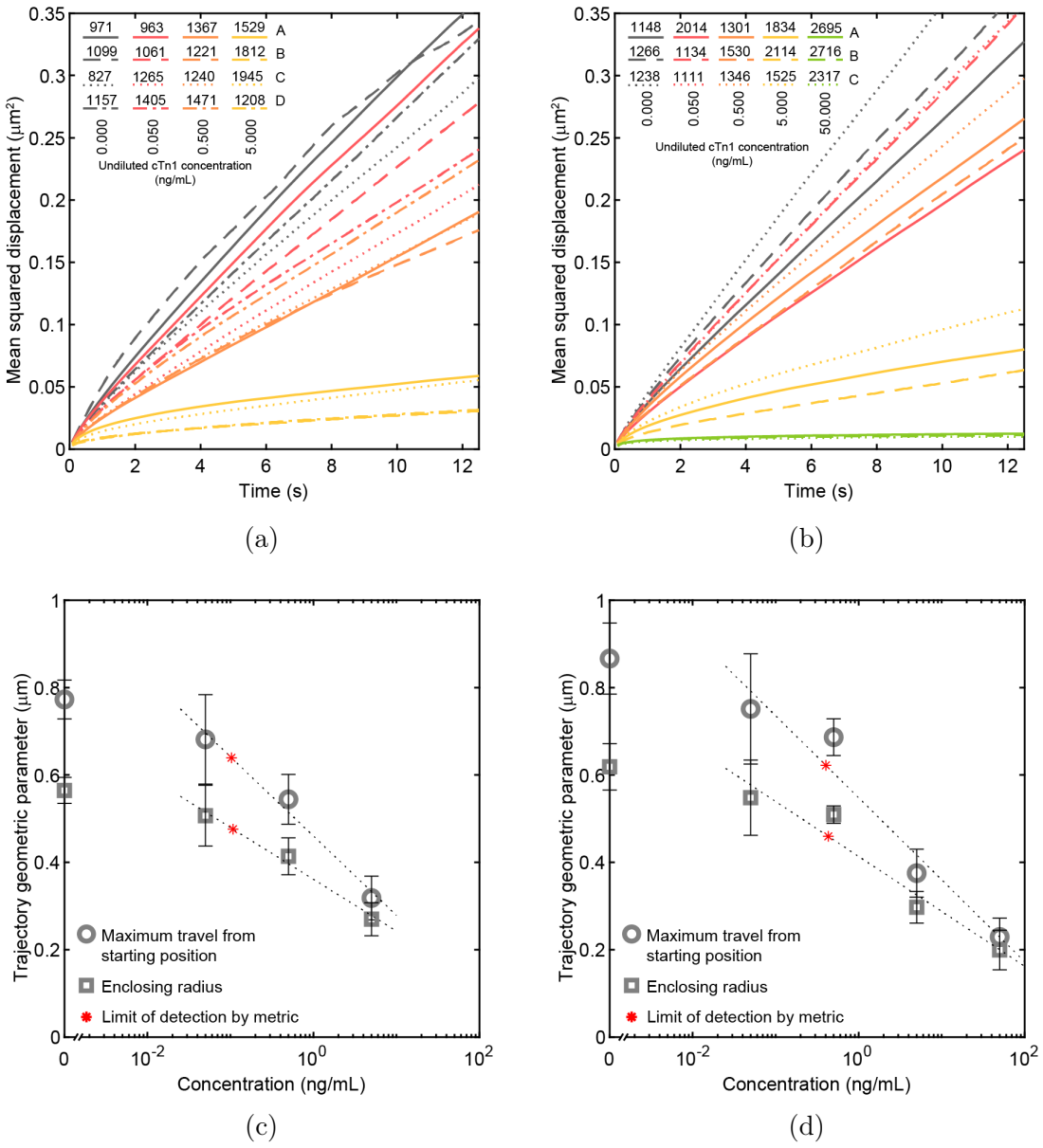

Figure 7-7: **Demonstration of cTnI sensing by integrated assay on different slides and in 10x diluted serum in TBSTCa + 1% (w/v) BSA.** (a,b) Ensemble average MSD versus time and (c,d) dose-response curves for geometry metrics. Plots in the first and second column represent trial 1 and 2, respectively. First column shows results using a 6 month old slide and second column shows results using a one week old slide. Error bars represent the standard deviation of the replicates. For each curve in MSD versus time plots, the number of beads analyzed to determine the mean value is indicated by the number over the corresponding line style in the legend.

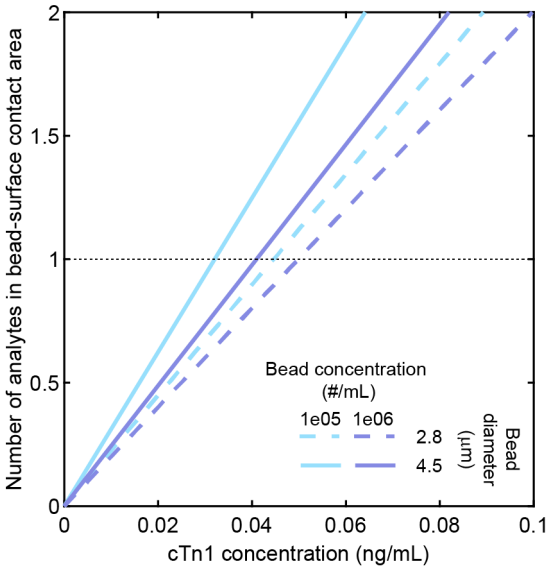

Figure 7-8: **Number of analytes in bead-surface contact area versus cTnI sample concentration.** The critical concentration, at which there is always one analyte instantaneously in the contact area, may be behind observations in Figure 7-7 and limit assay sensitivity.

replicates, suggesting something inherent to the assay is behind this observation. We hypothesize that the number of analytes in the bead-surface contact area, which directly controls probability of bead tethering, may manifest in this behavior. For a given bead, bead concentration, capture (settling) time, analyte and receptor, the concentration at which there is one analyte always instantaneously in the bead-surface contact area can be estimated based on the bound analyte density on the beads. Above this critical concentration, we would predict more consistent signals between replicates, while at concentrations lower than this critical concentration, one would expect only a fraction of beads with bound analyte to show confined motion at any time, leading to noisy signals. When this calculation is performed for the current conditions, one finds that this critical concentration is 0.041 ng/mL (Figure 7-8), which corresponds to an undiluted concentration of 0.410 ng/mL, very close to the orange curve cTnI undiluted concentration, lending validity to our hypothesis. Taken together, this points to the number of analytes per bead potentially limiting the sensitivity of our assay. To increase sensitivity, lowering this critical concentration could be achieved by

methods that increase the bead-surface contact area (such as using larger beads or PEG spacers that effectively make the antibody "longer") or that increase the bound density of analytes (such as using lower bead concentrations or longer capture times). However, all of these modifications come with tradeoffs that must be weighed during the design process; for example, longer capture times would increase the time to result and larger beads would increase the potential for NSB due to larger contact area (see Figure 4-3b).

Several metrics show promise in quantifying cTnI at clinically relevant levels (Table 7.5), with minimum LODs around 0.1 ng/mL. This is ∼5x the LODs of current point-of-care assays (∼0.02 ng/mL [168, 170, 182]) and on par with previous generation high sensitivity assays (LODs ∼ 0.1 - 1 ng/mL [164]). In both trials, the most robust measures are the geometry metrics and their dose-response curves for each trial is shown in Figure 7-7c and 7-7d. Though limited by the smaller concentration range tested, the quadruplicate first trial shows more robust metrics due in part due to better linearity and lower variability in the blank condition. For example, the RSD in maximum travel at the 0.000 ng/mL is 5.8 and 9.4% for the first and second trial, respectively, which manifests in ∼3-8x higher LODs in the second trial. Trials with more concentrations are needed to confirm the response curve and LODs definitively. While we used linear response curves in the data shown here due to limited data points, a greater number of data points could reveal trends better fit by other models, such as the sigmoid response curves seen often in ELISA [24, 183]. Nonetheless, our current results give initial promising evidence that our assay can quantify cTnI at levels relevant for clinical practice.

The wider concentration range in the second trial suggests that our current assay has at least a two orders of magnitude dynamic range, but additional concentrations above 50.000 ng/mL need to be trialed to establish this definitively. For a given metric, the upper limit of the dynamic range will be determined by the concentration which causes the metric to be indistinguishable from that of a population of stuck beads and depends upon the bead size and microscopy conditions such as magnification, frame rate and illumination. For the geometry metrics, based on 728 epoxy 4.5 μm

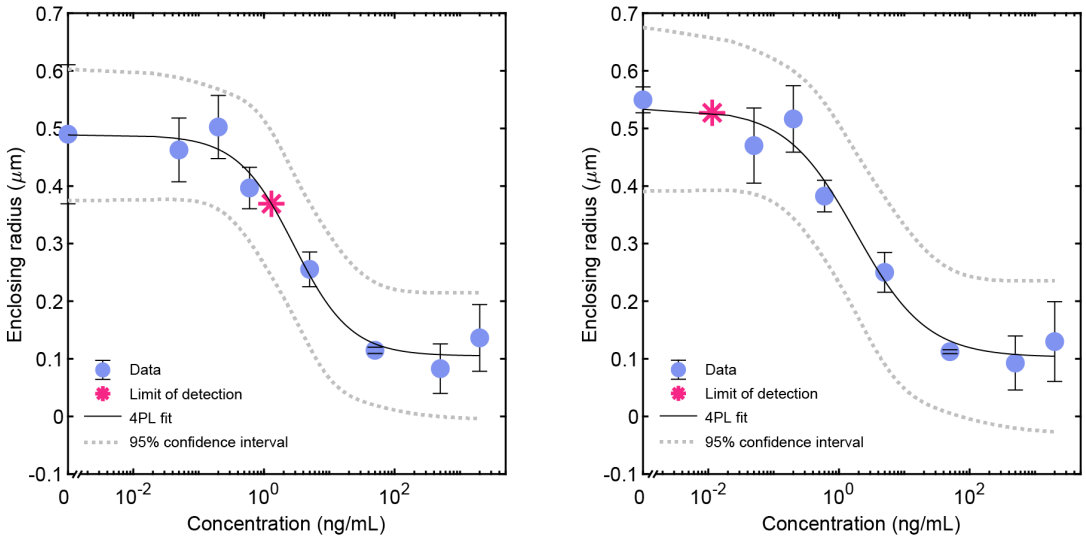

Figure 7-9: **Demonstration of cTnI sensing by integrated assay on different slides and in 10x diluted serum in TBSTCa + 1% (w/v) BSA using concentrations spanning 5 orders of magnitude.** (a) Enclosing radius dose-response curve using data from four replicates, illustrating the effect of outlier data on assay performance metrics. (b) Enclosing radius dose-response curve using data from three replicates, excluding the outlier replicate, illustrating the potential gains in assay performance when variation is minimized. In both plots, error bars are the standard deviation of the replicates included in the plots.

beads stuck to a glass slide at the microscopy conditions used in these experiments, the enclosing radius and the maximum travel were found to be 0.049 and 0.054 μm, respectively. In the 50.000 ng/mL concentration in trial two, the enclosing radius and maximum travel were determined to be 0.199 and 0.229 μm, respectively, suggesting that the dynamic range of our assay is likely broader than that reflected by this experiment.

To examine the dynamic range of our assay, we conducted another experiment utilizing cTnI concentrations spanning five orders of magnitude and tested in quadruplicate. Figure 7-9 shows dose-response curves from this trial using the enclosing radius as the quantification metric. In Figure 7-9a, all four replicates are used to construct the dose-response curve, which predicts an LOD of $\sim$1 ng/mL and a dynamic range of at least three orders of magnitude. The LOD is increased in this trial compared

Table 7.5: **Estimated cTnI assay LOD (ng/mL) using 9705/20C6 antibody pair in 10x diluted serum in TBSTCa + 1% (w/v) BSA and on different slides**

	Trial 1		Trial 2		Trial 3	Trial 3
	LOD	R^2	LOD	R^2	Quadruplicate	Triplicate
MSD at 5s	0.171	0.882	0.350	0.883	1.280	0.200
Maximum travel	0.103	0.980	0.403	0.946	1.340	0.082
Enclosing radius	0.108	0.985	0.431	0.941	1.300	0.012
Slope-intercept distance	0.557	0.937	0.572	0.958	1.440	0.131
Diffusivity	0.109	0.958	0.803	0.946	N/A	N/A
Clumped fraction	139.9	0.734	0.127	0.789	N/A	N/A

to previous trials and is heavily influenced by the variation between the replicates, especially at lower concentrations. One replicate was a clear outlier and contributed to large variance seen in the the 0.000 ng/mL condition; the relative standard deviation of the four replicates at this concentration was 0.25. This variation likely arises from surface chemistry, as has been highlighted previously, and influenced LODs measured by all metrics (Table 7.5).

To illustrate potential sensitivity that can be achieved when experiment repeatability is higher, we replotted dose-reponse curves from this trial using the three replicates that showed similar results (Figure 7-9b). Estimated LOD by enclosing radius using this subset of the data is 0.012 ng/mL, two orders of magnitude lower than when considering data from all four replicates. LODs predicted by other metrics showed a similar trend (Table 7.5). This clearly suggests that our present assay format can achieve LODs on par with previous generation high sensitivity cTnI tests if variability can be decreased via surface chemistry optimization.

Overall, our experiments demonstrate that our integrated bead-based sandwich assay can detect cTnI at clinically relevant levels but in a stand-alone format with a single manual transfer/mixing step. Compared to current commercially available POC assays, our assays has several user advantages (Table 7.6). Current approved POC assays each use a specific automated instrument that can run one sample at a time. While this cuts down on manual handling by the operator, it leads to decreased throughput. In contrast, beyond our device, our assay utilizes a microscope, an

Table 7.6: **Comparison of our integrated assay to commercially available POC assays for cTnI.**

	POC assays[+]	Our assay
LOD (ng/mL)	0.02	0.1-1[*]
Time (min)	15	20
Sample	Whole blood, plasma, serum	Serum
Instrumentation	Specific bench-top or hand-held device	Microscope
Throughput	One sample at a time	Modular, multiple samples

[+] Average of six assays found in [182]; performance of these POC assays is also discussed in [168, 169].
[*] Depends upon metric used and trial, see Table 7.5

instrument commonly found in most levels of labs. Aided by bead settling, the assay procedure does not rely on manual steps or automated pumping, which decouples performing the assay from analyzing the assay such that tests can be carried out in parallel and quickly analyzed after the settling process. These aspects give our assay advantages in terms of user-experience, adaptability, distribution and throughput, making it suitable for decentralized settings. While our prototype device used manual pipetting, it is envisioned that the final device could take the form factor of a cuvette and mixing would be achieved through device inversion.

Current POC assays accept a variety of samples, including whole blood. We used serum in our experiments since it is specified as the standard reference matrix for regulatory testing. One disadvantage with using serum is that it must be separated from other blood components, which is typically done by centrifugation of blood collected in a special tube containing reagents to activate the complement cascade. This adds another step and instrumentation to the assay procedure, so it would be optimal if our assay could also accept whole blood samples. To ensure robust performance and analysis for this matrix type, modifications to the device would be necessary. For instance, a background of blood cells would make microscopy of beads difficult. Sequestration of blood cells from beads after mixing could be achieved via a filter or density barrier at the bottom of the well.

How could we improve the current assay to achieve increased performance in

terms of sensitivity? In this bead-surface system, sensitivity is controlled by the interaction of the beads with the surface and variability between sensing surfaces is currently the largest challenge for our assay. Results suggest that the density of bound analyte on the beads controls sensing of bead confinement and the ability to differentiate low concentration samples from the blank condition. Using larger beads and lower bead concentrations may be one way to achieve higher bound analyte density. However, theoretical data presented in Figure 7-8 suggest that improvements by these adjustments may only result in minimal, ∼1.3x gains in sensitivity. These adjustments would also have tradeoffs that would need to be evaluated in the development process. Optimizing surface chemistry to ensure that all beads without analyte move freely would help to increase sensitivity. Including BSA made MSD more consistent between slides, suggesting NSB was not optimally mitigated in previous buffer trials. Other functionalization chemistrys could also be explored. Another method could be using zwitterionic surface coatings, which by our data and literature studies [62,63], have been shown to decrease NSB even when coated at small thicknesses. Other blocking agents, such as casein or polymer-based reagents, could also be explored to examine if they more robustly block surfaces in this specific application. Trialing these modifications methodically is important, as a combination of these factors would likely lead to the best performing assay.

7.4 Conclusion

Using a prototype device that integrates capture-while-settling and bead diffusion and requires a single manual sample transfer step, we demonstrated sensing of cTnI in a clinically relevant matrix with a LOD of ∼0.1 ng/mL. Though this sensitivity is decreased compared to that of commercially available POC devices, it is similar to previous generation high sensitivity automated laboratory assays and our device has user-friendly advantages that make it more suitable for the constraints found in decentralized settings. The stand-alone device lends itself to high-throughput analysis using simple microscopy and an automated image analysis algorithm, all aspects that

make our platform widely distributable and not reliant on specific, low-throughput analysis instrumentation. The current iteration returns results within 20 minutes, less than the typical primary care appointment time and only slightly greater than that of current POC assays. This is especially relevant for cTnI, the elevated presence of which indicates the emergent condition of cardiac injury. In its current iteration, our assay already meets many of the ASSURED ideals for POC diagnostics [148, 162], suggesting its suitability for resource-limited settings. However, our assay is limited by variability originating from the sensing surface, which needs to be optimized for full clinical utility. With further improvements to enhance sensitivity, our platform could quantify cTnI with accuracy of automated lab-based or POC systems with a usability profile approaching that of lateral flow assays, a step forward in filling gaps in decentralized bioanalysis.

THIS PAGE INTENTIONALLY LEFT BLANK

Chapter 8

Conclusion and outlook

8.1 Summary and contributions

Motivated by the gap in bioassays for decentralized settings, this thesis described an affinity assay platform suitable for point-of-care bioanalysis based on the integration of bead settling with mechanical actuation of microspheres. This combination was hypothesized to enable a standalone assay which does not depend on complicated and dedicated external instrumentation, multiple manual manipulations, specialized knowledge or custom materials. All of these aspects provide advantages that could also make our platform widely deliverable. The development and validation of our method took place in six chapters:

- **Chapter 2** presented a framework for analyzing the physics of bead-based analyte capture based on scaling relationships and synthesis of results from multiple fields. Using these methods, we analyzed the capture-while-settling mechanism to determine the limiting physics for this method over a range of bioanalytes. Results suggest that, while capture-while-settling does not provide a mass transport advantage for smaller analytes, it does for larger analytes predominantly through interception. We subsequently compared the mass transport-limited capture of protein analytes on settling beads to that on a stagnant bead array, such as might be found in an ELISA well, and predicted

that the capture-while-settling mechanism enhances mass transport significantly when compared to stagnant diffusion to a planar bead array, even for small analytes. It is our hope that this framework can aid other scientists and engineers in designing and selecting bead-based capture methods suitable for their specific application.

- **Chapter 3** described actuation of microspheres via gravity- or vibration-induced sedimentation as a method to differentiate between nonspecifically and specifically bound beads, and ultimately determine analyte concentration by stuck bead count. We iteratively investigated surface coatings that yielded the lowest nonspecific binding (NSB), leading to a surface functionalization that formed the foundation for subsequent work. In trials using the FcMBL-mannan model system, we found that both gravity- and vibration-aided methods were able to differentiate between mannan concentrations. However, the performance of this assay was limited by variations in surface chemistry.

- **Chapter 4** discussed iRMA, which utilizes bead rolling on a inclined plane to tether analyte-bound beads and remove beads without analyte. Analytical modeling of the processes involved in iRMA for SARS-CoV-2 virions initially validated our concept, suggesting that the combination of bead settling and bead rolling using 7-11 μm silica beads could return a result in $<$30 minutes. While initial experimental results for bead rolling on inclined planes at 60 or 80° seemed promising, we found that NSB and bead quality limited the realization of this assay.

- **Chapter 5** introduced naturally occuring bead motion via thermal diffusion as a sensing mechanism. Using the FcMBL-mannan model assay, we demonstrated that this sensing mechanism has at least picomolar sensitivity, a relevant concentration for many clinical analytes. By using different bead concentrations and surface manipulations, we showed that the sensitivity of the assay is controlled by the bead-bound analyte density and that inverting the slide to promote additional gravity-induced sedimentation of weakly held beads could increase

sensitivity. We examined other quantification metrics aside from mean squared displacement, with our results suggesting that other metrics could yield more sensitive quantification. Finally, we initially demonstrated the ability to differentiate between mannan concentration using an integrated capture-while-settling and diffusion assay, with estimated initial detection limits of ∼1 ng/mL. These results build on previous diffusion-based assays, but extend the mechanism to using larger beads, amenable to lower powered microscopy, and analysis by novel metrics.

- **Chapter 6** theoretically and experimentally explored NSB in the context of bead-surface systems. Theoretical models of the main physical force behind bead-surface NSB, the van der Waals (vdW) force, suggested that a combination of surface coatings could decrease the force of these interactions by ∼1000x. Experiments involving PEG-coated beads of two different sizes, different hydrogel or polymer coated surfaces and buffer with and without Tween 20, suggested that, though surface coatings do decrease bead-surface interactions, chemical interactions maybe the largest contributor to NSB in our systems, as the addition of Tween 20 nearly eliminated NSB in some cases. We performed an initial FcMBL-mannan bead diffusion experiment using the best performing coating, a zwitterionic (ZI) polymer, in buffer with Tween 20 and showed preliminary evidence of enhanced sensitivity using this surface. The work in this chapter contributes more theoretical and empirical evidence to bead-surface NSB, which remains relatively under investigated, and lays the foundation for future experiments using ZI-coated surfaces.

- **Chapter 7** integrated capture-while-settling and bead diffusion in a prototype device towards demonstration of cardiac troponin I (cTnI) sensing. After screening of capture and detection antibody pairs, we demonstrated detection of cTnI in buffer with a limit of detection of 0.010 ng/mL, on par with current point-of-care (POC) handheld devices [169, 170]. When serum was trialed as the matrix, we found that it completely fouled the surfaces, leading to no distin-

guishable signal. Despite iterative experiments, the specific cause of this fouling could not be pinpointed. However, diluting serum in buffer with 1% (w/v) BSA retained bead motion and this matrix was used to demonstrate the integrated assay with a minimum limit of detection of 0.100 ng/mL, which is ∼5x higher than current POC assays, but with the added advantage of increased usability. Notably, in both the buffer and the diluted serum experiment, variation on a single sensing surface, between surfaces from the same lot and between surfaces from different lots was observed. This is currently the largest bottleneck to achieving greater sensitivity, and mitigation will require improved manufacturing of surface coatings or use of reference beads or surfaces.

Our current results place the capture-while-settling + bead diffusion assay squarely in the gap described in Chapter 1 (Figure 8-1). By tuning bead density and size, so that capture can occur passively and without a separate module, and integrating this with a naturally-occurring phenomena to produce a quantifiable signal in a single device, indicative of analyte concentration, our platform combines the high sensitivity of ELISA-based assays with the ease-of-use profile of LFAs. This represents an important step in the progress towards an ideal decentralized assay.

8.2 Proposed future work and outlook for our diagnostic platform

This work provided the initial validation for the proposed sensing system. Subsequent work should focus on optimizing the current system through various theoretical and experimental investigations. As extensively mentioned through this thesis and well-noted in the literature, NSB is the main barrier to realizing increased sensitivity in assays. Therefore, first and foremost, future work should focus on increasing the robustness of the planar sensing surface, as this seems to cause the most variation in our assay. Strategies to do this include:

- Determination of coating thickness or functional group density variation across

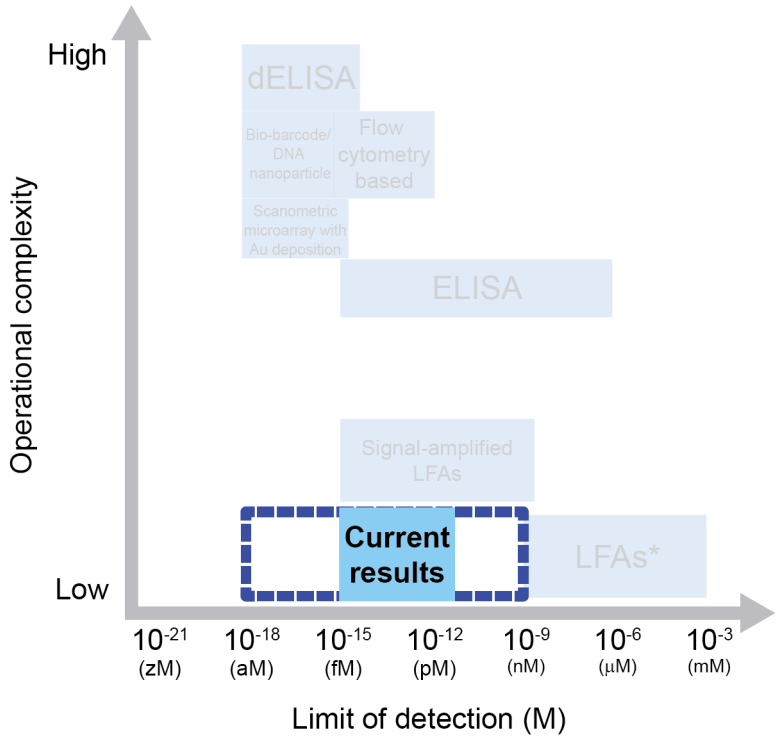

Figure 8-1: **Comparison of the described bead settling + diffusion assay with the current affinity assay landscape.** The demonstrated performance of 0.010 - 1 ng/mL sensitivity (depending on the matrix) within 20 minutes places our assay squarely in the gap between high sensitivity ELISA-based assays and LFAs, suggesting our platform has merit for decentralized testing.

the currently used slides via atomic force microscopy or ellipsometry.

- Characterization of the assay using other blocking agents, including casein or polymer blockers, to see if a different blocking molecule increases assay robustness, in both buffer and diluted serum matrices.

- Optimization of ZI coating and functionalization protocols to create robust antibody-functionalized ZI-coated sensing surfaces towards investigating their ability to decrease NSB and increase sensitivity of the current assay.

- Exploration of image processing algorithms that retain sufficient statistical power but filter the data to uncover signals that may be masked by large confined bead backgrounds.

- Determination of the dynamic range of the current assay through replicate experiments using concentrations sweeps over 5+ orders of magnitude.

- Further experimentation with the 560/9707 antibody pair to determine if this combination shows better performance in buffer and diluted serum. Additionally, optimization of bead concentration should take place for both antibody pairs, since this is a critical parameter to achieve sensitivity.

Additionally, provided a suitable affinity agent can be identified, our platform can be extended to other clinically relevant biomarkers as well as other applications in food or water contaminant monitoring, which can suffer from the same gaps as decentralized diagnostics. Given the ease-of-use and initial sensitivity demonstrated in this work, it would be warranted to explore the needs and use-cases for bioanalysis in these spaces.

Bibliography

[1] Kenneth A. Sikaris. Enhancing the clinical value of medical laboratory testing. *Clinical Biochemist Reviews*, 38(3):107–114, 2017.

[2] World Health Organization. The selection and use of essential in vitro diagnostics. Technical report, 2021.

[3] Amy L. McGuire, Stacey Gabriel, Sarah A. Tishkoff, Ambroise Wonkam, Aravinda Chakravarti, Eileen E.M. Furlong, Barbara Treutlein, Alexander Meissner, Howard Y. Chang, Núria López-Bigas, Eran Segal, and Jin Soo Kim. The road ahead in genetics and genomics. *Nature Reviews Genetics*, 21(10):581–596, 2020.

[4] Kenneth A. Fleming, Susan Horton, Michael L. Wilson, Rifat Atun, Kristen DeStigter, John Flanigan, Shahin Sayed, Pierrick Adam, Bertha Aguilar, Savvas Andronikou, Catharina Boehme, William Cherniak, Annie NY Cheung, Bernice Dahn, Lluis Donoso-Bach, Tania Douglas, Patricia Garcia, Sarwat Hussain, Hari S. Iyer, Mikashmi Kohli, Alain B. Labrique, Lai Meng Looi, John G. Meara, John Nkengasong, Madhukar Pai, Kara Lee Pool, Kaushik Ramaiya, Lee Schroeder, Devanshi Shah, Richard Sullivan, Bien Soo Tan, and Kamini Walia. The Lancet Commission on diagnostics: transforming access to diagnostics. *The Lancet*, 398(10315):1997–2050, 2021.

[5] Harika Yadav, Devanshi Shah, Shahin Sayed, Susan Horton, and Lee F. Schroeder. Availability of essential diagnostics in ten low-income and middle-income countries: results from national health facility surveys. *The Lancet Global Health*, 9(11):e1553–e1560, 2021.

[6] Tobias M. Holden, Reese A.K. Richardson, Philip Arevalo, Wayne A. Duffus, Manuela Runge, Elena Whitney, Leslie Wise, Ngozi O. Ezike, Sarah Patrick, Sarah Cobey, and Jaline Gerardin. Geographic and demographic heterogeneity of SARS-CoV-2 diagnostic testing in Illinois, USA, March to December 2020. *BMC Public Health*, 21(1):1–13, 2021.

[7] Benjamin Heidt, Williane F. Siqueira, Kasper Eersels, Hanne Diliën, Bart Van Grinsven, Ricardo T. Fujiwara, and Thomas J. Cleij. Point of care diagnostics in resource-limited settings: A review of the present and future of PoC in its most needed environment. *Biosensors*, 10(10), 2020.

[8] Nitika Pant Pai, Caroline Vadnais, Claudia Denkinger, Nora Engel, and Madhukar Pai. Point-of-Care Testing for Infectious Diseases: Diversity, Complexity, and Barriers in Low- And Middle-Income Countries. *PLoS Medicine*, 9(9), 2012.

[9] Enrique Valera, Aaron Jankelow, Jongwon Lim, Victoria Kindratenko, Anurup Ganguli, Karen White, James Kumar, and Rashid Bashir. COVID-19 Point-of-Care Diagnostics: Present and Future. *ACS Nano*, 15(5):7899–7906, 2021.

[10] Simon Rattle, Oliver Hofmann, Christopher Price, Larry J. Kricka, and David Wild. Lab-on-a-chip, micro- and nanoscale immunoassay systems, and microarrays. In *The iImunoassay Handbook*, pages 175–202. 2013.

[11] Michael M. Kaminski, Omar O. Abudayyeh, Jonathan S. Gootenberg, Feng Zhang, and James J. Collins. CRISPR-based diagnostics. *Nature Biomedical Engineering*, 5(7):643–656, 2021.

[12] Yilin Liu, Li Zhan, Zhenpeng Qin, James Sackrison, and John C. Bischof. Ultrasensitive and Highly Specific Lateral Flow Assays for Point-of-Care Diagnosis. *ACS Nano*, 15(3):3593–3611, 2021.

[13] Jobie Budd, Benjamin S. Miller, Nicole E. Weckman, Dounia Cherkaoui, Da Huang, Alyssa Thomas Decruz, Noah Fongwen, Gyeo-Re Han, Marta Broto, Claudia S. Estcourt, Jo Gibbs, Deenan Pillay, Pam Sonnenberg, Robyn Meurant, Michael R. Thomas, Neil Keegan, Molly M. Stevens, Eleni Nastouli, Eric J. Topol, Anne M. Johnson, Maryam Shahmanesh, Aydogan Ozcan, James J. Collins, Marta Fernandez Suarez, Bill Rodriguez, Rosanna W. Peeling, and Rachel A. McKendry. Lateral flow test engineering and lessons learned from COVID-19. *Nature Reviews Bioengineering*, 1(1):13–31, 2023.

[14] George M. Whitesides. The origins and the future of microfluidics. *Nature*, 442(7101):368–373, 2006.

[15] Eric K. Sackmann, Anna L. Fulton, and David J. Beebe. The present and future role of microfluidics in biomedical research. *Nature*, 507(7491):181–189, 2014.

[16] Daniel T. Chiu, Andrew J. DeMello, Dino Di Carlo, Patrick S. Doyle, Carl Hansen, Richard M. Maceiczyk, and Robert C.R. Wootton. Small but Perfectly Formed? Successes, Challenges, and Opportunities for Microfluidics in the Chemical and Biological Sciences. *Chem*, 2(2):201–223, 2017.

[17] Azadeh Nilghaz, Liyun Guan, Weirui Tan, and Wei Shen. Advances of Paper-Based Microfluidics for Diagnostics - The Original Motivation and Current Status. *ACS Sensors*, 1(12):1382–1393, 2016.

[18] C. Wyatt Shields, Korine A. Ohiri, Luisa M. Szott, and Gabriel P. López. Translating microfluidics: Cell separation technologies and their barriers to commercialization. *Cytometry Part B - Clinical Cytometry*, 92(2):115–125, 2017.

[19] Kwi Nam Han, Cheng Ai Li, and Gi Hun Seong. Microfluidic chips for immunoassays. *Annual Review of Analytical Chemistry*, 6:119–141, 2013.

[20] Byoung Hoon Kang, Youngseop Lee, Eun Sil Yu, Hamin Na, Minhee Kang, Hee Jae Huh, and Ki Hun Jeong. Ultrafast and Real-Time Nanoplasmonic On-Chip Polymerase Chain Reaction for Rapid and Quantitative Molecular Diagnostics. *ACS Nano*, 15(6):10194–10202, 2021.

[21] Guanglei Fu, Yabin Zhu, Kui Xu, Weihua Wang, Ruixia Hou, and Xiujun Li. Photothermal Microfluidic Sensing Platform Using Near-Infrared Laser-Driven Multiplexed Dual-Mode Visual Quantitative Readout. *Analytical Chemistry*, 91(20):13290–13296, 2019.

[22] Mohamed S. Draz, Anish Vasan, Aradana Muthupandian, Manoj Kumar Kanakasabapathy, Prudhvi Thirumalaraju, Aparna Sreeram, Sanchana Krishnakumar, Vinish Yogesh, Wenyu Lin, Xu G. Yu, Raymond T. Chung, and Hadi Shafiee. Virus detection using nanoparticles and deep neural network-enabled smartphone system. *Science Advances*, 6(51):1–13, 2020.

[23] David M. Rissin, Cheuk W. Kan, Todd G. Campbell, Stuart C. Howes, David R. Fournier, Linan Song, Tomasz Piech, Purvish P. Patel, Lei Chang, Andrew J. Rivnak, Evan P. Ferrell, Jeffrey D. Randall, Gail K. Provuncher, David R. Walt, and David C. Duffy. Single-molecule enzyme-linked immunosorbent assay detects serum proteins at subfemtomolar concentrations. *Nature Biotechnology*, 28(6):595–599, 2010.

[24] Limor Cohen, Naiwen Cui, Yamei Cai, Padric M. Garden, Xiang Li, David A. Weitz, and David R. Walt. Single Molecule Protein Detection with Attomolar Sensitivity Using Droplet Digital Enzyme-Linked Immunosorbent Assay. *ACS Nano*, 14(8):9491–9501, 2020.

[25] Limor Cohen and David R. Walt. Single-Molecule Arrays for Protein and Nucleic Acid Analysis. *Annual Review of Analytical Chemistry*, 10(1):345–363, 2017.

[26] Jwa-min Nam, C Shad Thaxton, and Chad A Mirkin. Nanoparticle-Based Bio – Bar Codes for the Ultrasensitive. *Science*, 301(September):1884–1887, 2003.

[27] Dongwoo Kim, Weston L. Daniel, and Chad A. Mirkin. Microarray-based multiplexed scanometric immunoassay for protein cancer markers using gold nanoparticle probes. *Analytical Chemistry*, 81(21):9183–9187, 2009.

[28] Curtis D. Chin, Vincent Linder, and Samuel K. Sia. Commercialization of microfluidic point-of-care diagnostic devices. *Lab on a Chip*, 12(12):2118–2134, 2012.

[29] S. P. Mulvaney, C. L. Cole, M. D. Kniller, M. Malito, C. R. Tamanaha, J. C. Rife, M. W. Stanton, and L. J. Whitman. Rapid, femtomolar bioassays in complex matrices combining microfluidics and magnetoelectronics. *Biosensors and Bioelectronics*, 23(2):191–200, 2007.

[30] S. P. Mulvaney, C. N. Ibe, C. R. Tamanaha, and L. J. Whitman. Direct detection of genomic DNA with fluidic force discrimination assays. *Analytical Biochemistry*, 392(2):139–144, 2009.

[31] S. P. Mulvaney, K. M. Myers, P. E. Sheehan, and L. J. Whitman. Attomolar protein detection in complex sample matrices with semi-homogeneous fluidic force discrimination assays. *Biosensors and Bioelectronics*, 24(5):1109–1115, 2009.

[32] Shawn P. Mulvaney, Carol N. Ibe, Jane M. Caldwell, Jay F. Levine, Lloyd J. Whitman, and Cy R. Tamanaha. Detection of mitochondrial DNA with the compact bead array sensor system (cBASS). *Frontiers in Pathogen Detection: From Nanosensors to Systems*, 7553(February 2009):71670V, 2009.

[33] Betsy Jean Yakes, Stacey M. Etheridge, Shawn P. Mulvaney, and Cy R. Tamanaha. Fluidic force discrimination assays: A new technology for tetrodotoxin detection. *Marine Drugs*, 8(3):565–576, 2010.

[34] H. Cumhur Tekin, Matteo Cornaglia, and Martin A.M. Gijs. Attomolar protein detection using a magnetic bead surface coverage assay. *Lab on a Chip*, 13(6):1053–1059, 2013.

[35] Matteo Cornaglia, Raphaël Trouillon, H. Cumhur Tekin, Thomas Lehnert, and Martin A.M. Gijs. Magnetic particle-scanning for ultrasensitive immunodetection on-chip. *Analytical Chemistry*, 86(16):8213–8223, 2014.

[36] M. Cornaglia, H. C. Tekin, T. Lehnert, and M. A.M. Gijs. Fine-tuning of magnetic and microfluidic viscous forces for specific magnetic bead-based immunocomplex formation. *Journal of Applied Physics*, 114(6), 2013.

[37] Matteo Cornaglia, Raphaël Trouillon, H. Cumhur Tekin, Thomas Lehnert, and Martin A.M. Gijs. Dose-response curve of a microfluidic magnetic bead-based surface coverage sandwich assay. *New Biotechnology*, 32(5):433–440, 2015.

[38] Victor N. Morozov, Stephanie Groves, Michael J. Turell, and Charles Bailey. Three minutes-long electrophoretically assisted zeptomolar microfluidic immunoassay with magnetic-beads detection. *Journal of the American Chemical Society*, 129(42):12628–12629, 2007.

[39] Yuri M. Shlyapnikov, Elena A. Shlyapnikova, Maria A. Simonova, Anna O. Shepelyakovskaya, Fedor A. Brovko, Ravilya L. Komaleva, Eugene V. Grishin, and Victor N. Morozov. Rapid simultaneous ultrasensitive immunodetection of five bacterial toxins. *Analytical Chemistry*, 84(13):5596–5603, 2012.

[40] Victor N. Morozov and Tamara Ya Morozova. Active bead-linked immunoassay on protein microarrays. *Analytica Chimica Acta*, 564(1):40–52, 2006.

[41] Tamara Y. Morozova and Victor N. Morozov. Force differentiation in recognition of cross-reactive antigens by magnetic beads. *Analytical Biochemistry*, 374(2):263–271, 2008.

[42] Gavin Garvey, David Shakarisaz, Federico Ruiz-Ruiz, Anna E.V. Hagström, Balakrishnan Raja, Carmen Pascente, Archana Kar, Katerina Kourentzi, Marco Rito-Palomares, Paul Ruchhoeft, and Richard C. Willson. Microretroreflector-sedimentation immunoassays for pathogen detection. *Analytical Chemistry*, 86(18):9029–9035, 2014.

[43] Ka Ram Kim, Hyeong Jin Chun, Kyung Won Lee, Kwan Young Jeong, Jae Ho Kim, and Hyun C. Yoon. Wash-free non-spectroscopic optical immunoassay by controlling retroreflective microparticle movement in a microfluidic chip. *Lab on a Chip*, 19(23):3931–3942, 2019.

[44] Emiel W.A. Visser, Leo J. Van Ijzendoorn, and Menno W.J. Prins. Particle Motion Analysis Reveals Nanoscale Bond Characteristics and Enhances Dynamic Range for Biosensing. *ACS Nano*, 10(3):3093–3101, 2016.

[45] Emiel W.A. Visser, Junhong Yan, Leo J. Van IJzendoorn, and Menno W.J. Prins. Continuous biomarker monitoring by particle mobility sensing with single molecule resolution. *Nature Communications*, 9(1), 2018.

[46] Koen E. Merkus, Menno W.J. Prins, and Cornelis Storm. Single-Bond Association Kinetics Determined by Tethered Particle Motion: Concept and Simulations. *Biophysical Journal*, 111(8):1612–1620, 2016.

[47] Alissa D. Buskermolen, Yu Ting Lin, Laura van Smeden, Rik B. van Haaften, Junhong Yan, Khulan Sergelen, Arthur M. de Jong, and Menno W.J. Prins. Continuous biomarker monitoring with single molecule resolution by measuring free particle motion. *Nature Communications*, 13(1):1–12, 2022.

[48] Kenji Akama, Niina Iwanaga, Koya Yamawaki, Masaki Okuda, Krupali Jain, Hiroshi Ueno, Naoki Soga, Yoshihiro Minagawa, and Hiroyuki Noji. Wash-And Amplification-Free Digital Immunoassay Based on Single-Particle Motion Analysis. *ACS Nano*, 2019.

[49] Kenji Akama and Hiroyuki Noji. Multiplexed homogeneous digital immunoassay based on single-particle motion analysis. *Lab on a Chip*, 20(12):2113–2121, 2020.

[50] Kenji Akama and Hiroyuki Noji. Multiparameter single-particle motion analysis for homogeneous digital immunoassay. *Analyst*, 146(4):1303–1310, 2021.

[51] Hao Shen, Lawrence J. Tauzin, Rashad Baiyasi, Wenxiao Wang, Nicholas Moringo, Bo Shuang, and Christy F. Landes. Single Particle Tracking: From Theory to Biophysical Applications. *Chemical Reviews*, 117(11):7331–7376, 2017.

[52] Andreas Frutiger, Alexander Tanno, Stephanie Hwu, Raphael F. Tiefenauer, János Vörös, and Nako Nakatsuka. Nonspecific Binding - Fundamental Concepts and Consequences for Biosensing Applications. *Chemical Reviews*, 121(13):8095–8160, 2021.

[53] D. Leckband, S. Sheth, and A. Halperin. Grafted poly(ethylene oxide) brushes as nonfouling surface coatings. *Journal of Biomaterials Science, Polymer Edition*, 10(10):1125–1147, 1999.

[54] Mengyi Li, Shuai Jiang, Johanna Simon, David Paßlick, Marie Luise Frey, Manfred Wagner, Volker Mailander, Daniel Crespy, and Katharina Landfester. Brush conformation of polyethylene glycol determines the stealth effect of nanocarriers in the low protein adsorption regime. *Nano Letters*, 21(4):1591–1598, 2021.

[55] Beatriz Pelaz, Pablo Del Pino, Pauline Maffre, Raimo Hartmann, Marta Gallego, Sara Rivera-Fernández, Jesus M. De La Fuente, G. Ulrich Nienhaus, and Wolfgang J. Parak. Surface Functionalization of Nanoparticles with Polyethylene Glycol: Effects on Protein Adsorption and Cellular Uptake. *ACS Nano*, 9(7):6996–7008, 2015.

[56] A. Halperin. Polymer brushes that resist adsorption of model proteins: Design parameters. *Langmuir*, 15(7):2525–2533, 1999.

[57] Deborah Leckband and Jacob Israelachvili. *Intermolecular forces in biology*, volume 34. MIT Libraries, 2001.

[58] P. G. de Gennes. Conformations of Polymers Attached to an Interface. *Macromolecules*, 13(5):1069–1075, 1980.

[59] Jacob Israelachvili. *Intermolecular and Surface Forces*. 2011.

[60] Yanxian Zhang, Yonglan Liu, Baiping Ren, Dong Zhang, Shaowen Xie, Yung Chang, Jintao Yang, Jiang Wu, Lijian Xu, and Jie Zheng. Fundamentals and applications of zwitterionic antifouling polymers. *Journal of Physics D: Applied Physics*, 52(40), 2019.

[61] Jacob Baggerman, Maarten M.J. Smulders, and Han Zuilhof. Romantic Surfaces: A Systematic Overview of Stable, Biospecific, and Antifouling Zwitterionic Surfaces. *Langmuir*, 35(5):1072–1084, 2019.

[62] Jihyun Byun, Soojeong Cho, Jeong Moon, Hongki Kim, Hyunju Kang, Juyeon Jung, Eun Kyung Lim, Jinyoung Jeong, Hyun Gyu Park, Woo Kyung Cho, and Taejoon Kang. Zwitterionic Polydopamine/Protein G Coating for Antibody Immobilization: Toward Suppression of Nonspecific Binding in Immunoassays. *ACS Applied Bio Materials*, 3(6):3631–3639, 2020.

[63] Ying Nien Chou, Fang Sun, Hsiang Chieh Hung, Priyesh Jain, Andrew Sinclair, Peng Zhang, Tao Bai, Yung Chang, Ten Chin Wen, Qiuming Yu, and Shaoyi Jiang. Ultra-low fouling and high antibody loading zwitterionic hydrogel coatings for sensing and detection in complex media. *Acta Biomaterialia*, 40:31–37, 2016.

[64] Srigokul Upadhyayula, Timothy Quinata, Stephen Bishop, Sharad Gupta, Noah Ray Johnson, Baharak Bahmani, Kliment Bozhilov, Jeremy Stubbs, Pamela Jreij, Pratima Nallagatla, and Valentine I. Vullev. Coatings of polyethylene glycol for suppressing adhesion between solid microspheres and flat surfaces. *Langmuir*, 28(11):5059–5069, 2012.

[65] N. V. Efremova, S. R. Sheth, and D. E. Leckband. Protein-induced changes in poly(ethylene glycol) brushes: Molecular weight and temperature dependence. *Langmuir*, 17(24):7628–7636, 2001.

[66] A. K. Kenworthy, K. Hristova, D. Needham, and T. J. McIntosh. Range and magnitude of the steric pressure between bilayers containing phospholipids with covalently attached poly(ethylene glycol). *Biophysical Journal*, 68(5):1921–1936, 1995.

[67] Asha Jacob, Leo J Van Ijzendoorn, Arthur M De Jong, and Menno W J Prins. Quantification of Protein Ligand Dissociation Kinetics in Heterogeneous Affinity Assays. *American Chemical Society*, 84:9287–9294, 2012.

[68] Naoko Sato, Yurina Aoyama, Junpei Yamanaka, Akiko Toyotama, and Tohru Okuzono. Particle Adsorption on Hydrogel Surfaces in Aqueous Media due to van der Waals Attraction. *Scientific Reports*, 7(1):1–10, 2017.

[69] Sang Jae Kim Hong Eui Yong, Karthikeyan Krishnamoorthy, Kim Tae Hyun. Modulation of substrate van der Waals forces using varying thicknesses of polymer overlays. *Journal of Industrial and Engineering Chemistry*, 580:690–699, 2020.

[70] Limor Cohen and David R. Walt. Single-molecule arrays for protein and nucleic acid analysis. *Annual Review of Analytical Chemistry*, 10:345–363, 2017.

[71] Chia-Hsien Hsu, Chihchen Chen, Daniel Irimia, and Mehmet Toner. Fast sorting of CD4+ T cells from whole blood using glass microbubbles. *Technology*, 03(01):38–44, 2015.

[72] Ziye Dong, Caroline C. Ahrens, Dan Yu, Zhenya Ding, Hyun Taek Lim, and Wei Li. Cell Isolation and Recovery Using Hollow Glass Microspheres Coated with Nanolayered Films for Applications in Resource-Limited Settings. *ACS Applied Materials and Interfaces*, 9(18):15265–15273, 2017.

[73] Shu-I Tu, J. Uknalis, M. Gore, Peter Irwin, and I. Feder. Factors Affecting the Bacterial Capture Efficiency of Immuno Beads: a Comparison Between Beads With Different Size and Density1. *Journal of Rapid Methods Automation in Microbiology*, 11(1):35–46, 2003.

[74] Peter Irwin, William Damert, Jeffrey Brewster, Andrew Gehring, and Shu-I Tu. Immuno-magnetic bead mass transport and capture efficiency at low target cell densities in phosphate-buffered saline. *Journal of Rapid Methods and Automation in Microbiology*, 10:129–147, 2002.

[75] Peter Irwin, William Damert, and Shu-I Tu. Immuno-magnetic bead mass transport and capture efficiency at high target cell densities in phosphate-buffered saline. *Journal of Rapid Methods and Automation in Microbiology*, 11:265–284, 2004.

[76] Xiao Li Chen, Hao Zheng, Wen Ge Li, You Hong Zhong, Xiao Ping Chen, and Jin Xing Lu. Direct blood culturing of Candida spp. On solid medium by a rapid enrichment method with magnetic beads coated with recombinant human mannan-binding lectin. *Journal of Clinical Microbiology*, 58(4), 2020.

[77] Z. Bukhari, R. M. McCuin, C. R. Fricker, and J. L. Clancy. Immunomagnetic separation of Cryptosporidium parvum from source water samples of various turbidities. *Applied and Environmental Microbiology*, 64(11):4495–4499, 1998.

[78] Xiaoli Wu, Junye Liu, Hongpeng Zhang, Hua Zhou, Wen Wang, Yuanyan Ma, Shimei Shen, Xuefei Cai, Ailong Huang, and Deqiang Wang. Immunomolecular assay based on selective virion capture by spike antibody and viral nucleic acid amplification for detecting intact SARS-CoV-2 particles. *Journal of Nanobiotechnology*, 20(1):1–12, 2022.

[79] Yuzhi Shi, Kim Truc Nguyen, Lip Ket Chin, Zhenyu Li, Limin Xiao, Hong Cai, Ruozhen Yu, Wei Huang, Shilun Feng, Peng Huat Yap, Jingquan Liu, Yi Zhang, and Ai Qun Liu. Trapping and Detection of Single Viruses in an Optofluidic Chip. *ACS Sensors*, 6(9):3445–3450, 2021.

[80] Grace D. Chen, Catharina J. Alberts, William Rodriguez, and Mehmet Toner. Concentration and purification of human immunodeficiency virus type 1 virions by microfluidic separation of superparamagnetic nanoparticles. *Analytical Chemistry*, 82(2):723–728, 2010.

[81] Hali Bordelon, Patricia K. Russ, David W. Wright, and Frederick R. Haselton. A Magnetic Bead-Based Method for Concentrating DNA from Human Urine for Downstream Detection. *PLoS ONE*, 8(7), 2013.

[82] Dongwoo Kim, Weston L. Daniel, and Chad A. Mirkin. Microarray-based multiplexed scanometric immunoassay for protein cancer markers using gold nanoparticle probes. *Analytical Chemistry*, 81(21):9183–9187, 2009.

[83] James J. Storhoff, Robert Elghanian, Robert C. Mucic, Chad A. Mirkin, and Robert L. Letsinger. One-pot colorimetric differentiation of polynucleotides with single base imperfections using gold nanoparticle probes. *Journal of the American Chemical Society*, 120(9):1959–1964, 1998.

[84] Jwa-min Nam, C Shad Thaxton, and Chad A Mirkin. Nanoparticle-Based Bio – Bar Codes for the Ultrasensitive Detection of Proteins. *Science*, 301(September):1884–1887, 2003.

[85] Stephen Bruinsma, Joshua Burgess, Daniel Schlingman, Agata Czyz, Natalie Morrell, Catherine Ballenger, Heather Meinholz, Lee Brady, Anupama Khanna, Lindsay Freeberg, Rosamond G. Jackson, Pascale Mathonet, Susan C. Verity, Andrew F. Slatter, Rooz Golshani, Haiying Grunenwald, Gary P. Schroth, and Niall A. Gormley. Bead-linked transposomes enable a normalization-free workflow for NGS library preparation. *BMC Genomics*, 19(1):1–16, 2018.

[86] T. Lea, F. Vartdal, K. Nustad, S. Funderud, A. Berge, T. Ellingsen, R. Schmid, P. Stenstad, and J. Ugelstad. Monosized, magnetic polymer particles: Their use in separation of cells and subcellular components, and in the study of lymphocyte function in vitro. *Journal of Molecular Recognition*, 1(1):9–18, 1988.

[87] John Ugelstad, Ørjan Olsvik, Ruth Schmid, Arvid Berge, Steinar Funderud, and Kjell Nustad. Immunoaffinity separation of cells using monosized magnetic polymer beads. In *Molecular Interactions in Bioseparations*, pages 229–244. 1993.

[88] Dennis Bray. *Cell Movements: From Molecules to Motility, 2nd Edition*. 2001.

[89] Dan Wu and Joel Voldman. An integrated model for bead-based immunoassays. *Biosensors and Bioelectronics*, 154(October 2019):112070, 2020.

[90] Ali Nadim. Modeling of mass transfer limitation in biomolecular assays. *Annals of the New York Academy of Sciences*, 1161:34–43, 2009.

[91] Lloyd A. Spielman. Particle capture from low-speed laminar flows. *Annual Review of Fluid Mechanics*, 9:297–319, 1977.

[92] Ralph E. Pasceri and S. K. Friedlander. The efficiency of fibrous aerosol filters: Deposition by diffusion of particles of finite diameter. *The Canadian Journal of Chemical Engineering*, 38(6):212–213, 1960.

[93] S. K. Friedlander. Mass and heat transfer to single spheres and cylinders at low Reynolds numbers. *AIChE Journal*, 3(1):43–48, 1957.

[94] Jonasz Słomka, Uria Alcolombri, Eleonora Secchi, Roman Stocker, and Vicente I. Fernandez. Encounter rates between bacteria and small sinking particles. *New Journal of Physics*, 22(4), 2020.

[95] Xiaoxiao Chen, Thomas F. Leary, and Charles Maldarelli. Transport of biomolecules to binding partners displayed on the surface of microbeads arrayed in traps in a microfluidic cell. *Biomicrofluidics*, 11(1), 2017.

[96] Lloyd A. Spielman. Particle capture from low-speed laminar flows. *Annual Review of Fluid Mechanics*, 9:297–319, 1977.

[97] S.K. Friedlander. A note on transport to spheres in Stokes flow. *AIChE Journal*, 7(2):7–8, 1961.

[98] R. Parnas and S. K. Friedlander. Particle deposition by diffusion and interception from boundary layer flows. *Aerosol Science and Technology*, 3(1):3–8, 1984.

[99] Kyoo Won Lee and James A Gieseke. Collection of aerosol particles by packed beds. *Environmental Science and Technology*, 13(4):466–470, 1979.

[100] S. K. Friedlander. Particle diffusion in low-speed flows. *Journal of Colloid And Interface Science*, 23(2):157–164, 1967.

[101] James W. Piper, Robert A. Swerlick, and Cheng Zhu. Determining force dependence of two-dimensional receptor-ligand binding affinity by centrifugation. *Biophysical Journal*, 74(1):492–513, 1998.

[102] Tadayuki Yago, Veronika I. Zarnitsyna, Arkadiusz G. Klopocki, Rodger P. McEver, and Cheng Zhu. Transport governs flow-enhanced cell tethering through L-selectin at threshold shear. *Biophysical Journal*, 92(1):330–342, 2007.

[103] Jered B. Haun and Daniel A. Hammer. Quantifying nanoparticle adhesion mediated by specific molecular interactions. *Langmuir*, 24(16):8821–8832, 2008.

[104] Jered B. Haun, Gregory P. Robbins, and Daniel A. Hammer. Engineering therapeutic nanocarriers with optimal adhesion for targeting. *Journal of Adhesion*, 86(1):131–159, 2010.

[105] Jered B. Haun, Lauren R. Pepper, Eric T. Boder, and Daniel A. Hammer. Using engineered single-chain antibodies to correlate molecular binding properties and nanoparticle adhesion dynamics. *Langmuir*, 27(22):13701–13712, 2011.

[106] Todd M. Squires, Robert J. Messinger, and Scott R. Manalis. Making it stick: Convection, reaction and diffusion in surface-based biosensors. *Nature Biotechnology*, 26(4):417–426, 2008.

[107] Byron Goldstein, Daniel Coombs, Xiaoyi He, Angel R. Pineda, and Carla Wofsy. The influence of transport on the kinetics of binding to surface receptors: Application to cells and BIAcore. *Journal of Molecular Recognition*, 12(5):293–299, 1999.

[108] Tamra Mason, Angel R. Pineda, Carla Wofsy, and Byron Goldstein. Effective rate models for the analysis of transport-dependent biosensor data. *Mathematical Biosciences*, 159(2):123–144, 1999.

[109] Kyung Chan Park, David C. Gaze, Paul O. Collinson, and Michael S. Marber. Cardiac troponins: From myocardial infarction to chronic disease. *Cardiovascular Research*, 113(14):1708–1718, 2017.

[110] Zunlong Ke, Joaquin Oton, Kun Qu, Mirko Cortese, Vojtech Zila, Lesley McKeane, Takanori Nakane, Jasenko Zivanov, Christopher J. Neufeldt, Berati Cerikan, John M. Lu, Julia Peukes, Xiaoli Xiong, Hans Georg Kräusslich, Sjors H.W. Scheres, Ralf Bartenschlager, and John A.G. Briggs. Structures and distributions of SARS-CoV-2 spike proteins on intact virions. *Nature*, 588(7838):498–502, 2020.

[111] Kenneth A. Davis, Barnaby Abrams, Sujata B. Iyer, Robert A. Hoffman, and James E. Bishop. Determination of CD4 antigen density on cells: Role of antibody valency, avidity, clones, and conjugation. *Cytometry*, 33(2):197–205, 1998.

[112] Gil U. Lee, David A. Kidwell, and Richard J. Colton. Sensing Discrete Streptavidin–Biotin Interactions with Atomic Force Microscopy. *Langmuir*, 10(2):354–357, 1994.

[113] Stephanie Allen, Xinyong Chen, John Davies, Martyn C. Davies, Adrian C. Dawkes, John C. Edwards, Clive J. Roberts, Joanna Sefton, Saul J.B. Tendler, and Philip M. Williams. Detection of antigen-antibody binding events with the atomic force microscope. *Biochemistry*, 36(24):7457–7463, 1997.

[114] Thomas F. Scherr, Christine F. Markwalter, Westley S. Bauer, David Gasperino, David W. Wright, and Frederick R. Haselton. Application of mass transfer theory to biomarker capture by surface functionalized magnetic beads in microcentrifuge tubes. *Advances in Colloid and Interface Science*, 246:275–288, 2017.

[115] U. Dammer, M. Hegner, D. Anselmetti, P. Wagner, M. Dreier, W. Huber, and H. J. Güntherodt. Specific antigen/antibody interactions measured by force microscopy. *Biophysical Journal*, 70(5):2437–2441, 1996.

[116] Y. Harada, M. Kuroda, and A. Ishida. Specific and quantized antigen-antibody interaction measured by atomic force microscopy. *Langmuir*, 16(2):708–715, 2000.

[117] Yong Tae Kim, Kyun Joo Park, Seyl Kim, Soon Ae Kim, Seok Jae Lee, Do Hyun Kim, Tae Jae Lee, and Kyoung G. Lee. Portable vibration-assisted filtration device for on-site isolation of blood cells or pathogenic bacteria from whole human blood. *Talanta*, 179(November 2017):207–212, 2018.

[118] Jeong Gun Lee, Kwang Ho Cheong, Nam Huh, Suhyeon Kim, Jeong Woo Choi, and Christopher Ko. Microchip-based one step DNA extraction and real-time PCR in one chamber for rapid pathogen identification. *Lab on a Chip*, 6(7):886–895, 2006.

[119] Bowen Shu, Chunsun Zhang, and Da Xing. A sample-to-answer, real-time convective polymerase chain reaction system for point-of-care diagnostics. *Biosensors and Bioelectronics*, 97(March):360–368, 2017.

[120] Vivek Kamat, Sulaxna Pandey, Kishore Paknikar, and Dhananjay Bodas. A facile one-step method for cell lysis and DNA extraction of waterborne pathogens using a microchip. *Biosensors and Bioelectronics*, 99(July 2017):62–69, 2018.

[121] Elena Boselli, Zhizhen Wu, Alexa Friedman, Birgit Claus Henn, and Ian Papautsky. Validation of Electrochemical Sensor for Determination of Manganese in Drinking Water. *Environmental Science and Technology*, 55(11):7501–7509, 2021.

[122] Bumseok Namgung, Taewoo Lee, Justin Kok Soon Tan, Daren Kiat How Poh, Soyeon Park, Kevin Ziyang Chng, Rupesh Agrawal, Sung Yong Park, Hwa Liang Leo, and Sangho Kim. Vibration motor-integrated low-cost, miniaturized system for rapid quantification of red blood cell aggregation. *Lab on a Chip*, 20(21):3930–3937, 2020.

[123] Joo H. Kang, Michael Super, Chong Wing Yung, Ryan M. Cooper, Karel Domansky, Amanda R. Graveline, Tadanori Mammoto, Julia B. Berthet, Heather Tobin, Mark J. Cartwright, Alexander L. Watters, Martin Rottman, Anna Waterhouse, Akiko Mammoto, Nazita Gamini, Melissa J. Rodas, Anxhela Kole, Amanda Jiang, Thomas M. Valentin, Alexander Diaz, Kazue Takahashi, and Donald E. Ingber. An extracorporeal blood-cleansing device for sepsis therapy. *Nature Medicine*, 20(10):1211–1216, 2014.

[124] Corina Fetecau, D. Vieru, and Constantin Fetecau. A note on the second problem of Stokes for Newtonian fluids. *International Journal of Non-Linear Mechanics*, 43(5):451–457, 2008.

[125] Benjamin T. Seiler, Mark Cartwright, Alexandre L.M. Dinis, Shannon Duffy, Patrick Lombardo, David Cartwright, Elana H. Super, Jacqueline Lanzaro, Kristen Dugas, Michael Super, and Donald E. Ingber. Broad-spectrum capture of clinical pathogens using engineered fc-mannose-binding lectin enhanced by antibiotic treatment [version 1; peer review: 2 approved]. *F1000Research*, 8, 2019.

[126] Mark Cartwright, Martin Rottman, Nathan I. Shapiro, Benjamin Seiler, Patrick Lombardo, Nazita Gamini, Julie Tomolonis, Alexander L. Watters, Anna Waterhouse, Dan Leslie, Dana Bolgen, Amanda Graveline, Joo H. Kang, Tohid Didar, Nikolaos Dimitrakakis, David Cartwright, Michael Super, and Donald E. Ingber. A Broad-Spectrum Infection Diagnostic that Detects Pathogen-Associated Molecular Patterns (PAMPs) in Whole Blood. *EBioMedicine*, 9:217–227, 2016.

[127] R. M. Dommett, N. Klein, and M. W. Turner. Mannose-binding lectin in innate immunity: Past, present and future. *Tissue Antigens*, 68(3):193–209, 2006.

[128] J. Sauvola and M. Pietikäinen. Adaptive document image binarization. *Pattern Recognition*, 33(2):225–236, 2000.

[129] Etienne Roux, Pauline Bougaran, Pascale Dufourcq, and Thierry Couffinhal. Fluid Shear Stress Sensing by the Endothelial Layer. *Frontiers in Physiology*, 11(July):1–17, 2020.

[130] Kristopher S. Cunningham and Avrum I. Gotlieb. The role of shear stress in the pathogenesis of atherosclerosis. *Laboratory Investigation*, 85(1):9–23, 2005.

[131] Emanuele Ostuni, Robert G. Chapman, R. Erik Holmlin, Shuichi Takayama, and George M. Whitesides. A survey of structure-property relationships of surfaces that resist the adsorption of protein. *Langmuir*, 17(18):5605–5620, 2001.

[132] P. Harder, M. Grunze, R. Dahint, G. M. Whitesides, and P. E. Laibinis. Molecular conformation in oligo(ethylene glycol)-terminated self-assembled monolayers on gold and silver surfaces determines their ability to resist protein adsorption. *Journal of Physical Chemistry B*, 102(2):426–436, 1998.

[133] K. Feldman, G. Hähner, N. D. Spencer, P. Harder, and M. Grunze. Probing resistance to protein adsorption of oligo(ethylene glycol)- terminated self-assembled monolayers by scanning force microscopy. *Journal of the American Chemical Society*, 121(43):10134–10141, 1999.

[134] Deborah Leckband and Jacob Israelachvili. *Intermolecular forces in biology*, volume 34. MIT Libraries, 2001.

[135] M. W. Turner. The role of mannose-binding lectin in health and disease. *Molecular Immunology*, 40(7):423–429, 2003.

[136] J. G. Kenna, G. N. Major, and R. S. Williams. Methods for reducing non-specific antibody binding in enzyme-linked immunosorbent assays. *Journal of Immunological Methods*, 85(2):409–419, 1985.

[137] Kathryn L. Brogan, Jae Ho Shin, and Mark H. Schoenfisch. Influence of surfactants and antibody immobilization strategy on reducing nonspecific protein interactions for molecular recognition force microscopy. *Langmuir*, 20(22):9729–9735, 2004.

[138] Rachel Pearce Pratt and Bruce Roser. Comparison of Blocking Agents. Technical report, 2014.

[139] Peter Esser. Blocking Agent and Detergent in ELISA. Technical report, 1991.

[140] Rajan Sharma, Yudhishthir S. Rajput, Poonam, Gaurav Dogra, and Sudhir K. Tomar. Estimation of sugars in milk by HPLC and its application in detection of adulteration of milk with soymilk. *International Journal of Dairy Technology*, 62(4):514–519, 2009.

[141] Angela Casillo, Antonio Fabozzi, Irene Russo Krauss, Ermenegilda Parrilli, Caroline I. Biggs, Matthew I. Gibson, Rosa Lanzetta, Marie Sousai Appavou, Aurel Radulescu, Maria L. Tutino, Luigi Paduano, and Maria M. Corsaro.

Physicochemical Approach to Understanding the Structure, Conformation, and Activity of Mannan Polysaccharides. *Biomacromolecules*, 22(4):1445–1457, 2021.

[142] Georgina M.S. Ross, Daniel Filippini, Michel W.F. Nielen, and Gert I.J. Salentijn. Unraveling the Hook Effect: A Comprehensive Study of High Antigen Concentration Effects in Sandwich Lateral Flow Immunoassays. *Analytical Chemistry*, 92(23):15587–15595, 2020.

[143] A. J. Goldman, R. G. Cox, and H. Brenner. Slow viscous motion of a sphere parallel to a plane wall-II Couette flow. *Chemical Engineering Science*, 22(4):653–660, 1967.

[144] Jeffrey R. Smart, Sean Beimfohr, and David T. Leighton. Measurement of the translational and rotational velocities of a noncolloidal sphere rolling down a smooth inclined plane at low Reynolds number. *Physics of Fluids A*, 5(1):13–24, 1992.

[145] K. P. Galvin, Y. Zhao, and R. H. Davis. Time-averaged hydrodynamic roughness of a noncolloidal sphere in low Reynolds number motion down an inclined plane. *Physics of Fluids*, 13(11):3108–3119, 2001.

[146] Edith S. Grabbe. Total Internal Reflection Fluorescence with Energy Transfer: A Method for Analyzing IgG Adsorption on Nylon Thin Films. *Langmuir*, 9(6):1574–1581, 1993.

[147] Yih Horng Tan, Maozi Liu, Birte Nolting, Joan G Go, Jacquelyn Gervay-hague, and Gang-yu Liu. A nanoengineering approach for investigation and regulation of protein immobilization. *ACS Nano*, 2(11):2374–2384, 2008.

[148] Kevin J. Land, Debrah I. Boeras, Xiang Sheng Chen, Andrew R. Ramsay, and Rosanna W. Peeling. REASSURED diagnostics to inform disease control strategies, strengthen health systems and improve patient outcomes. *Nature Microbiology*, 4(1):46–54, 2019.

[149] O Neth, D L Jack, A W Dodds, H Holzel, N J Klein, and M W Turner. Mannose-binding lectin binds to a range of clinically relevant microorganisms and promotes complement deposition. *Infection and immunity*, 68(2):688–93, feb 2000.

[150] S. H. Behrens and D. G. Grier. The charge of glass and silica surfaces. *Journal of Chemical Physics*, 115(14):6716–6721, 2001.

[151] Nadine Tarantino, Jean Yves Tinevez, Elizabeth Faris Crowell, Bertrand Boisson, Ricardo Henriques, Musa Mhlanga, Fabrice Agou, Alain Israël, and Emmanuel Laplantine. Tnf and il-1 exhibit distinct ubiquitin requirements for inducing NEMO-IKK supramolecular structures. *Journal of Cell Biology*, 204(2):231–245, 2014.

[152] H. Qian, M. P. Sheetz, and E. L. Elson. Single particle tracking. Analysis of diffusion and flow in two-dimensional systems. *Biophysical Journal*, 60(4):910–921, 1991.

[153] Michael J. Saxton and Ken Jacobson. Single-particle tracking: Applications to membrane dynamics. *Annual Review of Biophysics and Biomolecular Structure*, 26:373–399, 1997.

[154] Marco A. Catipovic, Paul M. Tyler, Josef G. Trapani, and Ashley R. Carter. Improving the quantification of Brownian motion. *American Journal of Physics*, 81(7):485–491, 2013.

[155] Søren Hansen and Uffe Holmskov. Structural aspects of collectins and receptors for collectins. *Immunobiology*, 199(2):165–189, 1998.

[156] C. Cozens-Roberts, J. A. Quinn, and D. A. Lauffenberger. Receptor-mediated adhesion phenomena. Model studies with the Radical-Flow Detachment Assay. *Biophysical Journal*, 58(1):107–125, 1990.

[157] V. Adrian Parsegian. *Van der Waals Forces: A Handbook for Biologists, Chemists, Engineers, and Physicists*. Cambridge University Press, 2005.

[158] Avshalom Offner and Guy Z. Ramon. The interaction of a particle and a polymer brush coating a permeable surface. *Journal of Fluid Mechanics*, 913:1–11, 2021.

[159] Klaus Arnold, Andreas Herrmann, Lothar Pratsch, and Klaus Gawrisch. The dielectric properties of aqueous solutions of poly(ethylene glycol) and their influence on membrane structure. *BBA - Biomembranes*, 815(3):515–518, 1985.

[160] Geir Fonnum, Christer Johansson, Astrid Molteberg, Steen Mørup, and Elin Aksnes. Characterisation of Dynabeads® by magnetization measurements and Mössbauer spectroscopy. *Journal of Magnetism and Magnetic Materials*, 293(1):41–47, 2005.

[161] J. Israelachvili. The different faces of poly(ethylene glycol). *Proceedings of the National Academy of Sciences of the United States of America*, 94(16):8378–8379, 1997.

[162] Cara S. Kosack, Anne Laure Page, and Paul R. Klatser. A guide to aid the selection of diagnostic tests. *Bulletin of the World Health Organization*, 95(9):639–645, 2017.

[163] Arman Postagian. Cardiac troponins. *General Medicine*, 6(3):32–37, 2004.

[164] Vinay S. Mahajan and Petr Jarolim. How to interpret elevated cardiac troponin levels. *Circulation*, 124(21):2350–2354, 2011.

[165] Ryan Wereski, Dorien M. Kimenai, Caelan Taggart, Dimitrios Doudesis, Kuan Ken Lee, Matthew T.H. Lowry, Anda Bularga, David J. Lowe, Takeshi Fujisawa, Fred S. Apple, Paul O. Collinson, Atul Anand, Andrew R. Chapman, and Nicholas L. Mills. Cardiac Troponin Thresholds and Kinetics to Differentiate Myocardial Injury and Myocardial Infarction. *Circulation*, 144(7):528–538, 2021.

[166] GBD 2019 Diseases and Injuries Collaborators. Global burden of 369 diseases and injuries in 204 countries and territories, 1990–2019: a systematic analysis for the Global Burden of Disease Study 2019. *The Lancet*, 396(10258):1204–1222, 2020.

[167] Alan H.B. Wu, Yue Jin Feng, Robert Moore, Fred S. Apple, Paul H. Mcpherson, Kenneth F. Buechler, and Geza Bodor. Characterization of cardiac-troponin subunit release into serum after acute myocardial infarction and comparison of assays for troponin T and I. *Clinical Chemistry*, 44(6):1198–1208, 1998.

[168] Dirk Westermann, Johannes Tobias Neumann, Nils Arne Sörensen, and Stefan Blankenberg. High-sensitivity assays for troponin in patients with cardiac disease. *Nature Reviews Cardiology*, 14(8):472–483, 2017.

[169] Louise Cullen, Paul O. Collinson, and Evangelos Giannitsis. Point-of-care testing with high-sensitivity cardiac troponin assays: the challenges and opportunities. *Emergency Medicine Journal*, pages 861–866, 2022.

[170] Beret E. Amundson and Fred S. Apple. Cardiac troponin assays: A review of quantitative point-of-care devices and their efficacy in the diagnosis of myocardial infarction. *Clinical Chemistry and Laboratory Medicine*, 53(5):665–676, 2015.

[171] J. Reinsberg. Different efficacy of various blocking reagents to eliminate interferences by human antimouse antibodies with a two-site immunoassay. *Clinical Biochemistry*, 29(2):145–148, 1996.

[172] David A Armbruster and Terry Pry. Limit of blank, limit of detection and limit of quantitation. *Clinical Biochemist Reviews*, 29 Suppl 1(August):S49–52, 2008.

[173] Danlu Wu, Milena Dumont Milutinovic, and David R. Walt. Single molecule array (Simoa) assay with optimal antibody pairs for cytokine detection in human serum samples. *Analyst*, 140(18):6277–6282, 2015.

[174] Gyeo Re Han, Hangil Ki, and Min Gon Kim. Automated, Universal, and Mass-Producible Paper-Based Lateral Flow Biosensing Platform for High-Performance Point-of-Care Testing. *ACS Applied Materials and Interfaces*, 12(1):1885–1894, 2020.

[175] Elisa Hemmig, Yuksel Temiz, Onur Gökçe, Robert D. Lovchik, and Emmanuel Delamarche. Transposing lateral flow immunoassays to capillary-driven microfluidics using self-coalescence modules and capillary-assembled receptor carriers. *Analytical Chemistry*, 92(1):940–946, 2020.

[176] Jill Tate and Greg Ward. Interferences in immunoassay. *Clinical Biochemist Reviews*, 25:105–120, 2004.

[177] Colin Selby. Interference in Immunoassay. *Annals of Clinical Biochemistry*, 36:704–721, 1999.

[178] Loris Wauthier, Mario Plebani, and Julien Favresse. Interferences in immunoassays: Review and practical algorithm. *Clinical Chemistry and Laboratory Medicine*, 60(6):808–820, 2022.

[179] Larry J. Kricka. Human anti-animal antibody interferences in immunological assays. *Clinical Chemistry*, 45(7):942–956, 1999.

[180] Thomas F. Fitzmaurice, Charles Brown, Nader Rifai, Alan H.B. Wu, and Kiang Teck J. Yeo. False increase of cardiac troponin I with heterophilic antibodies. *Clinical Chemistry*, 44(10):2212–2214, 1998.

[181] Robert V. Vogt, Donald L. Phillips, L. Omar Henderson, Wanda Whitfield, and Francis W. Spierto. Quantitative differences among various proteins as blocking agents for ELISA microtiter plates. *Journal of Immunological Methods*, 101(1):43–50, 1987.

[182] Ya hui Lin, Yang Zhang, Yu tao Liu, Kai Cui, Jin suo Kang, and Zhou Zhou. How to choose a point-of-care testing for troponin. *Journal of Clinical Laboratory Analysis*, 34(7):1–9, 2020.

[183] Samantha A. Byrnes, Toan Huynh, Tim C. Chang, Caitlin E. Anderson, James J. McDermott, Ciela I. Oncina, Bernhard H. Weigl, and Kevin P. Nichols. Wash-Free, Digital Immunoassay in Polydisperse Droplets. *Analytical Chemistry*, 92(5):3535–3543, 2020.